MAGNETOM Flash

The Magazine of MR

Issue Number 2/2009
ASTRO/ESTRO Edition

SIEMENS

Clinical

Product News

41

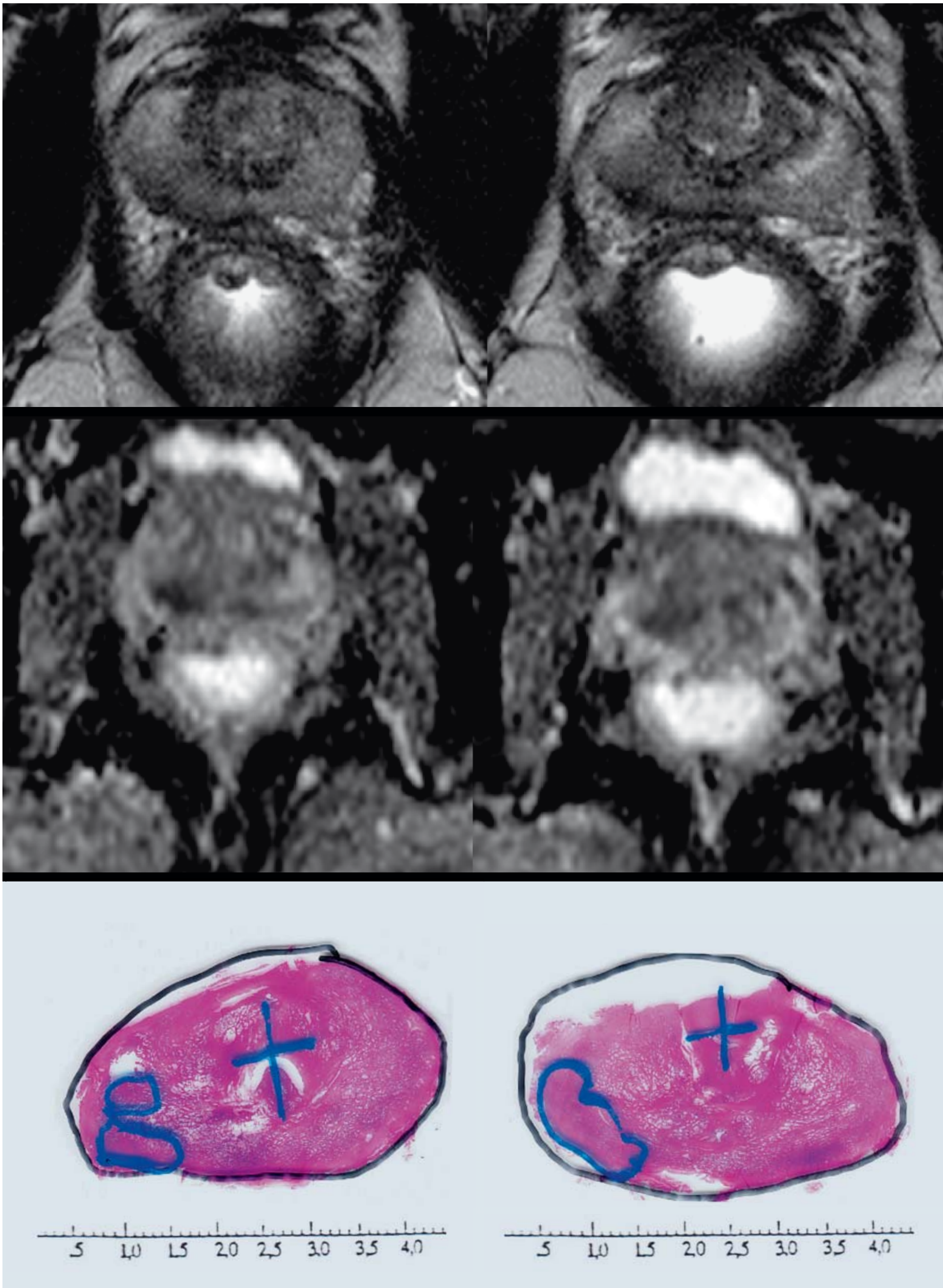

Matthias Lichy, M.D.

Dear MAGNETOM user,

Diffusion-weighted imaging (DWI) is currently one of the fastest-emerging applications for the precise detection and characterisation of lesions in the body. We explore the integration of this method in a variety of clinical scenarios. Prostate imaging, for example, is explored in an article on pre-operative local staging at 3Tesla.
In addition, *syngo* REVEAL enables us to obtain information about tumor viability, as shown in an extensive case report on a patient with nonsecretory multiple myeloma.
DWI techniques can also be used to gather additional information about perfusion within one scan. Background information about the ‘intravoxel incoherent motion’ (IVIM) technique and its clinical relevance in the differentiation of pancreatic lesions are examined in the article by Re et al., German Cancer Research Center.

The introduction of the *syngo* MR B17 software offers a variety of new industry-unique applications with a special focus on oncology. We have expanded the capabilities of the continuous table move technique (*syngo* TimCT) to include an application for tumor staging and to improve workflow. However, we can also improve workflow by using existing techniques based on our Tim technology, such as *syngo* TWIST - a technique for highly temporal resolved MR angiography (case reports by Merkle et al. on imaging of pelvic congestive syndrome).
The *syngo* MR B17 software also introduces non contrast-enhanced MR angiography techniques that provide detailed information on vessel diseases in patients who until recently had to be rejected for MRI for several reasons, including a high risk of NSF or known severe allergic reactions to former contrast applications. The first results revealed in this issue are promising and we have great expectations that this imaging technique will soon establish itself in our daily clinical routine.

We are sure you will enjoy reading this latest edition of Flash!

Matthias Lichy, M.D.

The Editorial Team

We appreciate your comments.
Please contact us at magnetomworld.med@siemens.com


Matthias Lichy, M.D.
Editor in Chief


Antje Hellwich
Associate Editor


Dagmar Thomsik-Schröpfer, Ph.D., MR Marketing-Products, Erlangen, Germany


Okan Ekinci, M.D.
Segment Manager
Cardiovascular MRI
Erlangen, Germany


Peter Kreisler, Ph.D.
Collaborations & Applications, Erlangen, Germany


Heike Weh,
Clinical Data Manager,
Erlangen, Germany


Bernhard Baden,
Clinical Data Manager,
Erlangen, Germany


Ignacio Vallines, Ph.D.,
Applications Manager,
Erlangen, Germany


Wellesley Were
MR Business Development Manager
Australia and New Zealand


Milind Dhamankar, M.D.
Sr. Director, MR Product Marketing, Malvern, USA


Michelle Kessler, US
Installed Base Manager,
Malvern, PA, USA


Gary R. McNeal, MS (BME)
Advanced Application Specialist,
Cardiovascular MR Imaging
Hoffman Estates, USA


Dr. Sunil Kumar S.L.
Senior Manager Applications,
Canada

Content

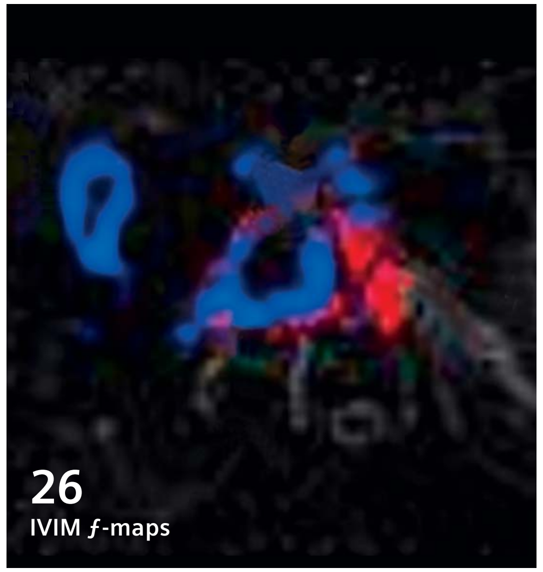

26
IVIM ƒ-maps

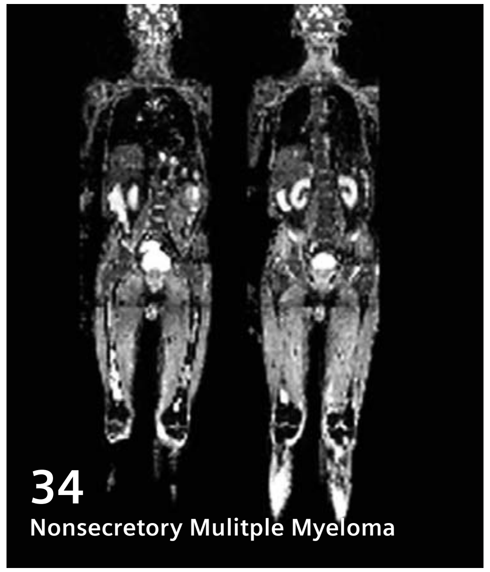

34
Nonsecretory Mulitple Myeloma

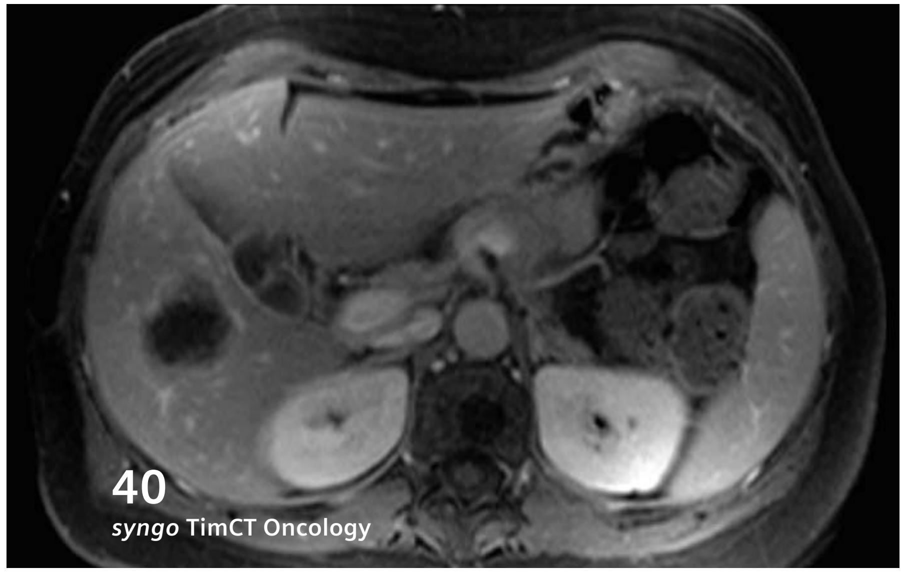

40
syngo TimCT Oncology

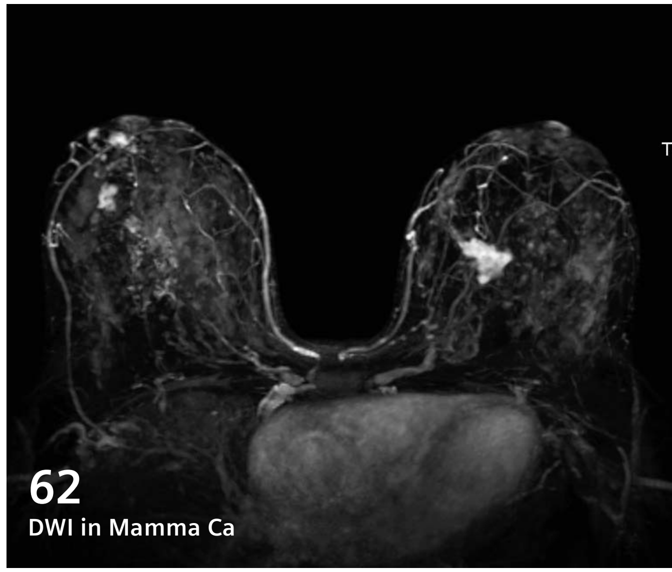

62
DWI in Mamma Ca

Product News

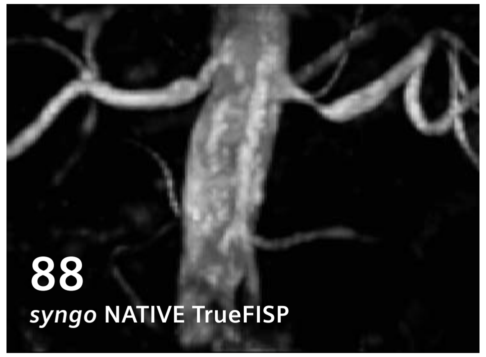

88
syngo NATIVE TrueFISP

See what is new
with software version
syngo MR B17.

Clinical Abdomen / Pelvis

Whole Body

Clinical Neurology

Clinical Cardiocascular

Clinical Women's Health

Clinical → How I do it

Technology

Product News

Assessment of Tumor Extension and Improved Localization for Planning and Nerve Sparing Radical Prostatectomy

Matthias Philipp Lichy, M.D. [1,4]; David Schilling[2], M.D; Claus H. von Weyhern[3], M.D.; Arnulf Stenzl[2], M.D.; Matthias Roehtke, M.D.[1]; Ralph Strecker, Ph.D.[4]; Wilhelm Horger[4]; Berthold Kiefer, Ph.D.[4]; Claus D. Claussen, M.D.[1]; Heinz-Peter Schlemmer, M.D., Ph.D.[1]

[1] *University Hospital Tübingen, Department of Diagnostic and Interventional Radiology, Tübingen, Germany*
[2] *University Hospital Tübingen, Department of Urology, Tübingen, Germany*
[3] *University Hospital Tübingen, Department of Pathology, Tübingen, Germany*
[4] *Siemens Healthcare Sector, Erlangen, Germany*

Introduction

Prostate cancer (PCa) is the most common malignancy in men and according to the update of the National Cancer Institute in 2005, the incidence of this malignancy in the United States of America is higher than for female breast cancer (2004: 165.3 PCa per 100.000 men; 126.4 breast cancer per 100.000 women). Also, with the widespread introduction of PSA testing a shift towards detection of PCa at an early stage of disease can be observed.

The potential of magnetic resonance imaging (MRI) for imaging PCa was already recognized and evaluated in the beginning of the wide introduction of MRI into clinical practice in the early 80's. Until recently, the combination of T2-weighted Turbo Spin Echo (T2w TSE) sequences and the application of an endorectal coil had still been considered as state-of-the-art for local tumor staging, in particular for magnetic field strengths up to 1.5 Tesla, whilst the main indication for MRI of the prostate in the daily clinical work-up had remained tumor staging for assignment of best therapy. However, clinical demands have changed dramatically during the last decade; while prostate-specific antigen (PSA) testing has significantly reduced the amount of advanced (T4/T3; N+, M+ stages) PCa at the time point of diagnosis, the refinement of surgical and radiotherapy treatment procedures like robot-assisted nerve sparing radical prostatectomy and intensity modulated radiotherapy have increased the demand for a dedicated and accurate imaging modality to provide all relevant information about extension and localisation of prostate cancer. Of course, it has been recognised since the early days of prostate MRI that due to hyperplasia of the central gland, prostatitis and bleedings (e.g. caused by former biopsies) the diagnostic accuracy of T2w TSE MRI can be clearly restricted for such a purpose. Therefore it seems to be only logical to include information provided by metabolic (MR spectroscopic imaging; MRSI) and functional imaging (diffusion-weighted imaging; *syngo* DWI and T1-weighted dynamic contrast enhanced MRI; T1w DCE) to improve the diagnostic performance of MRI.

With the introduction of the 3T MR scanner and associated increase in signal-to-noise (SNR) there is now the potential to acquire all this information without the use of an endorectal coil. Based on literature data, the application of an endorectal coil at 3T will increase the sensitivity for the detection of tumor penetration of the capsule; nevertheless, for tumor localization within the gland e.g. for planning of radiotherapy or MRI-guided biopsies and also for follow-up, deformation of the prostate introduced by the endorectal coil can be disadvantageous.

The potential of state-of-the-art MRI at 3T without endorectal coil is presented in this case report article. In both shown cases, MRI was able to improve therapy planning and the surgical outcome clearly. To improve the image quality especially of the diffusion-weighted imaging (*syngo* DWI), after a digital rectal examination 50 to 100 ml ultrasound gel was administered per rectum in both cases. Sequence parameters for the shown MR examinations were:

1. T2-weighted MRI Turbo Spin Echo (TSE) sequences:

Transversal T2w TSE:
TR 6330 ms, TE 101 ms, PAT factor 2 (*syngo* GRAPPA), FOV 200 x 200 mm, matrix 310 x 320, slice thickness 3 mm, 3 averages, acquisition time 3:04 min.

Coronal T2w TSE:
TR 4440 ms, TE 101 ms, PAT factor 2 (*syngo* GRAPPA), FOV 200 x 200 mm, matrix 310 x 320, slice thickness 3 mm, 2 averages, acquisition time 3:44 min.

Sagittal T2w TSE:
TR 5000 ms, TE 101 ms, PAT factor 2 (*syngo* GRAPPA), FOV 200 x 200 mm, matrix 310 x 320, slice thickness 3 mm, 2 averages, acquisition time 2:40 min.

2. Diffusion-weighted imaging (*syngo* DWI):

Single shot echo planar imaging (EPI):
TR 3800 ms, TE 70 ms, PAT factor 2 (*syngo* GRAPPA), SPAIR fat suppression technique, FOV 221 x 260 mm, matrix 102 x 160, 3 scan trace, ADC-mapping (Inline), **b-values:** 0 / 100 / 400 / 800 s/mm^2, slice thickness 3.6 mm, 6 averages, acquisition time 2:40 min.

3. 3D MR spectroscopic imaging:

TR 750 ms, TE 145 ms, voxel size (interpolated) 0.5 x 0.5 x 1.1 cm, averages 8, Hamming filter, spectral lipid and water suppression, acquisition time 9:14 min.

4. 3D dynamic contrast enhanced T1-weighted imaging:

syngo TWIST (GRE with echo sharing): TR 3.5 ms, TE 1.4 ms, PAT factor 2, no fat suppression, slice thickness 3.6 mm, FOV 260 x 260 mm, matrix 144 x 192, 1 average, 70 measurements, acquisition time for one data set was 04:58 min; contrast media was injected via a cubital vein in a standardized flow and dosage with the start of the first measurement (Magnevist, Bayer Schering, Germany).

→ Visit www.siemens.com/magnetom-world
for practical information on MR spectroscopic imaging of the prostate in clinical routine.

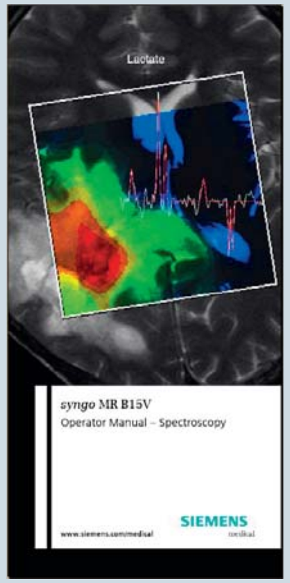

Lactate

syngo MR B15V
Operator Manual – Spectroscopy

www.siemens.com/medical

SIEMENS
medical

Starting on page 64 of the *Operator Manual – Spectroscopy* you'll find
- positioning of the patient and coil
- planning the VOI
- measurement and
- examples of spectra.

The manual also includes the evaluation of spectroscopic data with the *syngo* Spectroscopy task card and provides detailed information on the workflow of a typical 1H MRS examination in the head and breast (*syngo* GRACE).

At **www.siemens.com/magnteom-world** you can download the manuals in German and English free-of-charge.

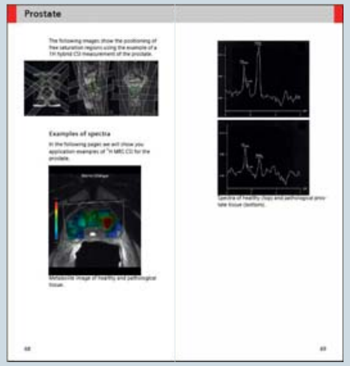

Case 1
Patient with stage T3a prostate cancer

This 61-year-old patient with biopsy proven prostate cancer and an initial total PSA level of 5.1 ng/ml was referred to our MRI unit one day before planned nerve sparing radical prostatectomy. MRI revealed a tumor with broad contact to the left dorsal capsule with main localization in the apico-medial peripheral zone and extension to the base.

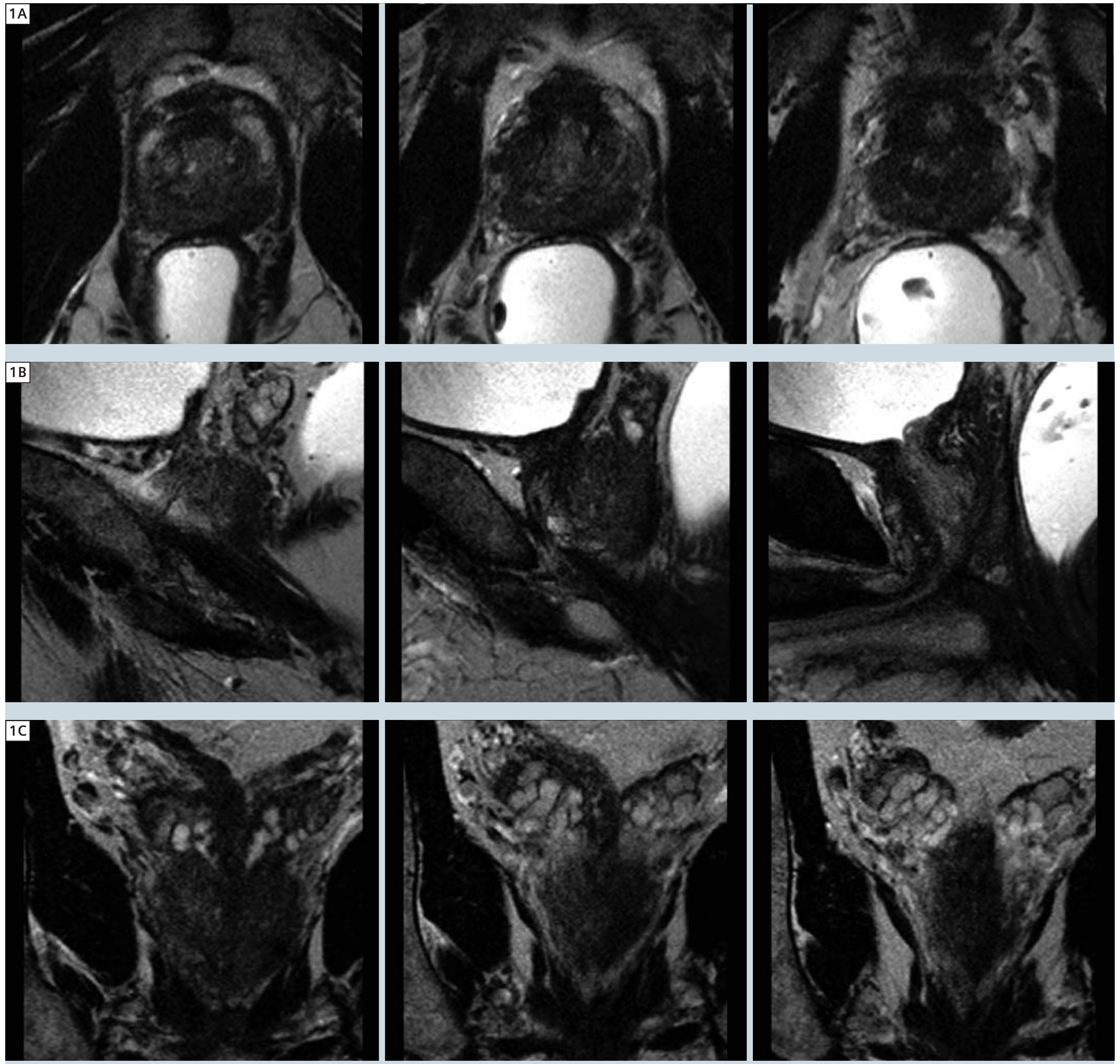

1 Exemplary chosen T2-weighted TSE images demonstrating the extent of the tumor suspicious findings (**A** transversal, **B** sagittal, **C** coronal).

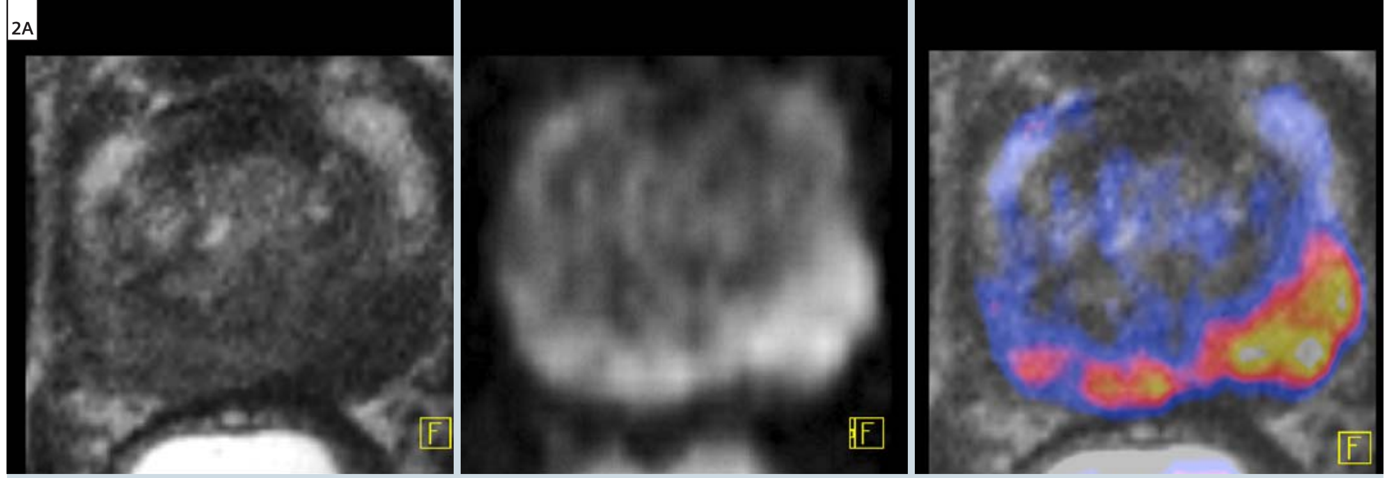

2A This figures show the clear restriction of the water diffusion within the tumorous areas. Left: T2-weighted TSE image, middle: original high b-value image (b = 800 s/mm²), right: overlay of *syngo* DWI and T2-weighted TSE image, showing perfect match, confirming the extension of the tumor.

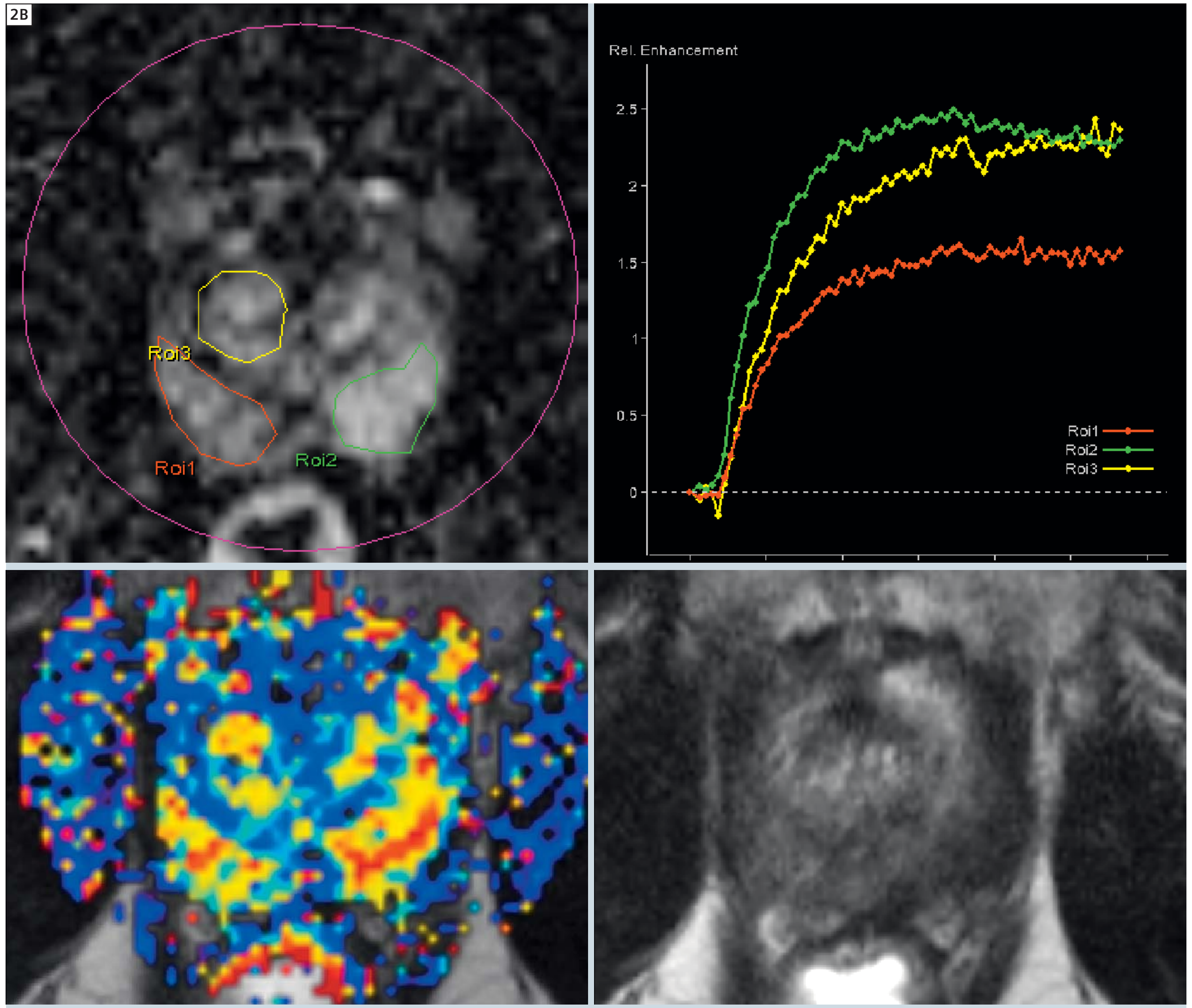

2B DCE T1-weighted image demonstrating the difference between the cancer and normal prostate tissue. Left: T1-weighted DCE image subtracted from a native mask image at the time point of the maximum peak of the signal-intensity-time curves (middle) within the tumor tissue. While standardized parameter maps do show only a slight side difference (Kep right upper image; right lower image T2-weighted reference), the signal-intensity-time curves are highly suspicious and correlate clearly with the morphologic changes on T2-weighted image.

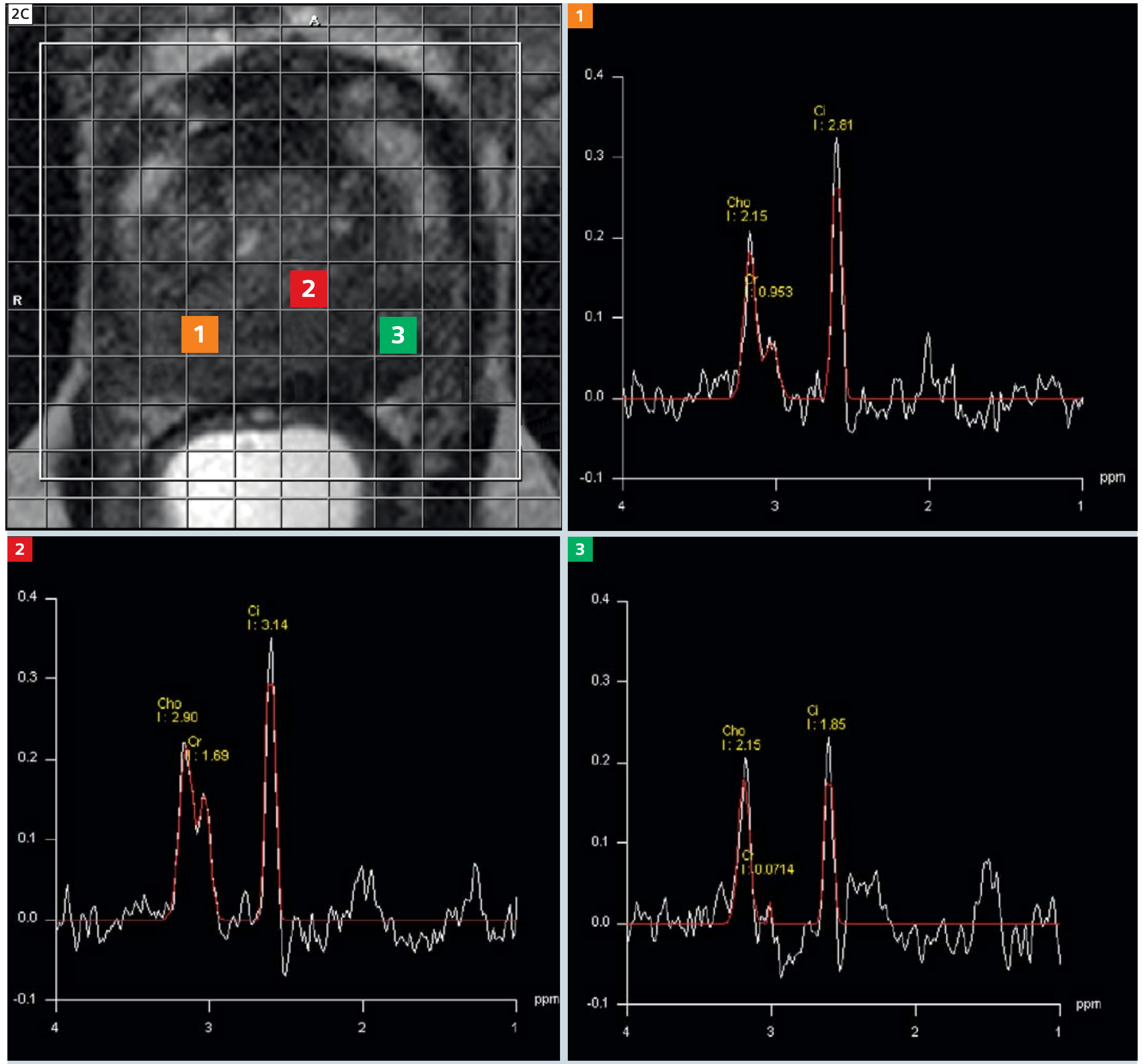

2C Exemplary chosen spectra from the base of the prostate, demonstrating the widespread tumor infiltration. In all voxels, a clear increase of the (Choline + Creatine) / Citrate ratio can be observed.

No seminal vessel infiltration and suspicious lymph nodes were found. Despite the lack of a clear extension beyond the capsule, the finding was highly suspicious for a micro penetration of the capsule, potentially negating a bilateral nerve sparing. The strong suspicion of a T3a stage was confirmed during the radical prostatectomy by an instantaneous section. To ensure oncological resection of the tumor, it was not possible to preserve the left nerve bundle. According to the MRI findings, the surgeons could spare the right nerve bundle. The prostate cancer was staged as pT3a pN0 (0/15) cM0 R0, Gleason Score 3 + 4 = 7.

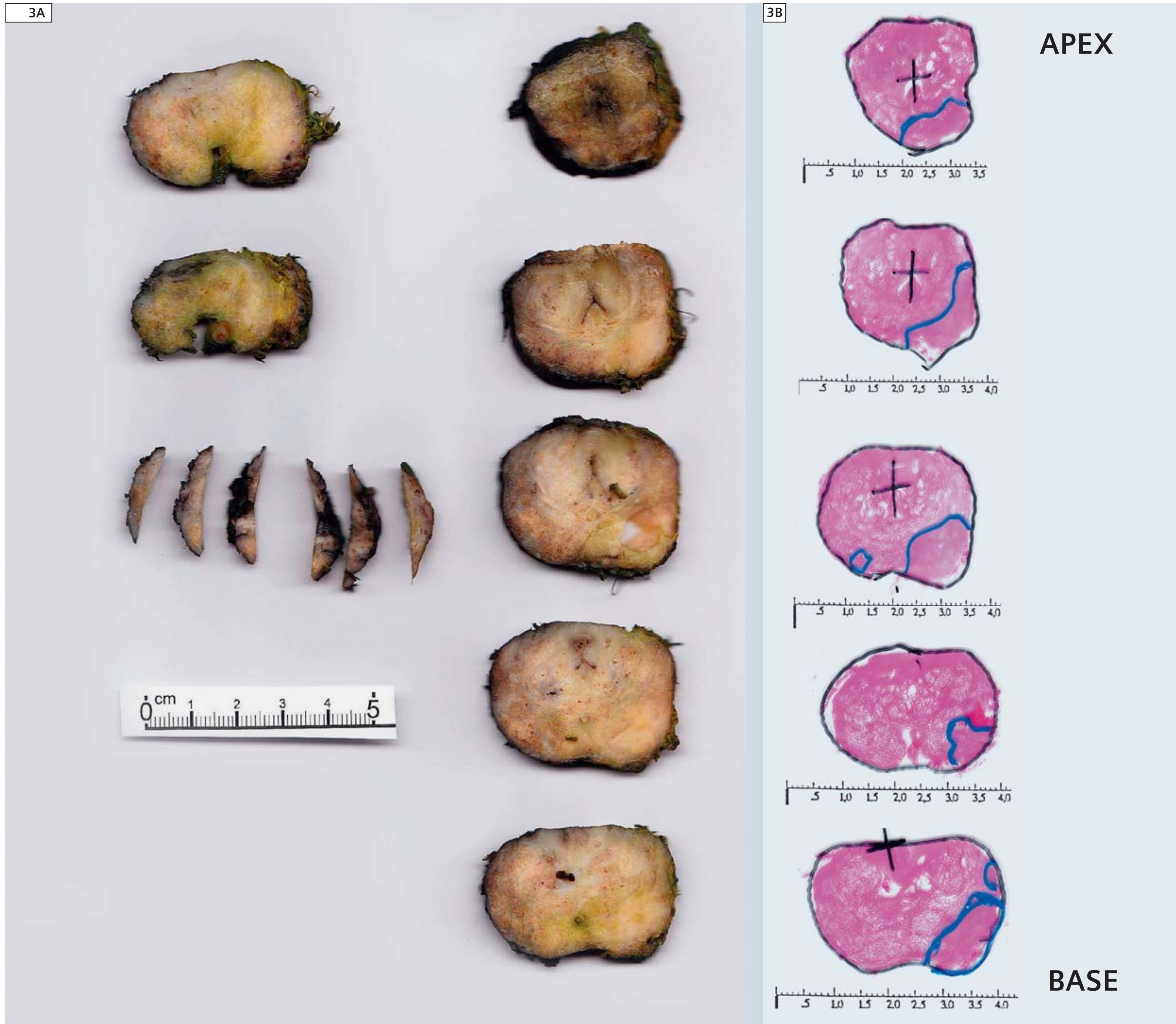

3 **A:** Macroscopic prostatectomy specimen before fixation, **B:** HE stained histopathology with marked extension of all tumor foci (blue line). A high concordance between MR findings and histophatology is obvious.

Case 2
Patient with stage T3b prostate cancer

This 63-year-old patient with biopsy-proven prostate cancer and a total PSA level of 7.51 ng/ml at the time point of surgery was referred to our MRI unit one day before planned nerve sparing radical prostatectomy. The medical history of the patient revealed a urothelium carcinoma (initial diagnosis made 6 years ago) and approx. one month before the planed radical prostatectomy, a resection of suspicious pulmonary findings was performed but no malignancy was found. The histopathology revealed heterotopic ossifications.
MRI revealed a tumor of the right dorsal gland within the peripheral zone with broad contact to the capsule. Additionally, in the right seminal vessel,

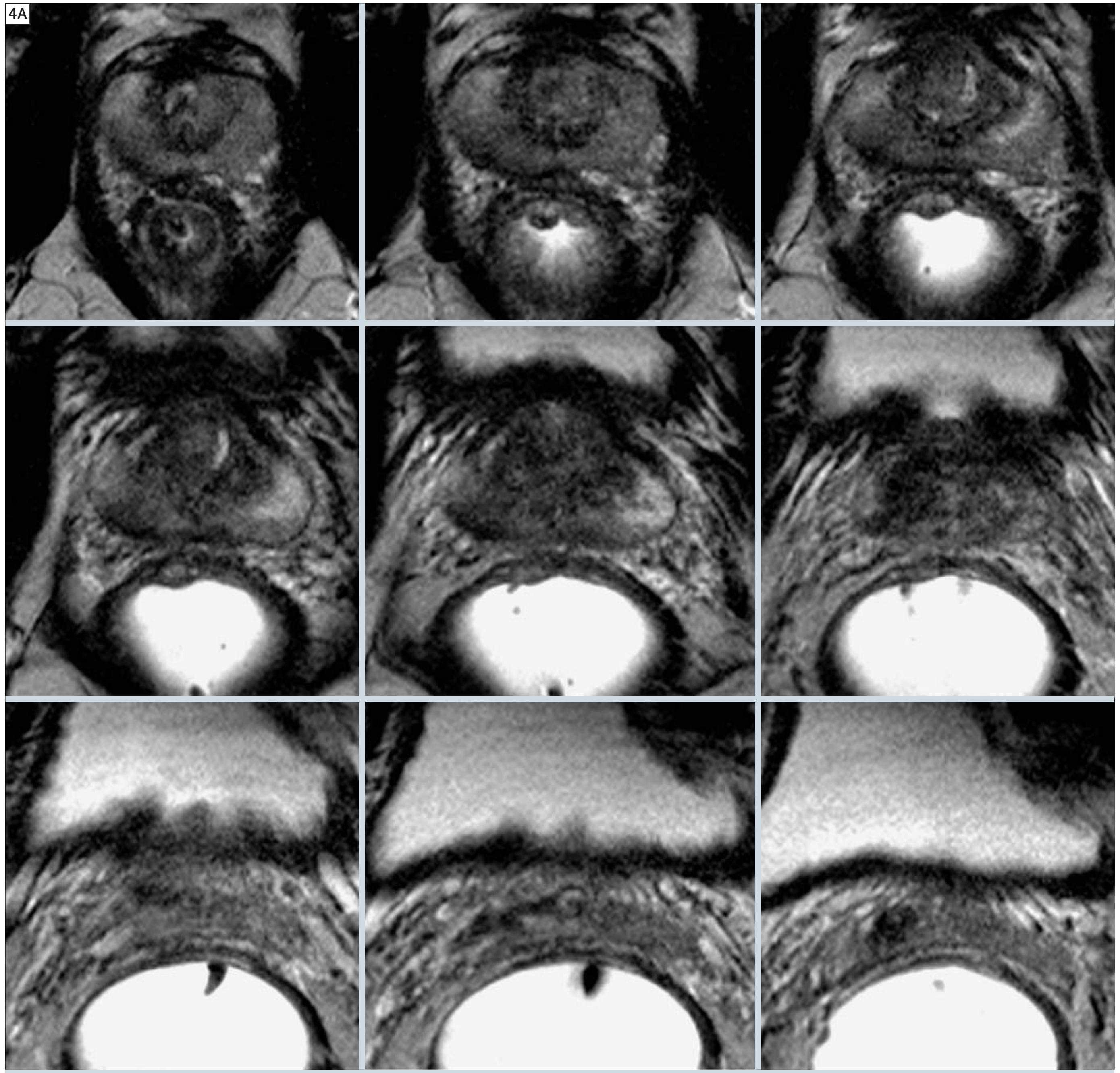

4A Exemplary chosen T2-weighted images (transversal) demonstrating the extent of the tumor suspicious findings. **D, E:** Corresponding ADC-maps, demonstrating the clear water diffusibility restriction also in the suspicious area within the right seminal vessel.

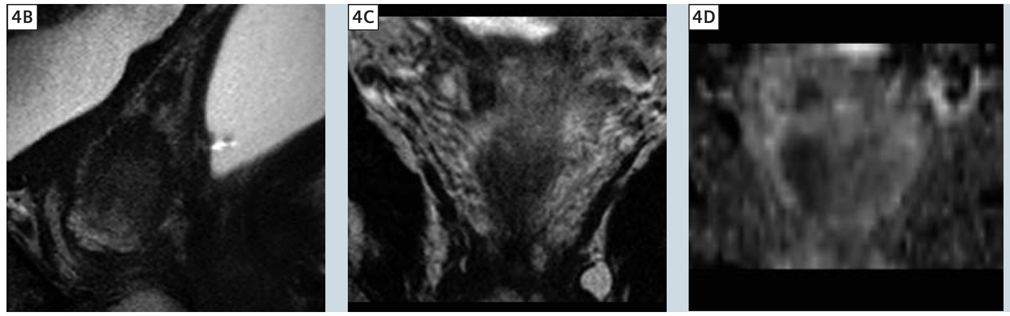

4B–D Exemplary chosen T2-weighted images (**B** sagittal, **C** coronal) demonstrating the extent of the tumor suspicious findings.
D: Corresponding ADC-maps, demonstrating the clear water diffusibility restriction also in the suspicious area within the right seminal vessel.

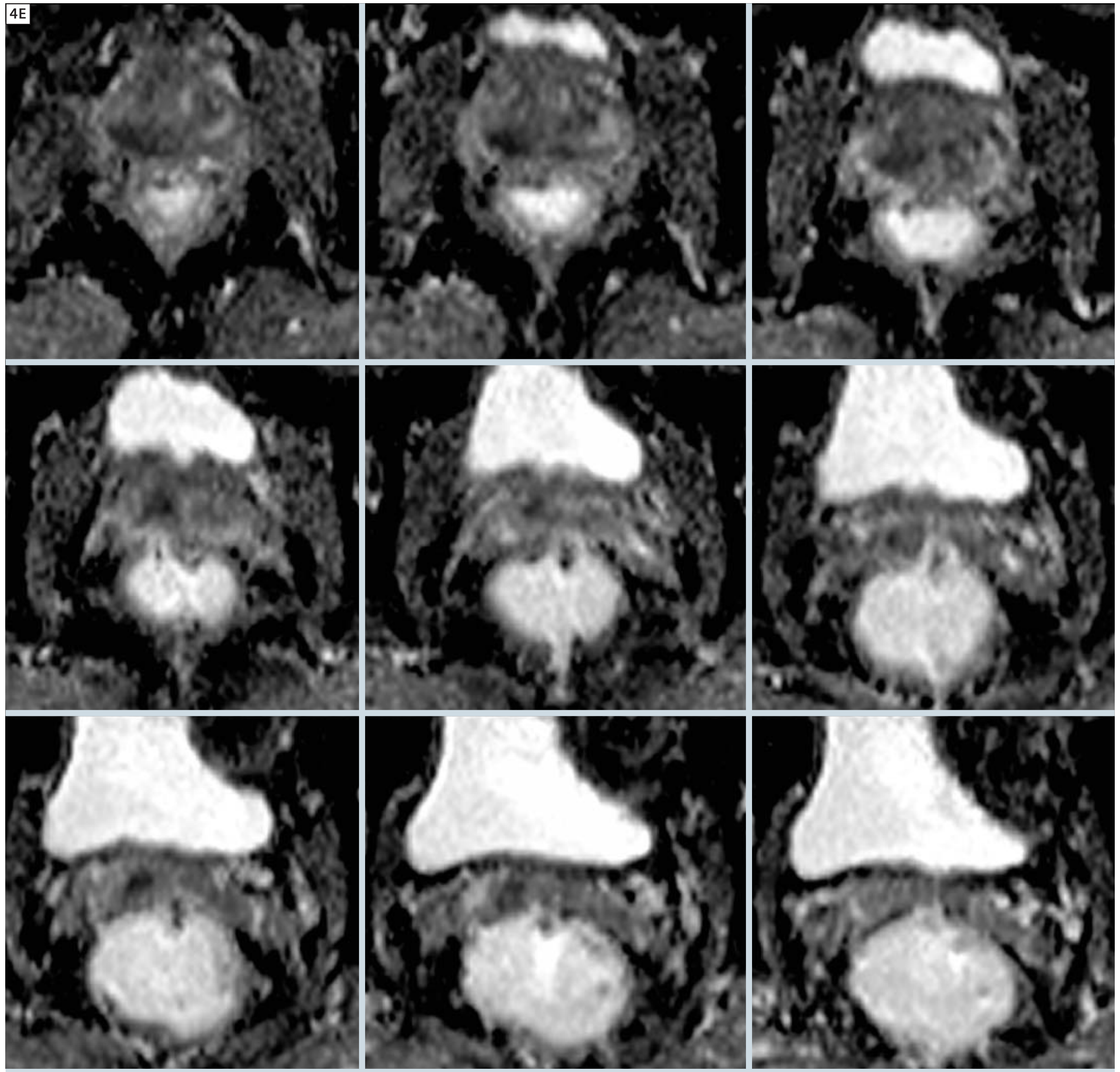

4E Corresponding ADC-maps, demonstrating the clear water diffusibility restriction also in the suspicious area within the right seminal vessel.

a T2-weighted hypointense and nodular configured area was detected. In combination with the clear restriction of the water diffusion, this finding was categorized as tumor and therefore a stage T3b was assumed. In agreement with MRI findings, the instantaneous section found capsule penetration with infiltration of the nerve bundles as well as extension towards the right seminal vessel and therefore no nerve sparing prostatectomy could be achieved (R0 resection). However, lymphadenectomy found positive pelvic lymph nodes. The prostate cancer was staged as pT3b pN1 (3/14) cMx, R0, L0, V0, Gleason Score 4 + 3 = 7.

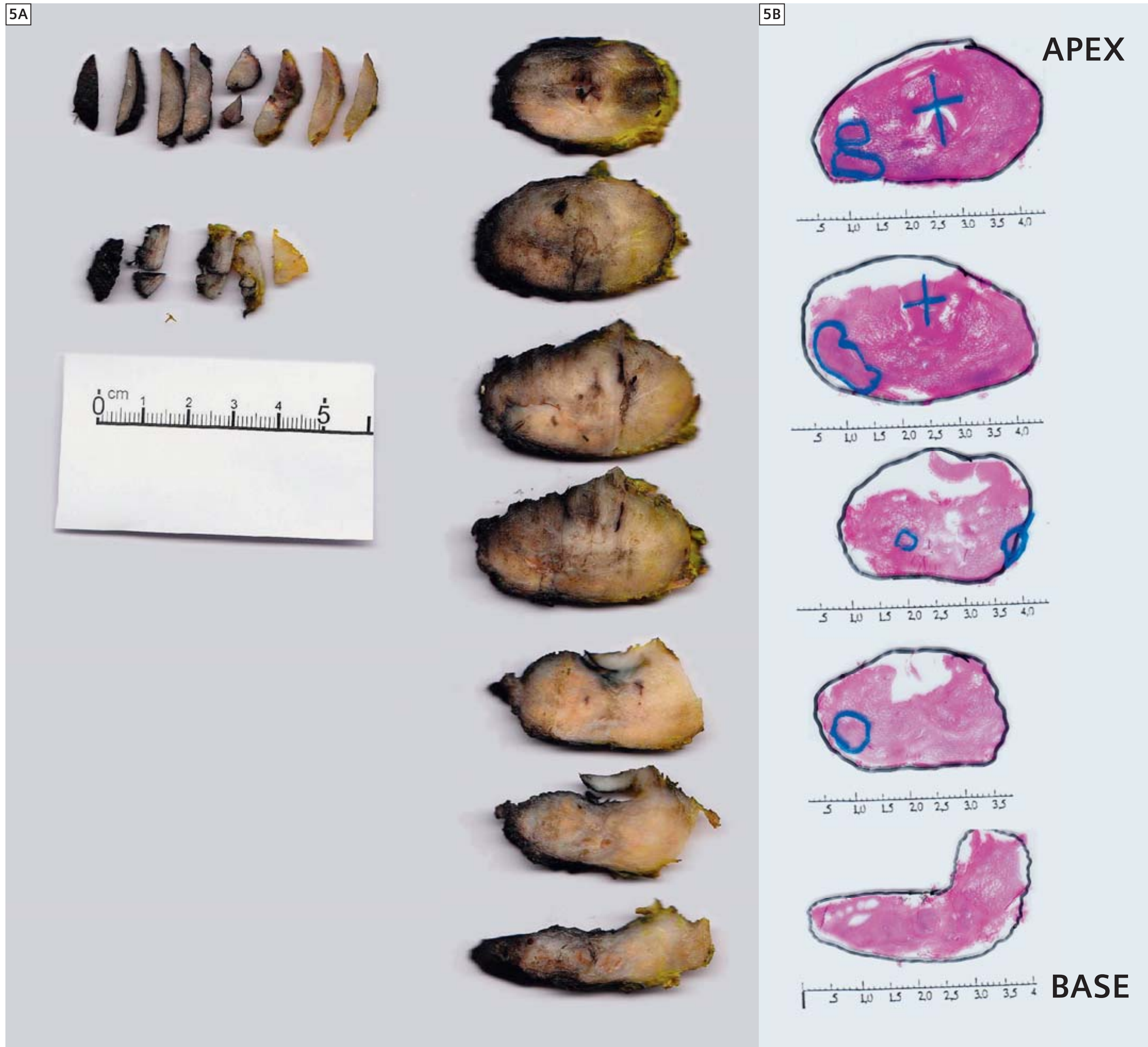

5 **A:** Macroscopic prostatectomy specimen before fixation, **B:** HE stained histopathology with marked extension of all tumor foci (blue line). A high concordance between MR findings and histophatology is obvious. The specimen of the seminal vessels and the lypmph nodes are not shown in this stage pT3b pN1case.

References

1 Goeb K, Engehausen DG, Krause FS, Hollenbach HP, Niedobitek G, Buettner M, Frangou P, Engelhard K (2007) MRI spectroscopy in screening of prostate cancer. Anticancer Res. 27(1B): 687–93.

2 Lichy MP, Anastasiadis AG, Aschoff P, Sotlar K, Eschmann SM, Pfannenberg C, Stenzl A, Claussen CD, Schlemmer HP (2007) Morphologic, functional, and metabolic magnetic resonance imaging-guided prostate biopsy in a patient with prior negative transrectal ultrasound-guided biopsies and persistently elevated prostate-specific antigen levels. Urology 69(6):1208.e5–8.

3 Anastasiadis AG, Lichy MP, Nagele U, Kuczyk MA, Merseburger AS, Hennenlotter J, Corvin S, Sievert KD, Claussen CD, Stenzl A, Schlemmer HP (2006) MRI-guided biopsy of the prostate increases diagnostic performance in men with elevated or increasing PSA levels after previous negative TRUS biopsies. Eur Urol 50(4):738–48; discussion 748–9.

4 Lichy MP, Pintaske J, Kottke R, Machann J, Anastasiadis A, Roell S, Hennenlotter J, Diergarten T, Schick F, Stenzl A, Claussen CD, Schlemmer HP (2005) 3D proton MR spectroscopic imaging of prostate cancer using a standard spine coil at 1.5 T in clinical routine: a feasibility study. Eur Radiol 15(4):653–60.

5 Kiessling F, Lichy M, Grobholz R, Heilmann M, Farhan N, Michel MS, Trojan L, Ederle J, Abel U, Kauczor HU, Semmler W, Delorme S (2004) Simple models improve the discrimination of prostate cancers from the peripheral gland by T1-weighted dynamic MRI. Eur Radiol 14(10): 1793–801.

6 Engelhard K, Hollenbach HP, Kiefer B, Winkel A, Goeb K, Engehausen D (2006) Prostate biopsy in the supine position in a standard 1.5-T scanner under real time MR-imaging control using a MR-compatible endorectal biopsy device. Eur Radiol 16(6): 1237–43.

7 Engelhard K, Hollenbach HP, Deimling M, Kreckel M, Riedl C (2000) Combination of signal intensity measurements of lesions in the peripheral zone of prostate with MRI and serum PSA level for differentiating benign disease from prostate cancer. Eur Radiol. 2000;10(12): 1947–53.

8 Scheenen TW, Heijmink SW, Roell SA, Hulsbergen-Van de Kaa CA, Knipscheer BC, Witjes JA, Barentsz JO, Heerschap A (2007) Three-dimensional proton MR spectroscopy of human prostate at 3 T without endorectal coil: feasibility. Radiology 245(2): 507–16.

9 Heijmink SW, Fütterer JJ, Hambrock T, Takahashi S, Scheenen TW, Huisman HJ, Hulsbergen-Van de Kaa CA, Knipscheer BC, Kiemeney LA, Witjes JA, Barentsz JO (2007) Prostate cancer: body-array versus endorectal coil MR imaging at 3 T--comparison of image quality, localization, and staging performance. Radiology 244(1):184–95.

10 Fütterer JJ, Engelbrecht MR, Jager GJ, Hartman RP, King BF, Hulsbergen-Van de Kaa CA, Witjes JA, Barentsz JO (2007) Prostate cancer: comparison of local staging accuracy of pelvic phased-array coil alone versus integrated endorectal-pelvic phased-array coils. Local staging accuracy of prostate cancer using endorectal coil MR imaging. Eur Radiol 17(4): 1055–65.

11 Fütterer JJ, Heijmink SW, Scheenen TW, Veltman J, Huisman HJ, Vos P, Hulsbergen-Van de Kaa CA, Witjes JA, Krabbe PF, Heerschap A, Barentsz JO (2006) Prostate cancer localization with dynamic contrast-enhanced MR imaging and proton MR spectroscopic imaging. Radiology 41(2): 449–58.

12 Fütterer JJ, Engelbrecht MR, Huisman HJ, Jager GJ, Hulsbergen-van De Kaa CA, Witjes JA, Barentsz JO (2005) Staging prostate cancer with dynamic contrast-enhanced endorectal MR imaging prior to radical prostatectomy: experienced versus less experienced readers. Radiology 237(2): 541–9.

13 Scheenen TW, Klomp DW, Röll SA, Fütterer JJ, Barentsz JO, Heerschap A (2004) Fast acquisition-weighted three-dimensional proton MR spectroscopic imaging of the human prostate. Magn Reson Med 52(1):80–8.

14 Engelbrecht MR, Huisman HJ, Laheij RJ, Jager GJ, van Leenders GJ, Hulsbergen-Van De Kaa CA, de la Rosette JJ, Blickman JG, Barentsz JO (2003) Discrimination of prostate cancer from normal peripheral zone and central gland tissue by using dynamic contrast-enhanced MR imaging. Radiology 229(1): 248–54.

15 Engelbrecht MR, Jager GJ, Laheij RJ, Verbeek AL, van Lier HJ, Barentsz JO (2002) Local staging of prostate cancer using magnetic resonance imaging: a meta-analysis. Eur Radiol 12(9): 2294–302.

16 Jager GJ, Severens JL, Thornbury JR, de La Rosette JJ, Ruijs SH, Barentsz JO (2000) Prostate cancer staging: should MR imaging be used?--A decision analytic approach. Radiology 215(2): 445-51.

17 Bloch BN, Furman-Haran E, Helbich TH, Lenkinski RE, Degani H, Kratzik C, Susani M, Haitel A, Jaromi S, Ngo L, Rofsky NM (2007) Prostate cancer: accurate determination of extracapsular extension with high-spatial-resolution dynamic contrast-enhanced and T2-weighted MR imaging--initial results. Radiology 245(1):176–85

18 Haider MA, van der Kwast TH, Tanguay J, Evans AJ, Hashmi AT, Lockwood G, Trachtenberg J (2007) Combined T2-weighted and diffusion-weighted MRI for localization of prostate cancer. AJR Am J Roentgenol 189(2):323–8.

19 Shukla-Dave A, Hricak H, Kattan MW, Pucar D, Kuroiwa K, Chen HN, Spector J, Koutcher JA, Zakian KL, Scardino PT (2007) The utility of magnetic resonance imaging and spectroscopy for predicting insignificant prostate cancer: an initial analysis. BJU Int 99(4):786-93.

20 JWang L, Zhang J, Schwartz LH, Eisenberg H, Ishill NM, Moskowitz CS, Scardino P, Hricak H (2007) Incremental value of multiplanar cross-referencing for prostate cancer staging with endorectal MRI. AJR Am J Roentgenol 188(1):99–104.

21 Akin O, Sala E, Moskowitz CS, Kuroiwa K, Ishill NM, Pucar D, Scardino PT, Hricak H (2006) Transition zone prostate cancers: features, detection, localization, and staging at endorectal MR imaging. Radiology 239(3):784–92.

22 White S, Hricak H, Forstner R, Kurhanewicz J, Vigneron DB, Zaloudek CJ, Weiss JM, Narayan P, Carroll PR (1995) Prostate cancer: effect of postbiopsy hemorrhage on interpretation of MR images. Radiology 195(2):385–90.

23 Singh AK, Guion P, Sears-Crouse N, Ullman K, Smith S, Albert PS, Fichtinger G, Choyke PL, Xu S, Kruecker J, Wood BJ, Krieger A, Ning H (2007) Simultaneous integrated boost of biopsy proven, MRI defined dominant intra-prostatic lesions to 95 Gray with IMRT: early results of a phase I NCI study. Radiat Oncol 18;2:36.

Contact
Matthias Lichy, M.D.
Siemens Healthcare
MR CRM MK CCA
Tel. +49 (9131) 84-3266
matthias.lichy@siemens.com

Case Reports: MRI-guided Prostate Biopsies

Karl Engelhard, M.D.

Diagnostic Radiology, Martha-Maria Hospital Nuernberg, Nuernberg, Germany

This article examines two important clinical cases for a better understanding of potential benefits, but also limitations, of MRI-guided prostate biopsies. All examinations were performed on a 1.5T system (MAGNETOM Symphony, Siemens Healthcare, Erlangen, Germany). Prior to the MRI-guided biopsy, an MRI examination with a combined endorectal body phased-array coil was performed. After insertion of the endorectal coil, the imaging protocol for localization of suspicious areas within the gland consisted of the following T2-weighted TSE sequences: Axial (TR 4.000 ms; TE 102 ms; slice thickness (ST) 3 mm; slice distance (GAP) 0.25; field of view (FOV) 160 mm; matrix 256 × 256); Coronal (TR 4.000 ms; TE 102 ms; ST 3 mm; GAP 0.25; FOV 200 mm; matrix 256 × 256); Sagittal (TR 4.560 ms; TE 106 ms; ST 3 mm; GAP 0.25; FOV 200 mm; matrix 230 × 256); Subsequently, a T1-weighted axial TSE sequence was applied (TR 700 ms; TE 12 ms; ST 4 mm; GAP 0.3; FOV 160 mm; matrix 192 × 256) from the prostate apex up to the seminal vesicle. In addition, a T1-weighted axial TSE sequence (TR 500 ms; TE 13 ms; ST 5 mm; GAP 0.3; FOV 300 mm; matrix 256 × 256) was applied through the regional lymph drain path from the prostate base up to the aorta bifurcation.

After localization of the tumor-suspicious areas, the endorectal coil was removed and the MR visible needle guide was inserted into the patient's rectum and guided to the area to be punctured close by the prostate capsule. The biopsies were performed by means of an MR-compatible biopsy gun (16 G; MRI Devices, Schwerin, Germany). Further information about the procedure can be found in: Engelhard K, Hollenbach HP, Kiefer B, Winkel A, Goeb K, Engehausen D. "Prostate biopsy in the supine position in a standard 1.5T scanner under real time MR-imaging control using a MR-compatible endorectal biopsy device." Eur Radiol. 2006 Jun;16(6):1237-43. Epub 2006 Feb 1.

Case 1

A 60-year-old patient with a PSA elevated to 10 ng/ml is shown. Transrectal ultrasound (TRUS) did not show a cancer-suspected lesion (Fig. 1), however, the endorectal MRT showed a small but cancer-suspected hypointense lesion in medio-lateral orientation in the middle peripheral gland, left (Fig. 2). MRI-guided punch biopsy was performed at the suspected site (Fig. 3), histology revealed an Adeno-Carcinoma (G1, Gleason 2 + 2 = 4). The patient was then referred to radical prostatectomy. Based prostatectomy specimen, pT3a G3 pN0 pM0, Gleason 3 + 4 = 7 was diagnosed with tumor cell layers in both lobes. Therefore it is important to stress that when the location of the biopsy site is determined solely by suspicious areas in the T2-weighted pulse sequence, not all tumor sites become visible.

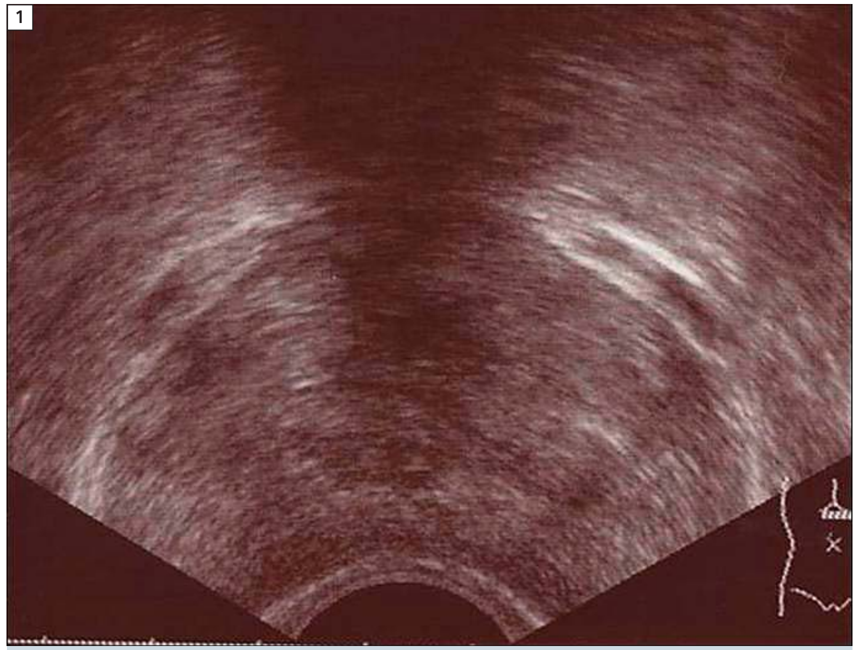

1 Transrectal ultrasound, no clear depiction of suspicious lesion possible.

2A Transversal T2w TSE MR demonstrating a small suspicious lesion within the left lateral zone.

2B Corresponding sagittal T2w slice.

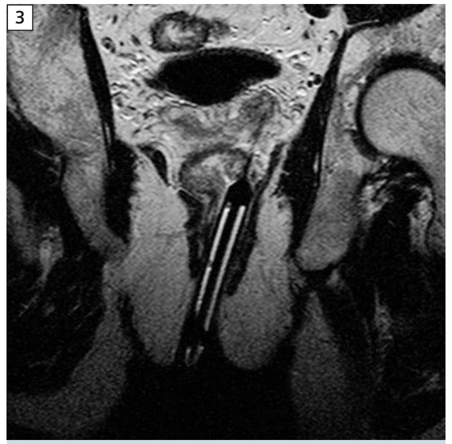

3 MR image in oblique orientation during biopsy.

Case 2

In the T2-weighted image, low-signal lesions within inhomogeneous adenoma structures could correspond to hypercellular carcinomas. As a differential diagnosis, sclerotic adenoma nodes rich in connective tissue also produce low signal. In this case, a 70-year-old patient with a PSA elevated to 12 ng/ml is shown. Before MRI-guided prostate biopsy, the patient has undergone three negative punch biopsies for evaluation of a TRUS-proven tumor (once with 6 samples, twice with 18 samples). The presence of a suspicious lesion was confirmed by T2w MRI and therefore the patient was referred to MRI-guided punch biopsy of the suspicious hypointense area in the ventral transition zone within adenoma structures (Figs. 4 and 5). Histology revealed sclerotic node formation with collagen-rich benign prostatic hyperplasia (BPH).

4 Transversal T2w TSE demonstrating irregular and unclear nodule in the ventral right central gland.

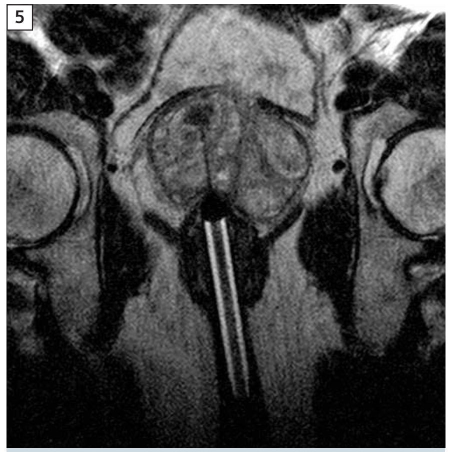

5 Corresponding MR image in oblique orientation taken during biopsy.

Contact
PD Dr. Karl Engelhard, M.D.
Martha-Maria Hospital Nuernberg
Dept. of diagnostic Radiology
Stadenstraße 58
90491 Nuernberg
Germany
k.engelhard@martha-maria.de

Case Report:
Echo Planar Diffusion Imaging for Detection of Prostate Cancer Recurrence Otherwise Occult to Imaging

Sarah Foster, M.D.; Nick Ferris, M.D.

Department of Diagnostic Radiology, Peter MacCallum Cancer Center, Melbourne, Australia

Background

Imaging of the "post-treatment" gland for prostate cancer can be especially challenging. Treatment for non-operable prostate cancer includes various combinations of chemotherapy (anti-androgen therapy), targeted radiation therapy, and brachytherapy (implanted seeds).

The majority of prostate cancers arise from the peripheral zone. Normal tissue in the peripheral zone has higher signal intensity on T2-weighted imaging than the central, transitional and periurethral zones. Malignancy can be detected on MRI as a low signal region within otherwise high signal peripheral zone tissue. The peripheral zone can, however, demonstrate focal or diffuse low signal in a number of clinical situations. Benign prostatic hypertrophy often results in a compressed peripheral zone which may have altered signal. Treatment for prostate cancer with anti-androgen therapy can result in diffuse low signal within the peripheral zone. Radiation therapy can also result in low signal, either diffusely or focally, depending on the radiation port. These changes are thought to reflect fibrous replacement of the normally glandular tissue. Additionally, brachytherapy seeds result in metallic susceptibility artifacts which obscure fine detail and can impair interpretation of certain MRI sequences, such as diffusion imaging or MR spectroscopy, within the prostate.

MRI of the post-treatment gland can thus be difficult, as areas of low signal may represent recurrent/residual disease, or merely be part of the spectrum of therapy change.

Ultrasound detection of prostate cancer can also be difficult in a hypertrophied gland due to the heterogeneity of tissue, making location of a discrete lesion challenging. Many lesions are ultrasound-occult.

1

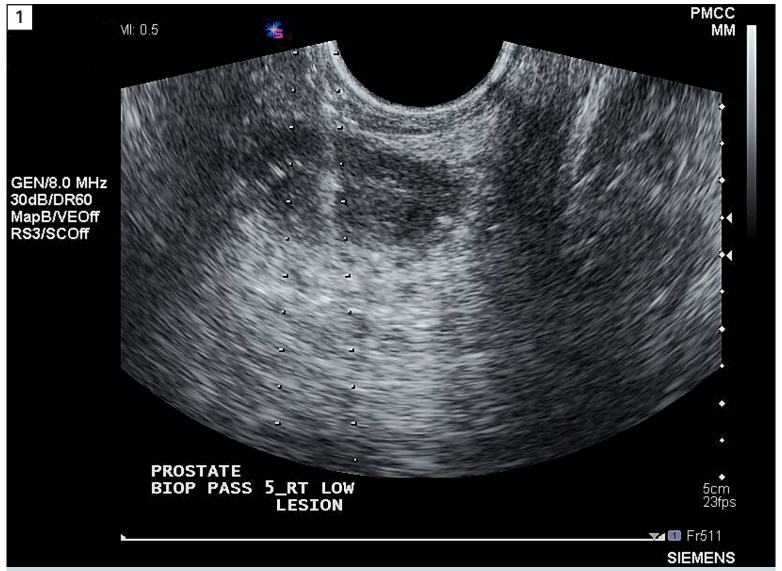

1 TRUS guided biopsy.

2

2 T2-weighted TSE sequence.

3

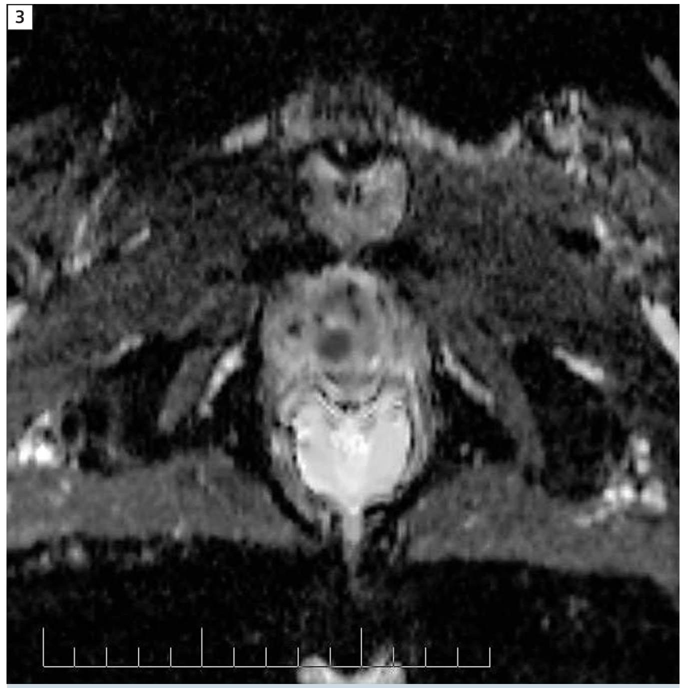

3 ADC map demonstrating focal restriction of water diffusion.

4

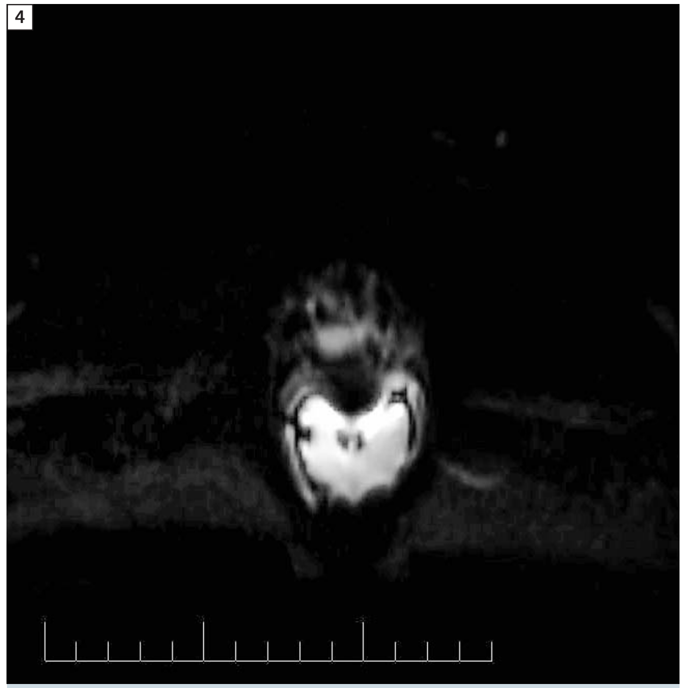

4 High b-value image at b = 800 s/mm^2.

A dilemma thus arises when a post-treatment patient presents with an increasing PSA level, suspicious for recurrence. The imaging many times is not sensitive or specific enough to confidently locate the residual or recurrent disease location to help steer biopsy.

We are trialling diffusion-weighted MR imaging at 3T to aid in improving detection of disease recurrence. The theory is that highly cellular tumor tissue will demonstrate significantly restricted diffusion, compared with normal stromal and glandular tissue.

Case scenario

The patient presented with a rising PSA following brachytherapy for stage T2a N0 M0 Gleason 6 prostate cancer. The disease was initially located in the right apex of the gland. The patient had a repeat MRI for restaging.

We scanned the patient using the Siemens 3T MAGNETOM Trio.

Sequences included:

- T1 TSE transverse
- T2 TSE transverse, coronal and sagittal,
- EPI Diffusion transverse with b-values of 50, 400 and 800, TR 4200 ms, TE 85 ms, matrix 192/144, 4 mm slice thickness; ADC-maps were reconstructed automatically from these with the system software.

A region of significantly restricted diffusion was detected in the right apex of the gland. At T2-weighted imaging, only a subtle low signal focus could be seen at this site. The T2-weighted sequences alone would have been difficult to interpret, as the peripheral zone demonstrated diffusely low T2 signal intensity, as well as some artifact at the site of the brachytherapy seeds.

The patient went on to have ultrasound imaging of the prostate, which did not distinguish a focal lesion in the prostate apex.

The prostate was biopsied under ultrasound guidance with samples obtained from the base, mid portion and apex of the gland, with extra samples from the right apex to correlate with the abnormal region of restricted diffusion on MRI. The biopsy confirmed recurrent prostate adenocarcinoma within the right apex, as suspected from the MRI.

Conclusions

Diffusion-weighted imaging using the Siemens 3T MAGNETOM Trio was helpful in identifying disease which would otherwise have been occult to imaging. This helped guide a successful ultrasound-guided biopsy to confirm disease recurrence. This has significant implications for the patient's prognosis, and decisions regarding further treatment.

Diffusion imaging has its limitations. False positive results can occur in the setting of haemorrhage, infection or artifact from implanted metal. When the findings are taken in the correct clinical setting, however, diffusion-weighted imaging may be a powerful adjunct to the detection of residual or recurrent disease in prostate adenocarcinoma.

Contact
Sarah Foster, M.D.
Department of Diagnostic Radiology
Peter MacCallum Cancer Center
St Andrew's Place
East Melbourne, Victoria 3002
Australia
Sarah.Foster@petermac.org

Characterization of Genitourinary Lesions Using Diffusion-Weighted Imaging at 3T MRI

Farhood Saremi, M.D.[1]; Helmuth Schultze-Haakh, Ph.D.[2]

[1] *Professor of Radiology and Medicine, University of California, Irvine (UCI), USA*
[2] *Siemens Medical Solutions USA, Cypress, CA, USA*

There is growing interest in the application of diffusion-weighted imaging (DWI) for the evaluation of lesions in the abdomen and pelvis [1–3]. DWI yields both qualitative and quantitative information that can be helpful in differentiating benign from malignant processes. The application of DWI is useful for tumor detection, tumor characterization, and in the evaluation of tumor recurrence or response to treatment [4–7].

DWI has been widely used in neuroimaging [8–11]. However, its application to body imaging was initially limited by the inherent motion sensitivity of the technique coupled with the presence of bulk physiologic motion in the abdomen. Routine extracranial application of DWI has become feasible following a series of technological advancements in MR imaging. These developments include faster imaging techniques with echo-planar imaging (EPI) and parallel imaging, high performance gradients, phased array multi-channel surface coils, and clinical use of higher magnetic field strengths [12–17]. Using new techniques, breathhold DWI sequences can be appended to existing imaging protocols without a significant increase in the total examination time.

In this review, we describe our experience in using DWI for the characterization of genitourinary tract lesions as done on our MAGNETOM Trio, A Tim System with the Body Matrix coils.

Basic understanding of DWI technique

DWI sequences are designed to detect alterations in thermally-induced random (Brownian) motion of water molecules within tissues also known as diffusion [8, 9]. Diffusion effects are very small to be visible by conventional MRI. A DWI sequence requires the addition of a symmetric pair of diffusion-sensitizing gradients with opposed polarity [8, 9]. In contrast to static molecules, the random displacement of moving water molecules in the period between application of the first and second opposed polarity gradient pulses results in dephasing and consequent loss of signal intensity. The degree of signal loss is proportional to the degree of water motion (mean diffusional path length), with the highest signal attenuation seen with bulk water.

The MR signal in DWI depends on two factors: the amplitude of random displacements of water molecules (related to the diffusion coefficient) and the b-value (the degree of diffusion-weighting). The optimal b-values for abdominal DWI have not yet been determined.

DWI is typically performed using at least two b-values (within a range of 0 to 1000 s/mm^2) to allow the calculation of the apparent diffusion coefficient (ADC).

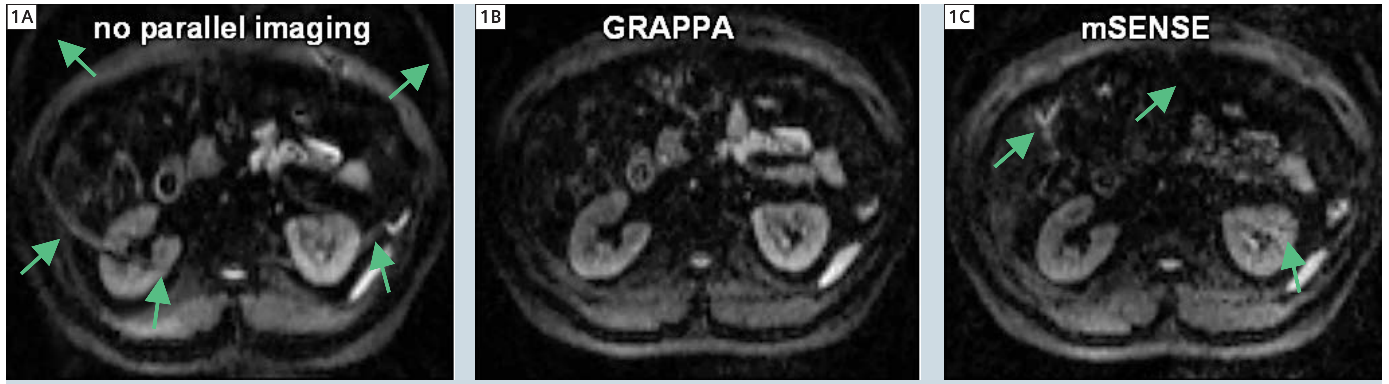

1 Breathhold diffusion-weighted images at b = 400 are obtained on our MAGNETOM Trio, A Tim System (with software version *syngo* MR B15) using fat suppressed single shot echo planar sequence without **(A)** and with **(B)** parallel imaging. scan time is 22 sec on both, and the field of view is 360 mm. TR is reduced from 3000 ms in A to 2600 ms in B and C. Two different parallel imaging techniques are used, *syngo* GRAPPA (**A** and **B**) and mSENSE **(C)**. Spectral fat suppression is employed in all. Note the ghost artifact (long arrows) superimposed on the kidneys on the image without parallel imaging, which is pushed to the periphery following application of *syngo* GRAPPA and mSENSE. The overall image quality is clearly improved with parallel imaging. *syngo* GRAPPA is a preferred technique as aliasing artifacts are less frequent than with mSENSE (small arrows). Note: improved signal intensity in the center of the abdomen with *syngo* GRAPPA.

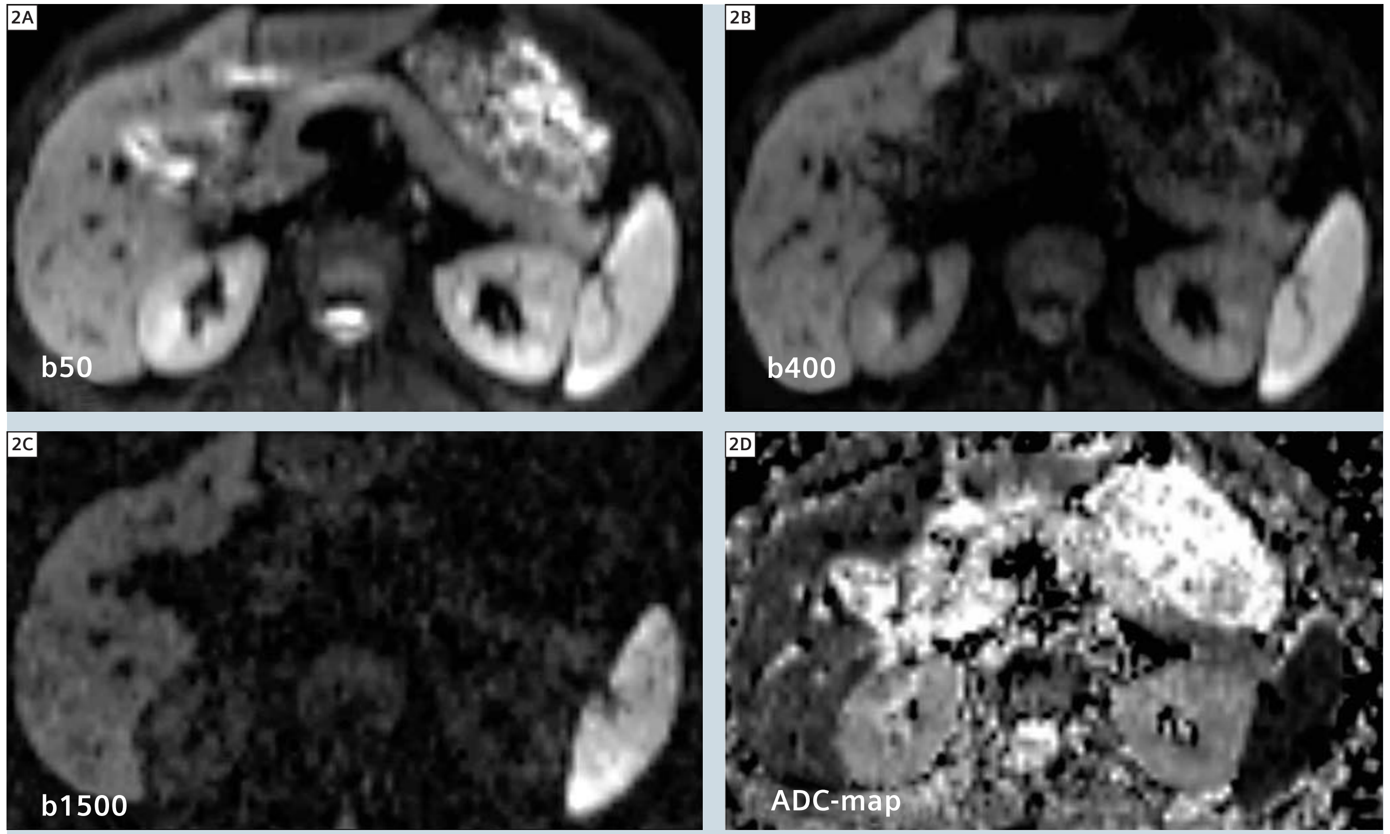

2 Abdominal DWI – Normal Appearance. ADC of the kidney is the highest among all abdominal organs, followed by the liver, pancreas, and spleen. As the b-value increases, the signal of normal kidney drops. The spleen remains bright and liver signal decreases mildly. Note that the signal of the left liver lobe is generally lower than the right lobe (which may be caused by transmitted cardiac pulsations). The center of the abdomen generally has no signal mostly due to susceptibility effect of gasterointestinal air. The bright signal in the ADC-map is stomach content, not a solid organ.

As the b-value is increased, sensitivity to the effects of diffusion increases at the expense of longer TE and worsened signal-to-noise ratio (SNR) and image distortion.

Imaging protocol at our institution

Most of the images shown herein were obtained using a 3 tesla (T) magnet (MAGNEOM Trio, Siemens Healthcare, Erlangen, Germany). We used a breathhold single-shot spin echo EPI combined with parallel imaging and spectral fat suppression [11–14]. Our DWI protocol is shown in Table 1.

In breathhold techniques, although the signal-to-noise ratio (SNR) is inferior compared with multiple averaging methods, the use of higher magnetic field strengths (e.g., 3 Tesla) and surface coils with more receiver channels (> 8) can compensate for poor SNR [17, 18]. We found spectral fat saturation technique more practical than STIR (short TI inversion recovery) for breathhold studies, since with STIR the acquisition time is longer and lesion visibility may be inferior compared with spectral fat saturation, especially in the center of the abdomen [19]. Parallel imaging is also essential for breathhold DW imaging. With parallel imaging, a shorter TE is possible which in fact increases the SNR and reduces susceptibility-induced image distortions [20–22] (Fig. 1). In our experience, *syngo* GRAPPA is more advantageous to mSENSE given the degree of off resonance and motion ghost artifacts associated with mSENSE (Fig. 1).

It is reported that the DW image quality is superior at 3T compared to 1.5 T and that small lesions are better visualized [17]. 3T is particularly useful at higher b-values. However, with 3T we should expect larger susceptibility-induced image distortions and signal loss, and more motion-related artifacts [18]. Traditionally, most DWI studies have reported b-values of below 1000 s/mm^2. However, the use of even greater b-values may be beneficial. For example, high grade tumors may retain their bright signal with b-values above 1000 s/mm^2, whereas low grade tumors will lose their signal [23]. High b-values have also been used effectively to assess early recurrences of a tumor [24].

Signal of normal tissues in DWI

The ADC of the kidney is the highest among all solid abdominal organs, followed by the liver, pancreas, and spleen [16, 25, 26] (Fig. 2). The ADC value of

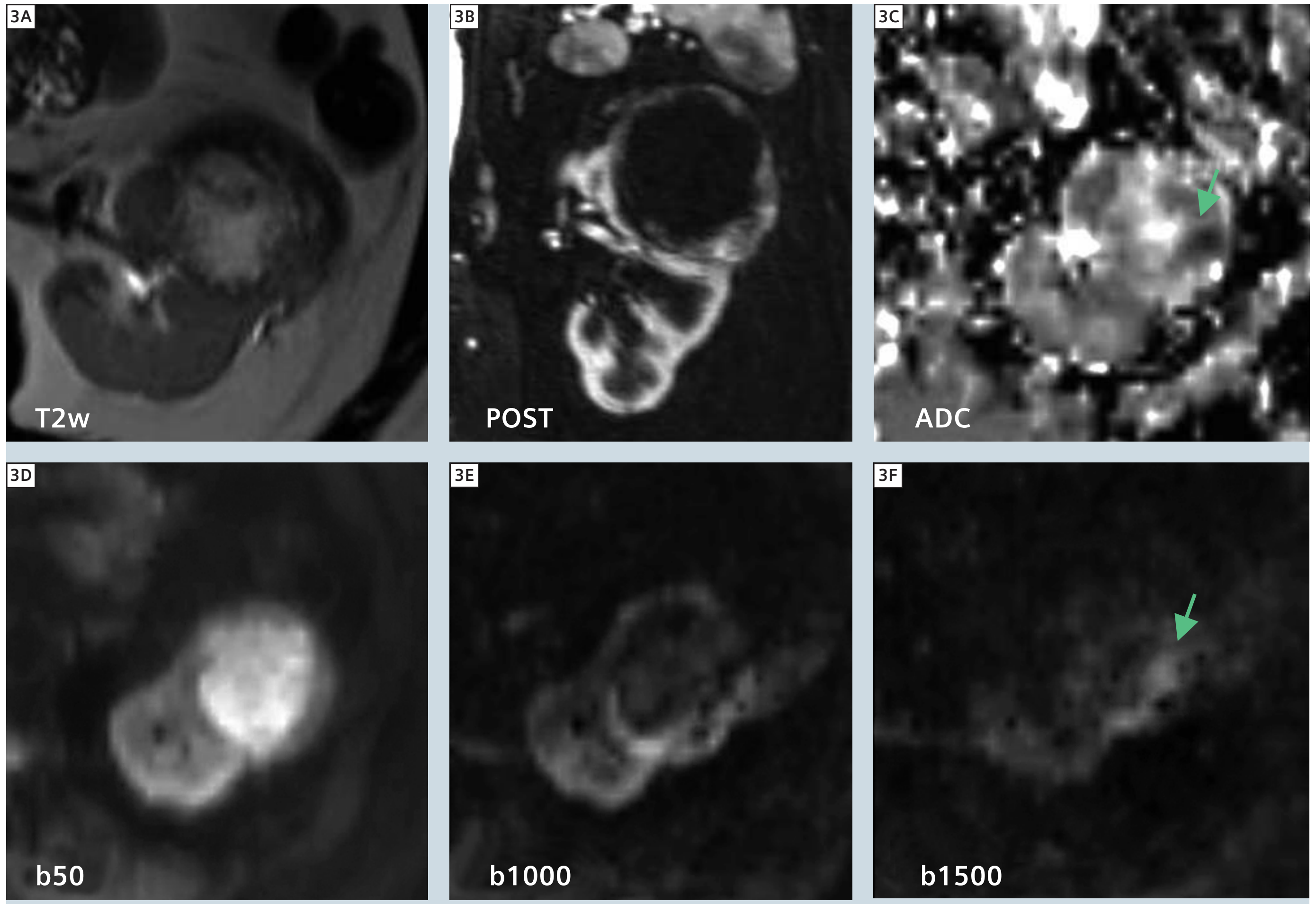

3 Cystic renal cell carcinoma. Axial T2-weighted (T2w) image of the left kidney demonstrates a large septated cystic lesion arising from the anterolateral margin of the left kidney. The bright signal intensity in the center of the lesion represents fluid. The anterior margin of the lesion shows lower signal intensity representing thickened fibrous capsule. The posterolateral margin of the lesion is mass-like and appears isointense to the normal renal parenchyma. Post contrast (post) image, DW images with b-values of 50, 1000, and 1500 s/mm^2, and ADC-map image are shown. Note the bright signal intensity of the fluid portions of the lesion on the b = 50 s/mm^2 image (related to T2 effects), as well as the bright signal intensity of the viable tumor on the b = 1500 s/mm^2 image which appears low in signal on the ADC-map image (secondary to restricted diffusion). Biopsy of the hypercellular region showed renal cell carcinoma (long white arrow). Also note that on the post-contrast image both the fibrous capsule and tumor demonstrate enhancement.

the renal cortex is generally higher than the medulla [27]. At high b-values, the signals from normal tissue such as blood vessels, muscle, and bowel will be suppressed. The kidneys, adrenal gland, and gallbladder lose their signal gradually and lose nearly all signal at b = 1000 s/mm^2 and above. In contrast, some normal structures such as the spleen, prostate, testes, ovaries, endometrium, and spinal cord retain their bright signal at the higher b-values.

Signal depletion in the center of the abdomen (pancreas) is common and likely related to susceptibility effects caused by gastrointestinal air. In the pelvis, the endometrium and endocervix show the highest signal values and appear bright on all DWI series. Junctional zone (inner layer of myometrium) and cervical body demonstrate the lowest ADC values. In other words, both appear low in signal on b = 50 s/mm^2 and bright on b = 1000 to b = 1500 s/mm^2. Normal myometrium is intermediate signal on all b-values.

Assessment of cystic lesions

The signal intensity of most simple cysts drops significantly on b = 500 s/mm^2 images and is lost completely on b = 1000-1500 s/mm^2 images. The presence of blood products and high proteinacious material within a cyst may result in loss of signal on T2-weighted (T2w) and low b-value DWI images (compared with simple cysts) due to magnetic susceptibility effects of their contents. A similar effect can be seen with infected cysts and abscesses.

ADC values of simple and complicated cysts are usually higher than solid lesions [28]. However, it should be noted that some overlap between the gross morphologic characteristics and ADC values of a complicated cyst and cystic renal cell carcinoma is not unusual.

While needle biopsy is considered a relatively safe procedure, the incidence of complications is not negligible. In our experience with biopsy of cystic neoplasms, attention to findings provided by DWI can be very helpful in selecting biopsy sites to maximize the likelihood of positive results and may prevent an unnecessary repeat biopsy or surgery (Fig. 3).

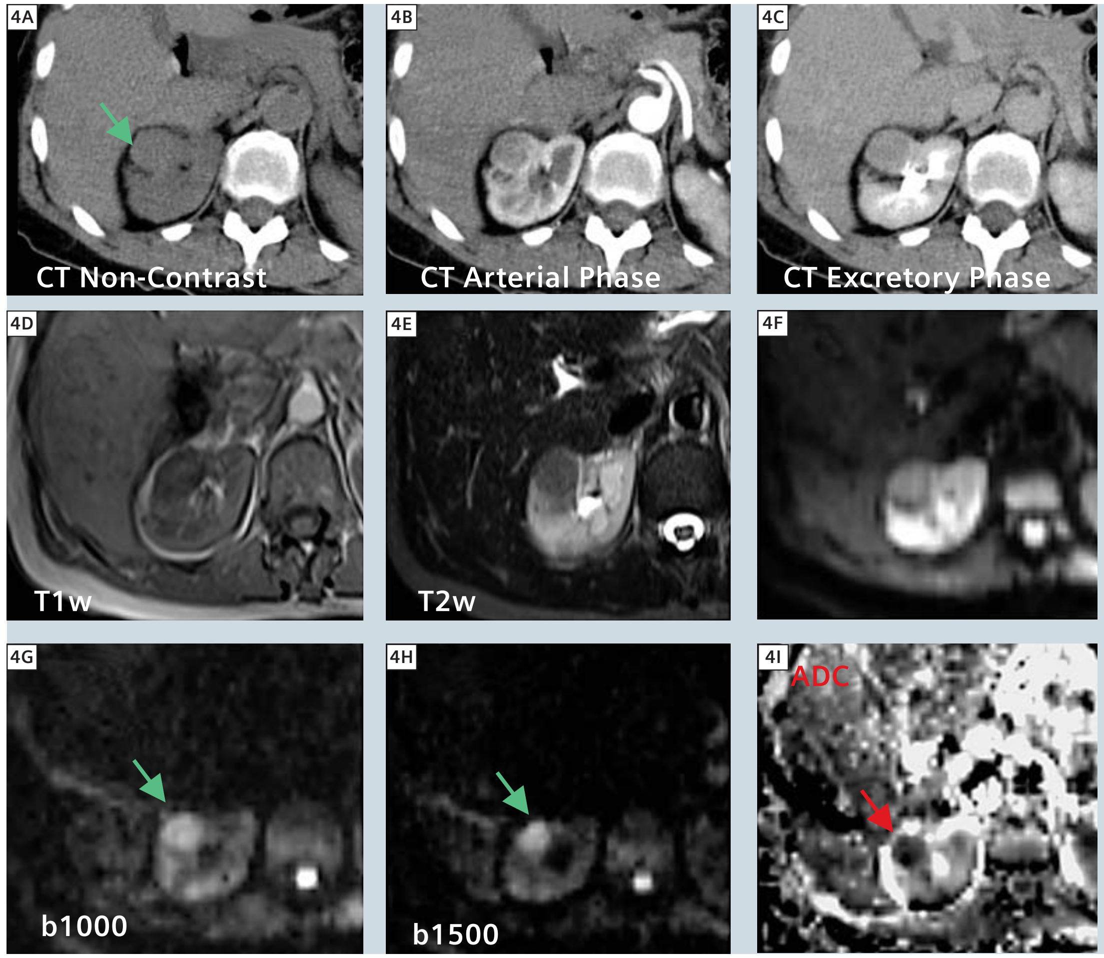

4 62-year-old male presented for evaluation of right renal mass. Computer Tomography (CT) images demonstrate mild enhancement of the mass on arterial phase and washout on the excretory phase. Further study with contrast enhanced MRI (three weeks later) showed mild enhancement on the arterial phase (image not shown) and heterogeneous signal on T1W and T2W images. DW images showed progressive signal enhancement of the mass (long arrows) with increasing b-values consistent with low ADC number. Percutaneous needle biopsy showed renal cell carcinoma. Radiofrequency ablation was performed.

Characterization of primary and metastatic tumors

DWI technique has been used successfully for the diagnosis and characterization of genitourinary lesions, including benign and malignant processes arising from the kidneys [29, 30], uterus [31], ovaries [32], and prostate [33], as well as for the detection of metastatic lesions in the liver, lymph nodes, and skeletal system [34–36].

Although ADC values have been demonstrated to differ significantly between benign and malignant lesions, it is not yet possible to confidently distinguish benign from malignant renal neoplasms on the basis of qualitative assessment of ADC measurements alone [37–40]. The degree of restriction to water diffusion in biologic tissue is inversely related to the tissue cellularity and the integrity of cell membranes [37–40]. As a consequence, diffusion is mostly restricted in highly cellular parts of a tumor because of a reduced extracellular space (Fig. 4). In contrast, diffusion is less restricted in hypocellular tumors and in tumors with glandular, necrotic, hemorrhagic, or cystic components (Fig. 3).

In most benign processes such as cysts or benign masses of low cellularity (e.g., typical cavernous hemangioma), the signal intensity on DWI decays with increasing b-value. This results in high signal intensities of such benign lesions on the ADC-map [29]. In contrast, slower signal decay or even signal enhancement with increasing b-values may indicate malignancy or viable hypercellular tissue (Fig. 4).

DWI and ADC-maps can be used to select optimal biopsy sites and to detect the presence of viable tumor on follow-up studies of patients after radiation or chemotherapy [41] (Fig. 3).

Pelvic masses

DWI performed with parallel imaging techniques has demonstrated potential as a method for differentiating benign from malignant pelvic lesions.

Both endometrial cancer and normal endometrium appear hyperintense on DW images [42]. However, the ADC values of high grade endometrial cancers are lower than those of normal endometrium and low grade cancers. “Cellular” leiomyomas, composed of compact smooth muscle cells with little or no collagen, tend to be brighter on T2-weighted and DW images

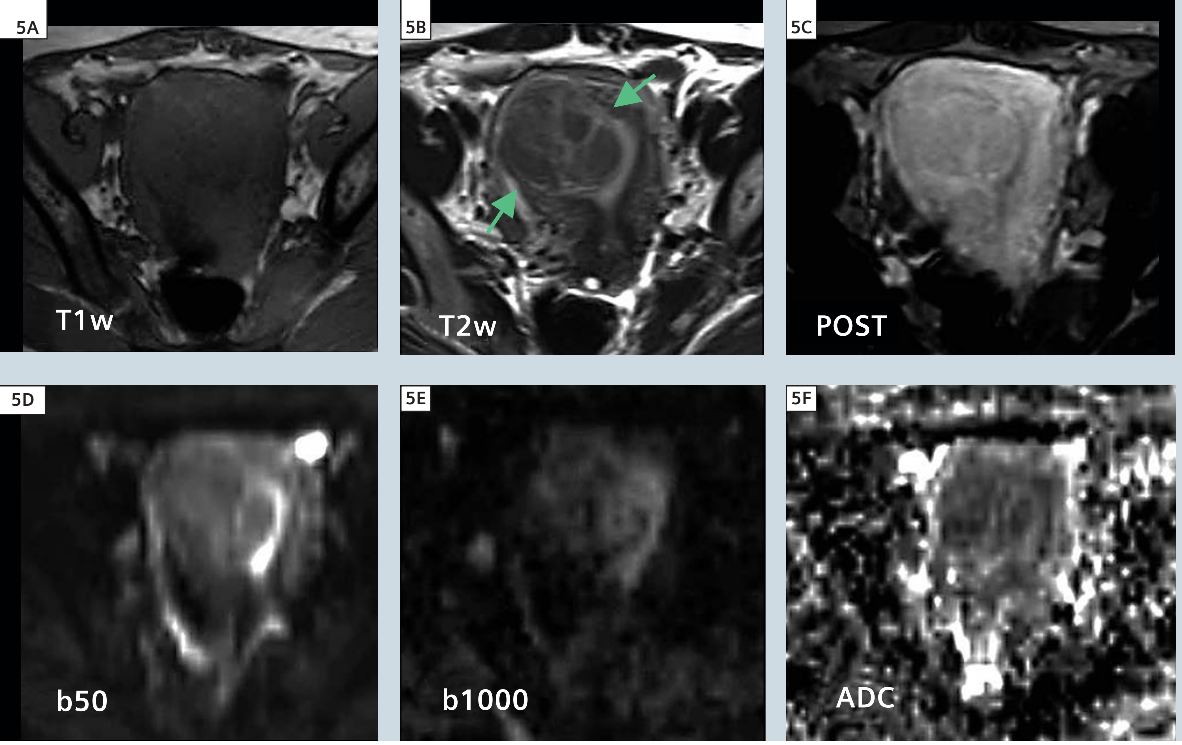

5 Benign cellular subendometrial fibroid in a 45-year-old patient (arrows). The mass demonstrates heterogeneous signal on DWI images with areas of mild restricted diffusion on ADC map consistent with hypercellularity. The tumor appears enhancing on post contrast (post) image. **Note:** high signal intensity of normal endometriun on all b = 50 and b = 1000 s/mm^2 values of DWI images.

(and darker on ADC images) compared with non-degenerated fibrous (collagenous) leiomyomas [31, 43, 44] (Fig. 5). The appearance of degenerated leiomyomas on DW images is quite variable. In patients with ovarian cancer, restricted diffusion is demonstrated not only at sites of primary malignancy but also in metastatic peritoneal implants [32].

It has been suggested in numerous reports that DWI together with T2w imaging can significantly improve identification of prostate cancers [33].

Conclusions

DW imaging in combination with 3T equipment, is a robust method to facilitate the diagnosis of genitourinary lesions with equivocal signal characteristics on routine MRI. It is not only helpful in differentiating benign from malignant processes, but can also be used as a tool for assessing possible tumor recurrence and to evaluate response to radiation treatment or chemotherapy on follow up scans.

Table 1: Diffusion-Weighted Imaging protocol on MAGNETOM Trio with software version *syngo* MR B15.

2D single shot spin echo EPI (EPI factor = 84)
b-values: 50, 400, 1000, and 1500 s/mm^2
Body Matrix coils: 8-channel, **BW:** 2056 Hertz/pixel
Fat suppression: normal Fat Sat
TR/TE: 2500–3000 s/mm^2 / 72 for b-values 50 and 1000, 2800-3000 s/mm^2 /78 for b-values 400 and 1500 s/mm^2
Total Imaging Time: 21–24 sec for each set
Matrix size: 84 x 128
Slice Thickness/Gap: 5/1.5 mm, 20 slices
Noise level: 0
Parallel imaging: *syngo* GRAPPA, acceleration factor = 2
Direction of diffusion gradients: 3-scan trace
Typical FOV with rectangular FOV
Typical resolution, pixel size

References

1 Namimoto T, Yamashita Y, Sumi S, Tang Y, Takahashi M. Focal liver masses: characterization with diffusion-weighted echo planar MR imaging. Radiology 1997; 204: 739–44.

2 Yamada I, Aung W, Himeno Y, Nakagawa T, Shibuya H. Diffusion coefficients in abdominal organs and hepatic lesions: evaluation with intravoxel incoherent motion echo-planar MR imaging. Radiology1999; 210:617–623.

3 Murtz P, Flacke S, Traber F, van den Brink JS, Gieseke J, Schild HH. Abdomen: diffusion-weighted MR imaging with pulse-triggered single-shot sequences. Radiology 2002;224 : 258–264.

4 Herneth AM, Guccione S, Bednarski M. Apparent diffusion coefficient: a quantitative parameter for in vivo tumor characterization. Eur J Radiol 2003; 45: 208–13.

5 Charles-Edwards EM, deSouza NM. Diffusion-weighted magnetic resonance imaging and its application to cancer. Cancer Imaging. 2006;6:135–43.

6 Thoeny HC, De Keyzer F. Extracranial applications of diffusion-weighted magnetic resonance imaging. Eur Radiol. 2007;17(6):1385–93.

7 Namimoto T, Awai K, Nakaura T, Yanaga Y, Hirai T, Yamashita Y. Role of diffusion-weighted imaging in the diagnosis of gynecological diseases. Eur Radiol. 2008 Oct 7. [Epub ahead of print].

8 Le Bihan D, Breton E, Lallemand D, Grenier P, Cabanis E, Laval-Jeantet M. MR imaging of intravoxel incoherent motions: application to diffusion and perfusion in neurologic disorders. Radiology 1986; 161: 401–7.

9 Le Bihan D, Breton E, Lallemand D, Aubin ML, Vignaud J, Laval-Jeantet M. Separation of diffusion and perfusion in intravoxel incoherent motion MR imaging. Radiology 1988; 168:497–505.

10 Moseley ME, Kucharczyk J, Mintorovitch J, et al. Diffusion-weighted MR imaging of acute stroke: correlation with T2-weighted and magnetic susceptibility-enhanced MR imaging in cats. AJNR Am J Neuroradiol 1990; 11: 423–9.

11 Rowley HA, Grant PE, Roberts TP. Diffusion MR imaging: theory and applications. Neuroimaging Clin N Am 1999; 9: 343–61.

12 Müller MF, Prasad P, Siewert B, Nissenbaum MA, Raptopoulos V, Edelman RR. Abdominal diffusion mapping with use of a whole-body echo-planar system. Radiology 1994; 190:475–478.

13 Chow LC, Bammer R, Moseley ME, Sommer FG. Single breath-hold diffusion-weighted imaging of the abdomen. J Magn Reson Imaging 2003; 18:377–382.

14 Yamashita Y, Tang Y, Takahashi M. Ultrafast MR imaging of the abdomen: echo planar imaging and diffusion-weighted imaging. J Magn Reson Imaging 1998; 8:367–374

15 Okada Y, Ohtomo K, Kiryu S, Sasaki Y. Breathhold T2-weighted MRI of hepatic tumors: value of echo planar imaging with diffusion-sensitizing gradient. J Comput Assist Tomogr 1998; 22:364–371.

16 Yoshikawa T, Kawamitsu H, Mitchell DG, et al. ADC measurement of abdominal organs and lesions using parallel imaging technique. AJR Am J Roentgenol. 2006;187(6):1521–30.

17 Matsuoka A, Minato M, Harada M, et al. Comparison of 3.0-and 1.5-tesla diffusion-weighted imaging in the visibility of breast cancer. Radiat Med. 2008;26(1):15–20.

18 Mürtz P, Krautmacher C, Träber F, Gieseke J, Schild HH, Willinek WA. Diffusion-weighted whole-body MR imaging with background body signal suppression: a feasibility study at 3.0 Tesla. Eur Radiol. 2007;17(12):3031–7.

19 Wenkel E, Geppert C, Schulz-Wendtland R, et al. Diffusion weighted imaging in breast MRI: comparison of two different pulse sequences. Acad Radiol. 2007;14(9):1077–83.

20 Taouli B, Martin AJ, Qayyum A, et al. Parallel imaging and diffusion tensor imaging for diffusion-weighted MRI of the liver: preliminary experience in healthy volunteers. AJR Am J Roentgenol. 2004;183(3):677–80.

21 Naganawa S, Kawai H, Fukatsu H, et al. Diffusion-weighted imaging of the liver: technical challenges and prospects for the future. Magn Reson Med Sci. 2005;4(4):175–86.

22 Skare S, Newbould RD, Clayton DB, Albers GW, Nagle S, Bammer R. Clinical multishot DW-EPI through parallel imaging with considerations of susceptibility, motion, and noise. Magn Reson Med. 2007;57(5):881–90.

23 Alvarez-Linera J, Benito-León J, Escribano J, Rey G. Predicting the histopathological grade of cerebral gliomas using high b value MR DW imaging at 3-tesla. J Neuroimaging. 2008;18(3):276–81.

24 Ichikawa T, Haradome H, Hachiya J, Nitatori T, Araki T. Diffusion-weighted MR imaging with single-shot echo-planar imaging in the upper abdomen: preliminary clinical experience in 61 patients. Abdom Imaging. 1999;24(5):456–61.

25 Kilickesmez O, Yirik G, Bayramoglu S, Cimilli T, Aydin S. Non-breath-hold high b-value diffusion-weighted MRI with parallel imaging technique: apparent diffusion coefficient in normal abdominal organs. Diagn Interv Radiol 2008;14 (2): 83–87.

26 Mardor Y, Pfeffer R, Spiegelmann R, et al. Early detection of response to radiation therapy in patients with brain malignancies using standard and high b-value diffusion-weighted MRI. J Clin Oncol 2003; 21:1094–1100.

27 Zhang J, Tehrani YM, Wang L, Ishill NM, Schwartz LH, Hricak H. Renal masses: characterization with diffusion-weighted MR imaging--a preliminary experience. Radiology 2008;247(2):458–64.

28 Cova M, Squillaci E, Stacul F, et al. Diffusion weighted MRI in the evaluation of renal lesions: preliminary results. Br J Radiol 2004; 77:851–857.

29 Thoeny HC, De Keyzer F, Oyen RH, Peeters RR. Diffusion-weighted MR imaging of kidneys in healthy volunteers and patients with parenchymal diseases: initial experience. Radiology 2005; 235:911–917.

30 Namimoto T, Yamashita Y, Mitsuzaki K, Nakayama Y, Tang Y, Takahashi M. Measurement of the apparent diffusion coefficient in diffuse renal disease by diffusion-weighted echo-planar MR imaging. J Magn Reson Imaging 1999; 9:832–837.

31 Tamai K, Koyama T, Saga T, et al.The utility of diffusion-weighted MR imaging for differentiating uterine sarcomas from benign leiomyomas. Eur Radiol. 2008;18(4):723–30.

32 Nakayama T, Yoshimitsu K, Irie H, et al. Diffusion-weighted echo-planar MR imaging and ADC mapping in the differential diagnosis of ovarian cystic masses: usefulness of detecting keratinoid substances in mature cystic teratomas. J Magn Reson Imaging. 2005;22(2):271–8.

33 Morgan VA, Kyriazi S, Ashley SE, DeSouza NM. Evaluation of the potential of diffusion-weighted imaging in prostate cancer detection. Acta Radiol. 2007;48(6):695–703.

34 Koh DM, Scurr E, Collins DJ, Pirgon A, Kanber B, Karanjia N et al. Colorectal hepatic metastases: quantitative measurements using single-shot echo-planar diffusion-weighted MR imaging. Eur Radiol. 2006;16(9):1898–905.

35 Herneth AM, Philipp MO, Naude J, et al. Vertebral metastases: assessment with apparent diffusion coefficient. Radiology 2002; 225:889–894.

36 Abdel Razek AA, Soliman NY, Elkhamary S, Alsharaway MK, Tawfik A. Role of diffusion-weighted MR imaging in cervical lymphadenopathy. Eur Radiol. 2006;16(7):1468–77.

37 Sugahara T, Korogi Y, Kochi M, et al. Usefulness of diffusion-weighted MRI with echo-planar technique in the evaluation of cellularity in gliomas. J Magn Reson Imaging 1999; 9:53–60.

38 Stadnik TW, Chaskis C, Michotte A, et al. Diffusion-weighted MR imaging of intracerebral masses: comparison with conventional MR imaging and histologic findings. AJNR Am J Neuroradiol. 2001;22(5):969–76.

39 Guo AC, Cummings TJ, Dash RC, Provenzale JM. Lymphomas and high-grade astrocytomas: comparison of water diffusibility and histologic characteristics. Radiology. 2002;224(1):177–83.

40 Squillaci E, Manenti G, Cova M, et al. Correlation of diffusion-weighted MR imaging with cellularity of renal tumours. Anticancer Res 2004; 24:4175–4179.

41 Razek AA, Megahed AS, Denewer A, Motamed A, Tawfik A, Nada N. Role of diffusion-weighted magnetic resonance imaging in differentiation between the viable and necrotic parts of head and neck tumors. Acta Radiol. 2008;49(3):364–70.

42 Tamai K, Koyama T, Saga T, et al. Diffusion-weighted MR imaging of uterine endometrial cancer. J Magn Reson Imaging. 2007;26(3):682–7.

43 Yamashita Y, Torashima M, Takahashi M, et al. Hyperintense uterine leiomyoma at T2-weighted MR imaging: differentiation with dynamic enhanced MR imaging and clinical implications. Radiology 1993; 189:721–725.

44 Murase E, Siegelman ES, Outwater EK, Perez-Jaffe LA, Tureck RW.Uterine leiomyomas: histopathologic features, MR imaging findings, differential diagnosis, and treatment. Radiographics. 1999;19(5):1179–97.

Contact
Farhood Saremi, M.D.
Professor of Radiology and Medicine
Chief, Cardiothoracic Division
Dept. of Radiological Sciences
University of California (UCI)
Medical Center
101 City Drive
Irvine, CA 92868
USA
fsaremi@uci.edu

Intravoxel Incoherent Motion (IVIM)* f-maps of Pancreatic Lesions

Re, Thomas Joseph, M.D., MSEE[1]; Klauss, Miriam, M.D.[2]; Lemke, Andreas, MSc[3,4]; Laun, Frederik, Ph.D.[4]; Simon, Dirk, MSc[1]; Delorme, Stefan, M.D.[1]; Stieltjes, Bram, M.D.[1]

[1]*German Cancer Research Center (DKFZ), Department of Radiology – E 010, Heidelberg, Germany*
[2]*Department of Diagnostic Radiology, University of Heidelberg, Heidelberg, Germany*
[3]*Department of Computer Assisted Clinical Medicine, University of Heidelberg, Mannheim,*
Faculty of Medicine, Mannheim, Germany
[4]*German Cancer Research Center (DKFZ), Department of Physics in Radiology – E 020, Heidelberg, Germany*

Abstract

Purpose: To illustrate our experience using diffusion-weighted (DW) derived IVIM perfusion fraction f images (f-maps) for the delineation of solid pancreatic lesions. Particular attention is given to the comparison of this experimental technique with the clinically established technique of ADC-mapping.

Methods: Seven representative cases (1 healthy volunteer, 4 pancreatic adenocarcinoma cases, and 2 pancreatitis cases) are presented. Each were examined with contrast-enhanced T1 and T2-weighted magnetic resonance (MR) and with echo-planar MR diffusion-weighted imaging (DWI) using eleven different b-values ranging from 0–800 s/mm^2. The DWI data was fitted to both the “Incoherent Intra-Voxel Motion” (IVIM) model and a linear apparent diffusion constant (ADC) equation, and the perfusion fraction f and ADC-maps were calculated. As a novel approach, ADC and f-map data was combined to identify vascular (high perfusion but low ADC) or bile duct (low perfusion but high ADC) voxels which were then color tagged on the f-map images.

Results / Conclusion: When compared to ADC-maps, f-maps improved the distinction between lesion and vessels, while ADC-maps more accurately identified adjacent pancreatic ducts. Images which integrate f and ADC data provided better lesion delineation than could be achieved with either technique alone. Since f-maps do not require ionizing radiation nor contrast agent, they could be considered an alternative to CT and contrast-enhanced MRI techniques in patients with specific contraindications as well as in screening and follow-up imaging programs.

Introduction

Contrast-enhanced magnetic resonance (MR) and computed tomography (CT) imaging are currently the standard imaging modalities for pancreatic lesions [1–3]. Their high diagnostic value unconsidered, they require intravenous contrast agent and, in the case of CT, ionizing radiation. Diffusion-weighted imaging (DWI) could prove a non-invasive alternative, since recent advances in scanner technologies, fast pulse sequences and parallel imaging have permitted its use in the abdomen where organ motion and tissue inhomogeneity have long prevented robust diffusion measurements [4–6]. Reports have shown that the DWI-derived apparent diffusion constant (ADC) can be used to monitor the pancreatic exocrine function in chronic pancreatitis [7, 8], for characterizing cystic lesions of the pancreas [9], and for detecting pancreatic cancer, which has a significantly lower ADC value than normal pancreas tissue [10–12].
Recently there has been growing interest in extracting perfusion information from diffusion-weighted data based on the intravoxel incoherent motion (IVIM) model [13–15] first presented by LeBihan in 1986 [16, 17]. In this model, the diffusion-weighted signal is considered to be effected by two distinct types of molecular motion: *diffusion*, due to thermal Brownian motion, and *perfusion*, due to the microcirculation in capillaries. The IVIM model is represented mathematically by the equation:

$$\frac{S}{S_0} = (1-f)\,e^{-bD} + f\,e^{-b(D+D^*)}$$

where S/S_0 is the signal decay measured in each individual voxel in the diffusion-weighted image, the b-value represents the strength of the diffusion weighting, D is the diffusion constant, D* is the pseudo diffusion coefficient, and f is the perfusion fraction. This equation is a biexponential with the first term representing the pure diffusion influence on the diffusion-weighted signal, while the second term represents the pure perfusion influence on the diffusion-weighted signal. The perfusion fraction (f) indicates the relative influence of the second perfusion term and thus is correlated to the perfusion or microcirculation in the capillaries of the tissue under study. In a recent work, f was shown to be significantly lower within pancreatic tumors than in healthy pancreatic tissue [18]. Another study showed similar results for chronic pancreatitis mass formations [19]. Furthermore, f was shown to be quantitatively superior to both ADC and D for characterizing pancreatic lesions [18]. Images created by mapping the f parameter as a gray scale (f-maps), hold important clinical information for both diagnosing and differentiating pancreatic lesions, but so far the reading of f-maps is unfamiliar to general radiologists. Thus, this pictorial essay aims to familiarize the clinician with this emerging imaging method. This work was generated within a cooperative project of Siemens Healthcare and the German national cancer center, diagnostic imaging for radio-oncology.

Materials and methods

Study population

This work was generated within a cooperative project of Siemens Healthcare and the German national cancer center, diagnostic imaging for radio-oncology. The study protocol was approved by the Institutional Review Board. Informed consent was obtained from all subjects prior to the examination. In 2008 (June-December), 3 healthy volunteers, 14 patients with histopathologically proven pancreatic carcinoma (11 men and 3 women, age range 43–82, mean age 62.6) and 8 histopathologically verified pancreatitis patients (7 men and 1 woman, age range 40–74, mean age 55.5) were included consecutively during this period.

MR examination

MR imaging was performed using a 1.5T scanner (MAGNETOM Avanto, Siemens Healthcare, Erlangen, Germany) with a maximum gradient strength of 45 mT/m using a six-element body-phased array coil and a 24-channel spine array coil. The routine pancreatic MR imaging protocol for the patient group consisted of TrueFISP imaging sequences (sagital, axial and coronal) (TR/TE = 437.2/1.16 ms), breathhold (in expiration) dual gradient echo (2D) T1-weighted (T1w) imaging in transversal orientation (TR/TE = 110/4.82 ms), breathhold (expiration) single-shot turbo spin-echo T2-weighted (T2w) imaging in transversal and coronal orientation (TR/TE = 250/20 ms) and MR cholangiopancreatography in breathhold (expiration) single-shot turbo spin-echo (TR/TE = 4500/789 ms).

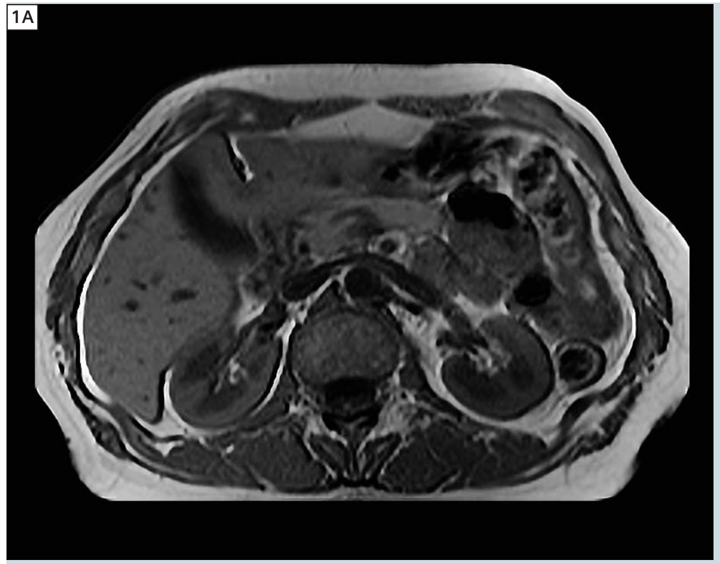

1 Axial T1-weighted image of a healthy volunteer.

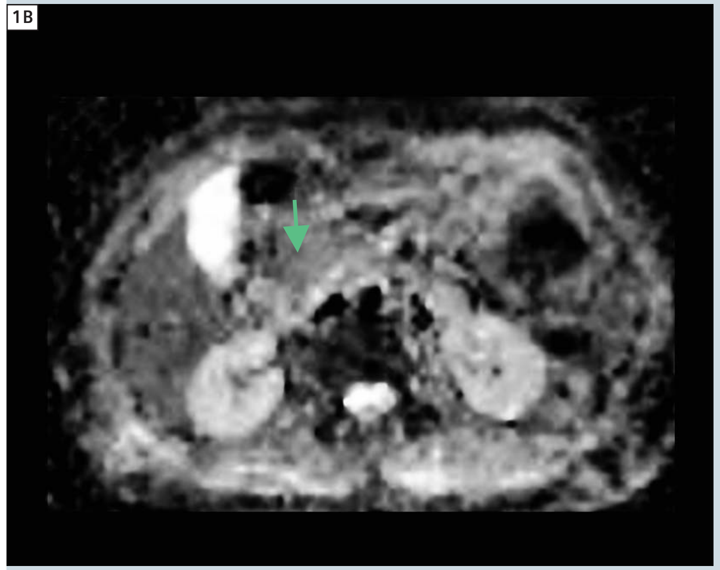

1 In the ADC-map it can be seen that the pancreas (green arrow) appears isointense to the liver.

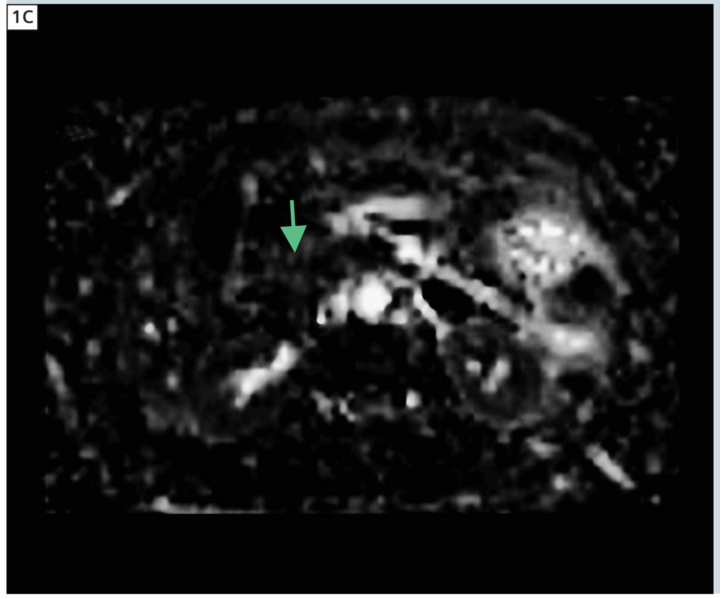

1 In the f-map, the pancreas (green arrow) shows a mixed hypo- and hyperintense signal.

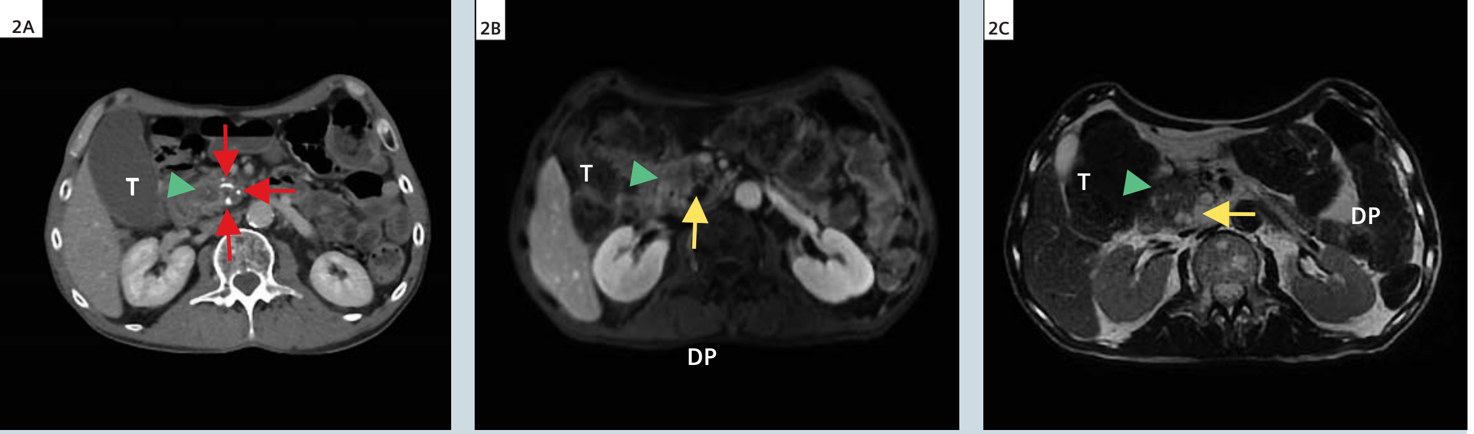

2 Axial contrast-enhanced CT **(A)**, contrast-enhanced T1w image **(B)** and T2w image **(C)** for a patient with chronic pancreatitis with calcifications (red arrows) within the pancreatic head (see CT on the left) as well as pancreatic cancer (green arrowhead). The dilated pancreatic duct can also be appreciated (yellow arrows). (T = tumor; DP = ductus pancreaticus).

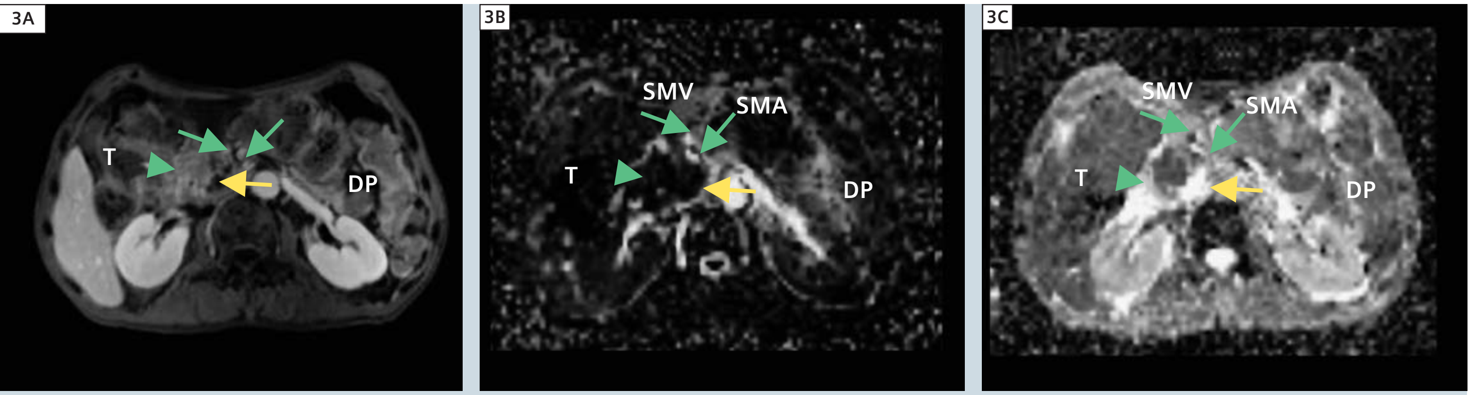

3 Axial T1w image **(A)**, f-map **(B)** and ADC map **(C)** in the same patient with pancreatic cancer as shown in figure 2. The carcinoma can be seen as a hypointense area in both the f and the ADC-map (green arrowhead). Note that the hypointense area in the f-map is larger than that in the ADC-map because in the f-map the dilated pancreatic duct (long arrows) adjacent to the tumor is as hypointense as the tumor itself. Also appreciated in these images are the superior mesenteric artery (SMA) and superior mesenteric vein (SMV) (green arrows), which both appear bright in the f-map and in the T1w image. In the ADC-map, the SMV is visible but the SMA is not. The tumor is more easily evidenced in the f-map than in the conventional imaging. (T = tumor; DP = ductus pancreaticus (yellow arrow); SMA = superior mesenteric artery; SMV = superior mesenteric vein).

DWI was performed in addition to the routine MR imaging protocol. Diffusion-weighted images were acquired using a single-shot echo-planar imaging (SE-EPI) pulse sequence in end expiration breath-hold with the following imaging parameters: TR = 1300 ms, TE = 60 ms, FOV = 350 × 273 mm^2, matrix size = 100 × 78, 14 slices, slice thickness/gap = 5/0.25 mm, 4 averages, bandwidth = 3000 Hz/Px, k-space based parallel imaging technique (*syngo* GRAPPA; Siemens Healthcare) used with an acceleration factor of two, b-values = 0, 25, 50, 75, 100, 150, 200, 300, 400, 600 and 800 s/mm^2 and a total measurement time of twelve minutes. The diffusion weighting was accomplished with a twice-refocused spin echo (TRSE) diffusion preparation and three orthogonal gradient directions (1,1,-1/2), (1,-1/2,1) and (-1/2,1,1) to obtain trace-weighted images. The acquisition was separated into blocks (b0, b25), (b0, b50)...(b0, b800) and each block was acquired in a single breathhold (TA = 26 s) to avoid motion artifacts.

CT examination

Computed tomography (CT) scans of the patients were obtained from referring institutions.

Post processing and data analysis

DW-images were post-processed using software developed in-house based on the open source imaging software ImageJ (http://rsb.info.nih.gov/ij) applying two approaches:

- biexponential Levenberg-Marquardt based fitting to the IVIM-model equation (1) (see above) separating the contribution of microperfusion and real diffusion in a DWI measurement. In this fit, the perfusion fraction f and the diffusion coefficient D were taken as free parameters, whereas the pseudo Diffusion Coefficient D* was fixed at 20 μm^2/ms.
- monoexponential linear least squares fitting to equation (2):

$$\ln \frac{S}{S_0} = -b(ADC)$$

using the total set of b-values yielding the Apparent Diffusion Coefficient ADC. The f parameter obtained through the first approach and the ADC parameter obtained through the second approach were mapped as a gray scale to create multi-slice f-map and ADC-maps.

For two specific cases, the f and ADC data were combined to identify vascular and bile duct voxels. Voxels with high perfusion ($f > 0.35$) but low ADC (ADC between 0.81 and 2.1 μm^2/ms) were classified as vascular while those with low perfusion ($f < 0.15$) but high ADC (ADC between 1.5 and 2.5 μm2/ms) were classified as ductal. A color overlay was then used to depict vascular (red) and bile duct (blue) voxels on the f-maps. Images and parameter maps were read by two experienced radiologists in consensus. Pancreatic lesions were first identified in the routine CT and MR images. The lesions were then visually identified in the corresponding ADC and f-maps.

Results

Healthy volunteer

An example of normal ADC and f-map findings, taken from one of the healthy volunteers is provided in figure 1. It can be seen that the pancreas (arrow) appears isointense to the liver in the ADC-map. In the f-map, the pancreas shows a mixed hypo- and hyperintense signal.

Pancreatic adenocarcinoma

Four cases of histopathologically confirmed adenocarcinoma are shown in figures 2 through 6.

Figure 2 shows a venous phase contrast CT, venous phase contrast T1w and T2w MRI for the first carcinoma case in which a lesion in the head of the pancreas is hypodense in CT and hypointense in both T1w and T2w MRI. Also note the dilated pancreatic duct (DP). The ADC, and f-map for this case, presented in figure 3, clearly show the lesion as an area of low apparent diffusion on the ADC and hypo-perfusion (hypointense) on the f-map. Compared to the healthy volunteer, note the extensive area of hypointensity in both the f-map and the ADC in the tumor region. Also note that the tumor stands out most prominently on the f-map. Furthermore, vessels are best delineated and hyperintense on the f-map. However, there is no clear demarcation between the tumor and the dilated duct on the f-map. This is better seen on the ADC map where the duct is relatively hyperintense when compared to the tumor.

Figure 4 shows a venous phase T1w, ADC and f-map for the second carcinoma patient. The lesion again appears as hypointense in T1w, as well as on both the ADC and f-map. Again, note the superior depiction of the tumor in the f-map where once more the vessels in the vicinity of the tumor are delineated

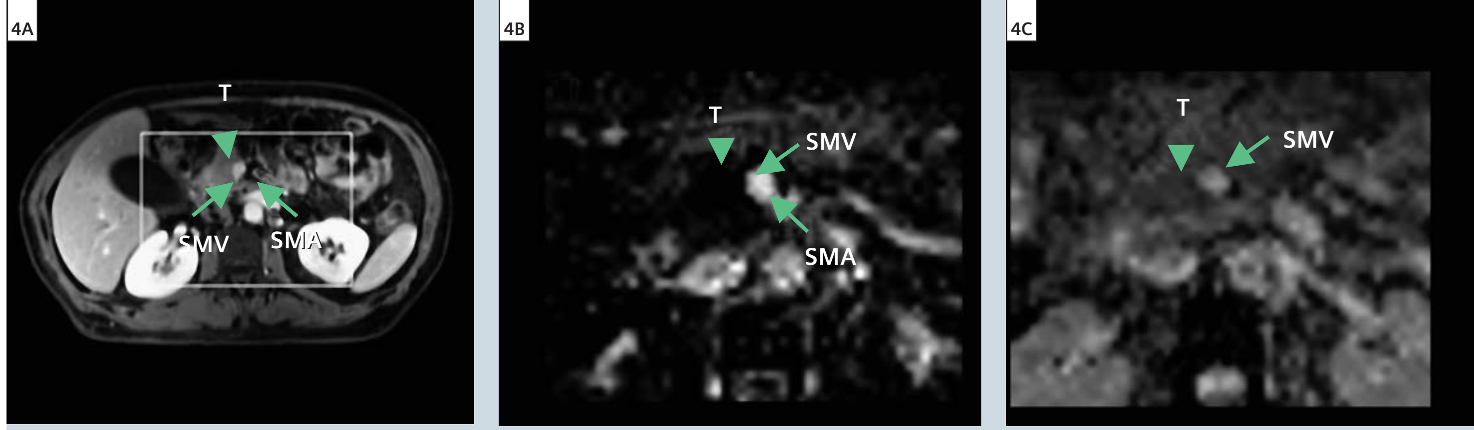

4 Patient with pancreatic cancer tumor in the head of the pancreas (green arrowhead). The tumor is better delineated in the f-map **(B)** than in the ADC-map **(C)**. Contact with the adjacent superior mesenteric vein (SMV) can be seen in all three images. Note that the superior mesenteric artery (SMA) is visible in the f-map but not in the ADC-map. T1w image **(A)** also provided for comparison. (white rectangle in T1w image = region displayed in other images; T = tumor; SMA = superior mesenteric artery; SMV = superior mesenteric vein).

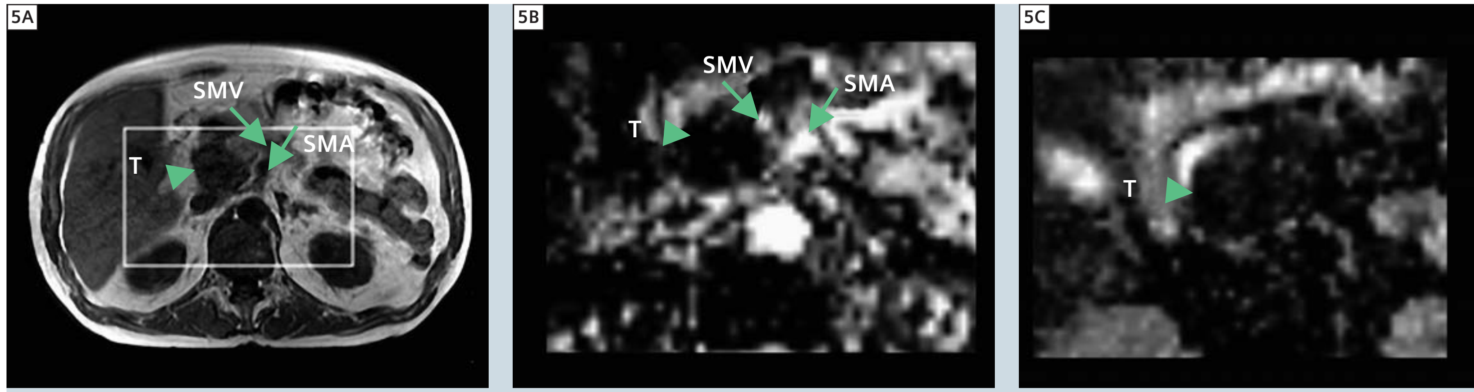

5 Axial T1w image **(A)**, f-map **(B)** and ADC-map **(C)** in a patient with pancreatic cancer in the head of the pancreas (green arrowhead). The tumor margins are better seen in the f-map than in the ADC-map. Furthermore, the superior mesenteric artery (SMA) and vein (SMV) can be seen in the f-map (green arrows) but not in the ADC-map. (White rectangle in T1w image = region displayed in other images; T = tumor; SMA = superior mesenteric artery; SMV = superior mesenteric vein).

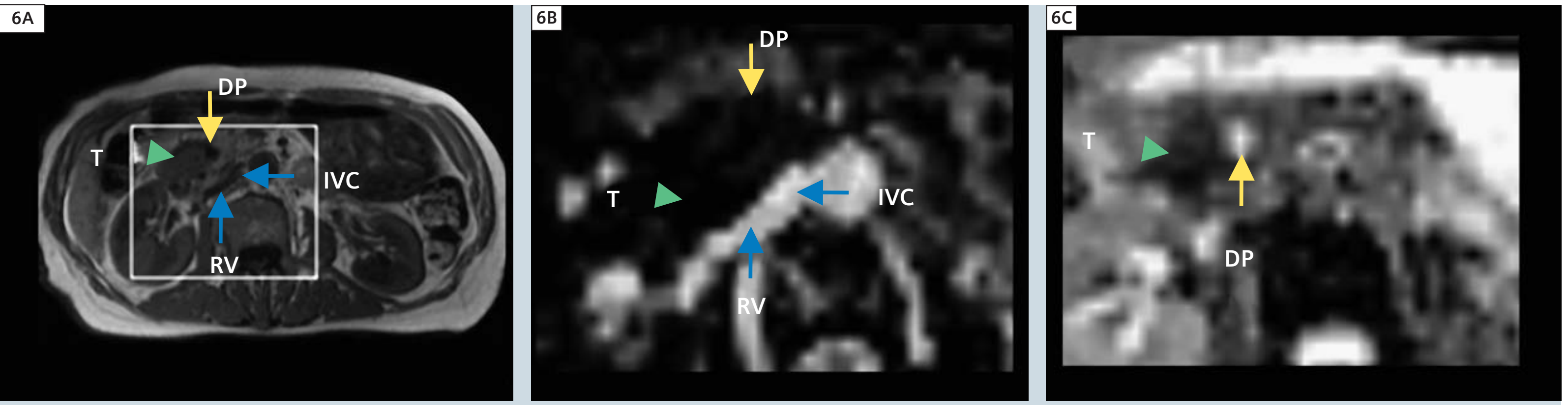

6 Patient with a pancreatic cancer in the head of the pancreas. Like in the case presented in figure 3, in the ƒ-map **(B)** the lesion can not be separately distinguished from the adjacent dilated pancreatic duct (DP), whereas the structures can be readily told apart in the ADC-map **(C)**. However, the ƒ-map provides much better visualization of the vasculature than the ADC-map, i.e., one can identify the inferior vena cava (IVC), renal vein (RV) and aorta **(A)**. T1w image (A) also provided for comparison. (White rectangle in T1w image = region displayed in other images; T = tumor; IVC = inf. vena cava, RV = renal vein, A = aorta).

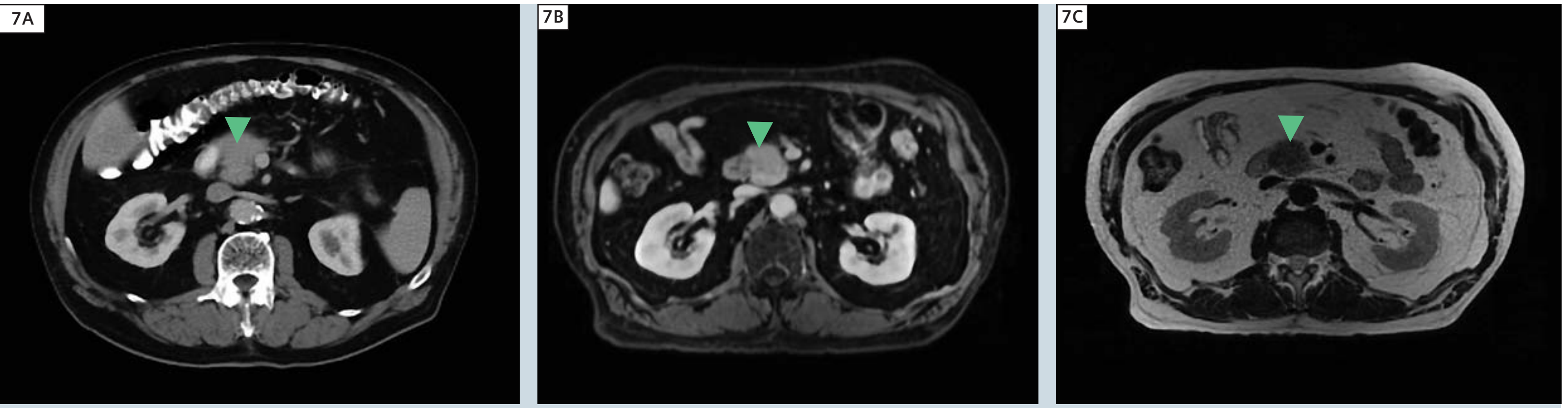

7 Axial venous phase contrast-enhanced CT **(A)**, portal phase contrast-enhanced T1w **(B)** and T2w **(C)** images of patient with histopathologically proven chronic pancreatitis in the head of the pancreas (green arrowhead). Note the mass-forming aspect of the lesion, and absence of calcifications in the CT.

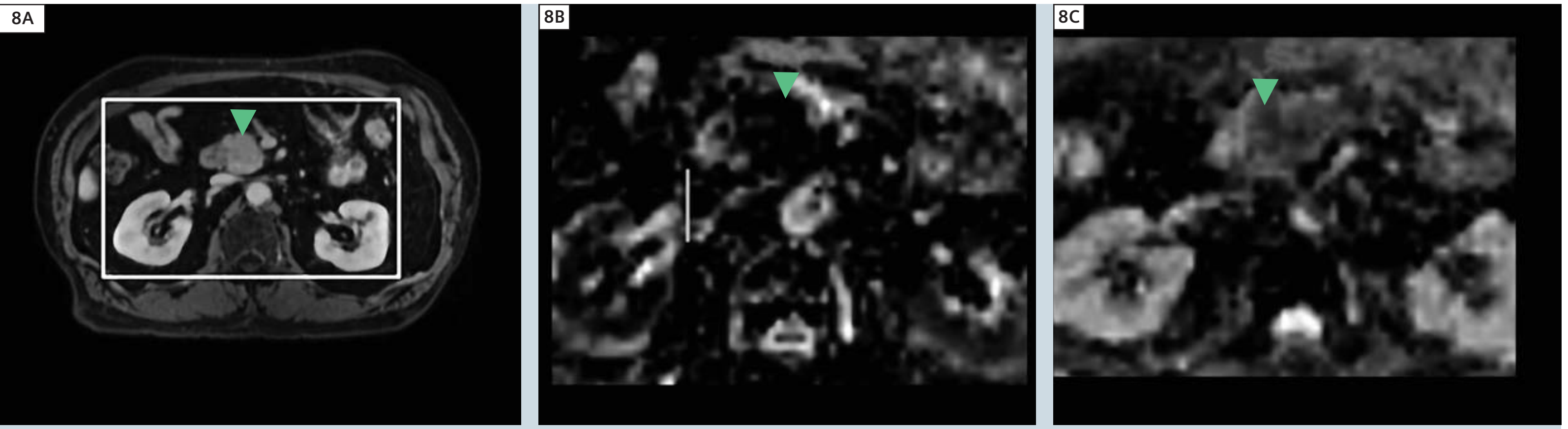

8 Axial portal phase contrast-enhanced T1w **(A)**, ƒ-map (B) and ADC-map **(C)** of the pancreatitis patient from figure 6. In the contrast-enhanced MRI a slightly hypointense lesion can be seen in the head of the pancreas (large white arrow). It appears markedly hypointense in the ƒ-map and only slightly hypointense on the ADC-map (white rectangle in T1w image = region displayed in other images).

clearly and appear hyperintense. Since no pancreatic duct is present in this slice, the tumor size is depicted accurately in the ƒ-map.

In the third carcinoma patient (Fig. 5), once more the tumor appears hypointense on the ƒ-map. Again, tumor contrast on the ƒ-map (5B) is higher than in the ADC-map (5C). In this case, the tumor appears larger than it is on the ADC-map because it is hardly discriminated from the neighboring vessel, whereas the ƒ-map, where the vessels are clearly seen as hyperintense, shows the tumor's correct size.

Contrary the previous case, the carcinoma in the fourth cancer patient (Fig. 6) is overestimated in the ƒ-map when compared to the ADC-map because it lies close to the dilated duct, and both are hypointense. In the ADC-map, the duct appears hyperintense and is thus more readily distinguishable from the lesion as previously seen in patient two (Fig. 4).

Chronic pancreatitis

Two cases of histopathologically confirmed pancreatitis mass lesions are shown in figures 7 through 9.

Figure 7 shows the venous phase contrast-enhanced CT, portal phase contrast-enhanced T1w, and T2w for the first pancreatitis patient. Note the mass-forming aspect of the lesion. On the ADC and ƒ-maps for the same case (Fig. 8), the pancreatitis lesion can be outlined as clearly hypointense in the ƒ-map. In the ADC-map, the lesion is partly hypo- and partly isointense compared to the surrounding tissue, and therefore hard to delineate. Note again that the poor lesion/vessel contrast might cause an overestimation of the total lesion size in the ADC-map (e.g. figure 5).

Figure 9 shows similar venous phase T1w, ADC, and ƒ-maps where the mass-forming pancreatitis is hypodense in the CT and hypointense in T1w/T2w images. Compared to the previous case, note that the lesion is hard to detect on both the conventional MRI and the ADC-map, but that it stands out in stark contrast against both the non-affected pancreatic parenchyma and the surrounding vessels in the ƒ-map.

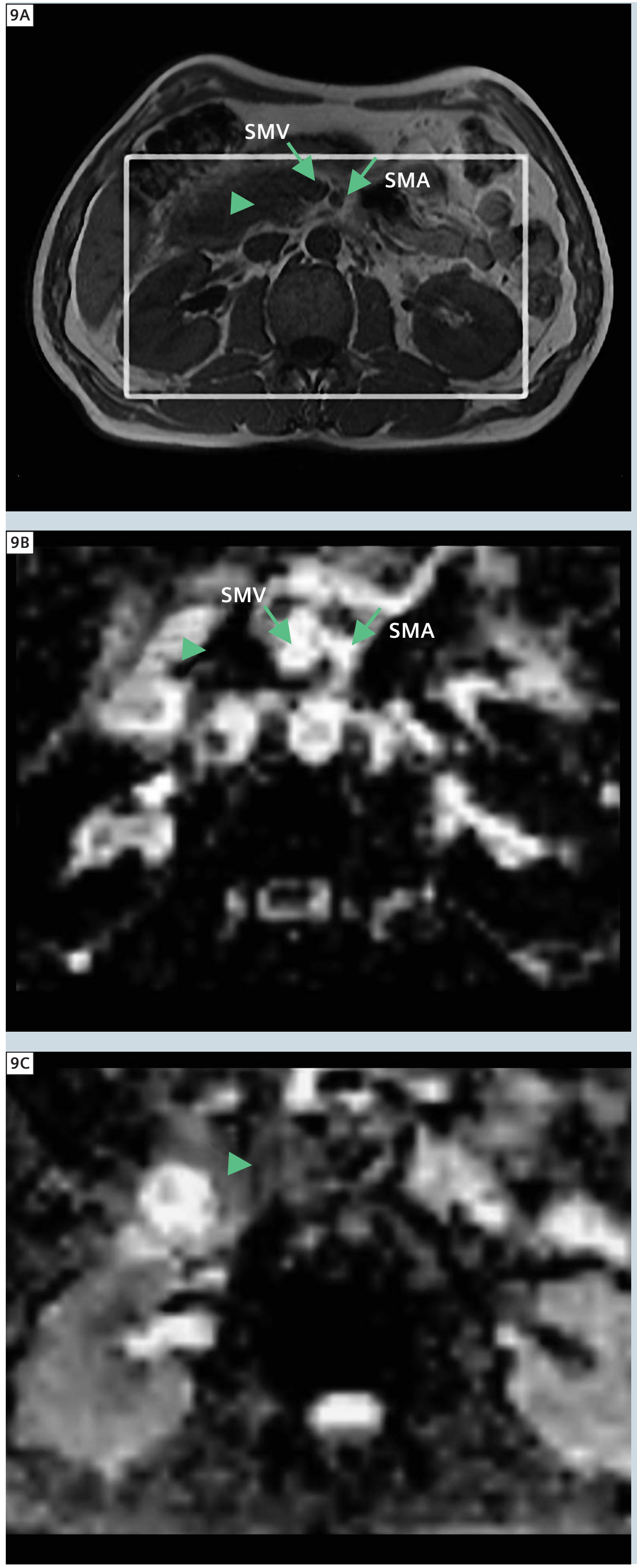

9 Axial T1w **(A)**, ƒ-map **(B)** and ADC-map **(C)** for a second patient with histopathologically proven chronic pancreatitis with mass-formation in the head of the pancreas (green arrowhead). The lesion is seen as a well-delineated, hypointense area in the ƒ-map, while it is less clearly delineated in the ADC-map. Also well-delineated in the ƒ-map as in the T1w image, are the superior mesenteric vein (SMV) and superior mesenteric artery (SMA) (green arrows). (SMA = superior mesenteric artery; SMV = superior mesenteric vein).

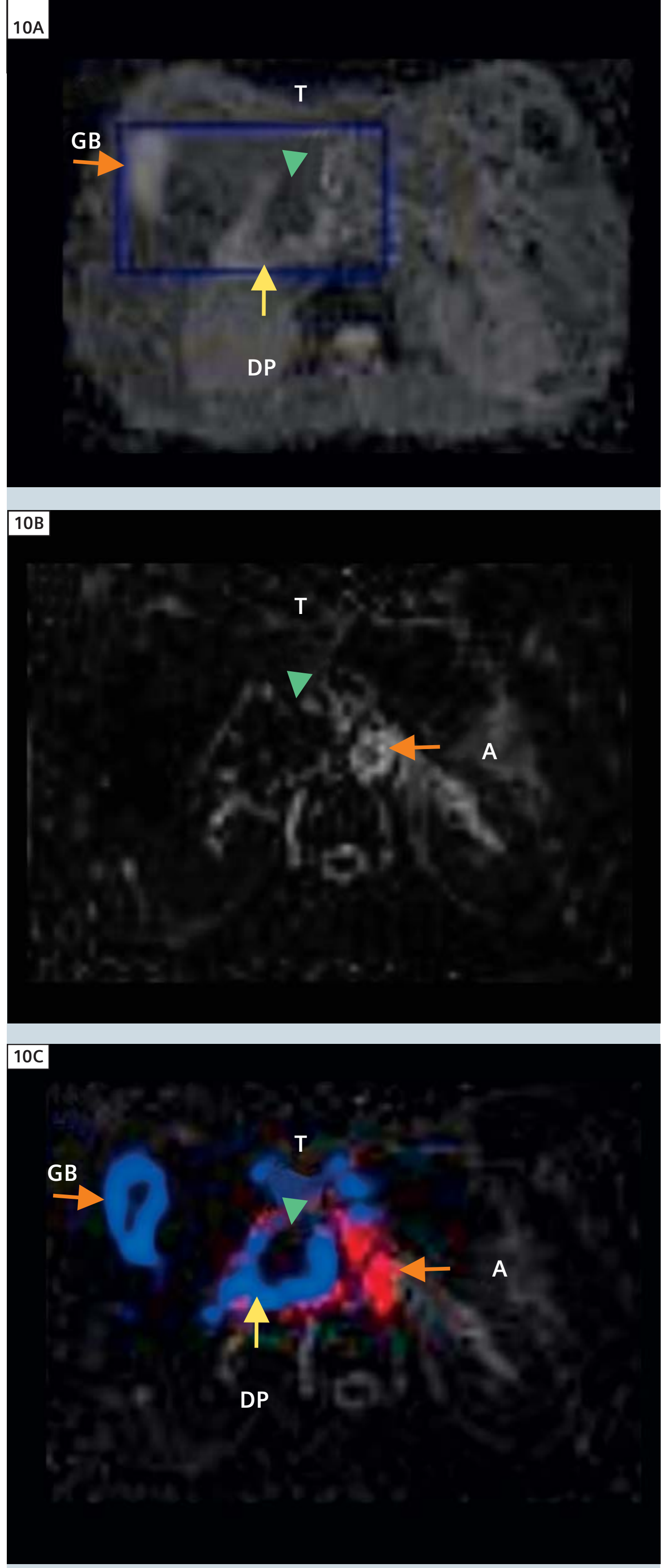

10 Axial ADC-map **(A)** and f-map **(B)** of the pancreatic carcinoma case previously presented in figures 2 and 3 along with an image which integrates both ADC- and f-map data **(C)**. In the integrated image **(C)**, a color mask is used to segment vascular (red) and ductal (blue) voxels according to f and ADC ranges described in the text. Note that the tumor is best delineated in the f-map if the pancreatic duct, which due to its curved path almost completely surrounds the tumor, is color-tagged according to the integrated data. (Dark blue rectangle in ADC-map = region of interest for calculating the color overlay; T = tumor; GB = gall bladder; DP = ductus pancreaticus; A = aorta).

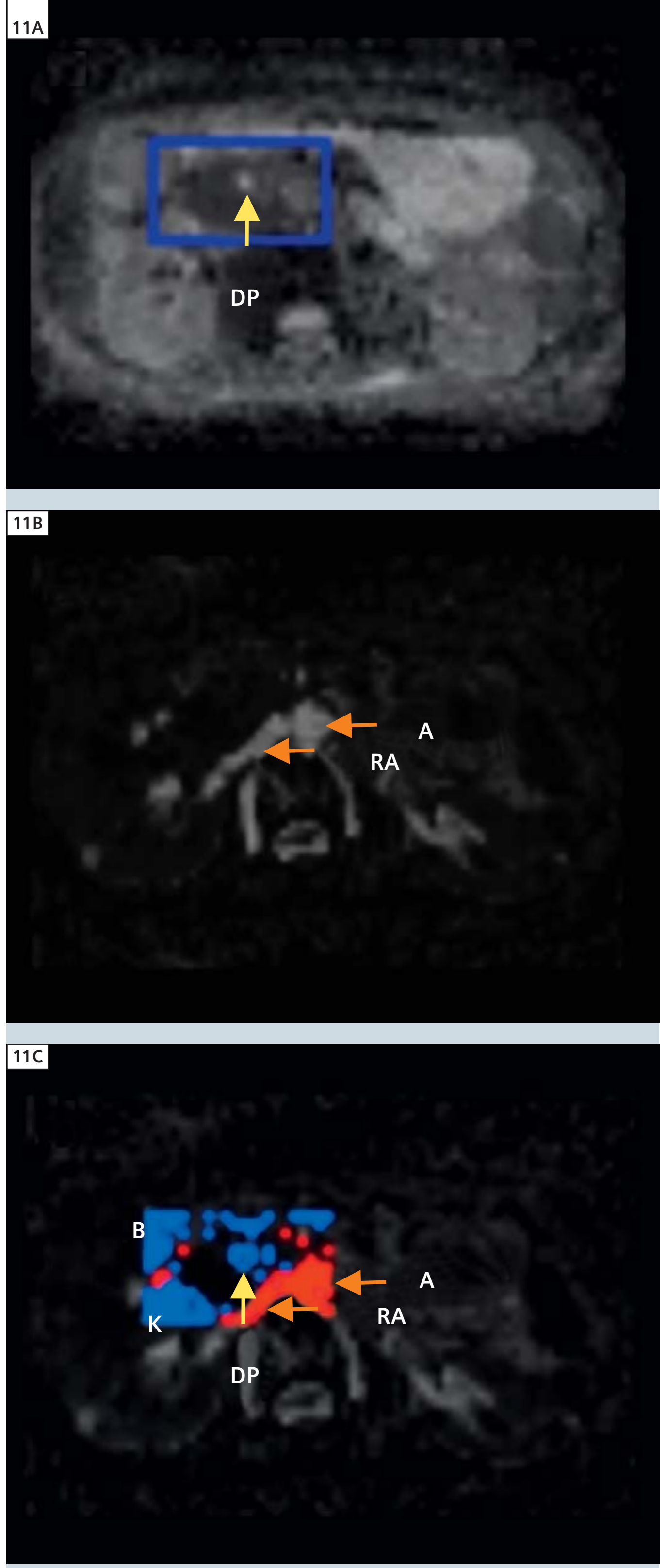

11 Patient previously presented in figure 6 with the ADC **(A)** and f-map **(B)**. Image **(C)** shows the f-map with a vascular (red) and ductal (blue) segmentation overlay calculated by integrating the ADC and f data. Note that the pancreatic duct inside the tumor region can be readily identified on the f-map only with the help of the overlay. (Dark blue rectangle in ADC-map = region of interest for calculating color overlay; T = tumor; GB = gall bladder; DP = ductus pancreaticus; A = aorta; K = kidney; B = bowel).

f-maps with an ADC overlay

As seen in the previous cases, the f-map is superior to the ADC-map considering tumor detection in general. Also, the f-maps show an increased tumor/vessel contrast when compared to the ADC-maps, but have the disadvantage that adjacent ductal structures may coalesce with the tumor. To circumvent this, we developed a method to integrate both f and ADC in single parameter images where based on their unique combination of ranges of f and ADC values, voxels were tagged as belonging to either vessels, ducts, or solid tissue.

In figure 10, the f and ADC-maps of the patient previously presented in figures 1 and 2 are presented once more (10A, B). Figure 10C shows a color overlay on the f-map where the pancreatic duct, the gall bladder and the bile ducts are marked blue and the vessels are marked red, defined by the previously described f and ADC ranges. Note that the tumor size can now be estimated correctly. Figure 11 shows the patient previously presented in figure 6 with the ADC and f-map (11A, B). Note that the duct inside the tumor region can be readily identified on the f-map when the color tags are used. Other areas also marked blue include the kidney and the bowel.

Conclusion

in the cases presented, IVIM-based f-maps calculated from multiple b-value-weighted magnetic resonance data enabled the delineation of pancreatic lesions and demonstrated advantages over ADC imaging in their ability to distinguish vessels from low-perfused lesions, a crucial element of pancreatic cancer staging. However, which is less apt for distinguishing between lesion and pancreatic or bile ducts as were the ADC-maps. By considering both ADC and f-maps in combination, better lesion delineation can be achieved than by considering either parameter separately. Concerning lesion pathology differentiation: based on the current experience, it does not seem possible to differentiate between pancreatic carcinoma and pancreatitis using only the imaging aspects of the lesion in the f-map. Further research should elucidate the potential of quantitative approaches as means to address this issue. An advantage of ADC and f-maps when compared to the current imaging standards of concentional CT and ceMRI, is that neither technique uses ionizing radiation nor contrast agent. Since the acquisition takes only approximately 10 minutes, they may be not only safer but also more cost-effective than CT or conventional MRI. Combined ADC/f-maps may be particularly well suited for the assessment of lesions in patients who can not tolerate contrast agents. In these cases, appropriately combined non-contrast agent T1w/T2w MRI, ADC and f-maps would be recommended. This combination of non-invasive, non-contrast agent techniques, also shows promise as a screening method for post-treatment follow-up.

---

*WIP - Work in progress. This information about this product is preliminary. The product is under development and not commercially available in the U.S., and its future availability cannot be ensured.

References

1 Gemmel C, Eickhoff A, Helmstadter L, et al. Pancreatic cancer screening: state of the art. Expert Rev Gastroenterol Hepatol 2009;3:89–96.

2 Tamm EP, Silverman PM, Charnsangavej C, et al. Diagnosis, staging, and surveillance of pancreatic cancer. AJR Am J Roentgenol 2003;180:1311–1323.

3 Tamm EP, Bhosale PR, Lee JH. Pancreatic Ductal Adenocarcinoma: Ultrasound, Computed Tomography, and Magnetic Resonance Imaging Features. Semin Ultrasound CT MRI 2007;28:330–338.

4 Colagrande S, Carbone SF, Carusi LM, Cova M, Villari N. Magnetic resonance diffusion-weighted imaging: extraneurological applications. Radiol med (2006) 111:392–419.

5 Koh DM, Collins DJ Diffusion-weighted MRI in the body: applications and challenges in oncology. AJR Am J Roentgenol 2007;188:1622–1635.

6 Yoshikawa T, Kawamitsu H, Mitchell D, Ohno Y, Ku Y, Seo Y, Fujii M, Sugimura K. ADC Measurement of Abdominal Organs and Lesions Using Parallel Imaging Technique, AJR 2006;187:1521–1530.

7 Czako L. Diagnosis of early-stage chronic pancreatitis by secretin-enhanced magnetic resonance cholangiopancreatography. J Gastroenterol 2007; 42[Suppl XVII]:113–117.

8 Balci NC, Momtahen AJ, Akduman EI, Alkaade S, Bilgin M, Burton FR. Diffusion-weighted MRI of the pancreas: correlation with secretin endoscopic pancreatic function test (ePFT). Acad Radiol. 2008 Oct;15(10):1264–8.

9 Inan N, Arslan A, Akansel G, Anik Y, Demirci A. Diffusion-weighted imaging in the differential diagnosis of cystic lesions of the pancreas. AJR Am J Roentgenol. 2008 Oct;191(4):1115–21.

10 Fattahi R, Balci NC, Perman WH, Hsueh EC, Alkaade S, Havlioglu N, Burton FR. Pancreatic diffusion-weighted imaging (DWI): comparison between mass-forming focal pancreatitis (FP), pancreatic cancer (PC), and normal pancreas. J Magn Reson Imaging. 2009 Feb;29(2):350–6.

11 Matsuki M, Inada Y, Nakai G, et al. Diffusion-weighed MR imaging of pancreatic carcinoma. Abdom Imaging 2007;32:481-483.

12 Muraoka N, Uematsu H, Kimura H, et al. Apparent diffusion coefficient in pancreatic cancer: characterization and histopathological correlations. J Magn Reson Imaging 2008;27:1302–1308.

13 Le Bihan D. Intravoxel incoherent motion perfusion MR imaging: a wake-up call. Radiology. 2008 Dec; 249(3): 748–52.

14 Lee SS, Byun JH, Park BJ, Park SH, Kim N, Park B, Kim JK, Lee MG. Quantitative analysis of diffusion-weighted magnetic resonance imaging of the pancreas: usefulness in characterizing solid pancreatic masses. J Magn Reson Imaging 2008;28:928–936.

15 Luciani A, Vignaud A, Cavet M, Nhieu JT, Mallat A, Ruel L, Laurent A, Deux JF, Brugieres P, Rahmouni A. Liver cirrhosis: intravoxel incoherent motion MR imaging-pilot study. Radiology. 2008 Dec;249(3):748–52.

16 Le Bihan D MR imaging of incoherent motions: application to diffusion and perfusion in neurologic disorders. Radiology 1986;161:401–407.

17 Le Bihan D Seperation of Diffusion and Perfusion in Intra Voxel Incoherent Motion MR Imaging Radiology 1988;168:497–505.

18 Lemke A, Schad LR, Laun F, Stieltjes B. Differentiation of pancreas carcinoma from healthy pancreatic tissue using a wide range of b-values: Comparison of ADC and IVIM parameters. Proc. Intl. Soc. Mag. Reson. Med. 17 (2009):666.

19 M. Klauss, A. Lemke, K. Grünberg, M. N. Wente, H-U. Kauczor, S. Delorme, L. Grenacher, and B. Stieltjes. Evaluation of low and high b-values for the differentiation between pancreatic carcinoma and chronic pancreatitis using Diffusion-Weighted Imaging. Proc. Intl. Soc. Mag. Reson. Med. 17 (2009): 4031.

Contact
Bram Stieltjes, M.D.
German Cancer Research Center (DKFZ)
Department of Radiology - E 010
Im Neuenheimer Feld 280
69120 Heidelberg
Germany
Tel.: +49(0)6221 42-2492
b.stieltjes@dkfz.de

Case Report:
Nonsecretory Multiple Myeloma MRI Monitoring of Therapy Response

Marius Horger, M.D.

University Hospital Tuebingen, Dept. of Diagnostic and Interventional Radiology, Tuebingen, Germany

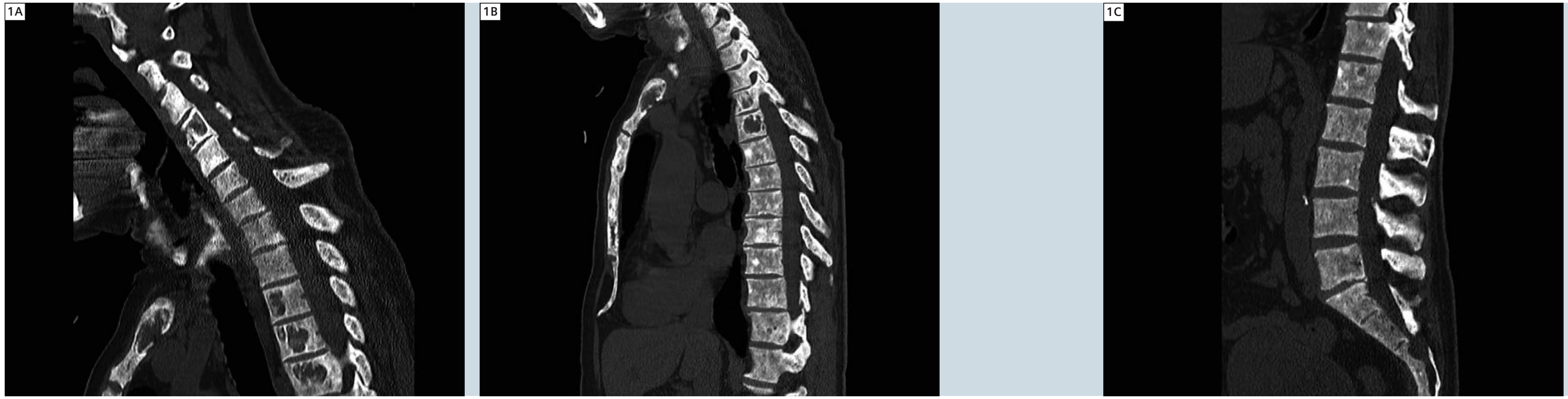

1 Low dose MDCT used for evaluation of myeloma. In the shown case, osteoscleroses is evident as well as multiple lytic lesions. Additionally medullar infiltration is present. **1A, B, C**: Sagittal reformation of MDCT (**A** cervical, **B** thoracic, **C** lumbar spine).

1 **1D, E, F**: Coronal MPR (**D** thoracic, **E** lumbar **F** pelvis).

Multiple myeloma (MM) is a malignant hematologic disorder characterized by the infiltration of neoplastic plasma cell into bone marrow. Detection of medullary involvement is best accomplished with the aid of MRI. Nevertheless, assessment of myeloma bone disease consisting of bone destruction due to increased activity of osteoclasts generally not accompanied by a comparable increase of osteoblasts function and consequently by new bone formation, is the hallmark of MM. Thus, competing imaging modalities are nowadays used for optimal patient management.

With the event of novel antimyeloma therapies, imaging monitoring, in addition to classical hematologic monitoring, has been advocated by many authors. Visualization of myeloma burden at baseline and during therapy is beneficial for more accurate patient management and prognostic evaluation. Therefore, whole-body imaging protocols are mandatory, especially for assessment of myeloma infiltration in all bone marrow cavities (medullary involvement) as well as for diagnosis of extramedullary involvement. These two myeloma manifestations can be displayed at best by joined multidetector Computed Tomography (MDCT) and MR imaging. Nonetheless, as we generally have to avoid IV contrast application, due to impaired renal function, evaluation of myeloma activity at follow up alone by means of nonenhanced studies (conventional imaging) proves generally difficult. Moreover, in some cases, medullary myeloma cell infiltrates do not entirely regress at time. With MRI, besides signal intensity abnormalities occurring during therapy, contrast enhancement is the sole finding in support of residual tumor vitality. At this point, the use of diffusion-weighted MRI could represent a practicable alternative to contrast studies or even tumor perfusion studies. The main informational gain from this approach could hence represent a much more accurate differentiation between new active and older inactive lesions which is otherwise not possible to detect with confidence, other than by using, for instance, additional functional imaging techniques such as FDG-PET.

We report in this case on a 73-year-old male patient with a nonsecretory multiple myeloma; the first manifestation of the disease with pathologic fracture of the clavicula was reported in 1996, however, definitive diagnoses of nonsecretory myeloma was two years later in 1998 after multiple frustrane bone biopsies. Histopathology revealed at this time point a high degree of osteoscleroses with infiltration of lymphocytes and plasma cells. The patient was treated initially with an Alexanian chemotherapy regimen (Melphalan and Prednison) and stayed for six years in good partial remission. Besides initial bone sclerosis, sclerosis of cancellous bone increased after therapy, hampering in part evaluation of bone marrow signal and CT-attenuation acquired for imaging surveillance.

At the time-point of presentation at our department for the whole body (wb) imaging detailed in this report, the patient received a long-term maintenance chemotherapy after successful therapy of tumor progression (histology: bone marrow infiltration of 95%) with normalization of Hb-levels in 2008. At the time-point of wb MRI, the patient had

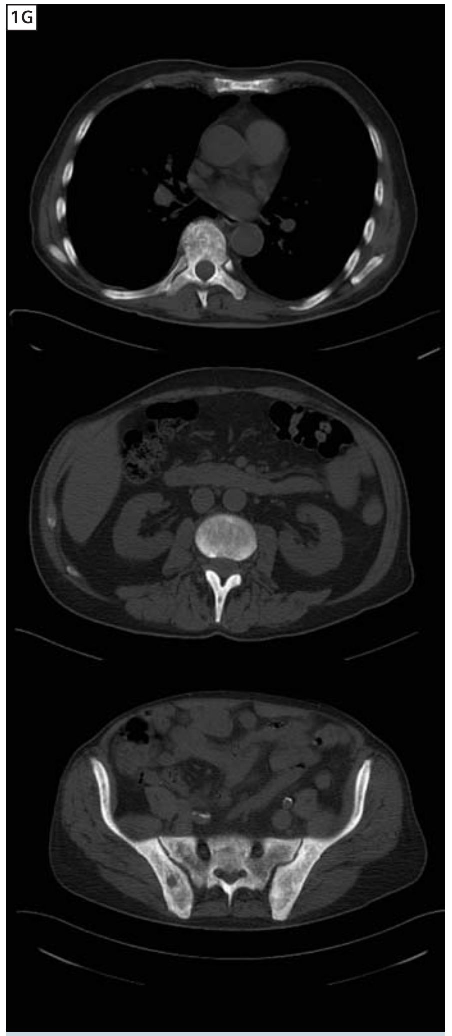

1 G: Original MDCT data sets (bone window).

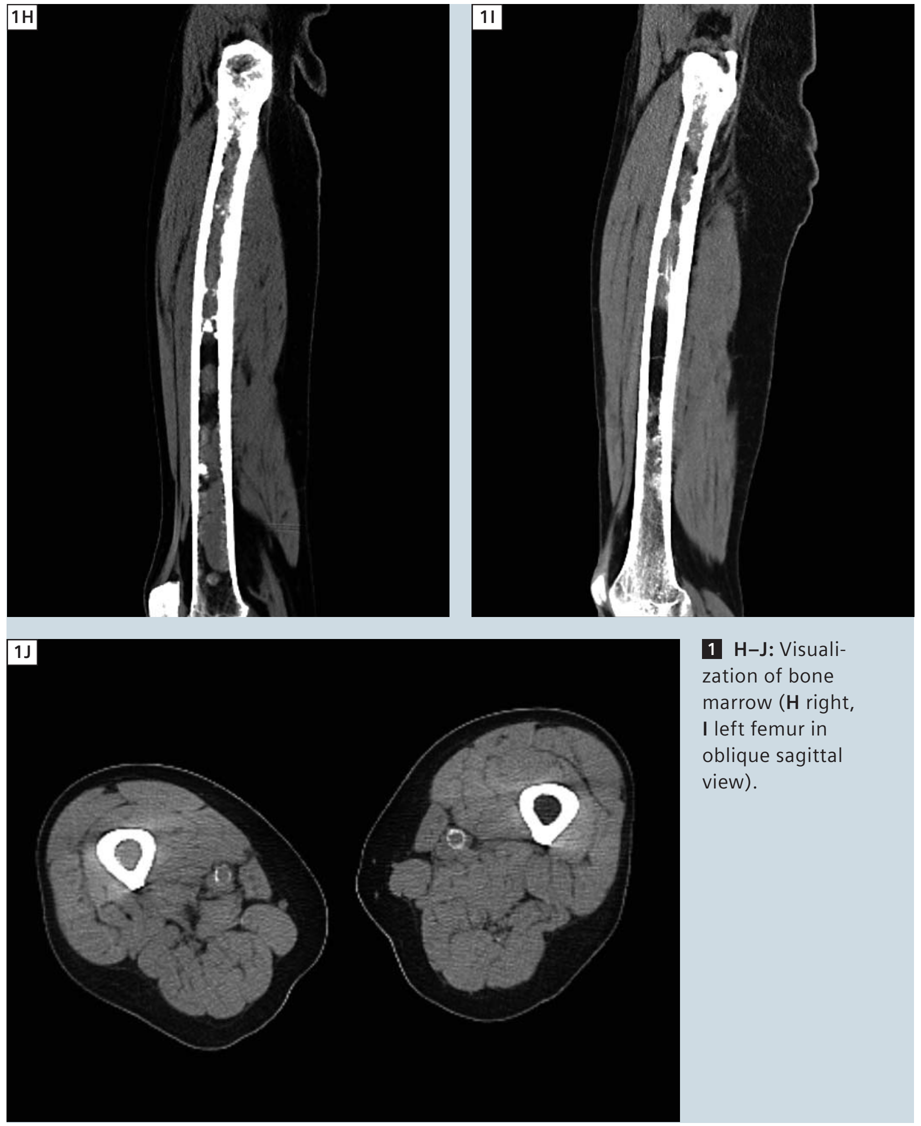

1 H–J: Visualization of bone marrow (**H** right, **I** left femur in oblique sagittal view).

been suffering from progressing dyspnoea for one week, with diminished appetite and adynamia. Also in line with the reduced general condition, slight lost of weight was documented (3 kg over the last three months). Blood parameters showed now anaemia, which was initially suspected to be mainly caused by chemotherapy scheme, and additionally infection parameters were positive. Therefore the patient received blood transfusion and antibiotics for symptomatic therapy. With the exception of a slight swelling of one ankle, inspection and vital parameters were normal; the patient also received long-term anticoagulation therapy because of former deep vein thromboses, although, D-Dimere were in normal range and no thromboses (Ultrasound (US) of the extremities) or pathologies of the lung (MDCT scan) were present at the time point of presentation. For evaluation of potential further progression of the non-secretory myeloma, a low-dose whole body CT scan follow-up was initially performed. This scan showed the already known scleroses of the bones with emphasis of the vertebrae and pelvis (Figs. 1A–G). However, a reduced density of medullar infiltration was reported while comparing the results with former wb MDCT scans (not shown). Nevertheless, medullar tumor foci were still present (Figs. 1H–J) and therefore residual tumor activity was diagnosed based on MDCT. There was no evidence, however, for a progression of the lytic lesions and no static hazard was reported. While low-dose wb MDCT has to be considered as the standard care for myeloma and is clearly superior to conventional x-ray, especially in case of nonsecretory myeloma, information of diffuse bone marrow infiltration is best provided by MRI. Therefore the patient was referred for a wb MRI.

Our myeloma protocol at 1.5 Tesla (MAGNETOM Avanto) includes coronal T1-weighted (T1w) and T2w TIRM images and whole-body diffusion-weighted imaging (DWI). Sequence parameters for single-shot EPI DWI (*syngo* REVEAL) were: TR / TE = 4500 / 59 ms, spectral fat suppression, slice thickness 4 mm, 4 averages, 192 matrix, PAT (*syngo* GRAPPA) factor of 2, averaged 3-scan trace at b-values of 50 and 800 s/mm^2, bandwidth 1530 Hz/Px, 30 slices per step; in total 13 positions had to be acquired in this patient. With a measurement time of approximately 2–3 min per step including automated shimming, a total measurement time for wb DWI of approximate 33 min resulted in this case. No contrast media was applied, for either CT or MRI. For comparison with coronal T1w and TIRM images, transversal acquired DWI images were reformatted and displayed in multiple oblique orientations with the *syngo* 3D task card; ADC-maps were generated automatically with the scanners integrated software (Inline Diffusion tool).

Based on morphology only, the MRI findings would be suggestive of high tumor load with special focus on the femora. Taking into account only the high b-value images, this diagnosis would be supported by DWI. However, based on wb ADC-mapping, a completely different picture became evident. Based on the high ADC values, high signal on the original b-value images had now to be interpreted as T2-shine through effect and not as a restriction of diffusivity. On the first look, this seems to contradict the results of the MDCT scan, where multiple nodules within the yellow marrow are present (compare figures 1H–J). But on the ADC-maps, different areas with high and very low diffusivity can be detected within the bone marrow of the femora as well as in the tibial bones; this indicates the presence of nodules with viable tumor, but the vast majority of these medullary findings have to be interpreted as transformed bone marrow after therapies with necrotic areas. T1w imaging, and especially DWI shows also remarkable dense bone marrow and / or tumor infiltration of the vetebra and pelvic bones. The high signal in original b-value imaging in combination with very low ADC values in particular is a clear indicator of high cellularity within

2 A: Multiplanar reconstruction (MPR) in coronal view of whole-body ADC images.
B: Transversal ADC-maps.

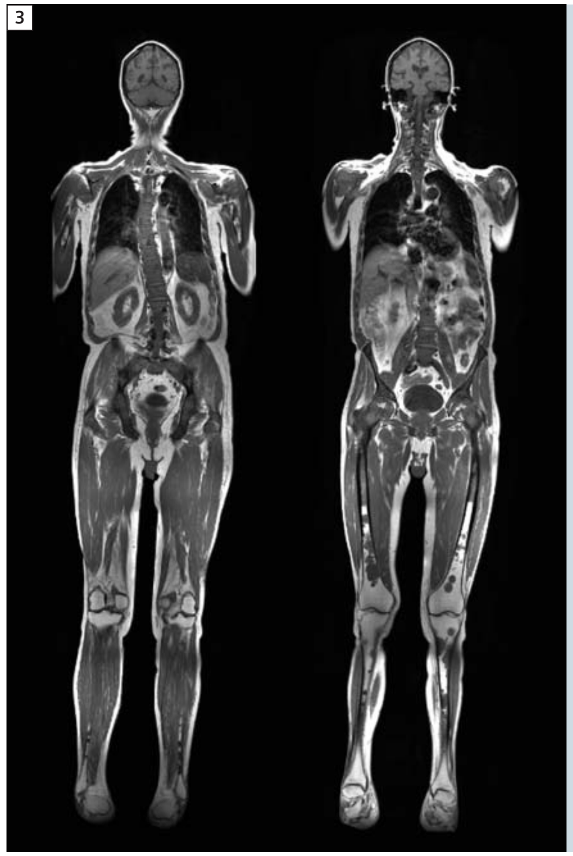

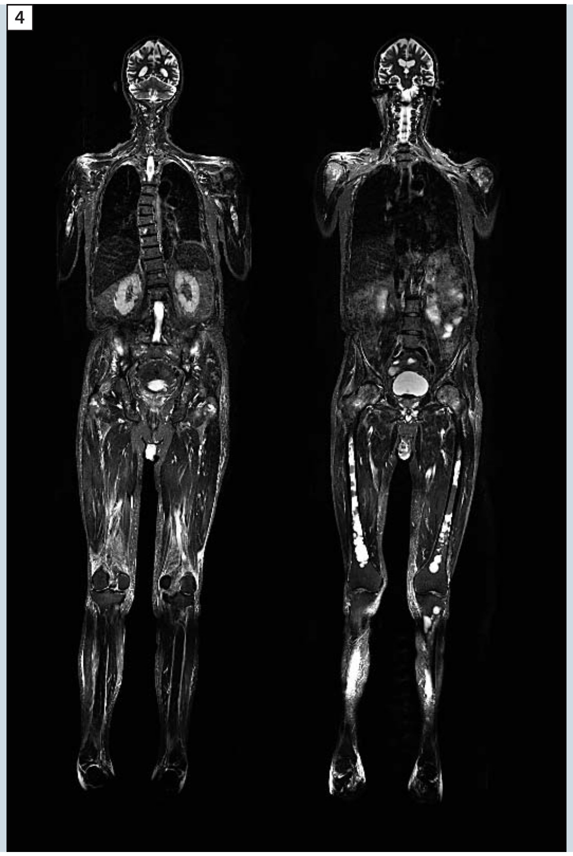

3 Corresponding whole-body T1w MRI.

4 Corresponding whole-body T2w TIRM MRI.

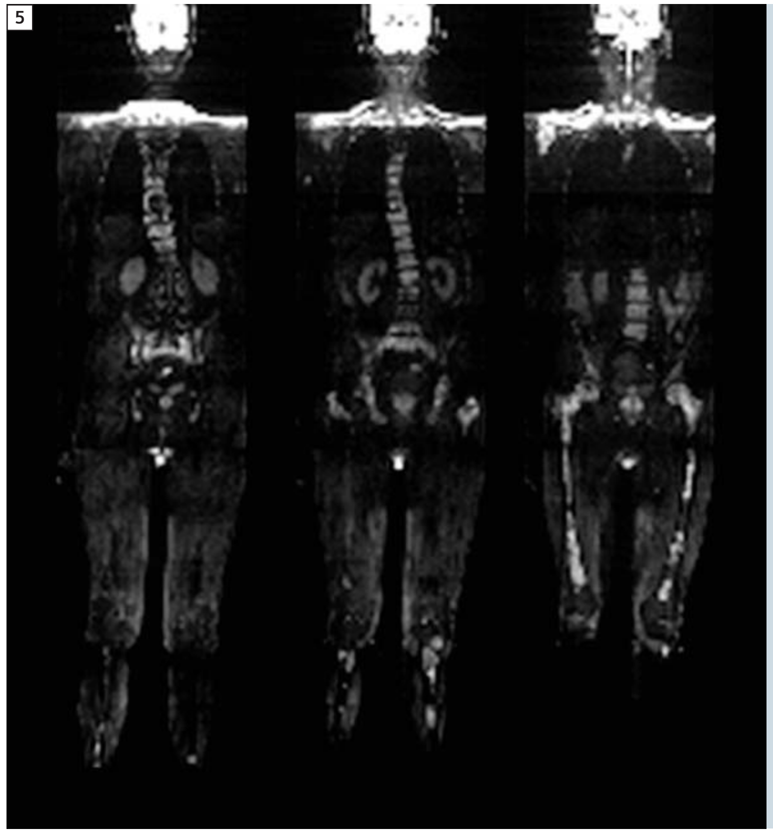

5 MPR of original b-value images in coronal view (b = 800 s/mm²).

6 Inverted maximum intensity projection (MIP) of b = 800 s/mm² images.

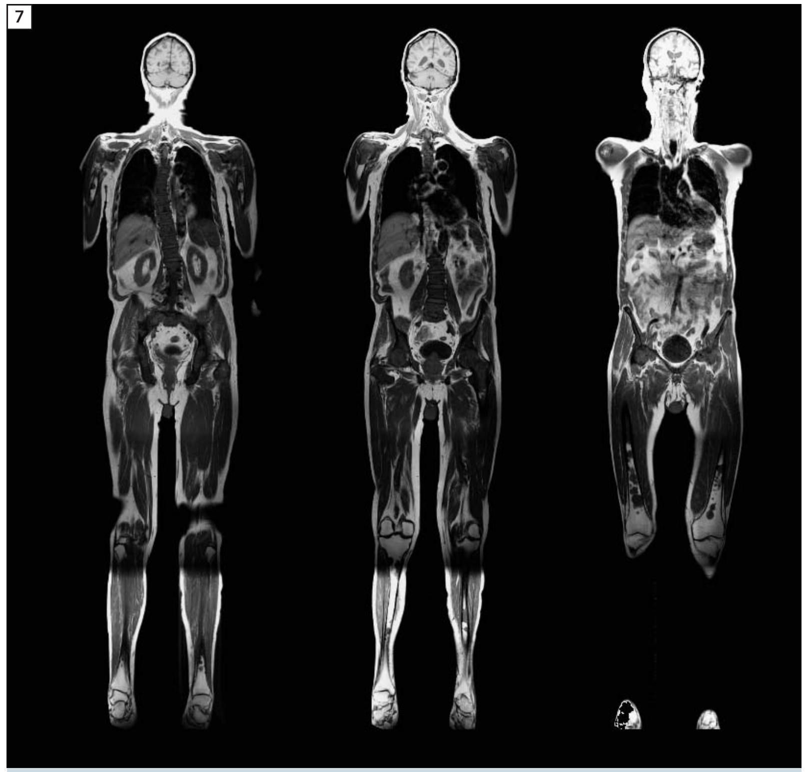

7 Short-term follow-up, T1w MRI.

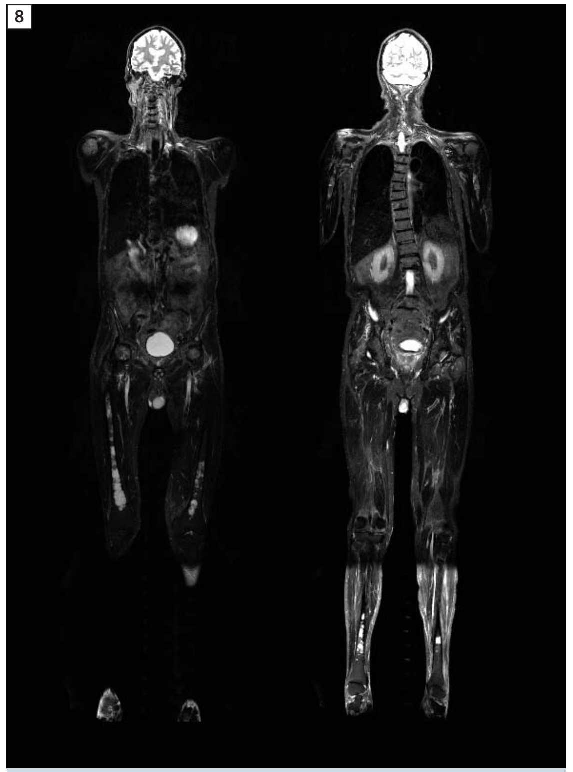

8 Short-term follow-up, T2w TIRM MRI.

the bone marrow; without DWI the signal lost on T1w MRI could also be interpreted as high density of bone matrix. Of course a definitive separation of myeloma infiltration and hyperproliferative / compensating hematopoietic system is challenging, given also the information provided by functional (DWI, perfusion) and metabolic imaging, and will be a challenge also for bone marrow biopsies. In this particular case, the patient's history and symptoms did support the MR diagnosis of tumor progression. The short-term follow up (Figs. 8–10) with MRI showed a tendency to progression of the nonsecretory myeloma.

Contact
Prof. Dr. Marius Horger
Department of Radiology
University Hospital of Tuebingen
Hoppe-Seyler-Str. 6
72076 Tuebingen
Germany
marius.horger@med.uni-tuebingen.de

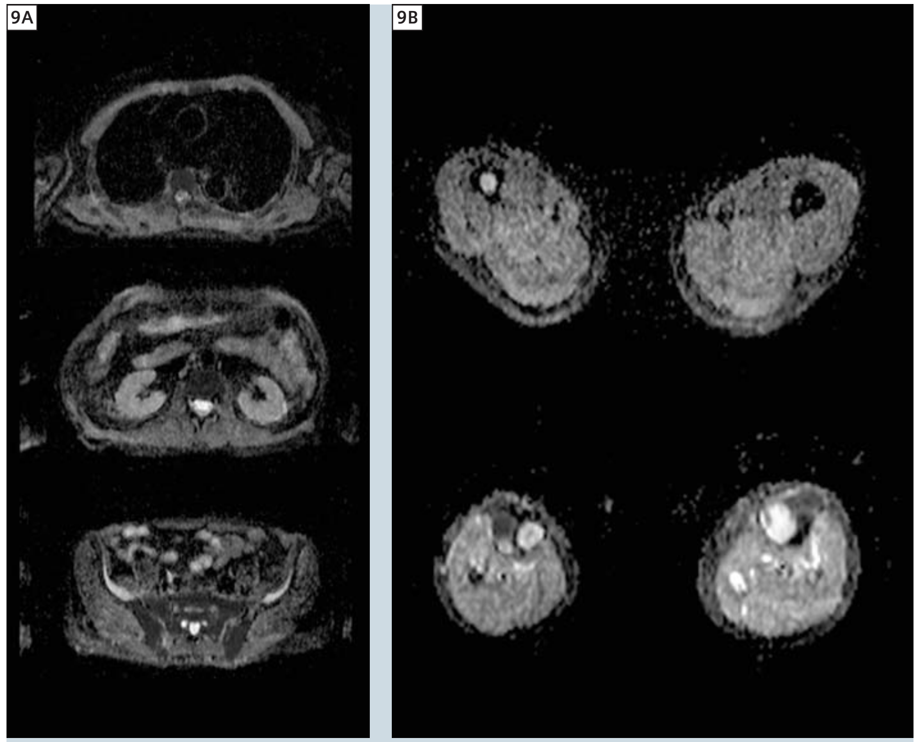

9 Short-term follow up, transversal oriented original ADC-maps.

Case Report:
Whole-body Oncologic Imaging with *syngo* TimCT

Eric Hatfield, M.D.[1]; Agus Priatna, Ph.D.[2]; John Kotyk, Ph.D.[1]; Benjamin Tan, M.D.[1]; Alto Stemmer[3]; Stephan Kannengiesser, Ph.D.[3]; Vamsi Narra, M.D.[1]

[1] *Mallinckrodt Institute of Radiology, Washington University School of Medicine, St Louis, Missouri, USA*
[2] *Siemens Healthcare, R&D Collaborations, St Louis, Missouri, USA*
[3] *Siemens Healthcare, MR PLM AW Oncology, Erlangen, Germany*

Introduction

Imaging has long been indispensible in the diagnosis of cancer and the management of oncology patients. More recently, the addition of physiologic information via positron emission tomography (PET) to the anatomic information of conventional computed tomography (CT) has revolutionized the detection of cancer and the monitoring of treatment response. With PET/CT, imaging evaluation goes beyond simple anatomic size criteria to measure the metabolic activity of malignant lesions, heralding an exciting new era of tailored therapy, improved efficacy, and lessened patient impact [1]. Magnetic resonance (MR) imaging can provide analogous anatomic and physiologic information in a single unfused modality. Combined with the anatomic detail of conventional sequences, diffusion-weighted imaging (DWI) has shown promise in both the detection of malignant lesions and monitoring response to therapy [2]. Future application of developing MR techniques to oncologic imaging will provide new insights into disease detection, therapy and surveillance. MR has the potential to provide multidimensional anatomic, functional, and metabolic oncologic evaluation without the administration of radiotracers. However, the development and application of MR in oncologic evaluations has historically been complicated by limited anatomic coverage. Whole-body imaging required in oncologic staging and surveillance has thus been infeasible given prohibitive scan times and patient impact. Tim (Total imaging matrix) technology improves on these coverage and time limitations by automating the table shifts and post-processing involved in multi-station exams. The next step in the solution lies in the combination of the Tim functionality with Continuous Table Movement (TimCT). For the first time, whole-body MR imaging is feasible and robust in conventional scan times, without off-isocenter artifacts or signal loss [3]. Anatomic coverage and time barriers now overcome, this innovation promises to unlock the full potential of MR in oncologic applications.

Method

Whole-body MR imaging was performed on a 3T MAGNETOM Trio, A Tim System, equipped with the *syngo* TimCT Oncology package. Three Body Matrix coils, the Spine Matrix, and the Head/Neck Matrix coil were used for imaging. The whole-body screening protocol was as follows:

(1) Fastview localizer: skull base through upper thighs localization was acquired in coronal, sagittal and axial orientations.
(2) TimCT HASTE: free breathing, skull base through upper thighs. Table speed 8 mm/s, slice thickness 5 mm, 256 base resolution.
(3) TimCT BLADE TIRM: free breathing, skull base through upper thighs. Table speed 4 mm/s, slice thickness 6 mm, 256 base resolution.
(4) TimCT Dixon: multiple breathhold, abdomen and pelvis. Table speed 8 mm/s, slice thickness 5 mm, 320 base resolution.
(5) TimCT T1w FLASH Fatsat: precontrast, free breathing, skull base through upper thighs. Table speed 8 mm/s, slice thickness 5 mm, 320 resolution.
(6) Inject contrast
(7) VIBE: breathhold, abdomen only. Acquired in the arterial and portal venous phases. Slice thickness 3 mm, 320 base resolution, minimum TE and TR, with Quick Fatsat fat suppression.
(8) TimCT T1w FLASH Fatsat: post contrast, free breathing, skull base through upper thighs. Table speed 8 mm/s, slice thickness 5 mm, 320 base resolution.
(9) Multi-step DWI with ADC: free breathing, skull base through upper thighs. b values 50 and 800 s/mm^2.

Total imaging time was approximately 40 minutes. All patients tolerated the examination without difficulty. For each patient, there was an approximately 2 month interval between TimCT whole-body screening and the prior conventional examinations.

Clinical cases

Oncologic patients were invited to volunteer for whole-body MR imaging with *syngo* TimCT Oncology and the above protocol. These images were compared with their prior routine imaging including FDG PET/CT, conventional contrast-enhanced CT (ceCT) and conventional MR. The studies were conducted under approved IRB and informed consent was obtained.

Patient 1

This is a 52-year-old female undergoing treatment for metastatic rectal adenocarcinoma. Figure 1 compares conventional ceCT with non-fat-suppressed T2-weighted TimCT HASTE, and fat-suppressed T2-weighted TimCT BLADE TIRM. Images were selected at sites of metastatic disease in the chest, abdomen and pelvis. Within the chest, image quality is preserved despite non-breathhold technique, allowing ready detection of relatively small lung lesions and subcarinal lymphadenopathy. A metastatic lesion in the right hepatic lobe has evolved between the two examinations, but remains well seen. Invasion of the primary rectal mass into the presacral fat planes is better appreciated on MR than prior ceCT.

Figure 2 compares conventional ceCT with post contrast fat-suppressed T1 TimCT FLASH at additional levels in the chest, abdomen and pelvis. Again, image quality is preserved despite non-breathhold technique. The contrast-enhanced MR evaluation reveals small lung lesions, peripheral viable and central necrotic regions of the hepatic mass, and small abscess collections within the post-treatment presacral space.

Figure 3 compares *syngo* TimCT images with conventional pre and post contrast MR images acquired at 1.5T. Image quality is preserved.

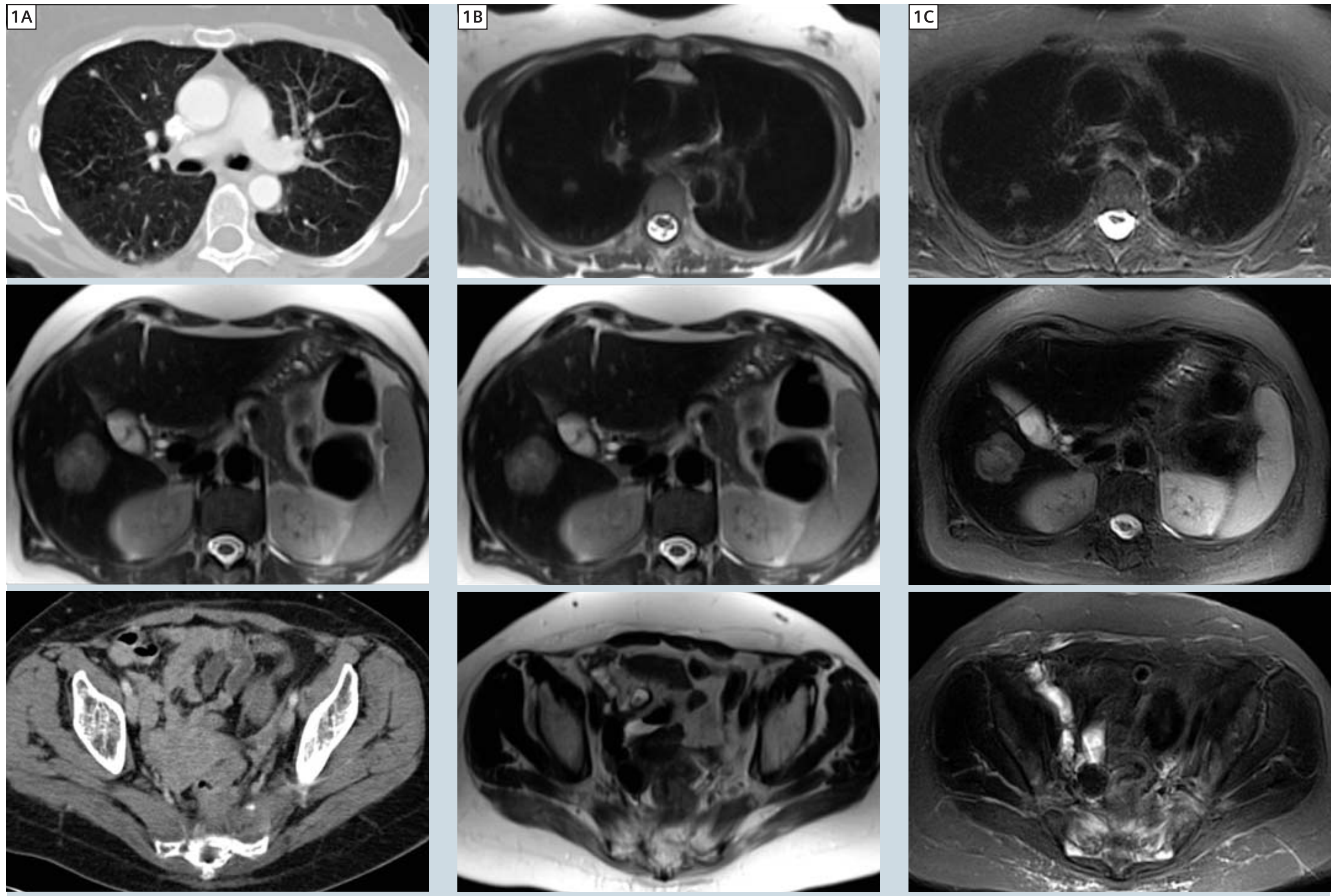

1 **(A)** ceCT, **(B)** TimCT HASTE, and **(C)** TimCT BLADE TIRM images selected from whole-body oncologic screening examinations.

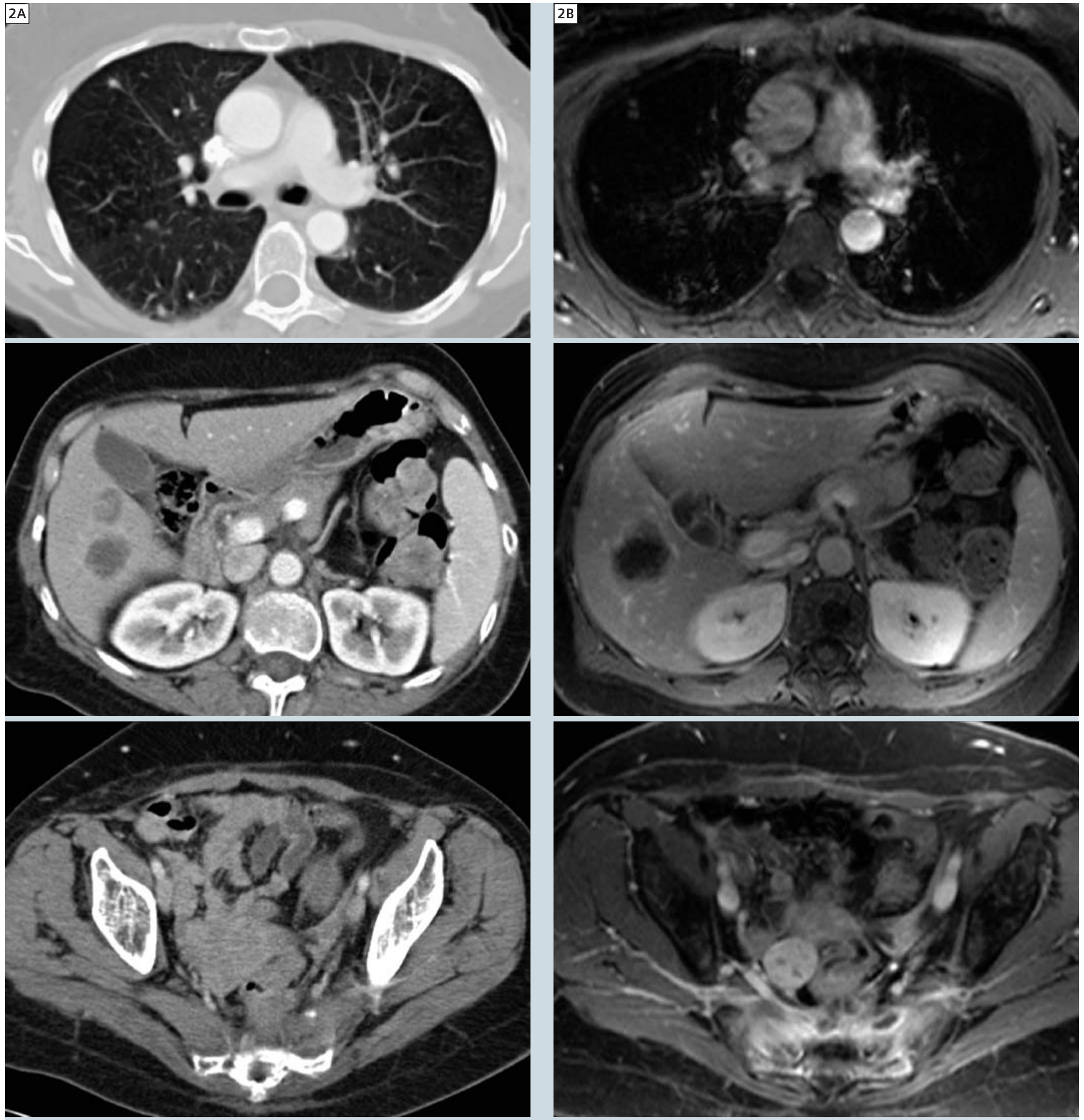

2 **(A)** ceCT and **(B)** TimCT T1 FLASH post contrast images selected from whole-body screening examinations.

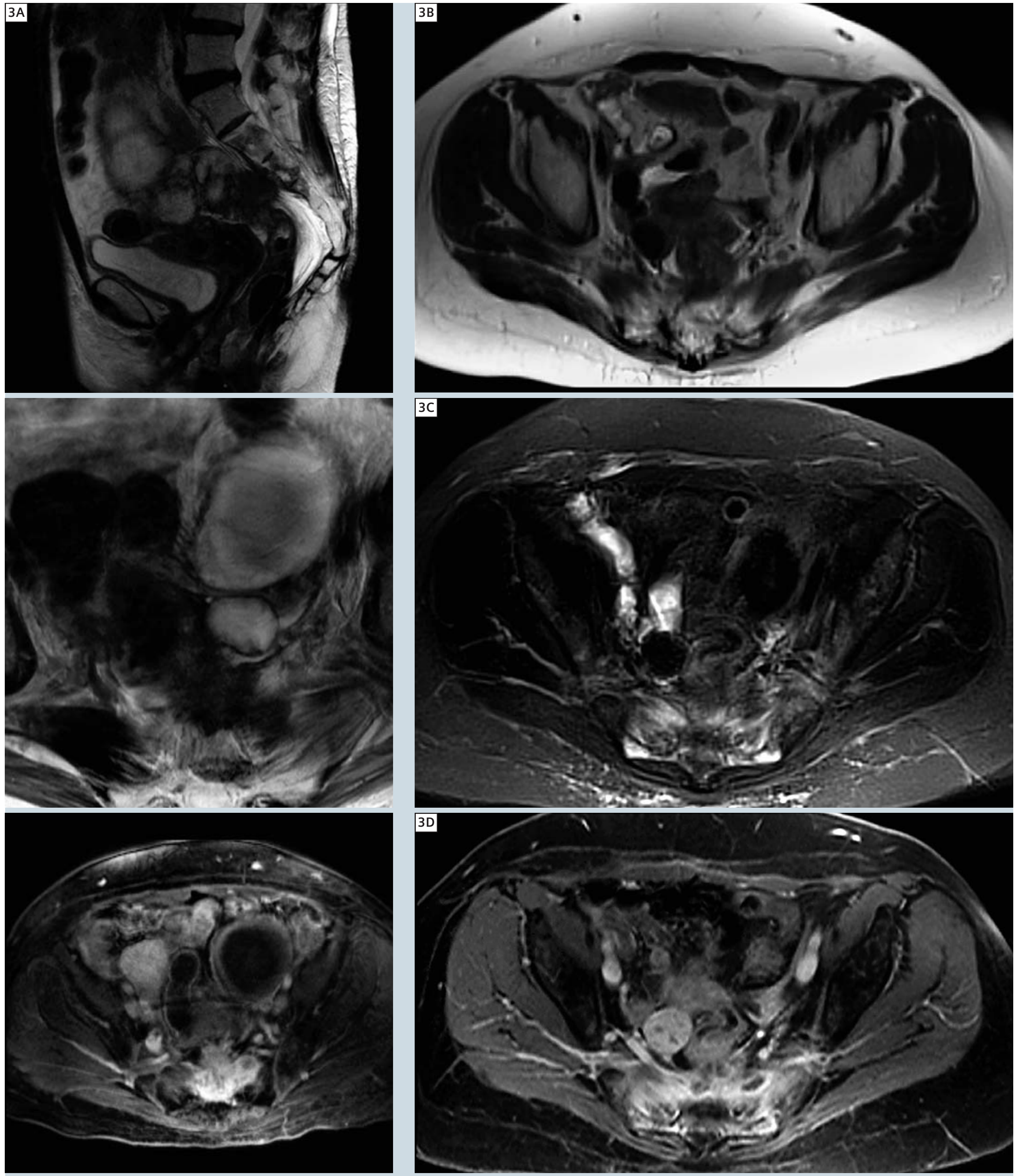

3 **(A)** Conventional MR images compared with **(B)** TimCT HASTE, **(C)** TimCT BLADE TIRM, and **(D)** TimCT T1 FLASH post contrast images selected from whole-body screening.

Patient 2

This is a 42-year-old female undergoing treatment for metastatic rectal adenocarcinoma. Figure 4 compares FDG PET/CT to TimCT HASTE and TimCT post contrast FLASH in the upper chest. A left supraclavicular lymph node metastasis is well demonstrated despite non-breath-hold technique.

Figure 5 compares FDG PET/CT ceCT and conventional MR with TimCT HASTE, BLADE, and post contrast FLASH. Multiple large liver metastases have progressed over the 2 month interval. The metabolically active regions of tumor are seen as peripheral T2 hyperintense, enhancing rims on MR and TimCT images, and are well-differentiated from central necrotic regions and the normal background liver.

Figure 6 makes a similar comparison in the pelvis. The primary rectal mass with invasion into the left perirectal fat is again well-demonstrated on the TimCT images.

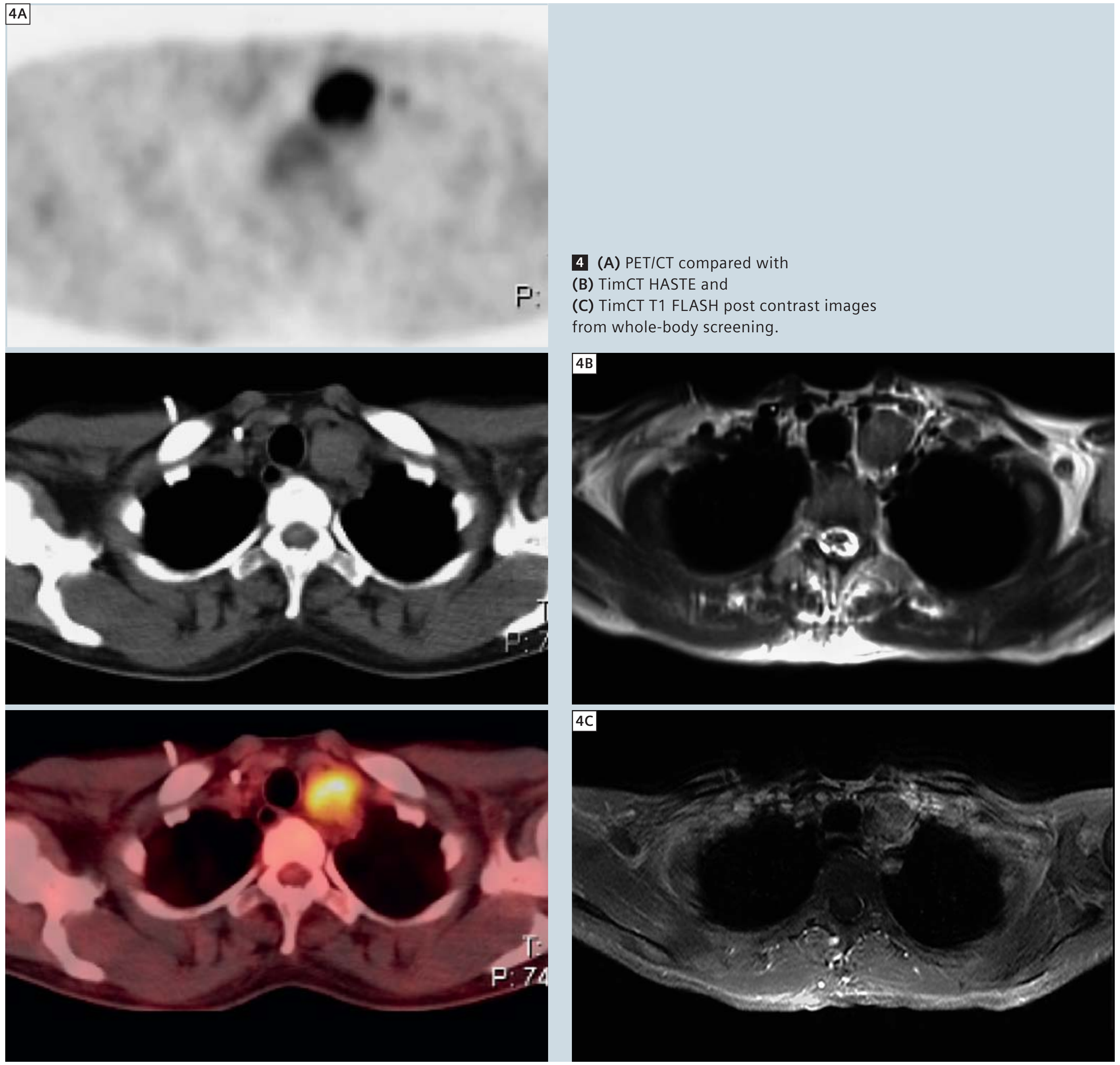

4 **(A)** PET/CT compared with **(B)** TimCT HASTE and **(C)** TimCT T1 FLASH post contrast images from whole-body screening.

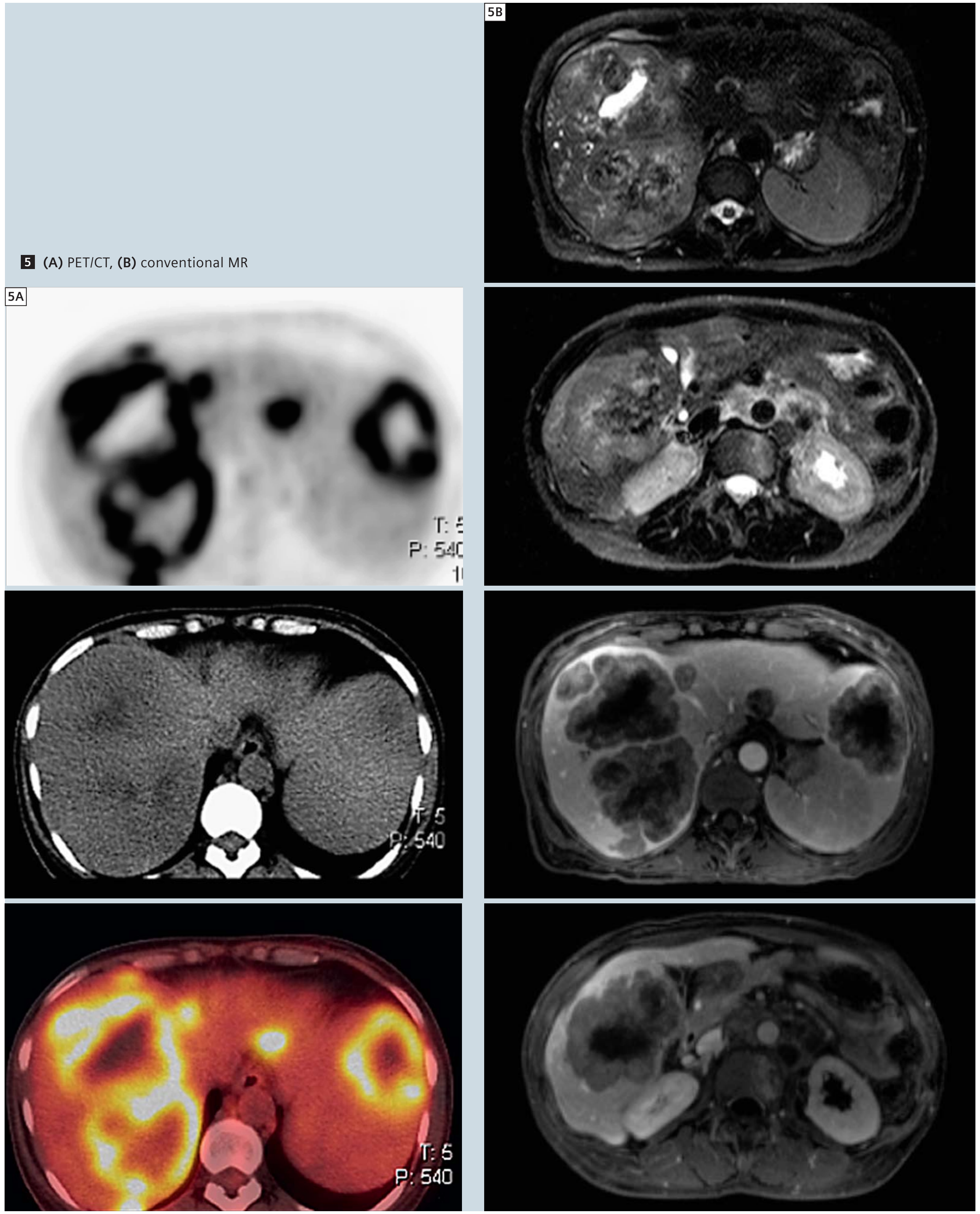

5 **(A)** PET/CT, **(B)** conventional MR

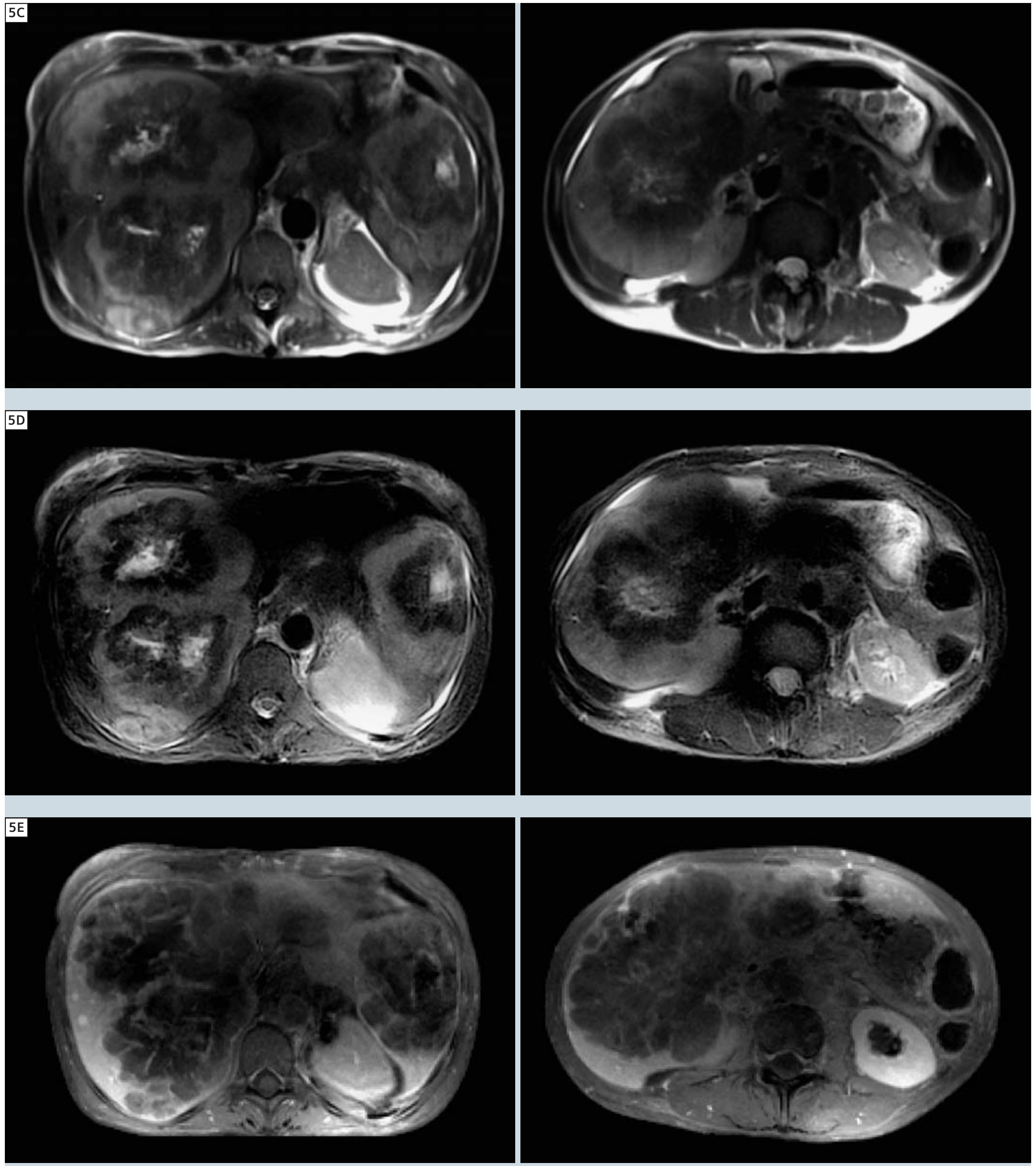

5 **(C)** TimCT HASTE, **(D)** TimCT BLADE TIRM, and **(E)** TimCT T1 FLASH post contrast images from whole-body screening.

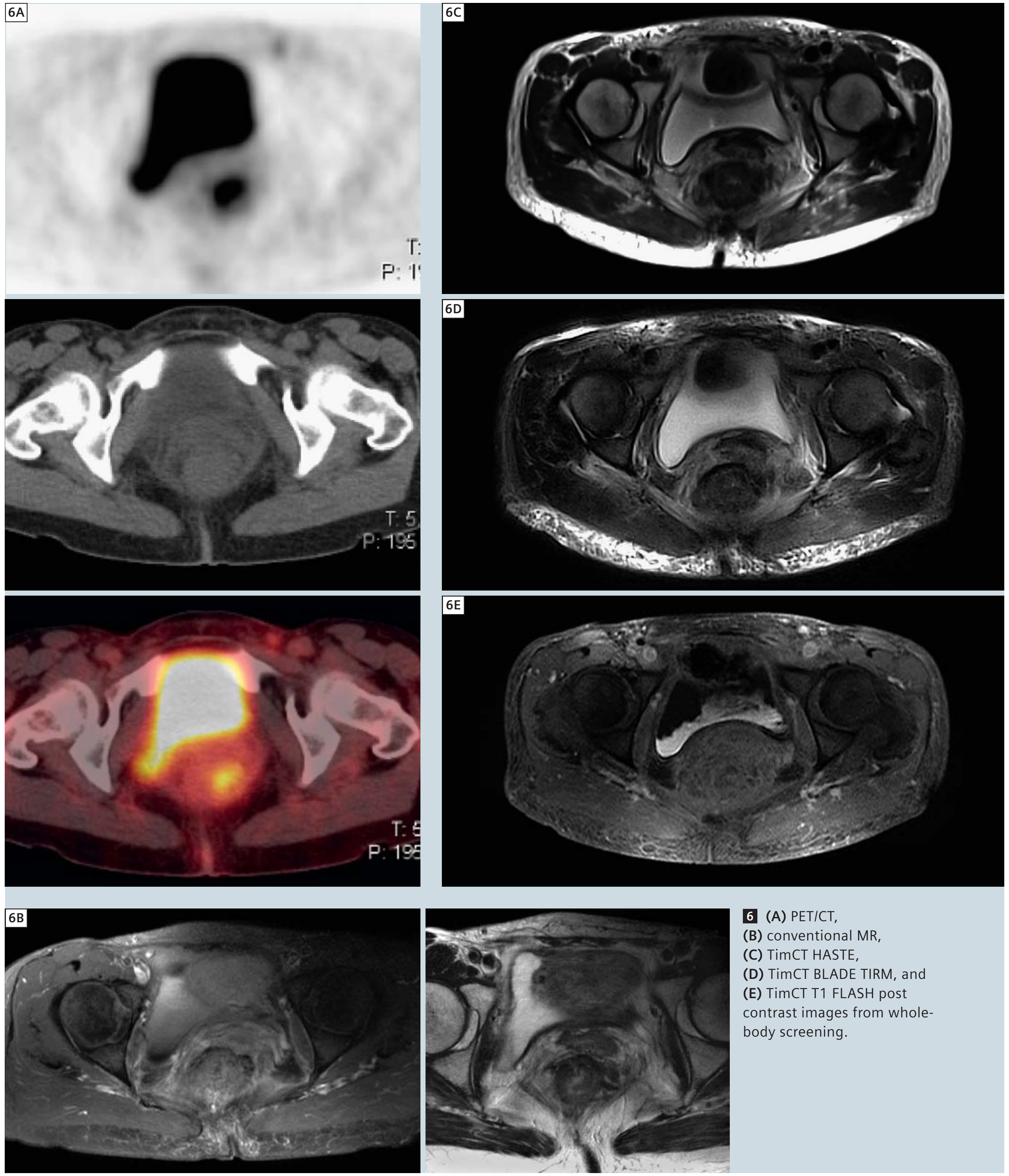

6 **(A)** PET/CT,
(B) conventional MR,
(C) TimCT HASTE,
(D) TimCT BLADE TIRM, and
(E) TimCT T1 FLASH post contrast images from whole-body screening.

Patient 3

This is a 60-year-old male patient undergoing treatment for metastatic colon cancer. Figure 7 compares PET/CT images with b = 800 diffusion-weighted and ADC images obtained during multi station whole-body imaging. The TimCT HASTE and pre / and post contrast FLASH images from the same examination are also included. The DWI/ADC images clearly delineate the peripheral metabolically active tumor as shown on PET from the central necrotic regions. Note the diffusion restriction in the small right anterior rib metastasis, also demonstrated on PET. The metabolically active regions are seen as peripheral rims of intermediate T2 hyperintensity and enhancement on the TimCT HASTE and post contrast FLASH images.

Conclusion

As these cases and images show, the addition of *syngo* TimCT functionality makes whole-body MR oncologic evaluation a viable reality. Extended, whole-body anatomic coverage is now possible without off-isocenter artifacts or signal loss. In-plane image quality with the TimCT application is maintained in comparison to conventional MR. Non-breath-hold technique did not limit diagnostic quality in these patients. Skull-base to upper thigh coverage was achieved in standard imaging times of 30–40 minutes. With the addition of DWI to conventional sequences, functional-anatomic information correlation is possible through the whole-body field of view, but does not require administration of radiotracers or long uptake periods. TimCT has removed the barriers to whole-body MR evaluation, promising a new era of MR applications in oncology.

7 **(A)** PET/CT

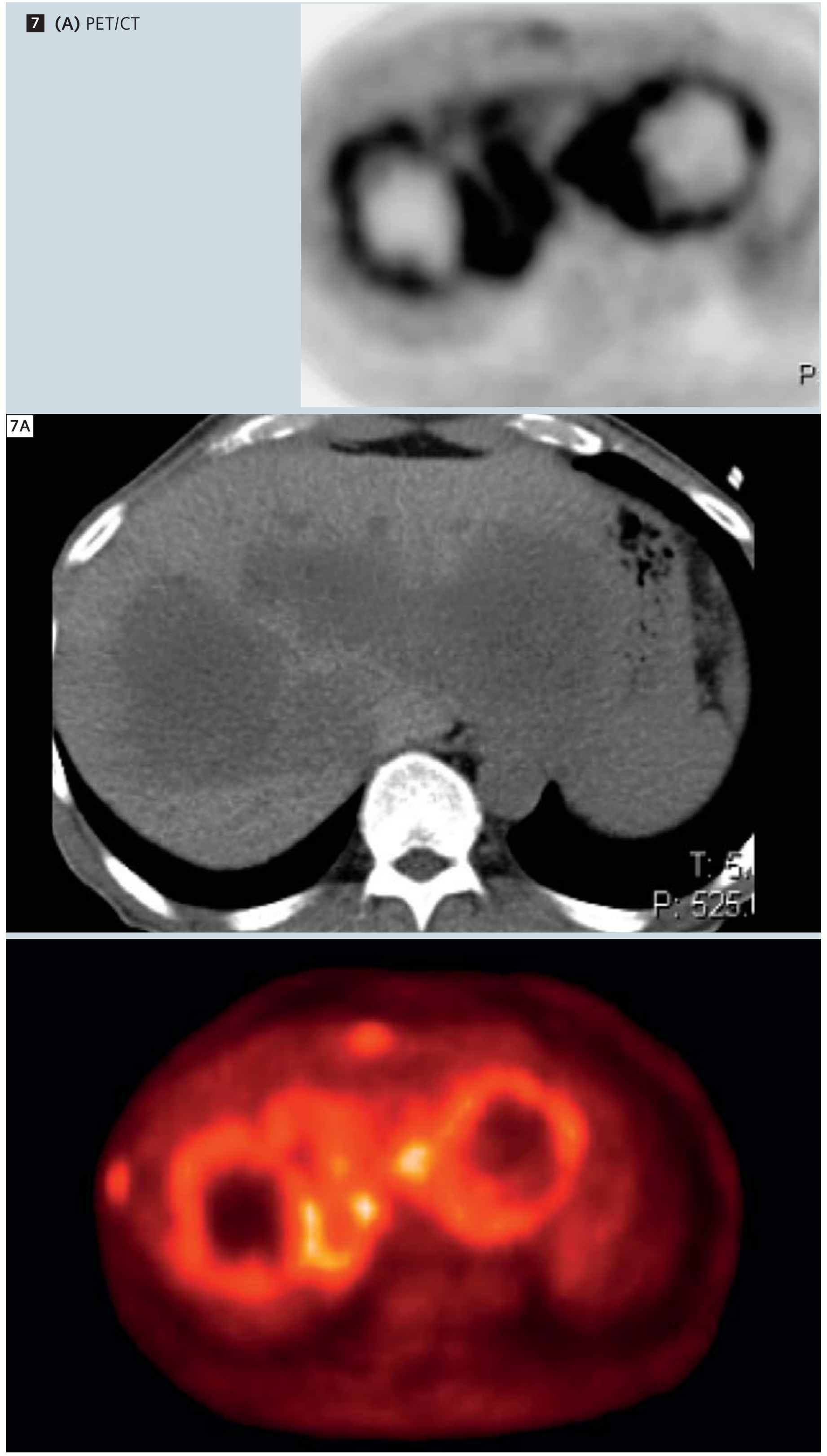

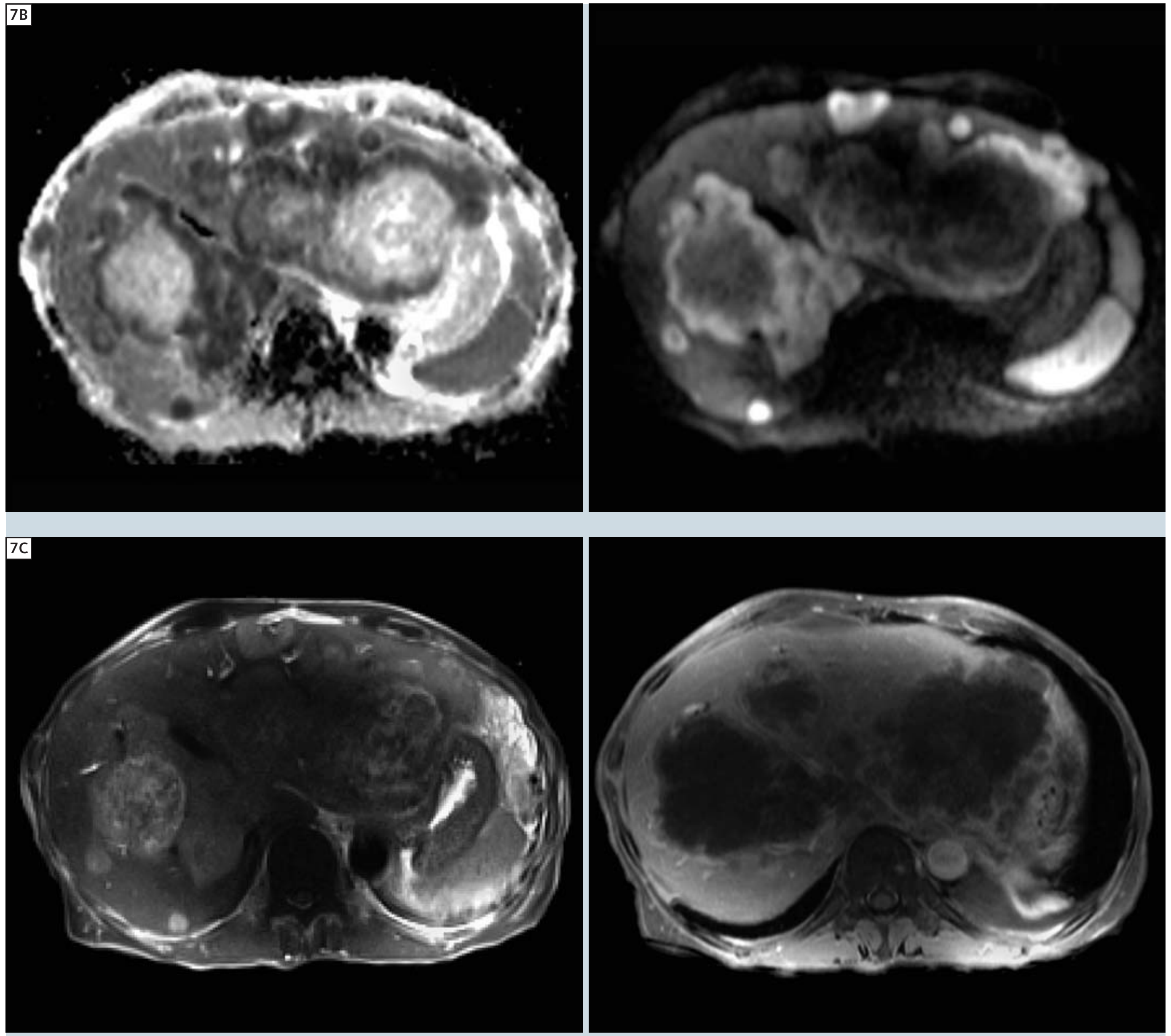

7 **(B)** multi-station diffusion-weighted and ADC, and **(C)** TimCT HASTE and post contrast T1w FLASH images.

References

1 Personalizing. Cancer Therapy with FDG PET: From RECIST to PERCIST. J Nucl Med. 2009, Vol. 50, Suppl 1.

2 Koh DM, Collins DJ. Diffusion-weighted MRI in the body: applications and challenges in oncology. AJR Am J Roentgenol. 2007 Jun; 188(6): 1622–35.

3 Sommer G, Schaefer, AO, et. al. Sliding multislice MRI for abdominal staging of patients with pelvic malignancies: a pilot study. J Magn Reson Imaging. 2008 Mar 27(3): 666–672.

Contact
Vamsi Narra, M.D.
Mallinckrodt Institute of Radiology
Washington University
School of Medicine
St. Louis, Missouri
USA
narrav@mir.wustl.edu

Case Report:
Glioblastoma Multiforme

Masahiro Ida, M.D.

Department of Radiology, Tokyo Metropolitan Ebara Hospital, Tokyo, Japan

Patient history

35-year-old female patient with known glioblastoma multiforme (GBM).

Image findings

Glioblastoma multiforme with surrounding edema is seen in the white matter of the left parieto-occipital region. Coronal STIR (Fig. 1A) and transversal T2-weighted (Fig. 1B) images obtained by using a 32-channel head coil at 3 Tesla (MAGNETOM Trio, A Tim System with software version *syngo* MR B15). Images demonstrate the multi-lobulated, intratumoral cystic components (green arrows) as well as the fine draining veins (blue arrows) in detail. A marked improvement is recognized in signal-to-noise (SNR), spatial resolution and contrast resolution on T2-weighted STIR images with a 32-channel head coil at 3T compared with conventional T2-weighted images (Fig. 1C) with a 12-channel Head Matrix coil at 1.5T (MAGNETOM Avanto).

Contact
Masahiro Ida, M.D.
Department of Radiology
Tokyo Metropolitan Ebara Hospital
4–5–10 Higahsi-Yukigaya, Ota-ku,
Tokyo 145–0065
Japan
rxb00500@gmail.com

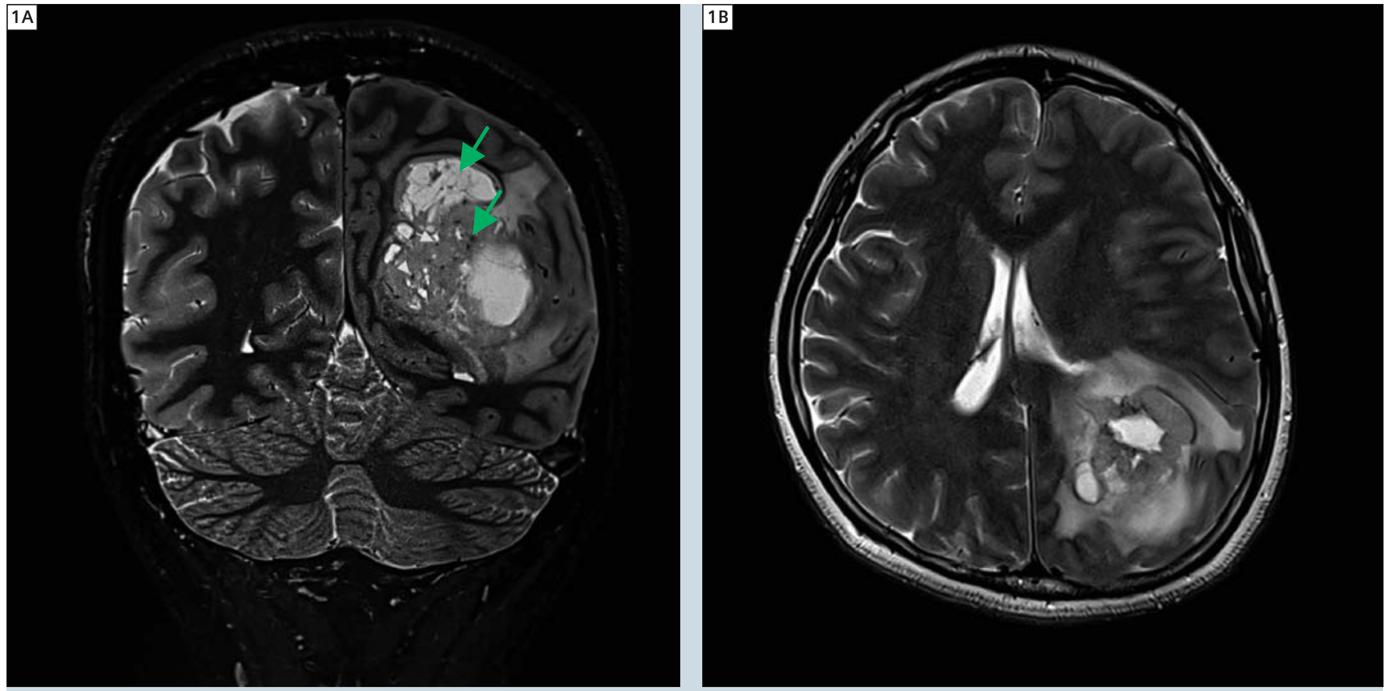

1A, B **A:** Coronal T2-weighted STIR image acquired with the 32-channel head coil on a 3T MAGNETOM Trio, A Tim System. Sequence parameters: slice thickness 2 mm, 19 slices, TE 6000 ms, TR 11 ms, TI 230 ms, bandwidth 225 Hz/Px, PAT factor 2, turbo factor 11, FOV 180 x 180 mm, matrix 518 x 576, 2 averages, acquisition time: 5:43 min. **B:** Transversal T2-weighted Turbo Spin Echo (TSE) image acquired with the 32-channel head coil on a 3T MAGNETOM Trio, A Tim System. Sequence parameters: slice thickness 3 mm, 45 slices, TR 4500 ms, TE 96 ms, bandwidth 180 Hz/Px, PAT factor 2, turbo factor 11, FOV 220 x 220 mm, matrix 384 x 512, 1 average, acquisition time: 3:28 min.

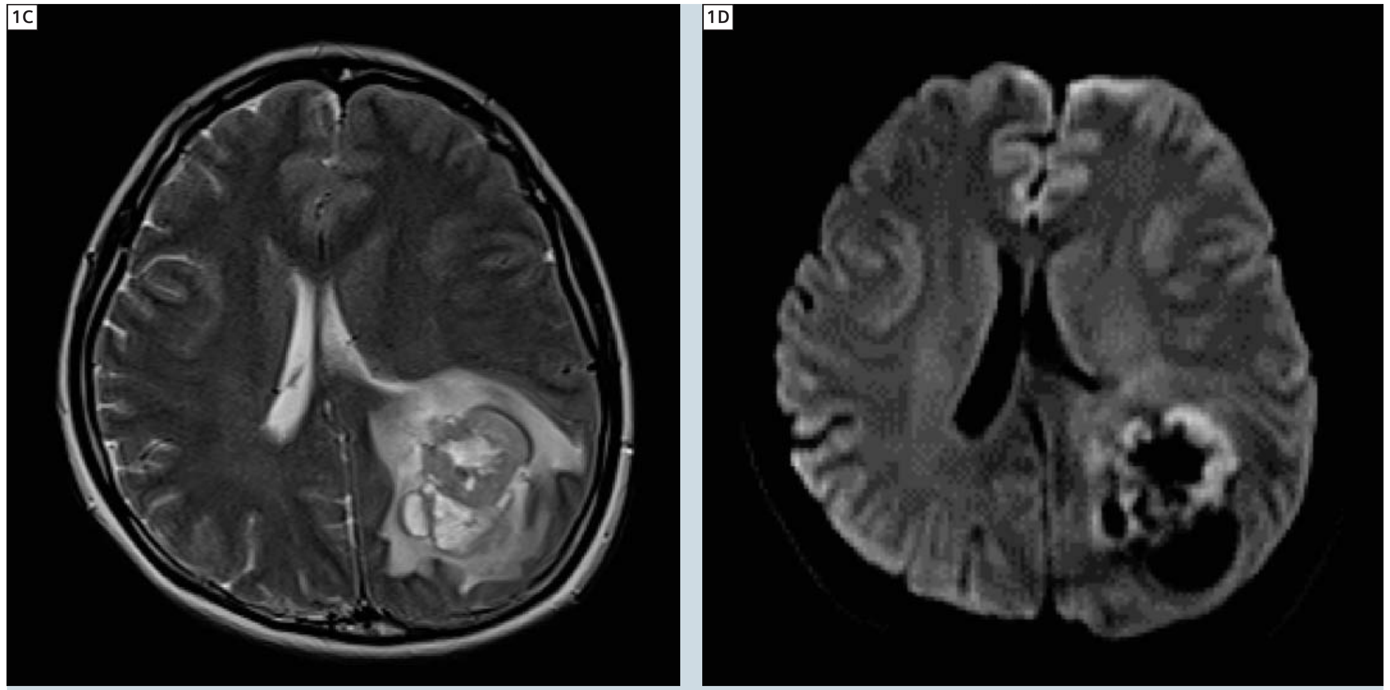

1C, D **C:** Transversal T2-weighted TSE image of the same patient but acquired with a 12-channel Head Matrix coil at 1.5 Tesla. Sequence parameters: slice thickness 5 mm, 24 slices, TR 4500 ms, TE 98 ms, bandwidth 100 Hz/Px, PAT factor 2, turbo factor 10, FOV 184 x 210 mm, matrix 196 x 320, 1 average, acquisition time: 1:00 min. **D:** Diffusion-weighted image (*syngo* DWI) acquired with the 32-channel head coil at 3T; the high-b-value image with b = 1000 s/mm^2 is shown. Sequence parameters: slice thickness 5 mm, 24 slices, TR 3000 ms, TE 77 ms, bandwidth 1420 Hz/Px, PAT factor 3, FOV 220 x 220 mm, matrix 112 x 160, 5 averages, acquisition time: 1:17 min.

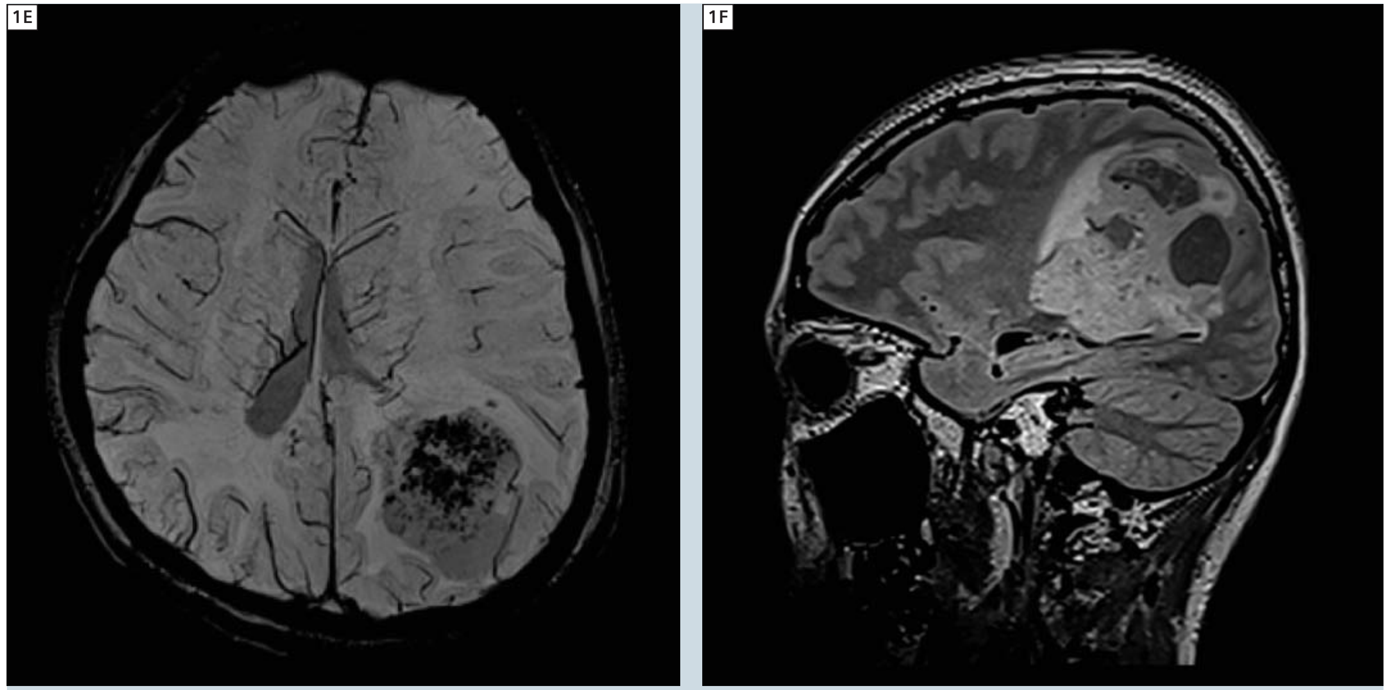

1E, F **E:** Susceptibility-weighted image (*syngo* SWI) acquired with the 32-channel head coil at 3T; thin minimum intensity projection (thin MinIP) image (axial orientation, thickness 9.6 mm). Sequence parameters: slice thickness 1.2 mm, 81 slices, TR 28 ms, TE 20 ms, bandwidth 120 Hz/Px, PAT factor 3, FOV 230 x 230 mm, matrix 320 x 320, 1 average, acquisition time: 6:01 min. **F:** Sagittal 3D FLAIR *syngo* SPACE image, acquired with the 32-channel head coil at 3T. Sequence parameters: slice thickness 1 mm, 176 slices, TR 5000 ms, TE 393 ms, TI 1800 ms, bandwidth 780 Hz/Px, PAT factor 4, turbo factor 145, FOV 250 x 250 mm, matrix 516 x 512, 1 average, acquisition time: 3:46 min.

Case Report: Non-Contrast Lower Limb MR Angiography Using NATIVE SPACE

Associate Professor Andrew Holden; Anna-Maria Lydon; Associate Professor Brett Cowan

Centre for Advanced MRI, Faculty of Medical and Health Sciences, University of Auckland, New Zealand

Patient history

A 55-year-old male presented with right leg calf claudication with the onset of pain occurring after walking 50 meters. He had a normal femoral pulse but an absent popliteal pulse on the right and normal pulses on the left.
The patient was imaged on a 1.5T Siemens MAGNETOM Avanto using the 8-channel, 16 element Peripheral Angio Matrix coil, combined with the Body and Spine Matrix coils. Standard contrast enhanced MR angiography was followed by the non-contrast NATIVE SPACE sequence at the femoro-popliteal station for comparison.

Sequence details

The SPACE acquisition is a high spatial resolution 3D TSE sequence offering the use of non-selective refocusing pulses and, thus, short echo spacings. The NATIVE SPACE technique relies on the inherent difference in signal between fast flowing blood during systole and the slower flowing blood during diastole to generate contrast. Two data sets were acquired after determining the trigger times from a "NATIVE scout mode" acquired from an artery within the imaging volume and subtracted. ECG cardiac gating was used.

Imaging findings

Contrast-enhanced MR angiography (Fig. 1) demonstrated an 8 cm long stenotic lesion in the distal right superficial femoral artery with the above knee popliteal artery being reconstituted by large profunda femoral artery collaterals. NATIVE SPACE MR angiography (Fig. 2) demonstrated an excellent correlation with the contrast-enhanced study in terms of lesion severity, length and collateral anatomy. Digital subtraction angiography (Fig. 3) confirmed the contrast and non-contrast MR angiographic findings.

Discussion

With recent concerns regarding the risk of nephrogenic sclerosing fibrosis (NSF) with gadolinium based contrast agents in renally impaired patients, there has been considerable interest in the development of MR techniques that do not require gadolinium chelates. NATIVE SPACE has considerable advantages over time of flight MR angiography. The sequence is acquired along the long axis of the vessel rather than perpendicular to the flow direction, resulting in extensive z-axis coverage without the flow saturation. NATIVE SPACE can be used as single or multi-station study and appears to be robust also if contrast has already been given, suggesting a role for 'recovery' if a contrast study is unsuccessful.

Contact
Associate Professor
Andrew Holden
Director of Interventional Radiology
Auckland City Hospital
2 Park Road
Grafton
Auckland 1023
New Zealand
AndrewH@adhb.govt.nz

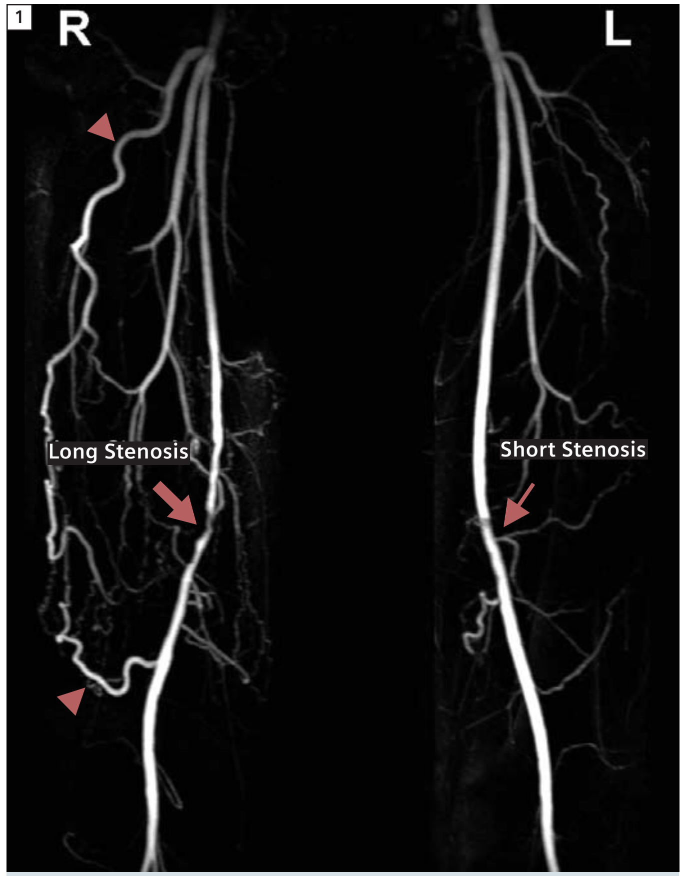

1 Contrast-enhanced MRA of the femoro-popliteal station demonstrating an 8 cm long stenotic lesion in the distal right superficial femoral artery (thick arrow) with the above knee popliteal artery being reconstituted by large profunda femoral artery collaterals (arrowhead). There is also a mild stenosis in the left superficial femoral artery (thin arrow) at a similar level.

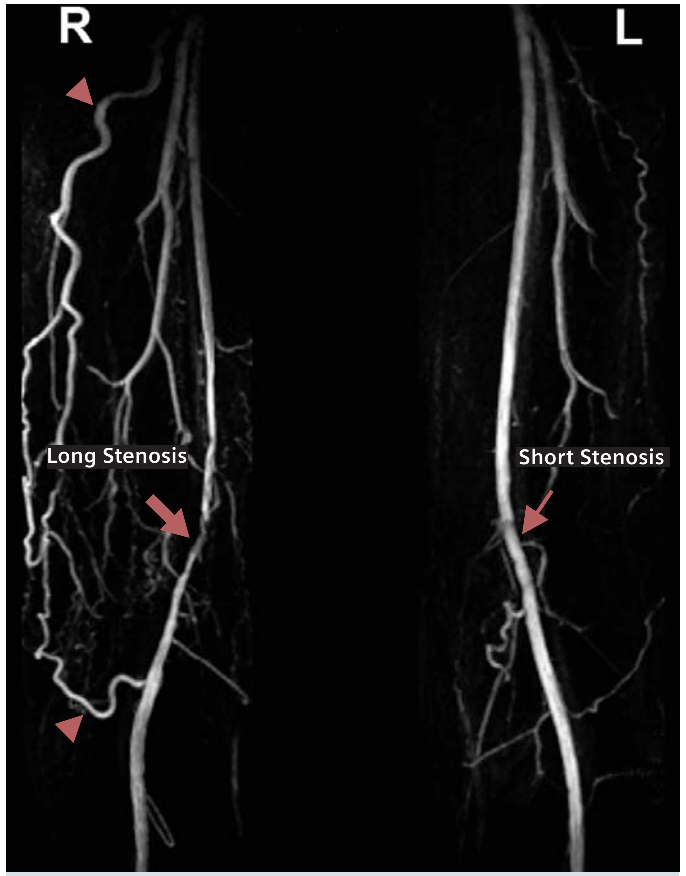

2 NATIVE SPACE MRA demonstrates excellent correlation with the contrast-enhanced study in terms of right superficial femoral artery lesion severity, length (thick arrow) and collateral anatomy (arrowhead). The mid left superficial femoral artery stenosis is again demonstrated (thin arrow).

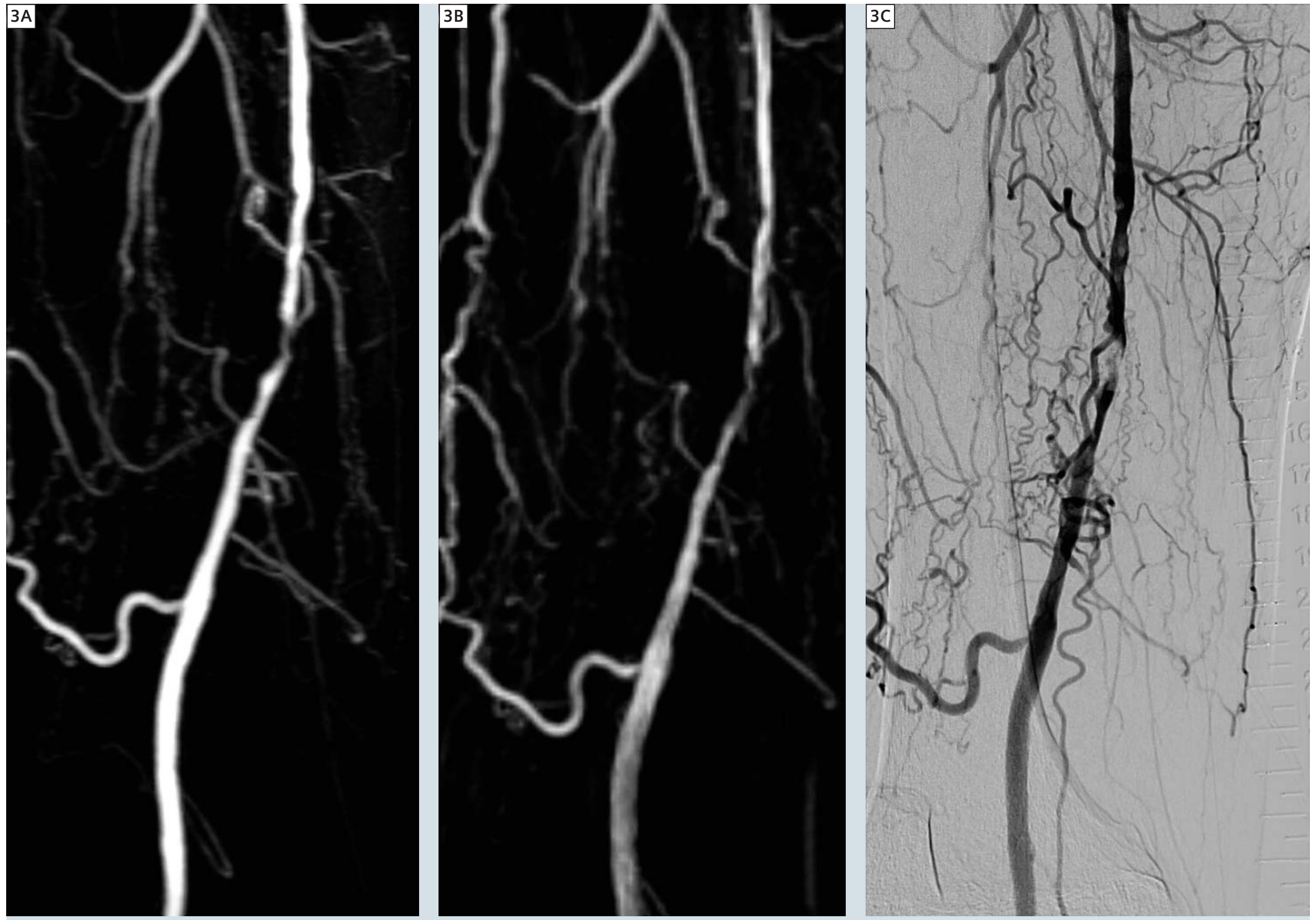

3 Magnified view of the distal right superficial femoral artery showing excellent correlation between the contrast-enhanced MRA **(A)**, NATIVE SPACE MRA **(B)** and digital subtraction angiography **(C)**.

Pre-Transplant Assessment of Potential Renal Donors with *syngo* Native True-FISP: Case Study and Initial Experience

Mellena D. Bridges, M.D.[1]; Anthony D. Schroeder[1]; Bradley D. Bolster, Jr., Ph. D.[2]; Kevin J. Johnson[2]

[1]Department of Radiology, Mayo Clinic, Jacksonville, FL, USA
[2]Siemens Healthcare, MR R&D Collaborations , Malvern, PA, USA

Background

At our institution, people who are willing to donate a kidney to a patient with end-stage renal disease undergo a rigorous pre-operative evaluation. In addition to psychological testing, counseling, and a complete panel of laboratory studies, the work-up includes an MR angiography (MRA). Since potential donors are generally young, healthy individuals, the primary purpose of the MRA is not to screen for atherosclerotic disease, but to provide a detailed map of the renal arteries. The intention is not only to protect the healthy donor from harm, but also to ensure that the chosen kidney will be up to the task of sustaining the patient in whom it will be placed.

Anatomic variants of the renal vasculature are very common, and have the potential to complicate a minimally invasive operation where the surgeon's field-of-view is limited. For example, the kidneys are often supplied by more than one artery, with accessory vessels occasionally originating as far afield as the common iliac arteries. Vessels can enter the kidney through the poles, rather than through the hilum. And even single arteries can bifurcate or trifurcate very quickly, well before they reach the renal hilum, and could be cut as the kidney is harvested.

Precise pre-operative knowledge of a donor's vascular anatomy is critical to the success of a renal transplant. Failure to predict and prepare for these kinds of variants can be disastrous since associated bleeding may be difficult to control and transection of an artery could lead to partial or even complete devascularization of the precious kidney, completely sabotaging the whole enterprise.

The donor will then have lost a kidney without a benefit to anyone.

The MRA is used during the first phase of the work-up to determine whether the donor actually has a suitable kidney, ruling out morphologic variants like horseshoe kidney or crossed-fused ectopia as well as renal malignancy. The arterial anatomy will largely determine the next phase of decision-making, for example, which of the kidneys should be harvested, and the appropriate surgical method. If there is no good alternative, some surgeons will accept a kidney with a dual blood supply and plan the operative approach accordingly. Some smaller vessels can, if necessary, be sacrificed. But, again, the surgeons have to be prepared to locate these via a more extensive dissection than would be required for a single artery.

Conventional contrast-enhanced MRA (ceMRA), however, is frequently suboptimal for this purpose. Image quality can suffer due to poor bolus timing, injector malfunction, patient motion, or obscuration of detail due to early filling of renal veins. Consequently, we have incorporated the *syngo* Native TrueFISP sequence into our routine MR protocol for renal donors. The technique often salvages an otherwise suboptimal conventional ceMRA. In addition, because venous contamination and tissue enhancement are strongly suppressed in the Native TrueFISP, the entire course of the renal artery is usually demonstrated very cleanly, with excellent visualization of the intrarenal arteries as well.

1A Routine MR work-up of a potential kidney donor. **(1A)** This maximum intensity projection (MIP) image from an axial volumetric *syngo* Native TrueFISP acquisition reveals a cluster of renal arteries arising in close proximity to each other, as well as an accessory left renal artery (arrowheads). Early branching vessels are also documented bilaterally (arrows), with the one on the left coursing directly to supply the upper pole.

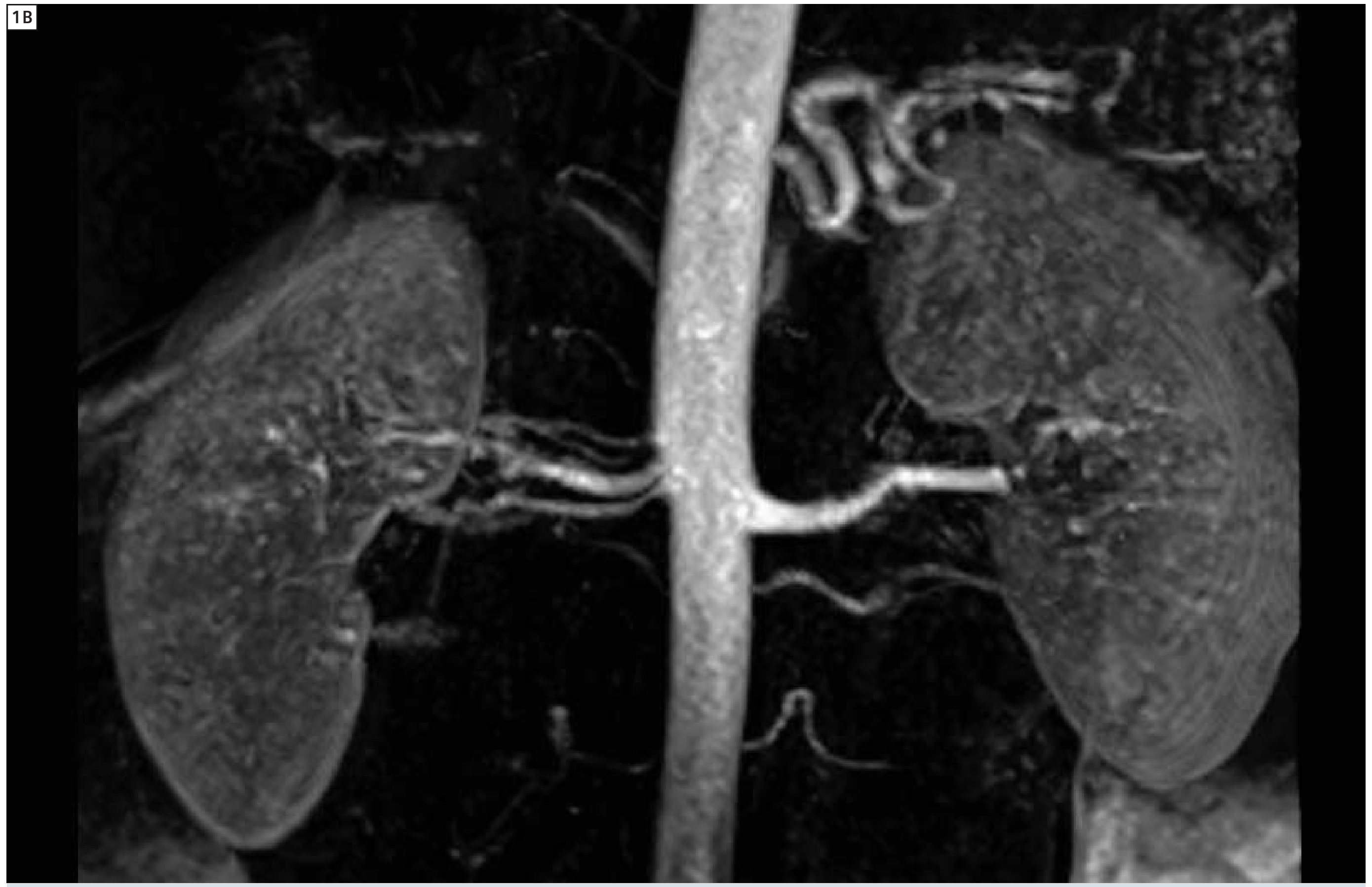

1B This vessel is nearly undiscernible on the conventional MRA, probably due to the subtle horizontal band of motion artifact passing through both kidneys. Further, the distinct elements of the group of renal arteries on the right are not as clearly depicted, and the branching is likewise obscured.

2A Another potential renal donor. **(2A)** Coronal MIP image reconstructed from an axial *syngo* Native TrueFISP acquisition clearly demonstrates the 2 bilateral renal arteries. The more inferior vessels (arrowheads) are smaller and could easily occlude if the decision was made to harvest one of these kidneys. Early bifurcation of the main right artery (arrow).

2B A MIP image from a conventional coronal MRA acquisition shows significant venous contamination, with obscuration of some arterial segments.

3 Coronal MIP reconstruction of a *syngo* Native TrueFISP data set in pre-operative work-up for renal tumor. The image lays out the intrarenal arteries quite well, without obscuration by the early parenchymal enhancement that often contaminates contrast-enhanced MRA. The technique clearly has potential to rule out fibromuscular dysplasia in the distal portion of the main arteries. It could also prove useful in the search for the tiny intrarenal aneurysms of polyarteritis nodosa.

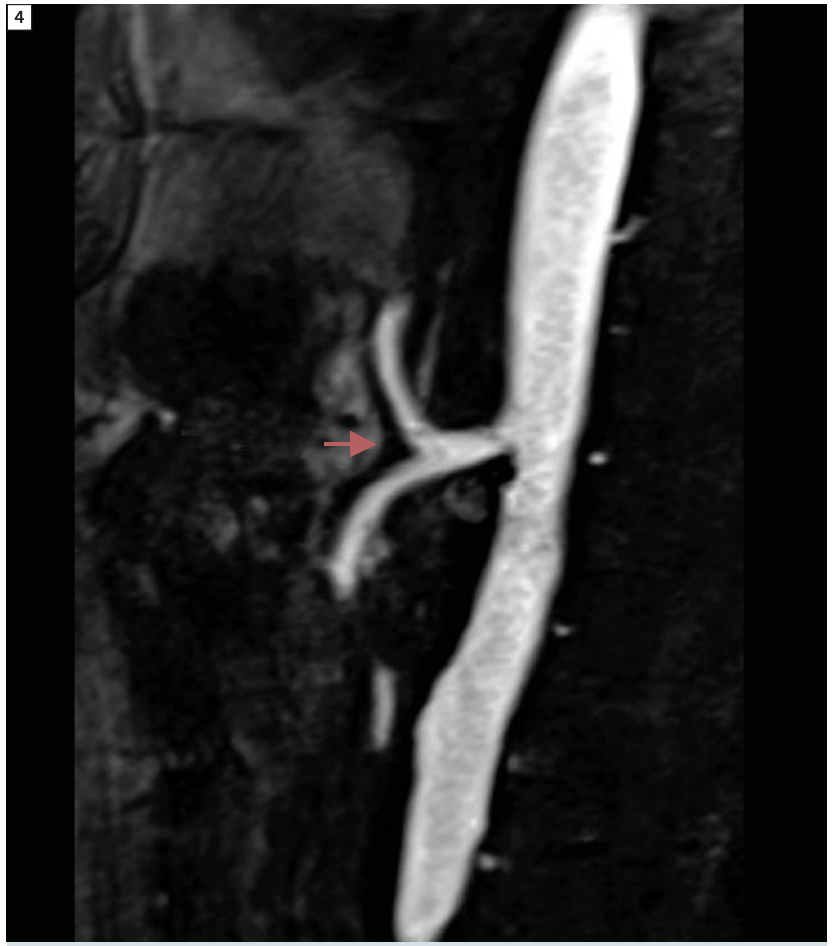

4 48-year-old woman with chronic abdominal pain who is also allergic to contrast agents. The examination was undertaken to exclude significant disease in the mesenteric vessels. The source images for this sagittal MIP through the upper abdominal aorta were actually acquired in the sagittal plane, for optimal visualization of the celiac and SMA ostia. Clearly, significant atheromatous disease is excluded, but the common celiac-SMA trunk, a normal variant, is nicely demonstrated (arrow).

Case study

A healthy 31-year-old male would like to donate a kidney to his father. The renal transplant service requested an MRA as part of the customary pre-transplant evaluation for potential donors.

Sequence details

The renal arterial anatomy of this patient was imaged first with *syngo* Native TrueFISP followed by conventional ceMRA. The Native TrueFISP volume was acquired in the axial plane, 120 slices with 1 mm through slice resolution. The acquisition was fat suppressed at a TR/TE = 878/1.8 ms and a flip angle of 90 degrees. A PAT factor of 2 was used with one average. Acquisition time was 3:10 min. Images have been aquired using our 1.5T MAGNETOM Espree with Spine and Body Matrix coils.

Imaging findings

The donor in question has very complex arterial anatomy, with four arteries supplying the right kidney, all arising from the aorta in close proximity to each other (Fig. 1). There are only two arteries on the left, but the superior artery quickly gives rise to a branch vessel that courses outside the hilum to enter the kidney through the upper pole renal tissue. Even with prior knowledge of this branch vessel from the *syngo* Native TrueFISP images, it was still not clearly delineated on the MRA, which is degraded by venous contamination and a band of horizontally-oriented pulsation artifact. This patient was ultimately rejected as a suitable donor. Harvesting would have been difficult and implantation into the recipient would have been even more challenging. Moreover, the small size of the branch vessel dramatically increased the likelihood of eventual stricture or thrombosis at the anastomosis.

Discussion and other examples

Figure 2 illustrates another example of duplicated renal vessels, with the *syngo* Native TrueFISP adding value to the information provided by the conventional MRA technique. Yet another potential application for the non-enhanced technique stems from its capacity to depict the intrarenal arteries in detail (Fig. 3). This ability is quite robust, as long as the patient's cardiac output is good and patient motion is minimized. If output is low or if the patient is dehydrated, signal will fall off rapidly as the aorta descends. Consequently, a significant limitation to aortic blood flow should discourage the radiologist from committing to a stand-alone Native TrueFISP for renal artery assessment. The technique's Z-axis limitations also dictate very careful placement of the acquisition volume, with its superior margin just above the vessels in question.

Figure 4 represents a change of the source acquisition to the sagittal plane for this scan designed to rule out atherosclerotic disease or clot in the larger arteries of the bowel mesentery. These images have been acquired using our 1.5T MAGNETOM Avanto with Spine and Body Matrix coils.

Contact
Mellena D. Bridges, M.D.
1450 San Pablo Road
Jacksonville, FL 32224
USA
Bridges.mellena@mayo.edu

Case Reports: Time-Resolved MRA Evaluation of Pelvic Congestion Syndrome

Charles Kim, M.D.[1]; Brian M. Dale, Ph.D.[2]; Elmar Merkle, M.D.[1]

[1]Duke University Medical Center, Durham, North Carolina, USA
[2]Siemens Medical Solutions, Inc., MR R&D, Morrisville, NC, USA

Case 1
Incompetent ovarian valves

Patient history

36-year-old female with ovarian cyst found on ultrasound and pelvic pain. A pelvic MRI was ordered for further evaluation.

Sequence details

syngo TWIST, 3D coronal (with coronal and sagittal MIP reformats), 40 partitions, 3 mm thickness, TR 2.54 ms, TE 1.01 ms, 88 s acquisition, 1.5 s/frame temporal resolution, 58 frames, 320 resolution, 400 mm FOV, 100% phase FOV, 78% phase resolution, 82% slice resolution, 1 average, 650 Hz/pixel BW, 25° flip angle.

Images have been acquired using our 1.5T MAGNETOM Avanto (software version *syngo* MR B15A) and the Body and Spine Matrix coils.

Imaging findings

The time-resolved coronal maximum intensity projection (MIP) images are shown in order during the mid arterial phase (A), late arterial phase (B), early venous phase (C), and mid venous phase (D). The left ovarian vein (blue arrows) is dilated and periuterine varices are present (arrowheads). The right ovarian vein (red arrows) is also prominent during the venous phase.

Results and discussion

The bilateral ovarian vein dilation and periuterine varices can be detected with many imaging modalities, such as static CT, MR, and ultrasound. However, by examining the temporal appearance of contrast in these time-resolved MRA images, it is evident that flow in the left ovarian vein is occurring caudally in a retrograde fashion. Therefore, the left ovarian vein valves are incompetent. Incompetent ovarian valves are the cause of pelvic congestion syndrome in women, which can cause chronic pelvic pain. On the other hand, examination of the temporal appearance of contrast throughout the right ovarian reveals that flow is in an anterograde fashion.

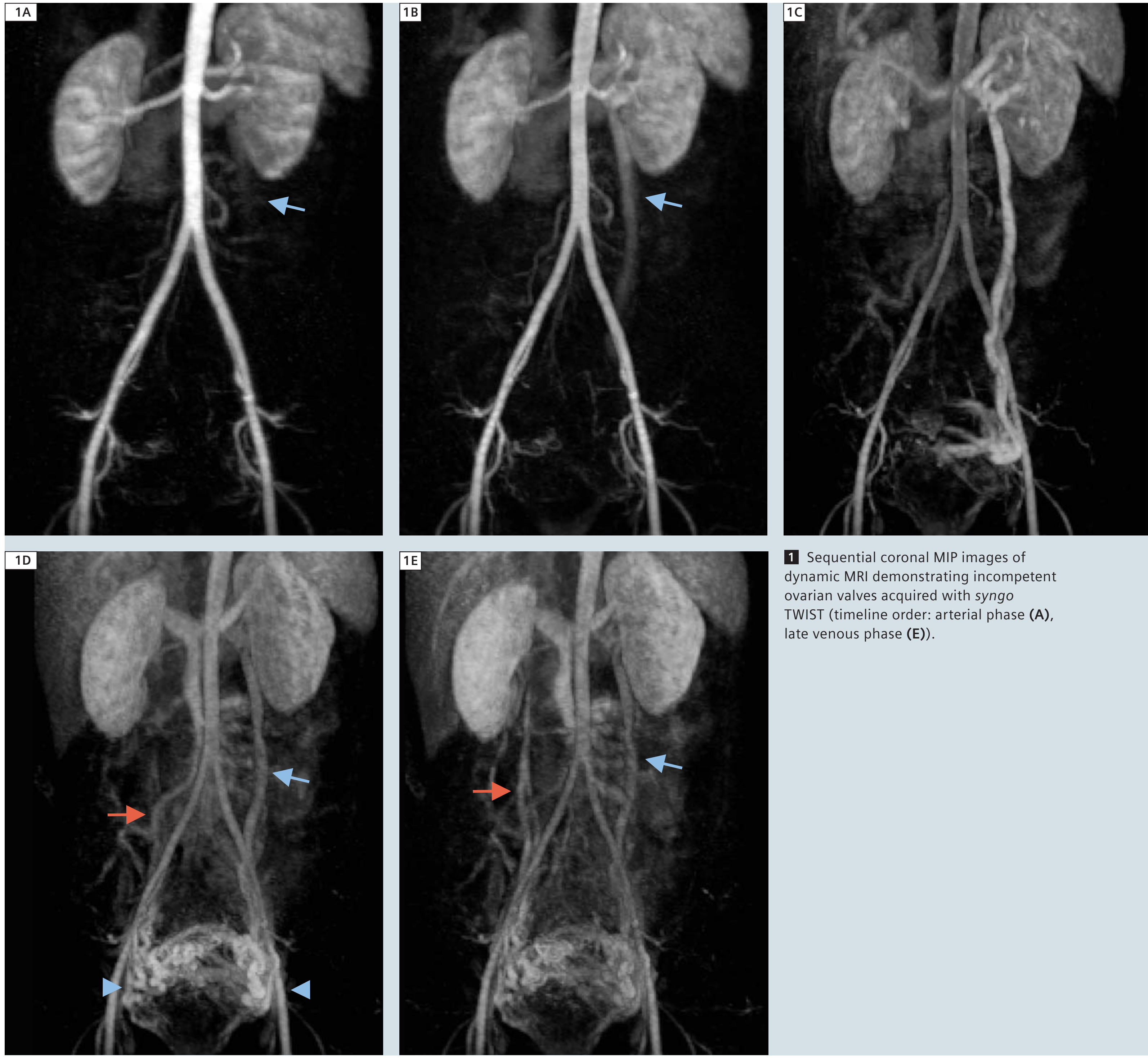

1 Sequential coronal MIP images of dynamic MRI demonstrating incompetent ovarian valves acquired with *syngo* TWIST (timeline order: arterial phase **(A)**, late venous phase **(E)**).

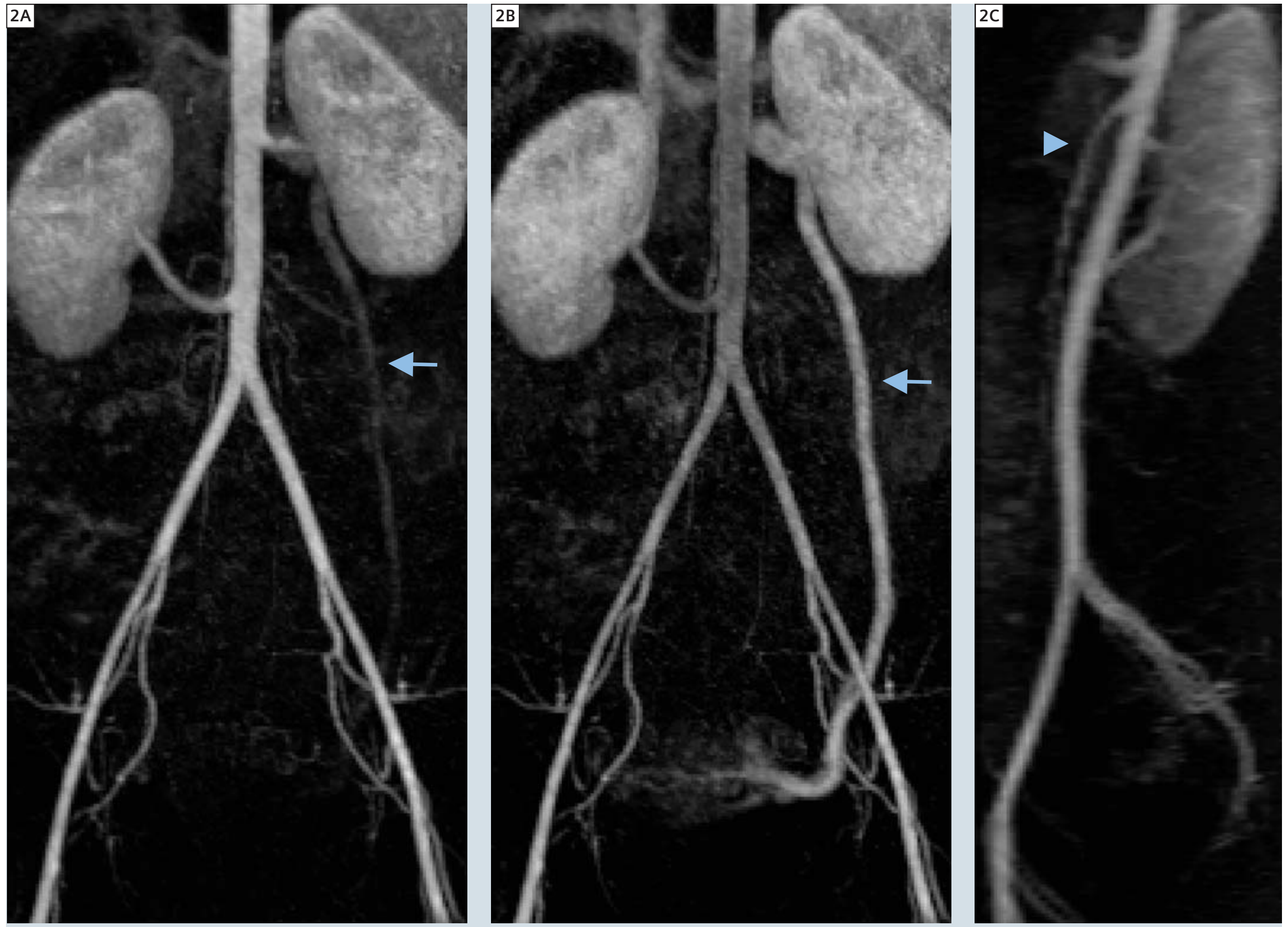

2 Sequential coronal MIP images of dynamic MRI in case of renal vein entrapment syndrome acquired with *syngo* TWIST (late arterial phase **(A)**, early venous phase **(B)**, sagittal view **(C)**).

Case 2
Renal vein entrapment syndrome

Patient history

27-year-old female for MRI follow up of an ovarian cyst.

Sequence details

syngo TWIST, 3D coronal (with coronal and sagittal MIP reformats), 40 partitions, 3 mm thickness, TR 2.54 ms, TE 1.01 ms, 92 s acquisition, 1.6 s/frame temporal resolution, 58 frames, 320 resolution, 400 mm FOV, 80% phase FOV, 78% phase resolution, 82% slice resolution, 1 average, 650 Hz/pixel BW, 25° flip angle. Images have been acquired using our 1.5T MAGNETOM Avanto (software version *syngo* MR B15A) and the Body and Spine Matrix coils.

Imaging findings

Again, sequential coronal MIP images during the late arterial phase (A) and early venous phase (B) demonstrate a prominent left ovarian vein (arrows). Additionally, the left renal vein is prominent in caliber, and appears to abruptly cutoff near the aorta with lack of continuity with the IVC. The sagittal MIP image during the arterial phase demonstrates that the superior mesenteric artery (SMA) (arrowhead) has a 34 degree angle with the aorta.

Results and discussion

Again, temporal examination of the coronal MIP images demonstrates retrograde flow through a dilated left ovarian vein. However in this case, the left renal vein demonstrates imaging characteristics compatible with 'nutcracker syndrome', also called left renal vein entrapment syndrome, which is caused by compression of the left renal vein between the SMA and aorta. Indeed, the angle between the SMA and aorta is unusually small (normal is greater than 60 degrees). This anatomic condition is a known cause of pelvic congestion syndrome.

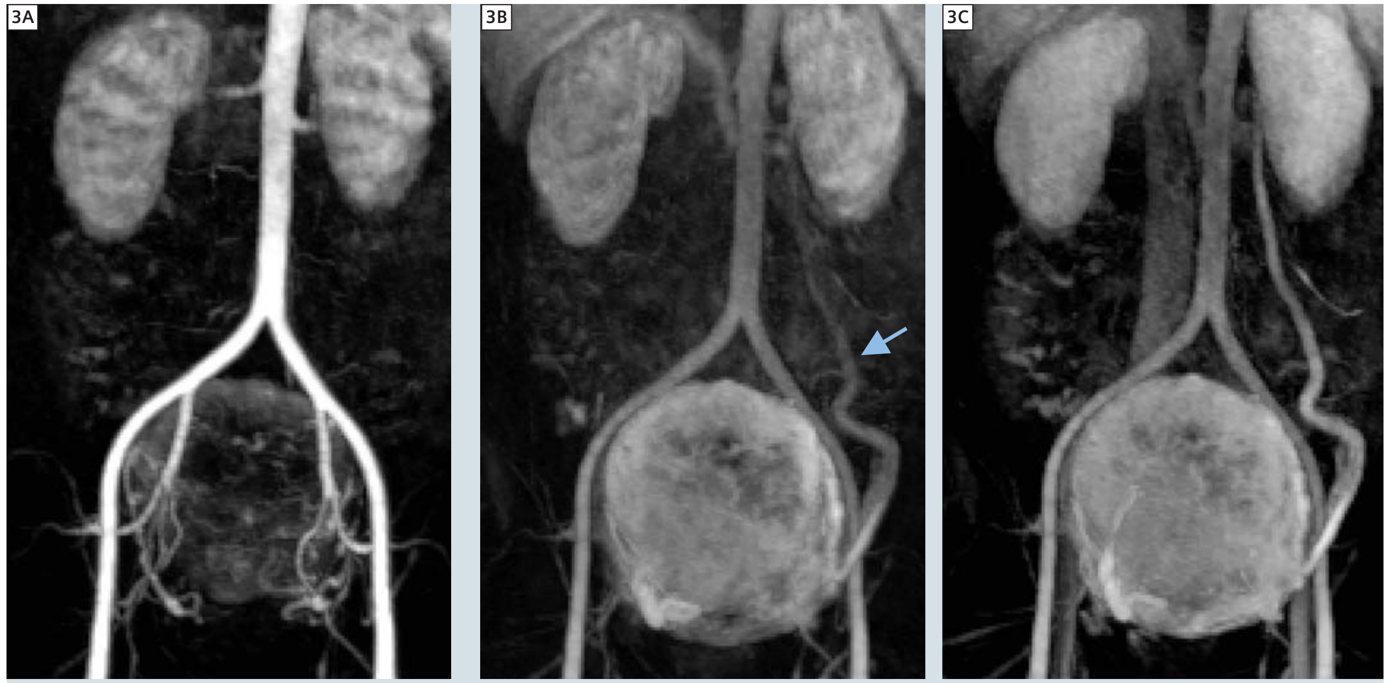

3 Sequential coronal MIP images of dynamic MRI in case of uterine leiomyomata acquired with *syngo* TWIST (arterial phase **(A)**, late arterial phase **(B)**, and venous phase **(C)**).

Case 3
Uterine leiomyomata

Patient history

37-year-old female with pre procedure MRI evaluation of uterine leiomyomata.

Sequence details

syngo TWIST, 3D coronal (with coronal and sagittal MIP reformats), 40 partitions, 3.3 mm thickness, TR 2.44 ms, TE 0.96 ms, 84 s acquisition, 1.4 s/frame temporal resolution, 58 frames, 256 resolution, 400 mm FOV, 81% phase FOV, 78% phase resolution, 82% slice resolution, 1 average, 650 Hz/pixel BW, 25° flip angle. Images have been acquired using our 1.5T MAGNETOM Avanto (software version *syngo* MR B15A) and the Body and Spine Matrix coils.

Imaging findings

Coronal MIP images during the arterial phase, late arterial phase, and venous phase. A dilated left ovarian vein is again noted. A large leimyomatous uterus is present.

Results and discussion

Although the venous phase image is quite similar compared to cases 1 and 2, temporal evaluation of the left ovarian vein opacification demonstrates normal anterograde flow. This underscores the utility of time-resolved MRA for the evaluation of pelvic congestion syndrome, since actual reflux is required to make the diagnosis.

Contact
Prof. Elmar M. Merkle, M.D.
Duke University Medical Center
Department of Radiology
Box 3808
Durham, NC 27710
USA
elmar.merkle@duke.edu

Case Report: Role of DWI for Lesion Discrimination in Breast MRI of Multifocal and Contralateral Breast Cancer

Evelyn Wenkel[1]; Christian Geppert[2]; Michael Uder[1]; Rolf Janka[1]

[1] *Radiologic Institute, University Hospital Erlangen, Germany*
[2] *Siemens Healthcare, Erlangen, Germany*

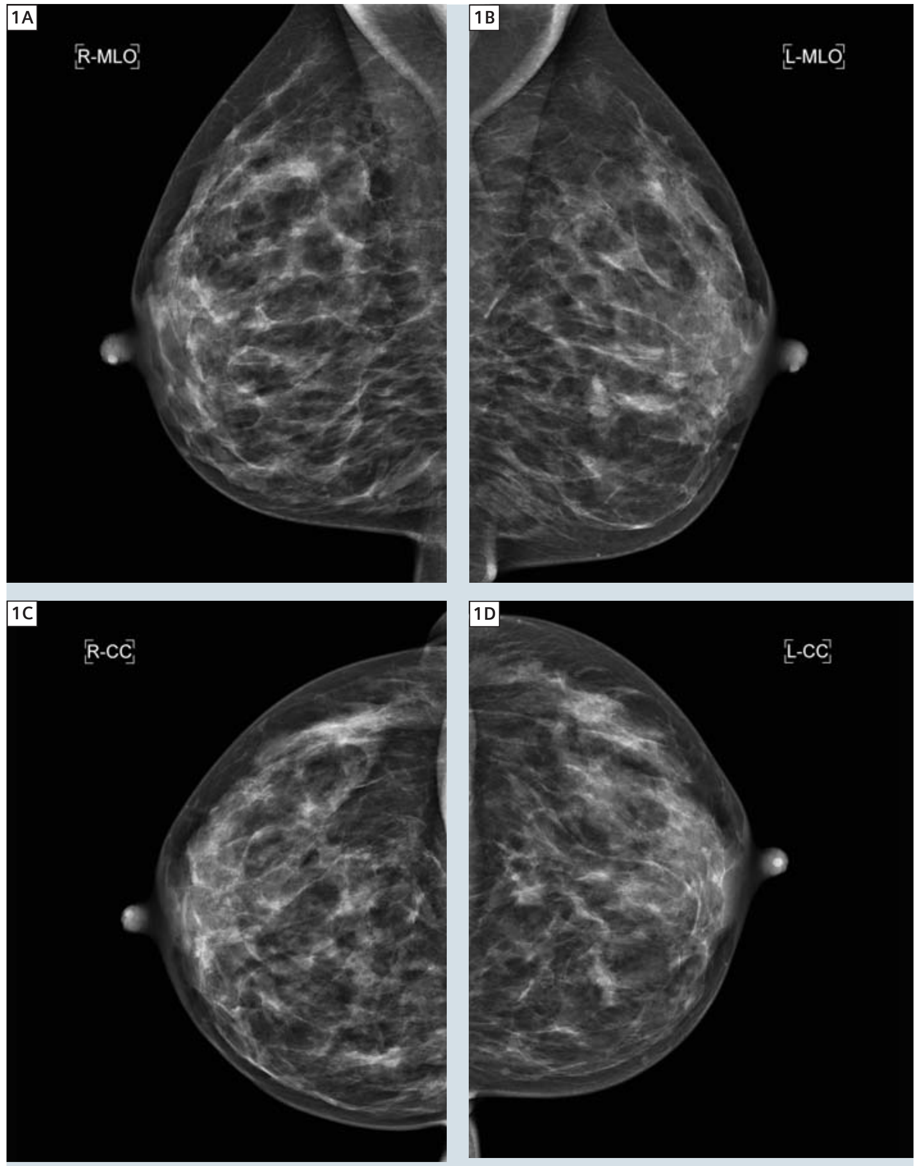

1 Mammography in mediolateral and craniocaudal projection of both breasts.

Patient history

We report on a 35-year-old woman who presented with a small nodule around the nipple which she palpated since one week. She had no prior breast surgery. She had a positive family history of breast cancer. One sister at 26 years of age and one sister at 33 years of age. Mammography showed inhomogeneous, symmetrically distributed fibroglandular breast tissue and no obvious abnormality (Fig. 1). On ultrasound the palpable nodule was oval in shape with inhomogeneous echogeneity and a size of 9 mm. It was classified as a BI-RADS 4 (1) lesion. Before the ultrasound guided biopsy an MRI of both breasts was performed for further evaluation of the palpable mass and due to the strong family history for breast cancer.

Sequence details

Images were acquired on a 1.5 T scanner (MAGNETOM Avanto, Siemens Healthcare) using a dedicated 4-channel diagnostic breast coil (Siemens Healthcare) with the patient in prone position.

Our standard breast MRI protocol includes the following sequences:

An axial **2D T2-weighted STIR pulse sequence** (TR/TE/TI, 7200/85/150 msec, FOV 380 x 380 mm, matrix = 512 x 358, resolution: 1.1 x 0.7 x 3.0 mm, acquisition time: 3:30 min),

A pre- and post-contrast **sagittal T1-weighted 3D gradient echo (GRE)** pulse sequence (TR/TE, 21/4.8 msec, FOV 180 x 180 mm, matrix = 512 x 512, resolution: 0.4 x 0.4 x 2.0 mm, acquisition time: 4:42 min),

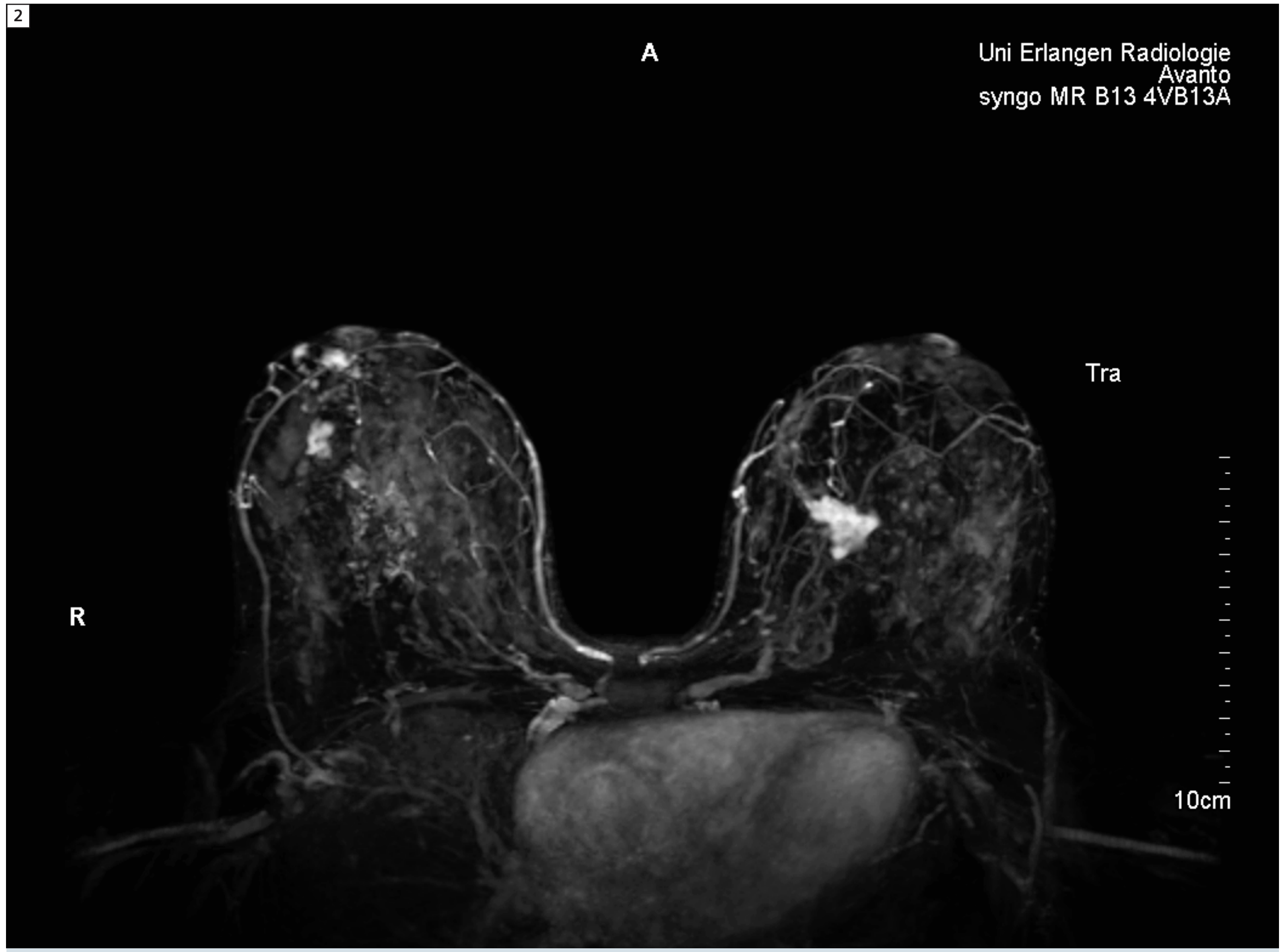

2 MIP-reconstruction. Two lesions in the right breast and one lesion in the left breast are delineated.

And an **axial 3D dynamic GRE pulse sequence** (TR/TE, 11/4.8 msec, FOV 360 x 360 mm, matrix = 512 x 430, resolution: 0.8 x 0.7 x 3 mm, acquisition time per time point: 1:07 min, total 6 time points including one native scan).

Diffusion-weighted (DW) images were acquired in axial slice orientation using a EPI-SE sequence. Fat signal suppression was obtained by applying water selective excitation pulses (TR/TE, 3200/89, FOV 340 x 170 mm, matrix = 236 x 118, resolution 1.4 x 1.4 x 4 mm). The relatively high spatial resolution could be achieved by using parallel imaging with GRAPPA acceleration factor of 2 in the anterior-posterior direction. DWI measurements were acquired in three averages of 26 slices with 4 mm slice thickness and b-values of 50, 400 and 800 s/mm^2 using 3-scan trace calculation resulting in a scan time of only 1:42 minute. Apparent diffusion coefficient (ADC) maps were calculated automatically using the scanner software.

Imaging findings

Besides inhomogeneous enhancing fibroglandular breast tissue two lesions in the right breast and a contralateral lesion in the left breast were identified on MRI. In the MIP reconstruction based on dynamic MRI the three lesions are clearly visible (Fig. 2). All three lesions were evaluated according to morphologic and dynamic MR features and DWI values. ADC values for malignant breast lesions range from 0.9 x 10^{-3} mm^2/s to 1.2 x 10^{-3} mm^2/s and for benign lesions from 1.5 x 10^{-3} mm^2/s to 1.8 x 10^{-3} mm^2/s (with cysts >2, if included) in recent publications [2–7]. In a series of our patients mean ADC values for malignant lesions were 0.9 x 10^{-3} mm^2/s (± 0.18) and for benign lesions 1.8 x 10^{-3} mm^2/s (± 0.42) [2].

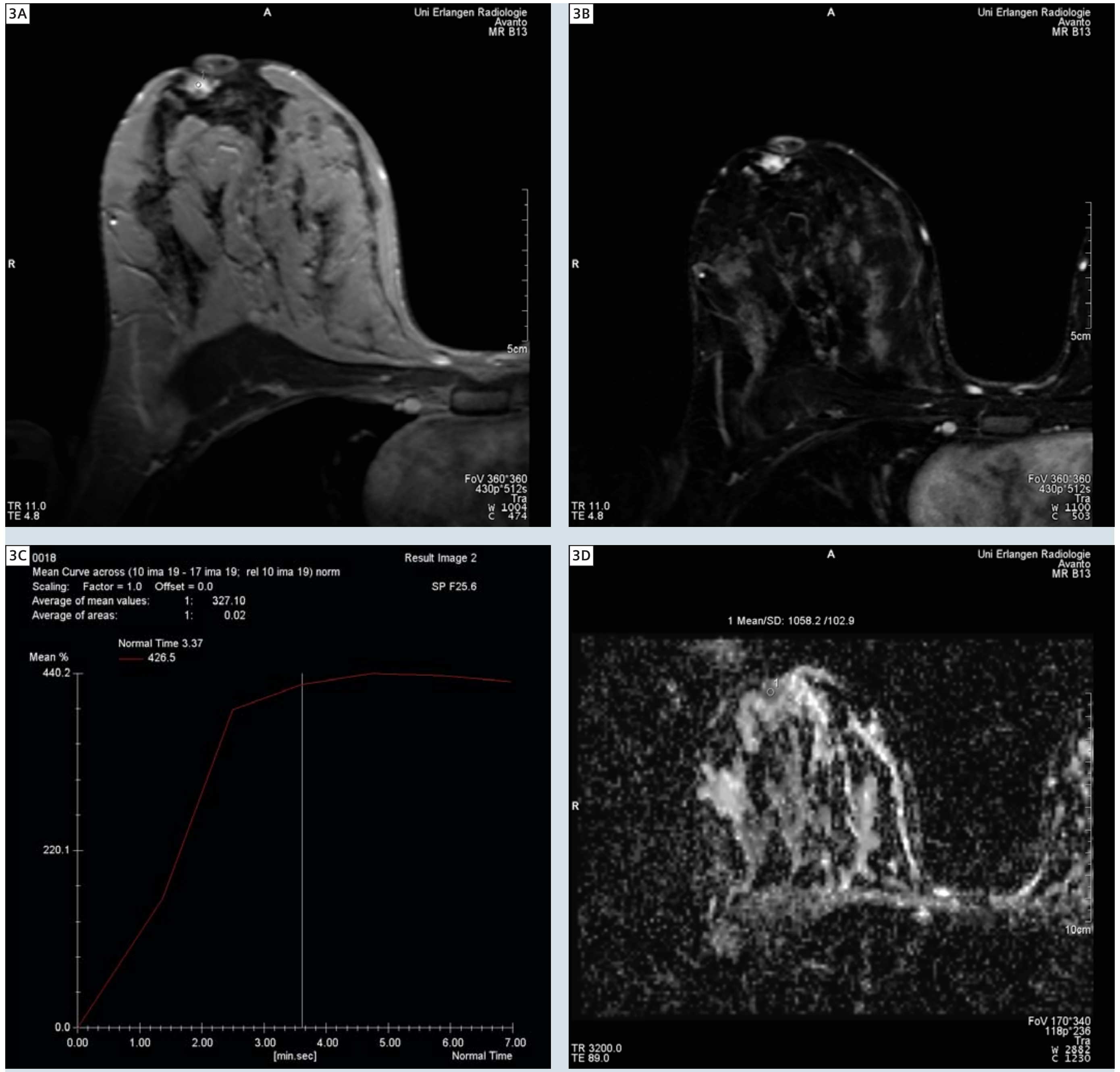

3 Lesion 1 in an early T1-weighted image with ROI for dynamic analysis **(A)**, subtraction image **(B)**, dynamic curve **(C)** and ADC value **(D)**. Mean ADC values and standard deviation are given in mm²/s.

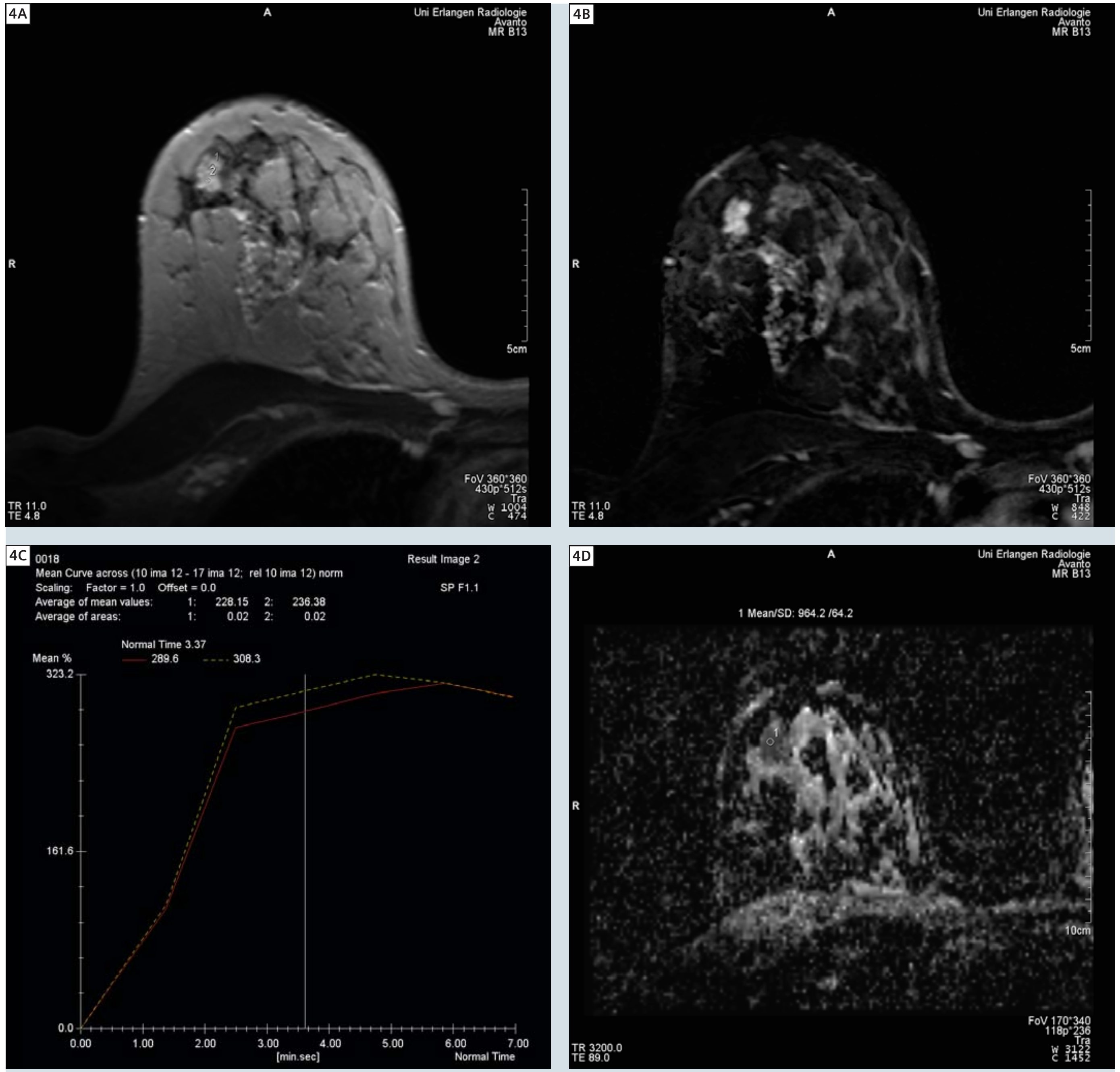

4 Lesion 2: T1-weighted image with ROI for dynamic analysis **(A)**, subtraction image **(B)**, dynamic curve **(C)** and ADC value **(D)**.

The oval to lobular shaped perimamillary lesion with a size of 8 x 9 mm (Fig. 3) corresponded to the palpable lesion. The second lesion (Fig. 4) in the right breast measured 1.1 x 0.7 cm and was located at 11 o'clock with lobulated to irregular margins. The irregular shaped mass in the left breast at 8 o'clock measured 1.9 x 2.1 cm (Fig. 5).

The signal-intensity (SI) time curve was initially steep in all lesions. The maximum SI of the lesion in the left breast was after 2 minutes followed by a fast SI decrease. The lesions in the right breast showed similar shaped SI time curves with continuous rise of the SI discretely after two minutes and with an SI plateau in the following dynamic scans. The ADC values indicated malignancy for all lesions with a value of 1.1 x 10^{-3} mm²/s in lesion 1, 1.0 x 10^{-3} mm²/s in lesion 2, and 0.7 x 10^{-3} mm²/s in lesion 3.

The lesions in the right breast were not clearly suggestive of malignant disease according to their morphologic features as potential differential diagnosis could be sclerosing adenosis, fibrocystic disease or fibroadenoma. Lesion 3 was highly suggestive of breast cancer in its morphological, dynamic and diffusibility criteria.

After the MRI a second look ultrasound was performed. The mass in the left breast was identified as an inhomogeneous area in the breast and biopsied ultrasound guided. Histology revealed an intermediate differentiated invasive, focally mucous producing breast cancer with intermediate grade DCIS. The ultrasound guided biopsy of the palpable lesion in the right breast was a highly differentiated invasive ductal breast cancer. The second lesion in the right breast could not be identified on ultrasound. An MR-guided vacuum assisted biopsy was performed of this lesion and histology revealed a highly differentiated invasive ductal breast cancer.

After neoadjuvant chemotherapy the patient underwent skin-sparing mastectomy of both sides. Histology of the mastectomy specimen revealed residuals of an intermediate grade DCIS of 2 cm in the outer quadrant of the right breast and an intermediate differentiated invasive breast cancer of 12 mm with one micrometastasis in an axillary lymph node.

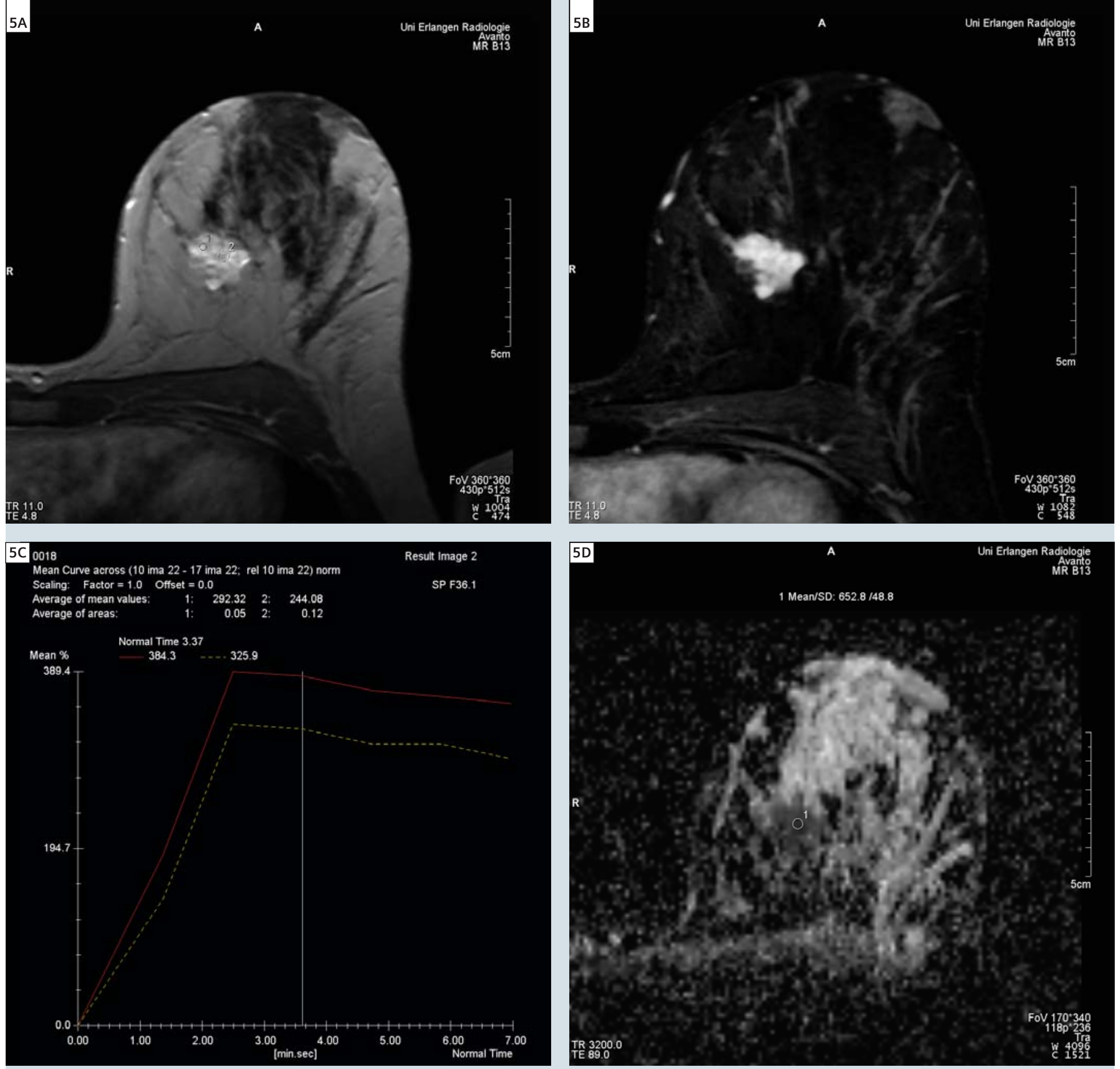

5 Lesion 3: T1-weighted image with ROI for dynamic analysis **(A)**, subtraction image **(B)**, dynamic curve **(C)** and ADC value **(D)**.

Conclusion

DWI can be helpful to support diagnosis of cancerous breast lesions.

References

1 ACR. Breast Imaging Reporting and Data System Atlas (BI-RADS Atlas), BI-RADS – Mammography, Fourth Edition. BI-RADS - Ultrasound, First Edition. BI-RADS – MR Imaging, First Edition. Reston, VA., 2003.
2 Wenkel E, Geppert C, Schulz-Wendtland R, et al. Diffusion weighted imaging in breast MRI: comparison of two different pulse sequences. Acad Radiol 2007; 14:1077–1083.
3 Woodhams R, Matsunaga K, Iwabuchi K, et al. Diffusion-weighted imaging of malignant breast tumors: the usefulness of apparent diffusion coefficient (ADC) value and ADC-map for the detection of malignant breast tumors and evaluation of cancer extension. J Comput Assist Tomogr 2005; 29:644–649.
4 Woodhams R, Matsunaga K, Kan S, et al. ADC mapping of benign and malignant breast tumors. Magn Reson Med Sci 2005; 4:35–42.
5 Kuroki Y, Nasu K, Kuroki S, et al. Diffusion-weighted imaging of breast cancer with the sensitivity encoding technique: analysis of the apparent diffusion coefficient value. Magn Reson Med Sci 2004; 3:79–85.
6 Rubesova E, Grell AS, De Maertelaer V, Metens T, Chao SL, Lemort M. Quantitative diffusion imaging in breast cancer: a clinical prospective study. J Magn Reson Imaging 2006; 24:319–324.
7 Marini C, Iacconi C, Giannelli M, Cilotti A, Moretti M, Bartolozzi C. Quantitative diffusion-weighted MR imaging in the differential diagnosis of breast lesion. Eur Radiol 2007; 17:2646–2655.

Contact
Dr. Evelyn Wenkel, M.D.
Friedrich-Alexander-University Erlangen-Nuernberg
Universityhospital Erlangen
Dept. of Radiology
Maximiliansplatz 1
91054 Erlangen
Germany
evelyn.wenkel@uk-erlangen.de

Diffusion-Weighted Imaging for Characterizing Breast Lesions Prior to Biopsy

Mitsuhiro Tozaki, M.D.[1]**; Katsuya Maruyama**[2]

[1] Breast Center, Kameda Medical Center, Chiba, Japan.
[2] Siemens Asahi Medical Technologies LTD., Tokyo, Japan

Introduction

Diffusion-weighted imaging (DWI) is characterized by superior lesion to background contrast, and it has been applied in the brain e.g. to diagnose early-stage cerebral infarction. When used to image the body, however, strong artifacts are created by the non-uniformity of the magnetic field. Recent development of MR technology has nearly overcome this obstacle and enabled the clinical application of DWI. DWI has shown great promise in the detection of most tumor types throughout the entire body. Regarding breast DWI, the potential role of the apparent diffusion coefficient (ADC) in characterizing breast lesions has been reported. Preliminary results showed that ADC value may be an effective parameter for distinguishing between benign and malignant breast lesions because tumor cellularity has a significant influence on ADC values [1–3].

Optimal b-values

However, there is no international consensus in regard to the usefulness of DWI for breast cancer or the optimal b-values. Therefore, we perform categorization visually based on multi-b-factor DWI (500, 1000, 1500, 2000 and 3000 s/mm^2), always applying the same window level and width. The significance of the five b-values at our institution is being investigated, particularly whether very high b-values of 2000 s/mm^2 or more might be useful for evaluating the effects of neoadjuvant chemotherapy. Currently, we routinely perform ADC calculations based on two b-values: 500 s/mm^2 and 1500 s/mm^2.

Interpretation of DWI: two-step evaluation for mass lesion

We previously reported the clinical usefulness of DWI using a two-step evaluation to detect rectal cancer [4]; we are testing a similar approach for breast mass lesions. First, high b-value ($b = 1500$ s/mm^2) images were assessed visually. Next, ADC values of mass lesions were calculated among the patients with positive results on DWI. The highest signal portion of the lesion was visually identified on original high b-value images, and a circular region of interest (ROI) was placed manually on that portion of the lesion. ADC values were calculated according to the equation

$$\text{ADC (mm}^2\text{/s)} = 1/b_2\text{-}b_1 \times \ln[\text{IS}(b_1)/\text{IS}(b_2)]$$

where IS(b_1) and IS(b_2) are the signal intensities resulting from two different gradient factors, $b_1 = 500$ and $b_2 = 1500$ s/mm^2.
At our institute, ADC measurements are not performed for non-mass type lesions because it is sometimes impossible to identify the highest signal portion at one location in the lesions.

1A–C

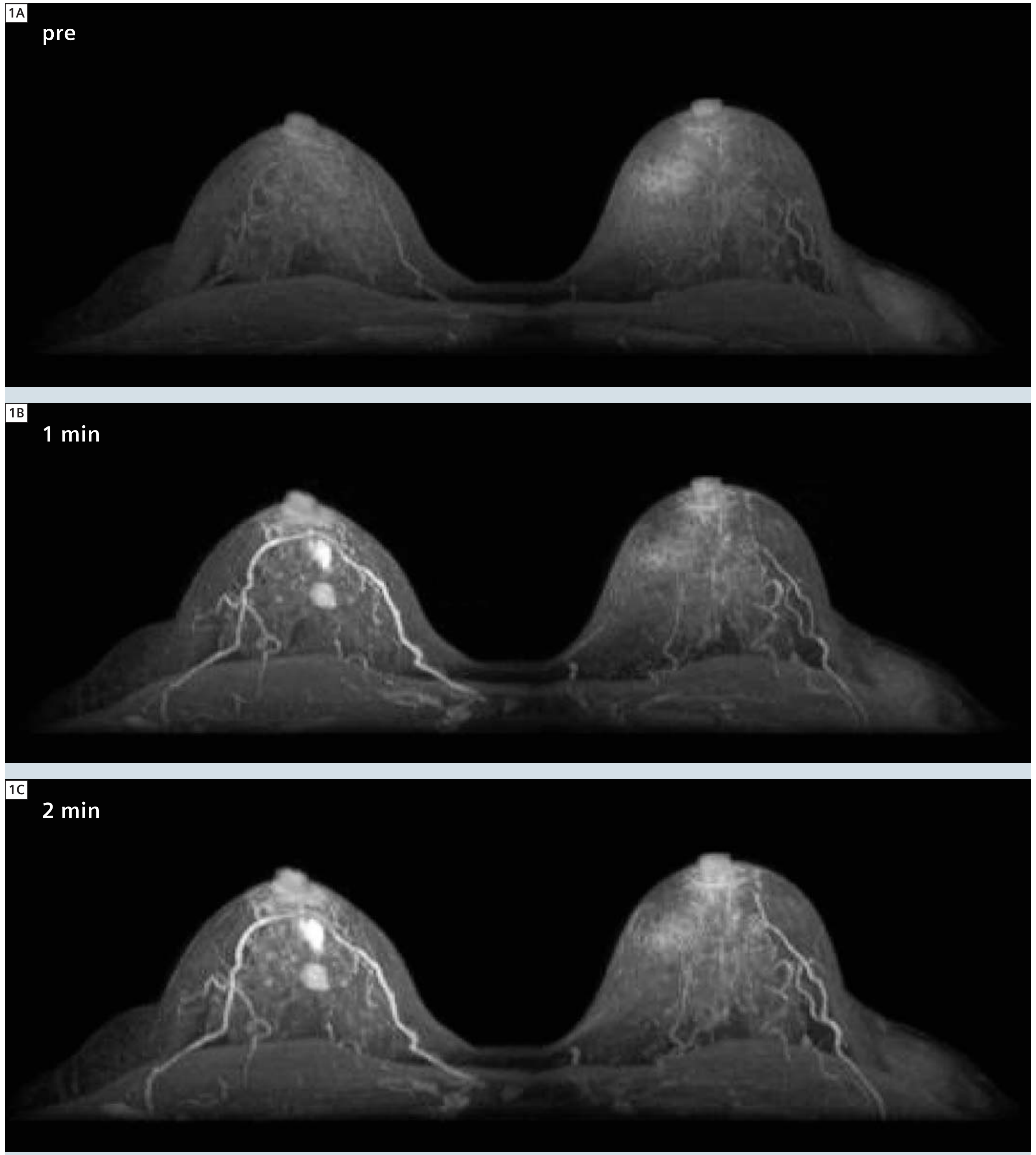

1A–C Dynamic MRI sequence using VIBE with iPAT: Enhanced T1-weighted images with fat saturation show 2 irregular masses in the right breast.

Retrospective study for 171 breast lesions prior to biopsy

Patients

Between November 2007 and May 2008, breast MRI was performed for 1,486 patients with breast disease at our institute. Among them, 165 patients who had 171 suspicious or highly suspicious lesions classified as Breast Imaging Reporting and Data System (BI-RADS)-MRI category 4 (n = 112) or 5 (n = 59), and who had a biopsy performed after MR examinations, were analyzed [5].

MR Sequences

MRI was performed using a 1.5 Tesla system (MAGNETOM Avanto; Siemens Healthcare, Erlangen, Germany) equipped with a double breast coil (Breast Matrix coil).
Before applying dynamic sequences, bilateral sagittal fat-suppressed T2-weighted images and coronal T1-weighted images were obtained. In addition, coronal diffusion-weighted images were acquired with a spin-echo-type single-shot echo-planar imaging sequence incorporating the *syngo* GRAPPA (generalized auto-calibrating partially parallel acquisition) algorithm for parallel acquisition. The parameters were as follows: TR/TE 8000/96 ms; field of view 33 cm; matrix 110 × 110; bandwidth 1684 Hz/Px; parallel acquisition factor 2; slice thickness 3 mm; acquisition time

1D

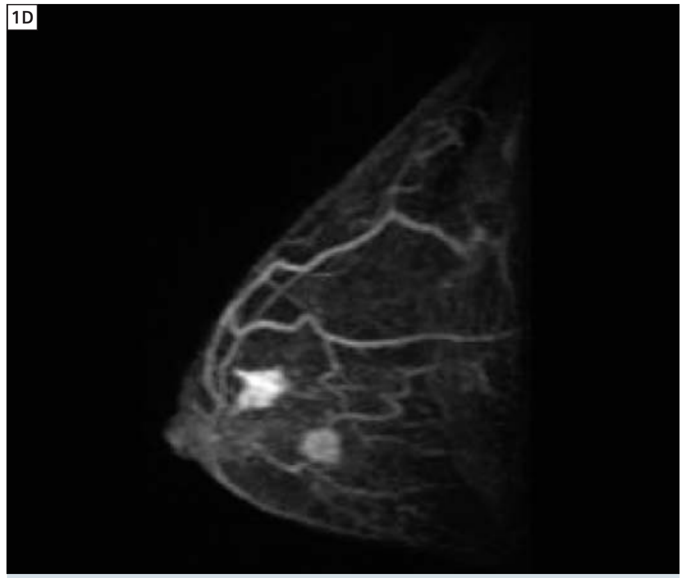

1D Subtracted image shows 2 irregular masses (BI-RADS-MRI category 4).

1E

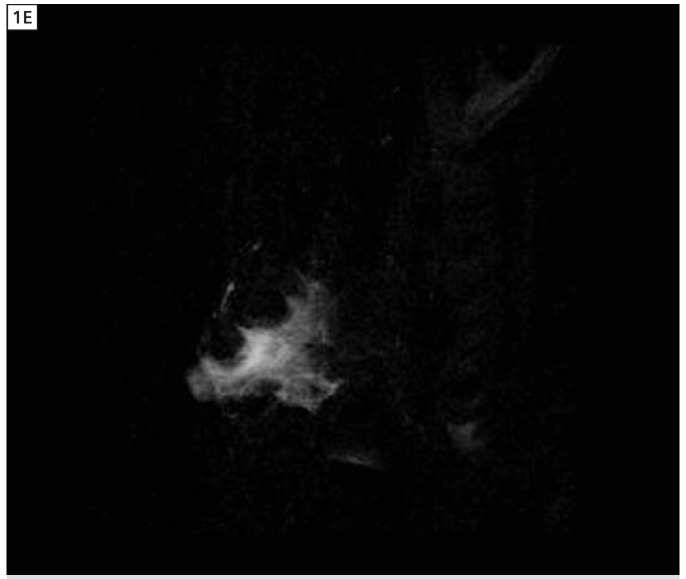

1E T2-weighted image shows no tumors.

1F

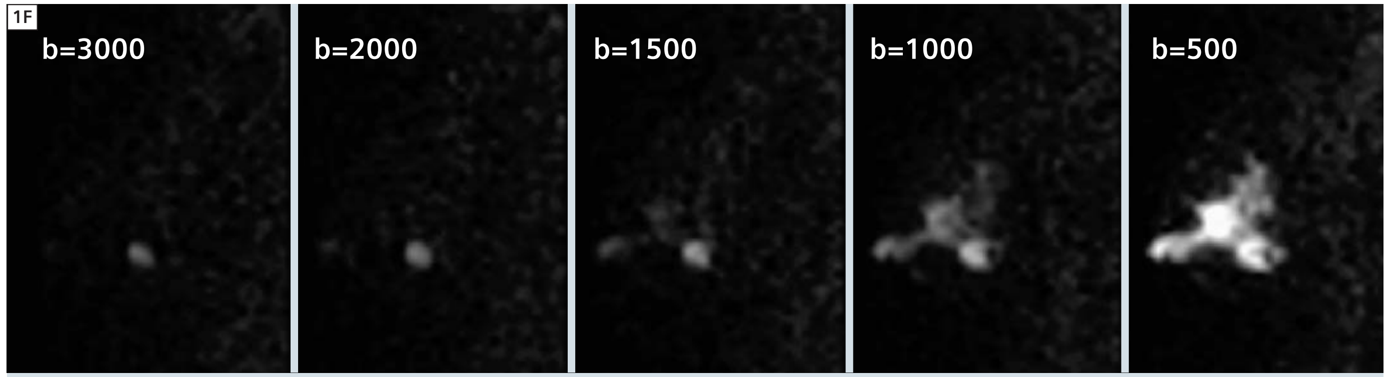

1F Sagittal multiplanar reconstruction (MPR) images constructed from diffusion-weighted images with b-factors of 500, 1000, 1500, 2000 and 3000 s/mm^2 show different signal intensity of 2 masses. The ADC of mass in upper portion was 1.88 x 10-3 mm^2/s, and that in lower portion was 0.76 x 10^{-3} mm^2/s. Histology of the lesions were benign proliferative disease (upper portion) and invasive ductal carcinoma (lower portion).

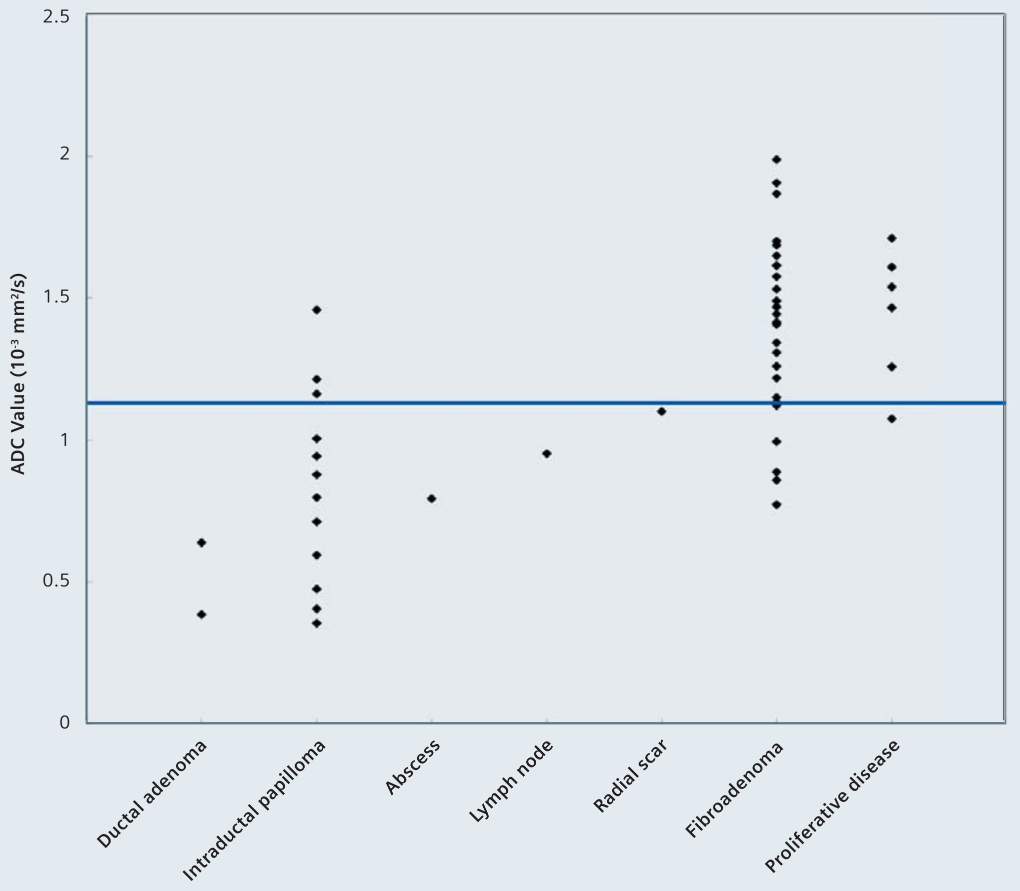

2 The ADC of benign masses: With the use of the two-step method of visual assessment of high b-value images and a cutoff ADC value of 1.13 x 10^{-3} mm^2/s, a specificity of 67% (43/64) and sensitivity of 97% (61/63) for mass lesions was obtained.

2.5 minutes. Motion-probing gradient pulses were applied along the X, Y, and Z directions with b-values of 500, 1000, 1500, 2000 and 3000 s/mm^2. SPAIR (Spectrally adiabatic inversion recovery) was used for fat suppression. Dynamic MRI using a 3D fat-suppressed VIBE (volumetric interpolated breath-hold examination) sequence with parallel acquisition [6] included three time-points and a native scan. Both breasts were examined in the coronal plane on the first-, second-, and third-phase dynamic images, acquired at 30 seconds, 1.5 minutes, and 4.5 minutes, respectively. The right and left breasts were examined sagittally using the VIBE sequence without parallel acquisition at 2.5 minutes and 3.5 minutes, that is, between the second- and third-phase images, respectively.

Results

No previous studies, to the best of our knowledge, have used visual assessment of high b-value images for the detection of breast lesions.

With the use of the two-step method of visual assessment of high b-value images and a cutoff ADC value of 1.13 x 10^{-3} mm^2/s, we achieved a specificity of 67% (43/64) and sensitivity of 97% (61/63) for mass lesions, regardless of the lesion size (Figs. 1–3).

The 21 false-positive mass lesions were histologically characterized as intraductal papilloma (n = 9), ductal adenoma (n = 2), fibroadenoma (n = 6), benign proliferative disease (n = 1), radial scar (n = 1), lymph node (n = 1), and abscess (n = 1).

Using this cutoff value (1.13 x 10^{-3} mm^2/s), only mucinous carcinoma was misclassified. Mucinous carcinoma consists of pure and mixed variants. While mucinous carcinoma with dominant mucus lakes may have such high ADC values, it can still be diagnosed using other methods. Micropapillary carcinoma also had a high ADC value (1.06 x 10^{-3} mm^2/s). This tumor was histologically characterized by a proliferation of tumor cell clusters within empty stromal spaces. We speculate that the water in the empty spaces could move more randomly as compared with that in the interstitium of invasive ductal carcinoma.

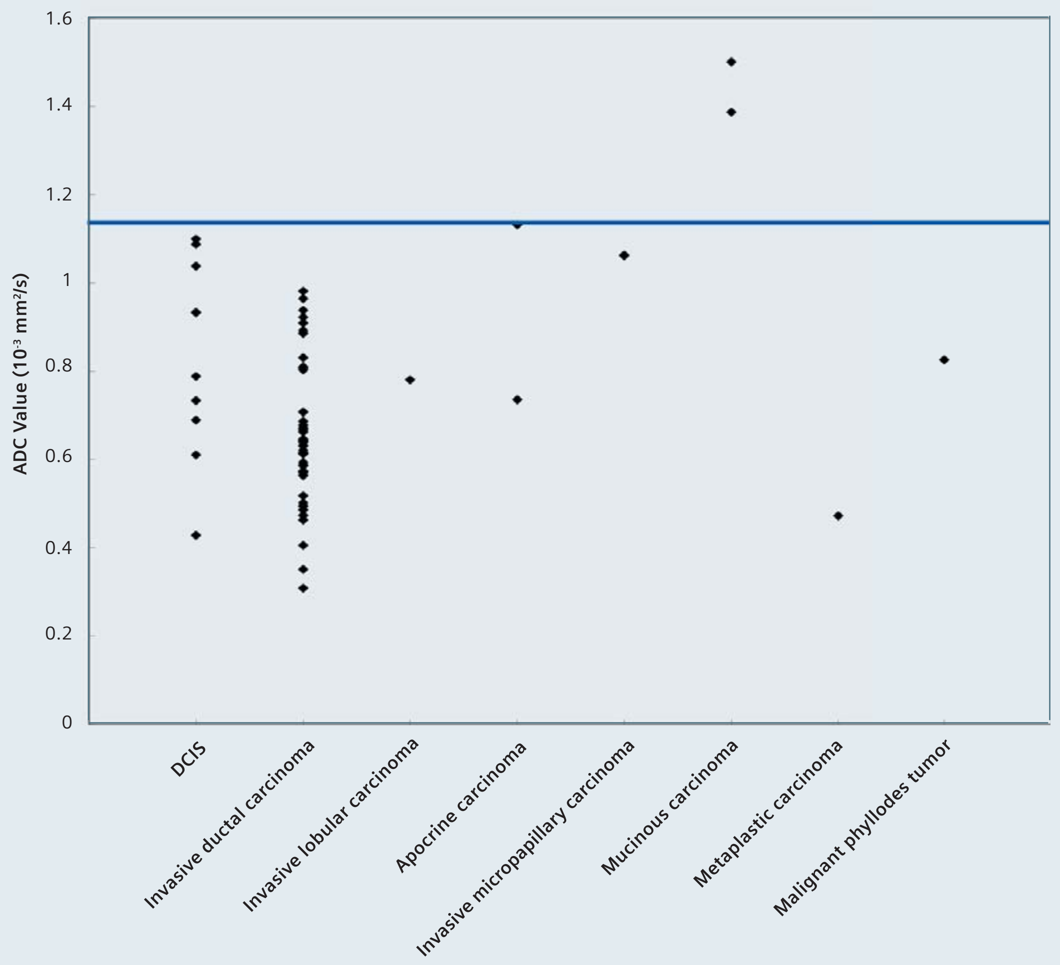

3 The ADC of malignant tumors: Except for the case with mucinous carcinoma, the maximum ADC value of the malignant tumors was 1.13 x 10^{-3} mm^2/s.

In summary, all of the cases of invasive carcinoma and mass-forming DCIS were diagnosed, whereas eight non-mass-type DCIS could not be diagnosed.

Conclusion

We believe that DWI is the only sequence which can visualize breast cancers with a high rate of detectability on non-enhanced MRI. Our results suggest that DWI may be helpful in reducing the number of unnecessary biopsies following categorization into BI-RADS-MRI 4 or 5 lesions. However, this modality still has potential pitfalls in relation to the diagnosis of non-mass-type breast lesions. We believe that non-mass-type lesions should be evaluated by morphological characteristics [5–7].

References

1 Sinha S, Lucas-Quesada FA, Sinha U, DeBruhl N, Bassett LW. In vivo diffusion-weighted MRI of the breast: potential for lesion characterization. J Magn Reson Imaging 2002;15:693–704.
2 Guo Y, Cai YQ, Cai ZL, et al. Differentiation of clinically benign and malignant breast lesions using diffusion-weighted imaging. J Magn Reson Imaging 2002;16:172–178
3 Rubesova E, Grell AS, De Maertelaer V, Metens T, Chao SL, Lemort M. Quantitative diffusion imaging in breast cancer: a clinical prospective study. J Magn Reson Imaging 2006;24:319–324.
4 Hosonuma T, Tozaki M, Ichiba N, et al. Clinical usefulness of diffusion-weighted imaging using low and high b-values to detect rectal cancer. Magnetic Resonance in Medical Sciences 2006; 5: 173–177.
5 Tozaki M, Fukuma E. 1H MR spectroscopy and diffusion-weighted Imaging of the breast: are they useful tools for characterizing breast lesions prior to biopsy? AJR Am J Roentgenol 2009 (in press).
6 Tozaki M, Igarashi T, Fukuda K. Breast MRI using the VIBE sequence: Clustered ring enhancement in the differential diagnosis of lesions showing non-masslike enhancement. AJR Am J Roentgenol 2006;187: 313–321.
7 Tozaki M, Fukuda K. High-spatial-resolution MRI of non-masslike breast lesions: interpretation model based on BI-RADS MRI descriptors. AJR Am J Roentgenol 2006;187:330–337.

Contact
Mitsuhiro Tozaki, M.D.
Breast Center
Kameda Medical Center
929 Higashi-cho
Kamogawa
Chiba 296-8602
Japan
e-tozaki@keh.biglobe.ne.jp

The Composer

Sandra Winsor

Centre for Advanced MRI, University of Auckland, New Zealand

The composing software is an image stitching program similar to stitching scenic photographs into a panoramic picture. The difference with the composer is that it stitches the image in the vertical direction. The reason we do this is that our MR systems have a maximum field-of-view (FOV) of 35–50 cm. The human anatomy is often larger than this, and by composing the images we can achieve an effective FOV of up to 205 cm. The software is able to compose multiple slices for example; eleven sagittal slices from the upper and lower spine can be composed to create a composite image of eleven sagittal slices of the whole spine. Multiple data sets can be composed to create whole body images (Fig. 1A and B), or simply two regions for a smaller area of interest (Fig. 1C). Whilst most radiologists are used to and prefer the original smaller data sets to report from, clinicians and patients benefit from the composed images by having a better perspective of lesions and their location in relation to the rest of the body. The simplest and most useful function of the composing software is composing localiser scans especially with the use of the Inline Composing. Workflow is optimised by scout images being automatically composed and loaded into the exam card for subsequent planning of images.

Most parts of the anatomy can be composed using the spine algorithm, which is based on bone structure but not limited to just the spine. Similarly, vascular studies can be composed using the angio algorithm.

1 **(A)** is a composed whole-body MR image that consists of six different data sets, each covering a different anatomical area as shown in **(B)**. The *syngo* composing software can also be used for image integration from all types of multi-step MR examinations as demonstrated in **(C)**.

1 **(A)** is a composed whole-body MR image that consists of six different data sets, each covering a different anatomical area as shown in **(B)**. The *syngo* composing software can also be used for image integration from all types of multi-step MR examinations as demonstrated in **(C)**.

Once images are composed the software will advise if there has been any mismatch between data sets. Any inadequate matches are indicated by red triangles at the mismatch points. If necessary, the images can be adjusted up / down, right / left, or front / back. A normalise filter will even out any signal intensity variations between the different data sets. (Visit www.siemens.com/magnetom-world for the technical aspects of the normalise filter: “Image Quality Improvement of Composed MR Images by Applying a Modified Homomorphic Filter” by V. Jellus et al.)

Certain criteria are required for the software to be able to compose the images:

1. Must come from the same frame of reference.
2. Must be distortion corrected.
3. Must be the same image type.
4. Cannot be rotated about the feet-head (FH) axis.
5. Can angle by 45° in the other axes.
6. Can have different matrix size, FOV, slice thickness or number of slices between data sets.

Frame of reference

To ensure that the series come from the same frame of reference, they need to be distortion corrected.

Once distortion correction has been applied, the images belong to the whole body coordinate system and have the same frame of reference.

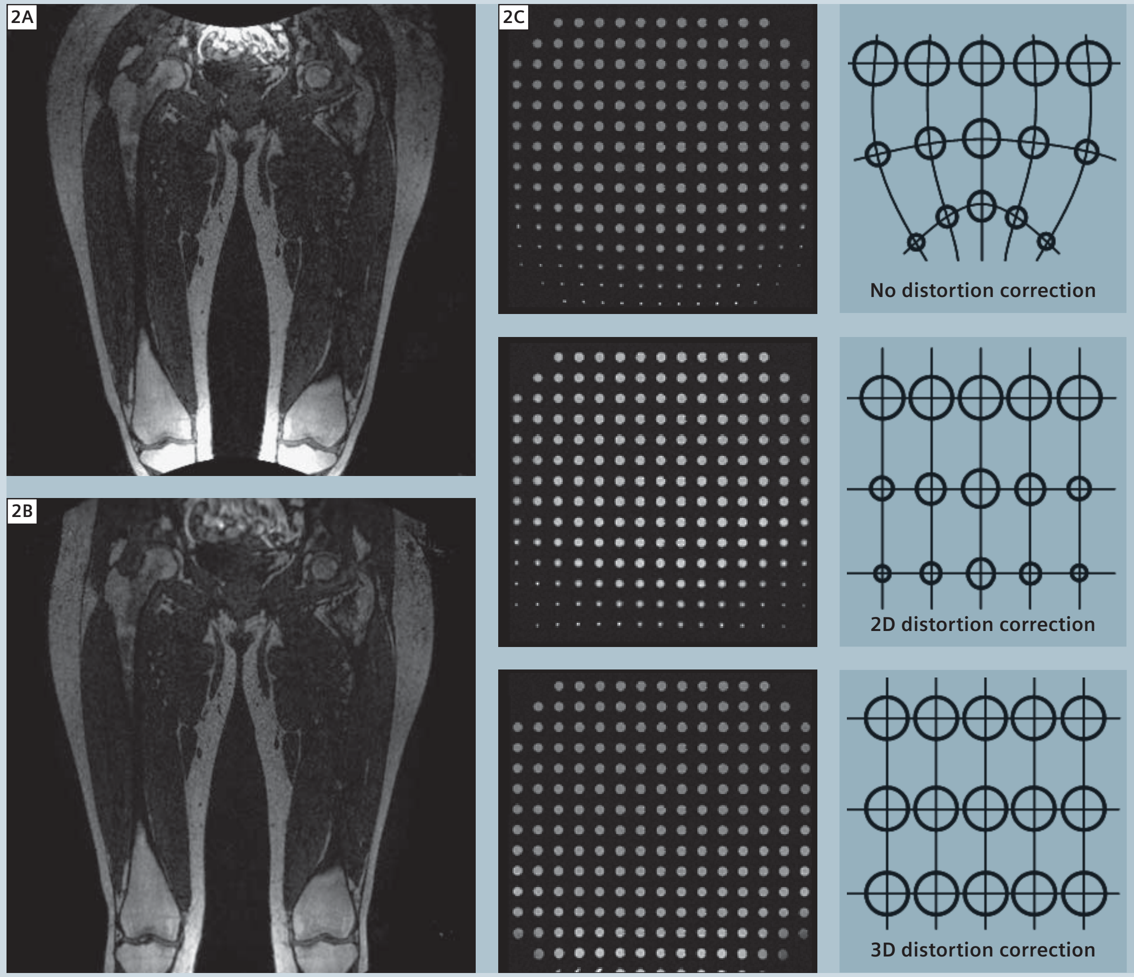

2 Figure **2A** demonstrates the influence of geometric distortion on large field-of-view MR images, especially present at the edges of the field-of-view. **(B)** shows the same image corrected by a distortion algorithm. The positive influence on the overall image quality is clearly visible. Distortion correction can be applied either as 2D or 3D algorithm; the influence on image information by a distortion correction is given in **(C)**.

Distortion correction

Images acquired on a large FOV will suffer from geometric distortion at the edges of the FOV (Fig. 2A). This is due to non-linearity over the length of the gradients. Geometric distortion can be corrected by applying either a 2D or 3D distortion correction filter (Fig. 2B). The advantage of the 3D distortion correction filter is the additional corrections in the through-plane direction (Fig. 2C).

Same sequence type

This requires the data to have been acquired by the same technique. It is not possible to compose gradient echo sequences with spin echo, or 2D sequences with 3D.

Planning the scan

When planning sagittal or coronal images, it is important not to rotate about the feet-head axis (Fig. 3B). If scans are rotated in this direction, the subsequent regions must be of the same angle. A difference of more than one degree will render the data sets unable to be composed. Angulations of up to 45 degrees in the other planes are acceptable for 2D sequences (Fig. 3 A and C), but with steeper angulations a limited number of composed images may result.

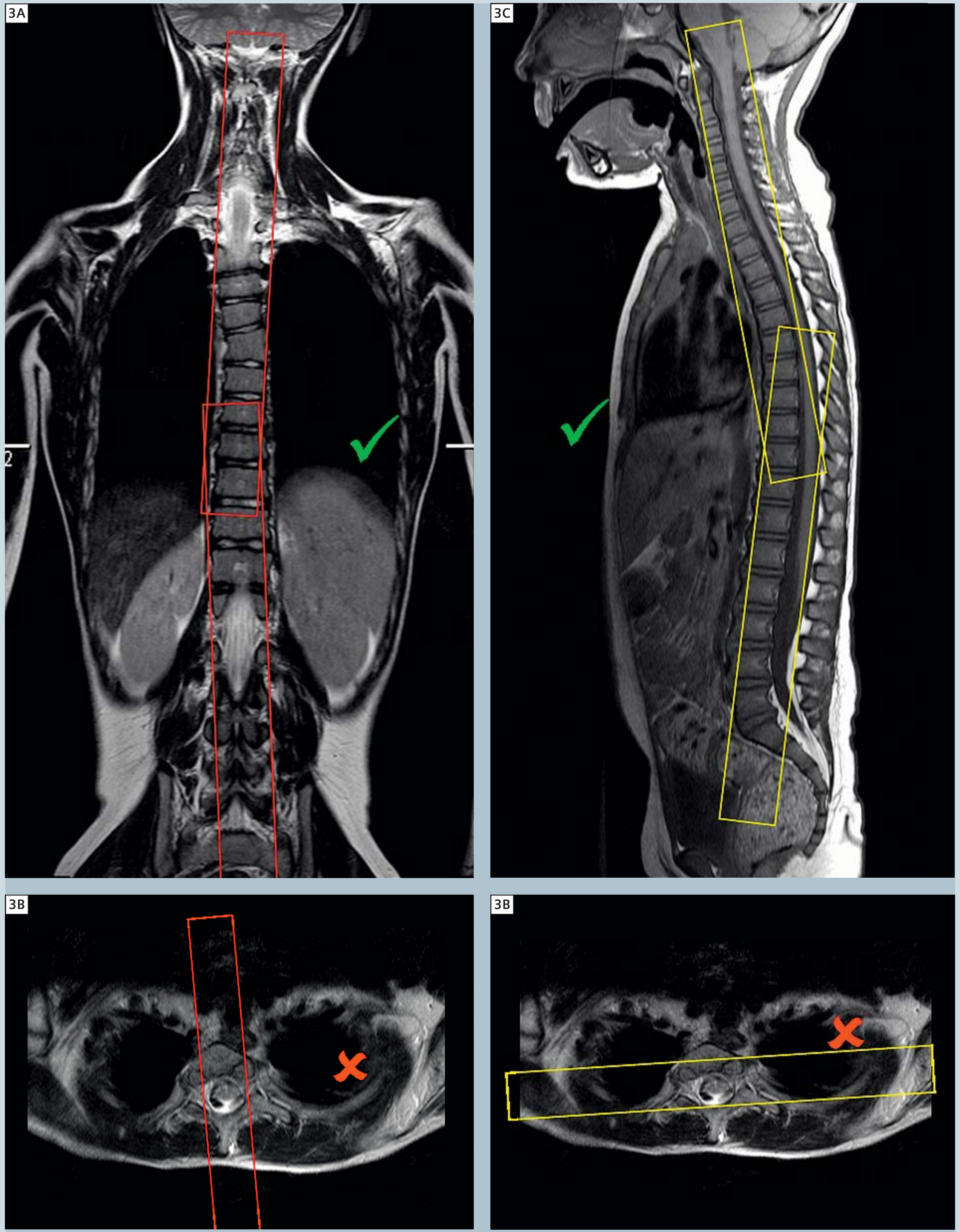

3 Planning the scan.

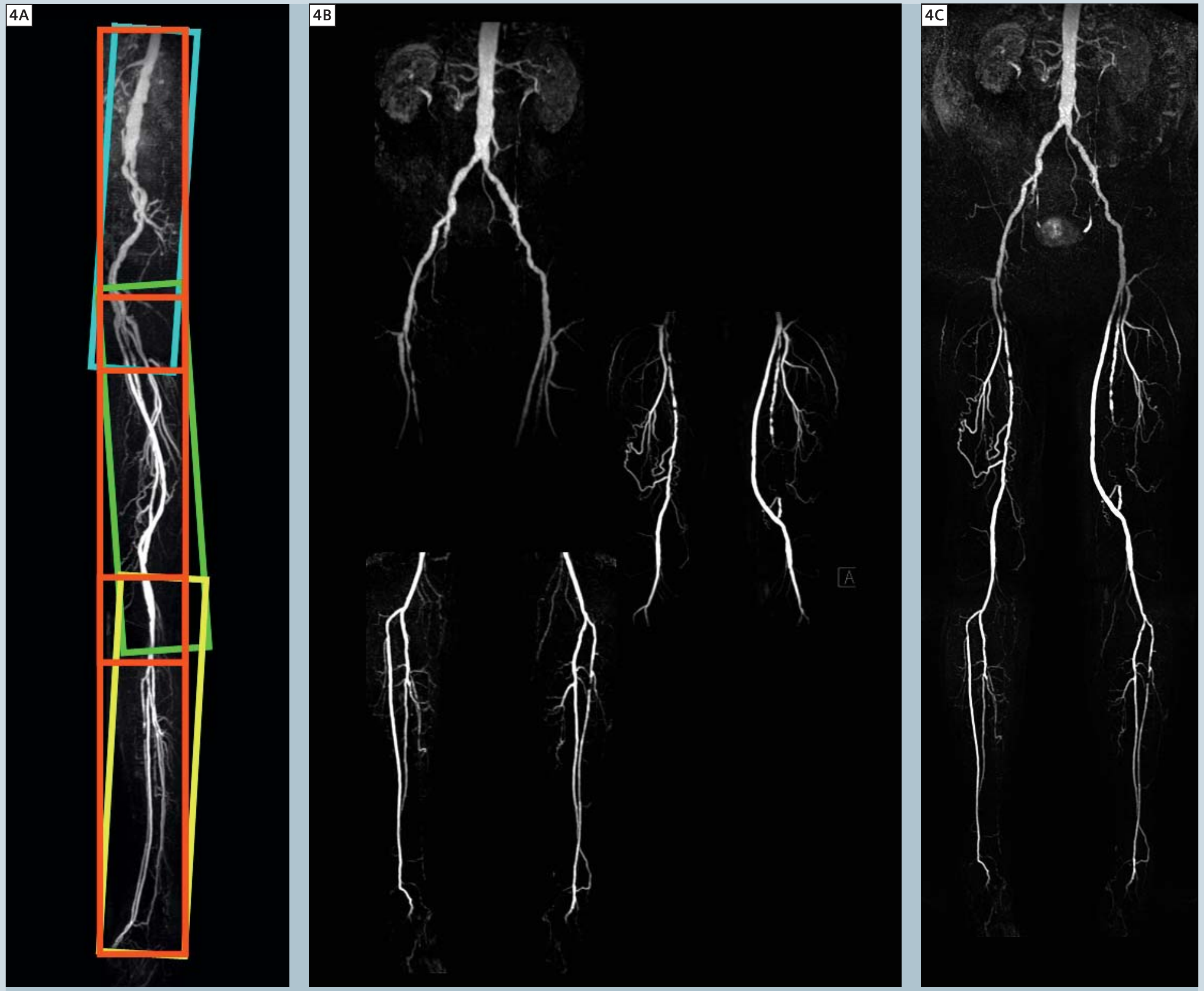

4 A composed 3D multi-step MR examination. **(A)** shows the regions of interest **(B)** their relative angulations. The resulting image provides a fast overview of the vessels **(C)**.

Be careful when planning 3D data sets as there is less leeway between angulations. While 3D data sets angled more than six degrees will compose, they may not be able to be used in any subsequent post processing such as MultiPlanar Reconstructions (MPR) or Maximum Intensity Projections (MIP). A warning will appear on screen that the images will be saved as secondary capture images. To avoid this, it is recommended to plan the sequences as straight as possible to ensure the regions will compose (Fig. 4A). This may require additional slices to include the required anatomy, but in vascular studies slice increases should not be to the detriment of accurate contrast timing (Fig. 4 B and C). Composing is a useful and rewarding post processing step applicable in almost any two or more region scans. With the use of Inline composing, original data sets can be automatically composed and saved to the database at the end of the last sequence acquisition.

Contact
Sandra Winsor
Charge Clinical MRT MRI
Centre for Advanced MRI
UniServices
University of Auckland
New Zealand
s.winsor@auckland.ac.nz

Try them on your system

Trial licenses for most of the applications featured in this issue of MAGNETOM Flash are available free of charge for a period of 90 days: Please contact your local Siemens representative for system requirements and ordering details. In the US, please visit us at **www.siemens.com/discoverMR**

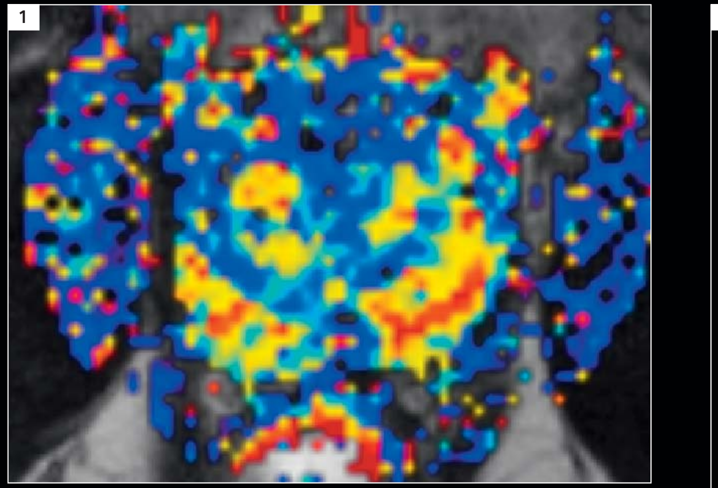

1 syngo Tissue4D visualizing and post-processing of T1-weighted dynamic 3D datasets (page 9).

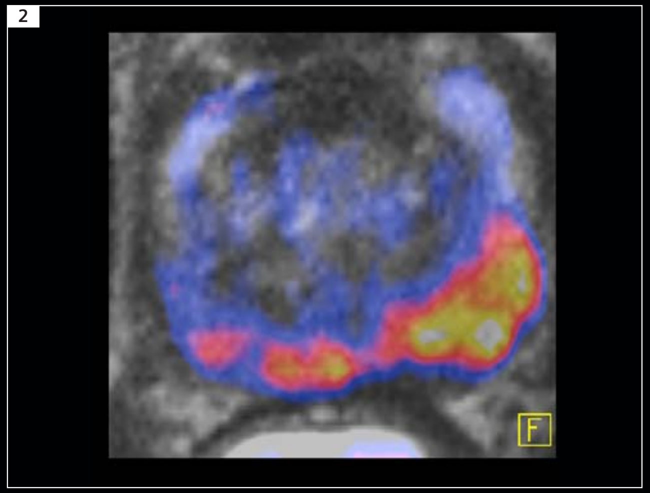

2 *syngo* Image Fusion and syngo REVEAL (Inline diffusion). EPI based diffusion-weighted imaging technique for the body (page 9).

3 *syngo* TimCT Oncology. Continuous table movement whole-body diffusion technique (page 42).

4 *syngo* SWI, susceptibility-weighted imaging helps to detect blood and iron deposits (page 51).

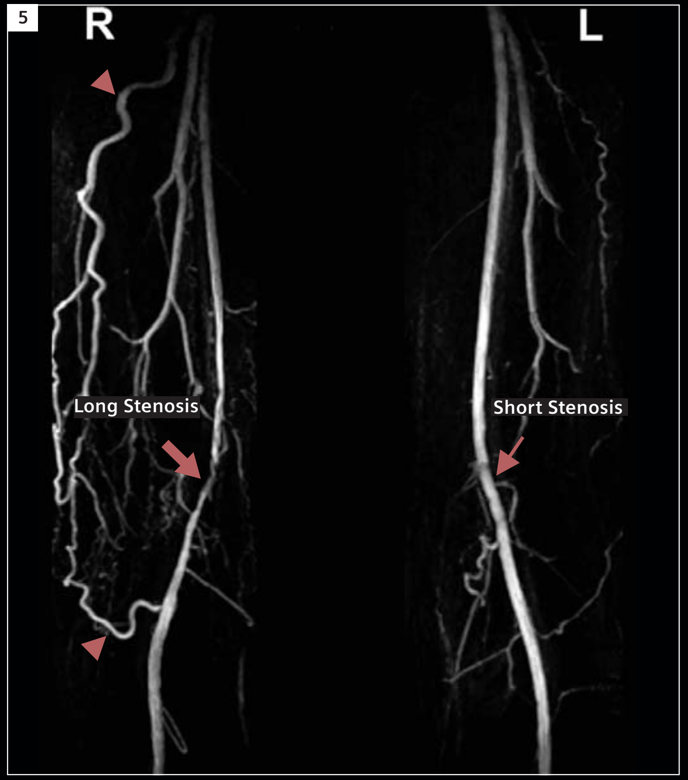

5 *syngo* NATIVE SPACE, MR Angiography (MRA) without contrast material (page 52).

32-Channel Head Coil Imaging at 3T

Thomas Benner

Athinoula A. Martinos Center for Biomedical Imaging, Department of Radiology, Massachusetts General Hospital and Harvard Medical School, Boston, MA, USA

The new 32-channel head coil for 3T provides considerable benefits over the standard Head Matrix coil. The coil sensitivity and therefore signal-to-noise ratio (SNR) is increased over the whole head [1]. Parallel imaging performance (better g-factor) is increased in any direction, including 2D acceleration for 3D imaging [2]. In practice, these advantages translate into image data with better quality where higher SNR, less distortion in EPI scans, higher resolution or shorter scan times can be traded off. All data in this report were acquired on a 3T MAGNETOM Trio, A Tim System scanner (software version *syngo* MR B15A, SP2). Two scan sessions were performed on a healthy appearing volunteer. In one session the standard 12-channel Head Matrix coil was used. In another session the 32-channel head coil was used.

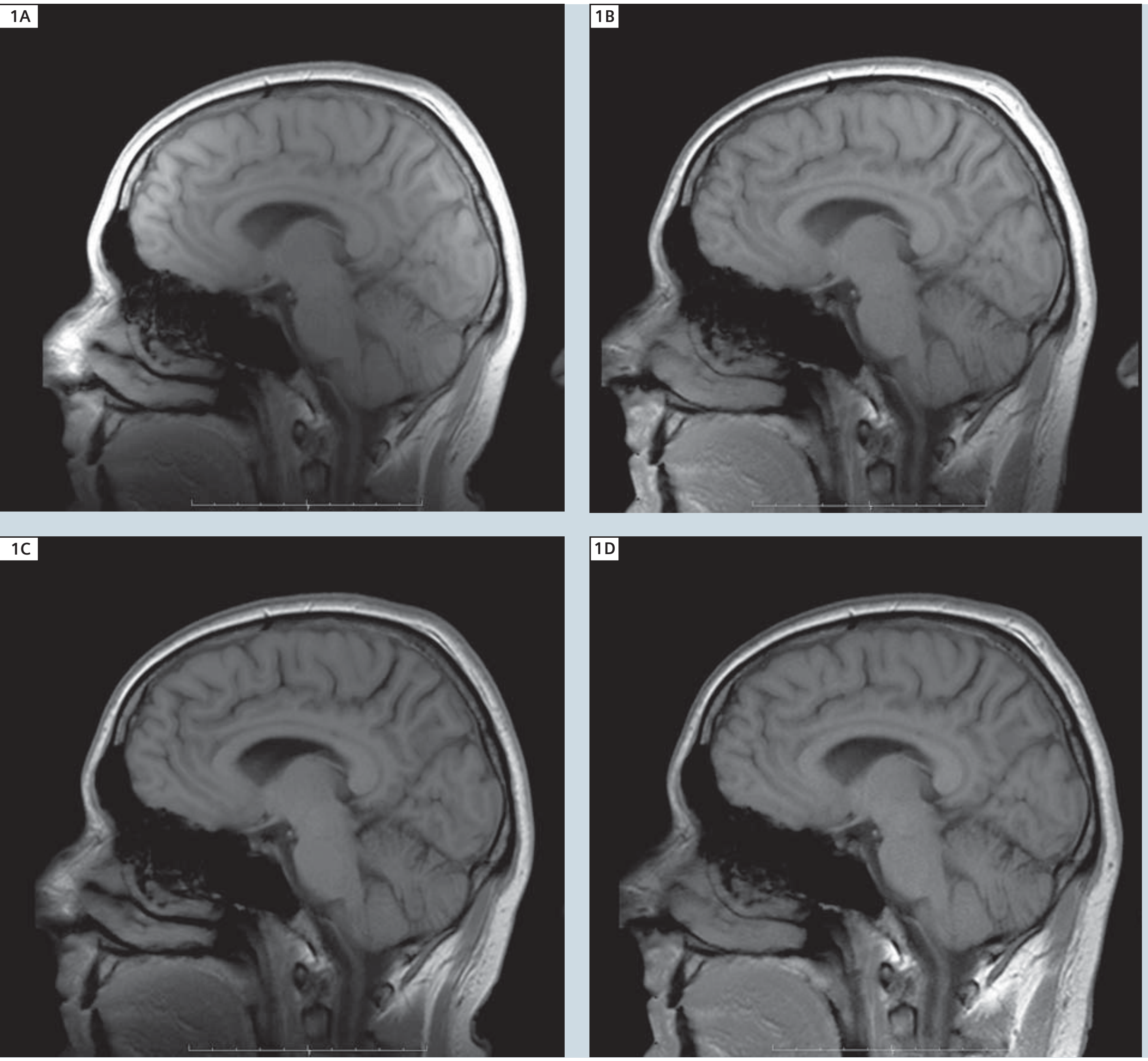

1 T1w 2D FLASH (sagittal orientation, PAT factor 2): top row: unfiltered images; bottom row: pre-scan normalized images; left column: 32-channel head coil; right column: Head Matrix coil. **32, Matrix:** T1w 2D FLASH (sagittal orientation, PAT factor 2), TR 280 ms, TE 2.57 ms, FOV 230 × 230 mm^2, matrix 256 × 256, 25 slices, slice thickness 5 mm, distance factor 20%, bandwidth 270 Hz/pixel, flip angle 70°, 1 acquisition, PAT mode GRAPPA, acceleration factor PE 2, reference lines PE 24, matrix coil mode auto (triple), reference scan mode integrated, coil combine mode adaptive combine, TA 0:39 min.

To ensure matching slice prescription, AutoAlign was run at the beginning of the session as well as in the middle of the session to adjust for potential subject motion during the study [3–5]. The following examples compare the 32-channel head coil to the Head Matrix coil in terms of image homogeneity, SNR, and parallel imaging performance.

Image homogeneity

The strong gradient of the coil sensitivities of the 32-channel head coil leads to a larger gradient of signal intensities from areas close to the coil elements to areas more distant from the coil elements as compared to the Matrix coil. Therefore, application of the pre-scan normalize filter is essential for homogeneous signal intensities over the whole scan volume. As can be seen from

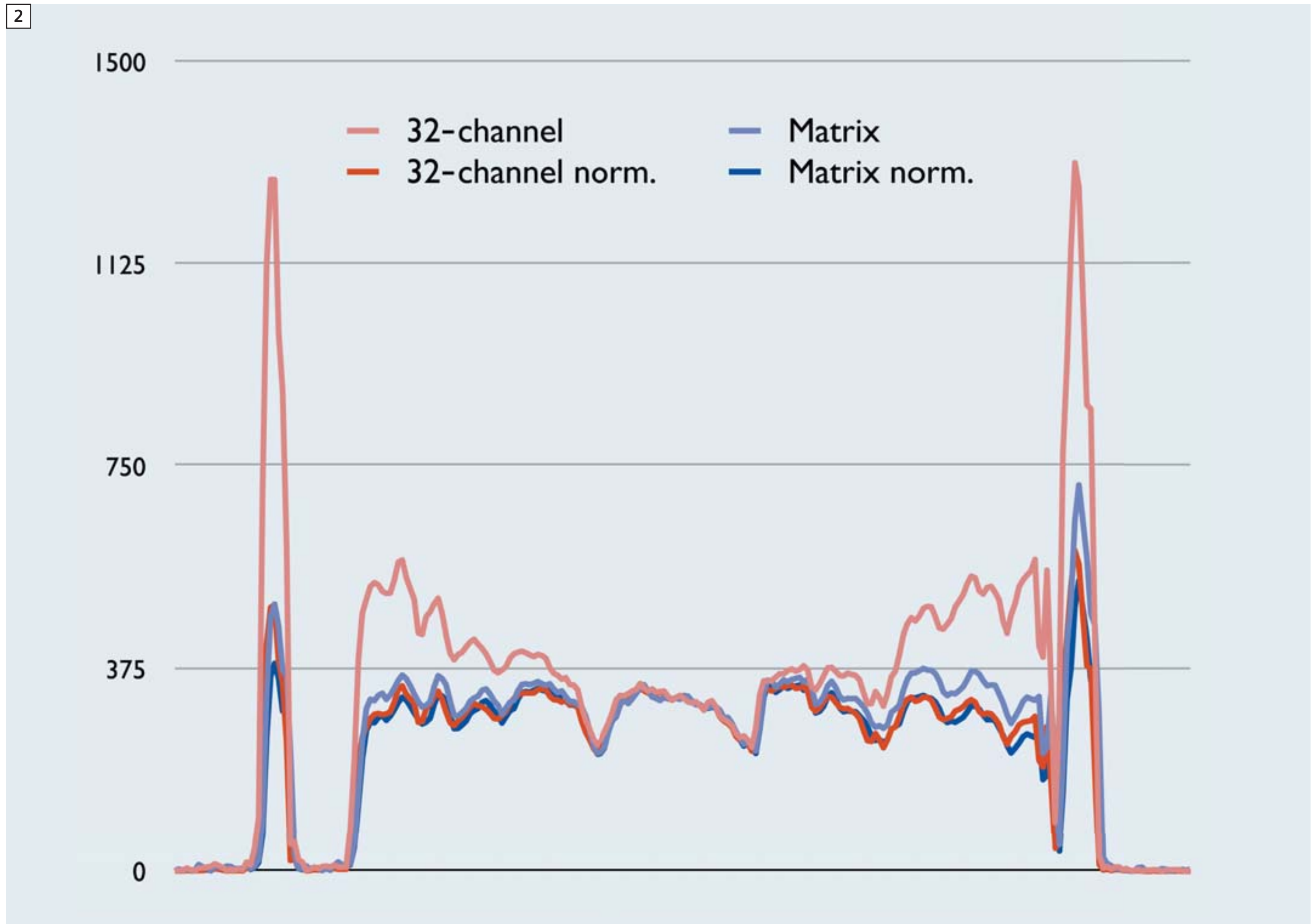

2 T1w 2D FLASH (sagittal orientation, PAT factor 2); horizontal signal intensity profiles for the center row of the images shown in Fig. 1, normalized to the mean signal intensity of the middle 16 pixels. Note the close match of the signal intensity profiles between 32-channel head coil and Head Matrix coil, demonstrating how well pre-scan normalize works. It also shows the very good performance of AutoAlign to align the slice prescription from one session to the other.

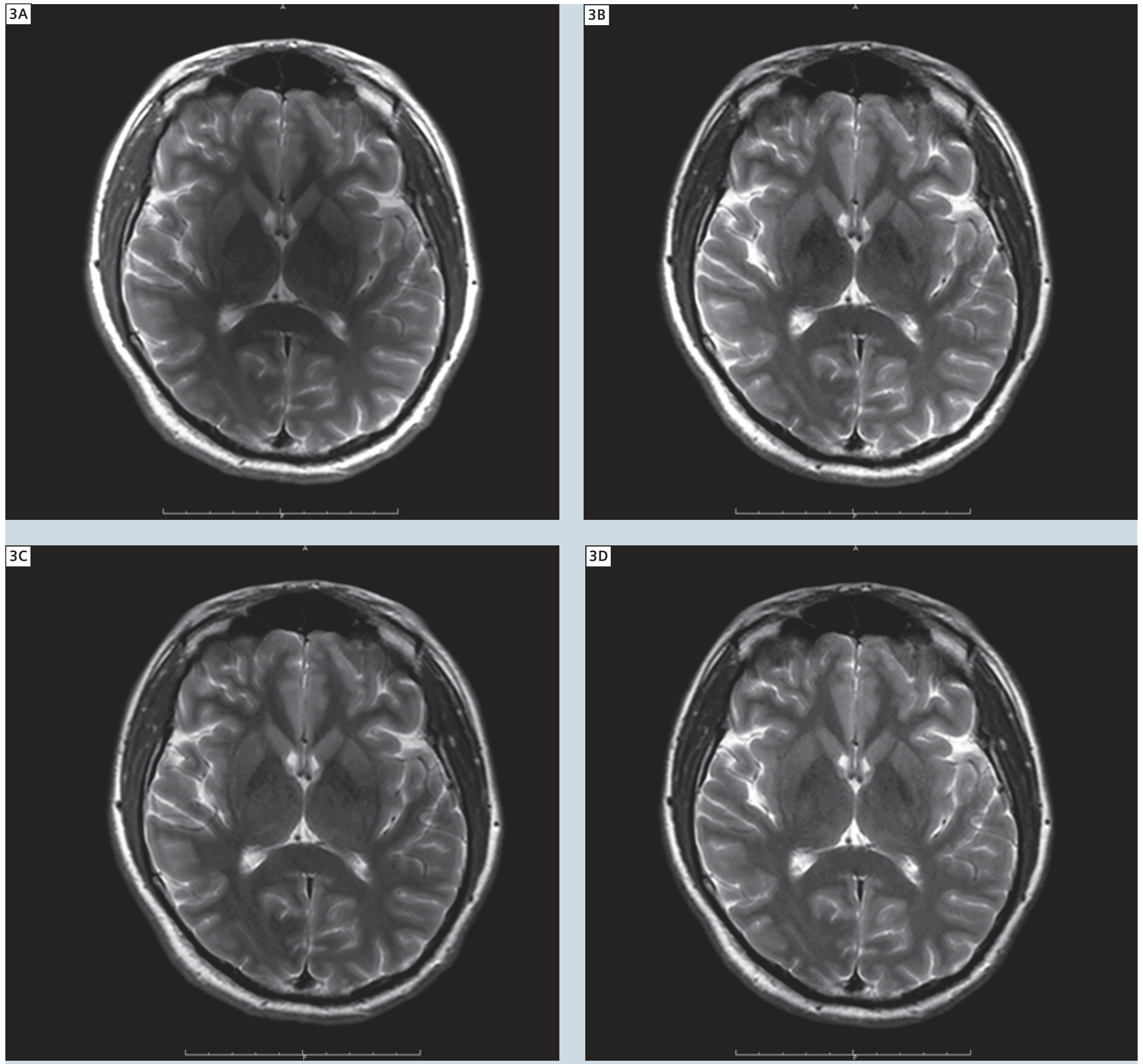

3 T2w TSE (transversal orientation, PAT factor 2); top row: unfiltered images; bottom row: pre-scan normalized images; left column: 32-channel head coil; right column: Head Matrix coil. **32, Matrix:** T2w TSE (transversal orientation, PAT factor 2, TR 6210 ms, TE 84 ms, FOV 220 × 192.5 mm², matrix 256 × 224, 25 slices, slice thickness 5 mm, distance factor 20%, bandwidth 260 Hz/pixel, flip angle 120°, turbo factor 26, 1 acquisition, PAT mode GRAPPA, acceleration factor PE 2, reference lines PE 35, matrix coil mode auto (triple), reference scan mode integrated, coil combine mode adaptive combine, TA 0:39 min.

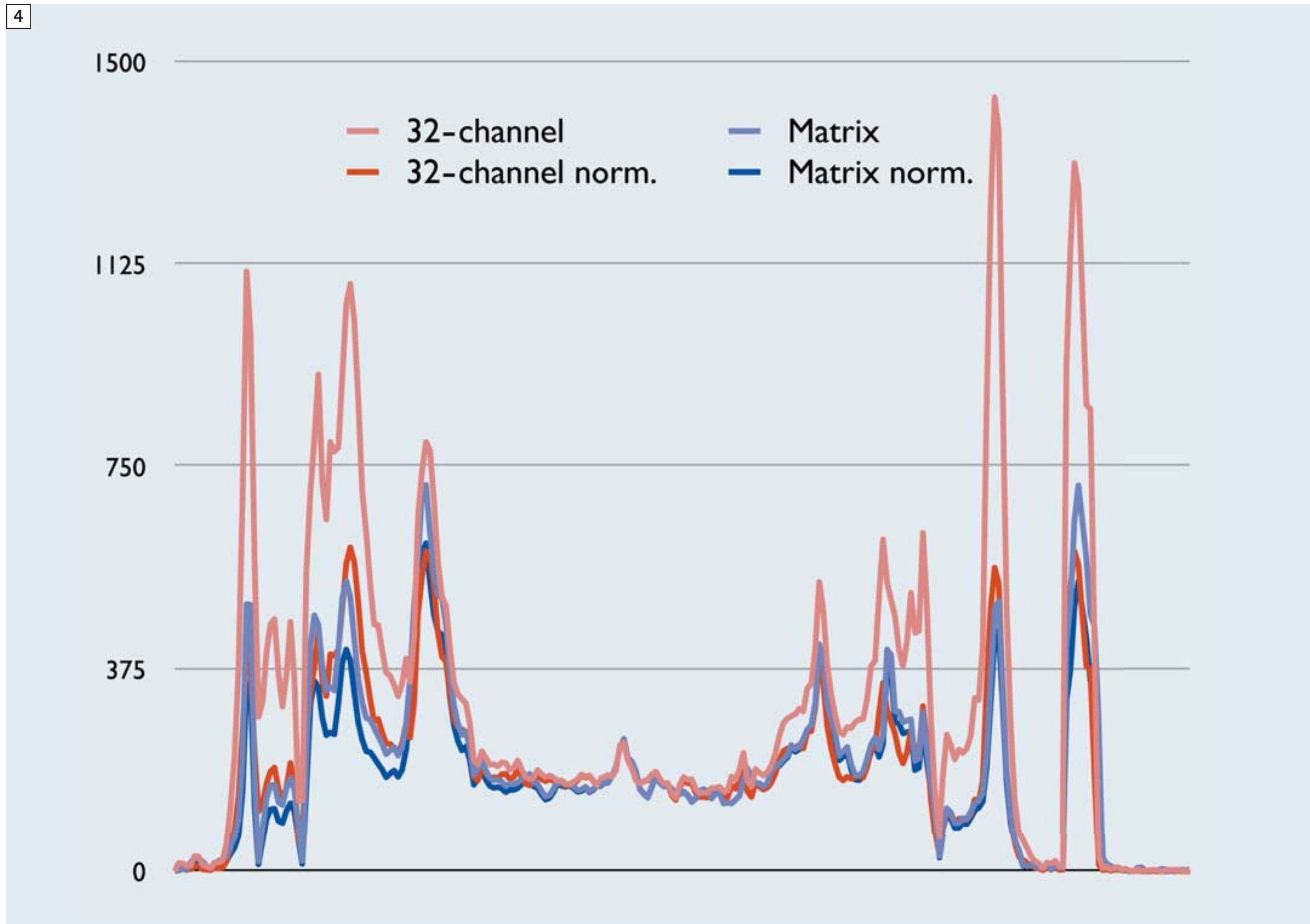

4 T2w TSE (transversal orientation, PAT factor 2; horizontal signal intensity profiles for the center row of the images shown in Fig. 3, normalized to the mean signal intensity of the middle 16 pixels. Note the close match of the signal intensity profiles between 32-channel head coil and Head Matrix coil, demonstrating how well pre-scan normalize works. It also shows the very good performance of auto-align to align the slice prescription from one session to the other.

Figures 1–4, the pre-scan normalize filter works well for both head coils. In case of the 32-channel head coil where the signal intensities become very high towards the periphery of the brain, application of the pre-scan normalize filter results in a flattened signal intensity profile very similar to that of the Head Matrix coil after application of the pre-scan normalize filter. Note, though, that the SNR gain of the 32-channel coil is retained. In comparison, the pre-scan normalize filter has little effect on the images from the Matrix coil.

SNR

Compared to the Head Matrix coil the SNR of the 32-channel head coil is ~20% better at the center of the brain and at least 100% better at the periphery of the brain [1]. The improved SNR can be easily appreciated in Fig. 5. A gradient of SNR from the periphery to the center of the brain can be seen for both coils. Increasing the PAT factor from 2 to 3 causes a drop in SNR that is more noticeable when using the Matrix coil, especially in the center of the brain, demonstrating the better g-factor of the 32-channel head coil.

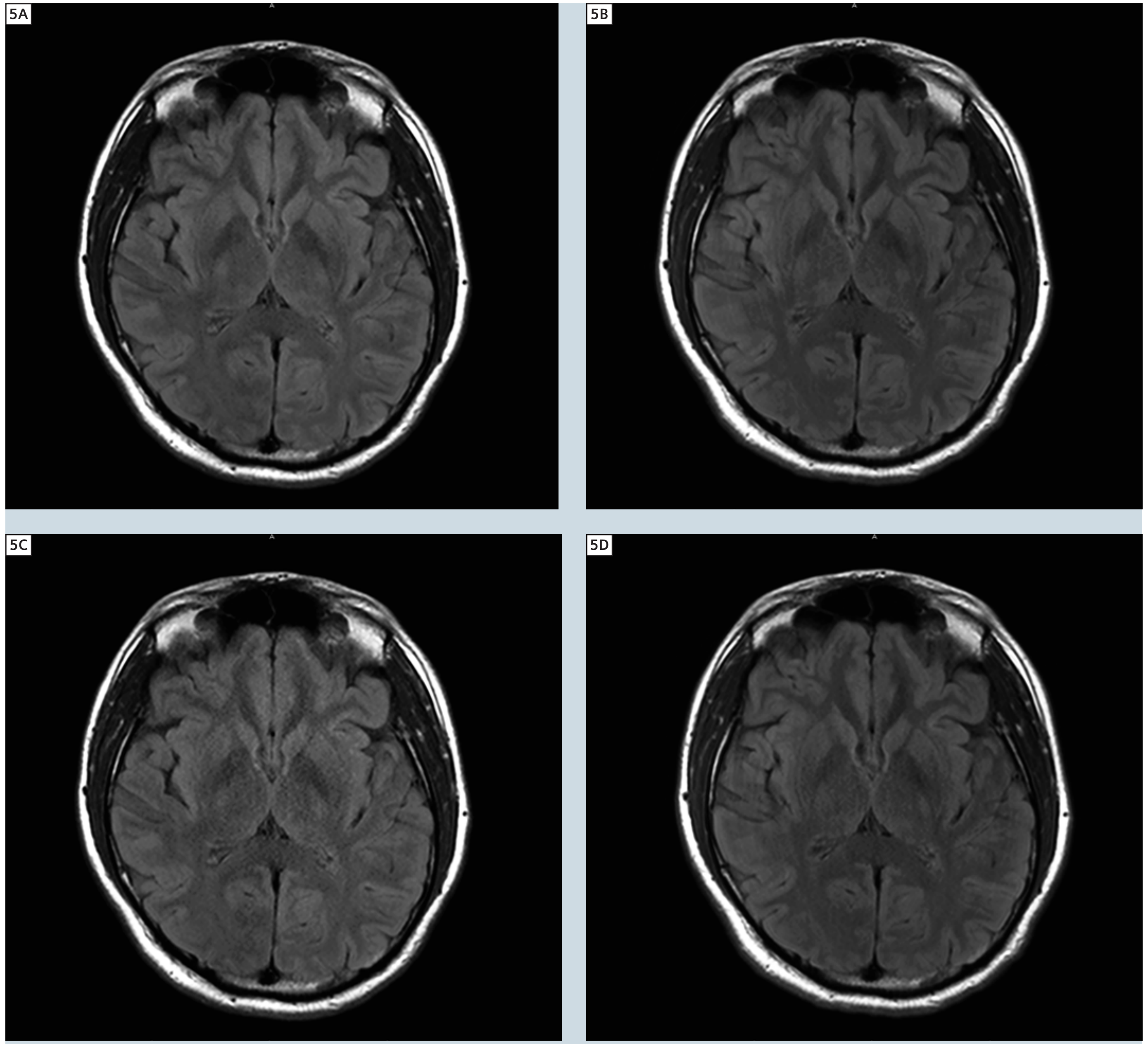

5 T2w TIRM (DarkFluid, transversal orientation, PAT factor 2 / 3); top row: PAT 2; bottom row: PAT 3; left column: 32-channel head coil; right column: Head Matrix coil. **32, Matrix:** T2w TIRM (DarkFluid, transversal orientation, PAT factor 2), TR 7000 ms, TE 81 ms, TI 2500 ms, FOV 220 × 192.5 mm^2, matrix 256 × 224, 25 slices, slice thickness 5 mm, distance factor 20%, bandwidth 271 Hz/pixel, flip angle 120°, turbo factor 16, 1 acquisition, 2 concatenations, PAT mode GRAPPA, acceleration factor PE 2, reference lines PE 31, matrix coil mode auto (triple), reference scan mode integrated, coil combine mode adaptive combine, pre-scan normalize filter, TA 2:08 min; **32, Matrix:** T2w TIRM (DarkFluid, transversal orientation, PAT factor 3), same as above but for: acceleration factor PE 3, reference lines PE 32, TA 1:40 min.

While image quality (SNR) is better when using the 32-channel head coil compared to Head Matrix coil at an PAT factor of 2, the difference becomes much more obvious when using an PAT factor of 2×2 (Fig. 6). Image quality of the PAT 2×2 scan with the 32-channel head coil (scan time 2:42 min) is comparable to the image quality of the PAT 2 scan with the Head Matrix coil (scan time 4:43 min) i.e. a 43% reduction of scan time can be achieved without image quality loss.

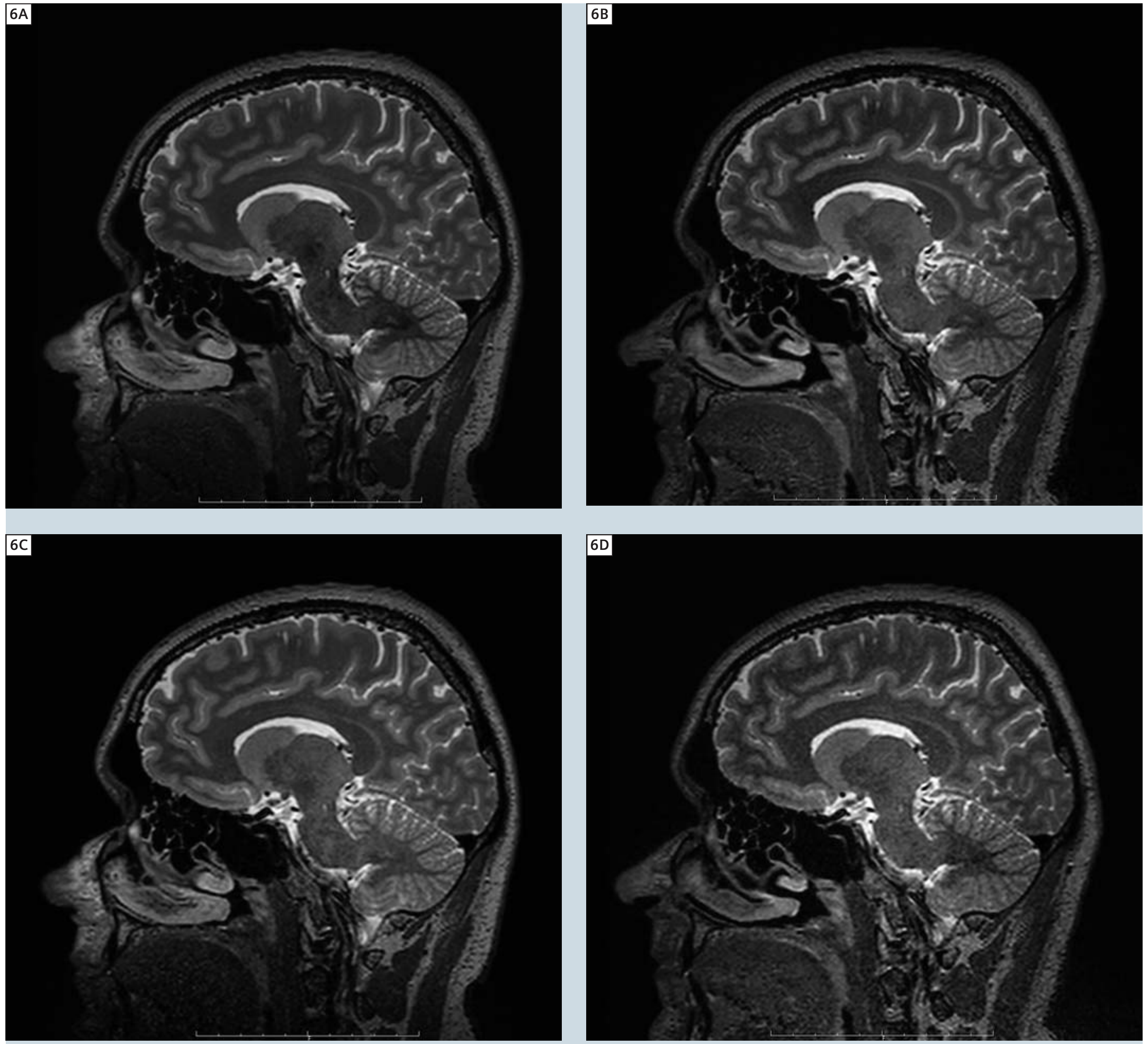

6 Isotropic T2w 3D SPACE (sagittal orientation, PAT factor 2 / 2x2); top row: PAT 2; bottom row: PAT 2×2; left column: 32-channel head coil; right column: Head Matrix coil. **32, Matrix:** Isotropic T2w 3D SPACE (sagittal orientation, PAT factor of 2), TR 3200 ms, TE 403 ms, FOV 250 × 250 mm^2, matrix 256 × 256, 176 slices per slab, slice thickness 1 mm, bandwidth 751 Hz/pixel, turbo factor 141, 1 acquisition, PAT mode GRAPPA, acceleration factor PE 2, reference lines PE 24, acceleration factor 3D 1, matrix coil mode auto (triple), reference scan mode integrated, coil combine mode adaptive combine, pre-scan normalize filter, TA 4:43 min; **32, Matrix:** Isotropic T2w 3D SPACE (sagittal orientation, PAT factor 2x2), same as above but for: acceleration factor 3D 2, reference lines 3D 24, TA 2:42 min.

Parallel imaging

Figures 7 and 8 demonstrate parallel imaging performance of the two head coils with increasing PAT factor for DTI (Diffusion Tensor Imaging) scans. At a PAT factor of 4 the image data becomes unusable for the Matrix coil while the 32-channel coil still provides reasonable image quality. Image quality of the 32-channel head coil data with PAT factors 3 and 4 compares well with image quality of the Matrix coil at PAT factors 2 and 3, respectively. The figures also show a decrease in distortions with increasing PAT factor because of the shorter EPI readout. Scan times are 0:41 min, 0:41 min and 0:49 min for PAT factors of 2, 3 and 4, respectively. In the case of EPI, scan times are not reduced with increasing PAT factor as is typically the case for non EPI scans. This is due to the increased number of PAT reference scans that are required with higher PAT factors.

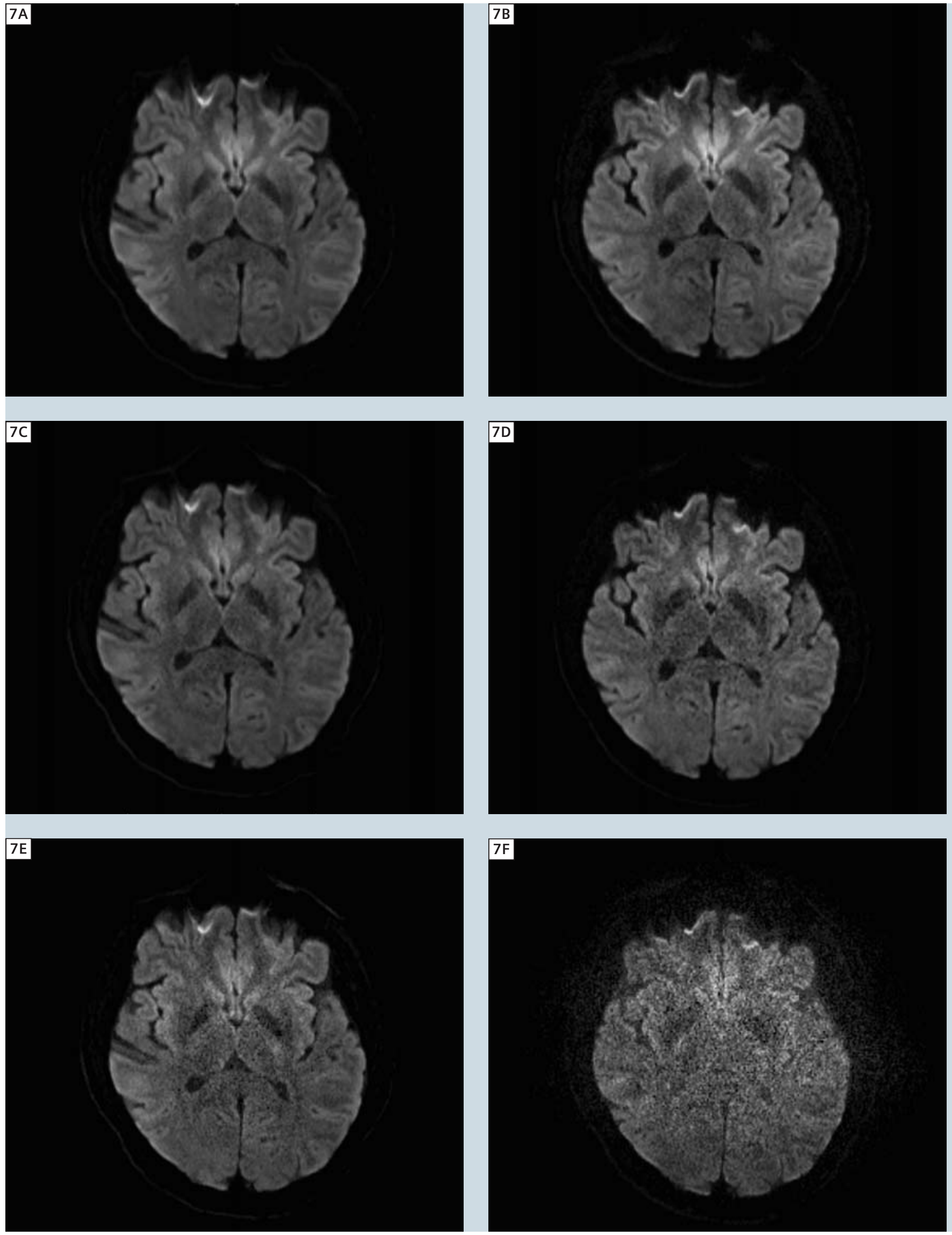

7 Diffusion-weighted imaging (DWI) 2D EPI (transversal orientation, 6 diffusion directions (MDDW), PAT factor 2 / 3 / 4); top row: PAT 2; middle row: PAT 3; bottom row: PAT 4; left column: 32-channel head coil; right column: Head Matrix coil. **32, Matrix:** DWI 2D EPI (transversal orientation, 6 diffusion directions (MDDW), PAT factor 2), TR 3900 ms, TE 94 ms, FOV 220 × 220 mm^2, matrix 192 × 192, phase partial Fourier 6/8, 25 slices, slice thickness 5 mm, distance factor 20%, bandwidth 1184 Hz/pixel, 1 acquisition, 2 diffusion weightings, b1 0 s/mm^2, b_2 1000 s/mm^2, 6 diffusion directions, PAT mode GRAPPA, acceleration factor PE 2, reference lines PE 40, matrix coil mode auto (triple), reference scan mode separate, coil combine mode adaptive combine, pre-scan normalize filter, TA 0:41 min; **32, Matrix:** DWI 2D EPI (transversal orientation, 6 diffusion directions (MDDW), PAT factor 3), same as above but for: acceleration factor PE 3, reference lines PE 48, TA 0:41 min; **32, Matrix:** DWI 2D EPI (transversal orientation, 6 diffusion directions (MDDW), PAT factor 4), same as above but for: acceleration factor PE 4, reference lines PE 128, TA 0:49 min.

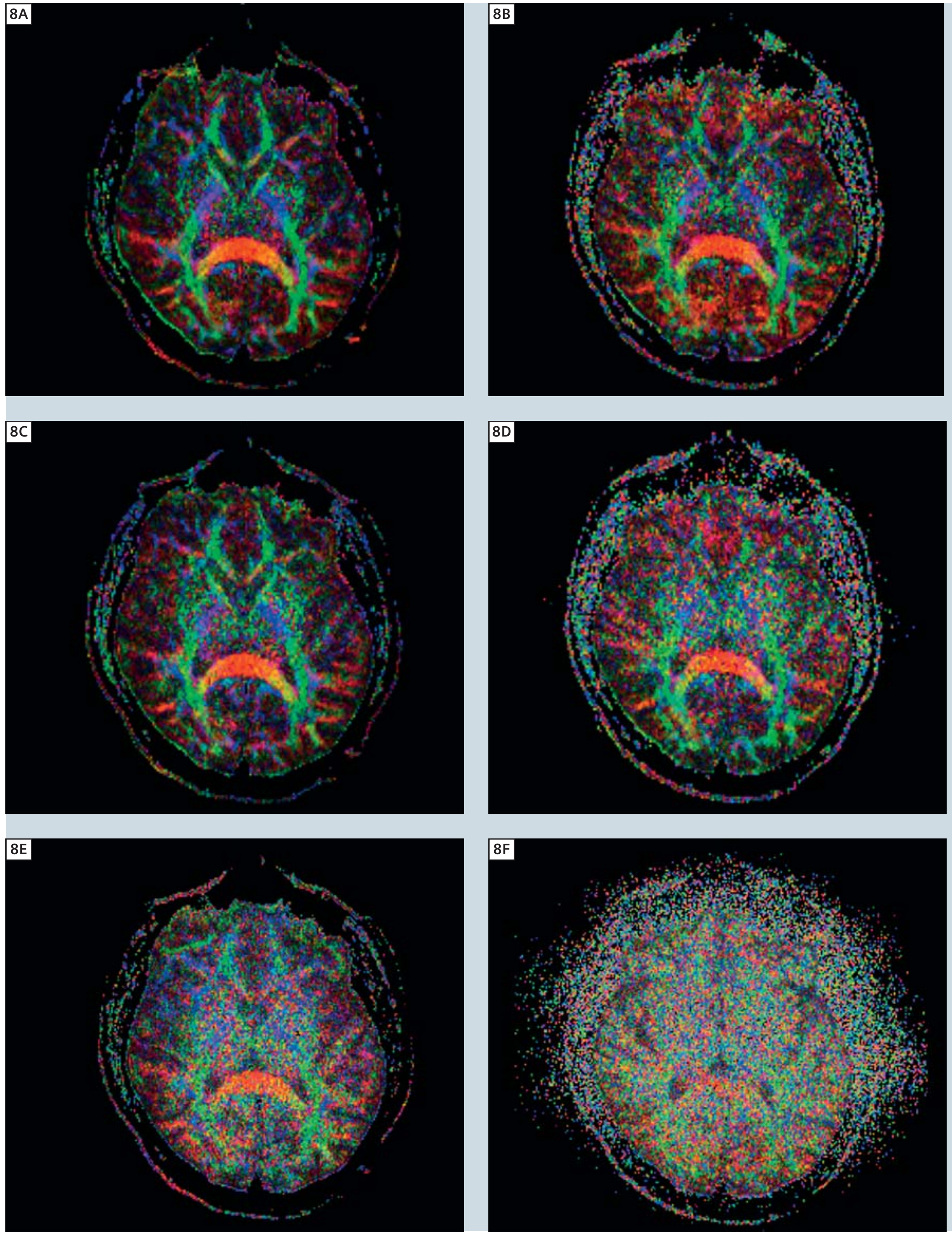

8 Diffusion-weighted imaging (DWI) 2D EPI (transversal orientation, 6 diffusion directions (MDDW), PAT factor 2 / 3 / 4); top row: PAT 2; middle row: PAT 3; bottom row: PAT 4; left column: 32-channel head coil; right column: Head Matrix coil. **32, Matrix:** DWI 2D EPI (transversal orientation, 6 diffusion directions (MDDW), PAT factor 2), TR 3900 ms, TE 94 ms, FOV 220 × 220 mm^2, matrix 192 × 192, phase partial Fourier 6/8, 25 slices, slice thickness 5 mm, distance factor 20%, bandwidth 1184 Hz/pixel, 1 acquisition, 2 diffusion weightings, b1 0 s/mm^2, b_2 1000 s/mm^2, 6 diffusion directions, PAT mode GRAPPA, acceleration factor PE 2, reference lines PE 40, matrix coil mode auto (triple), reference scan mode separate, coil combine mode adaptive combine, pre-scan normalize filter, TA 0:41 min; **32, Matrix:** DWI 2D EPI (transversal orientation, 6 diffusion directions (MDDW), PAT factor 3), same as above but for: acceleration factor PE 3, reference lines PE 48, TA 0:41 min; **32, Matrix:** DWI 2D EPI (transversal orientation, 6 diffusion directions (MDDW), PAT factor 4), same as above but for: acceleration factor PE 4, reference lines PE 128, TA 0:49 min.

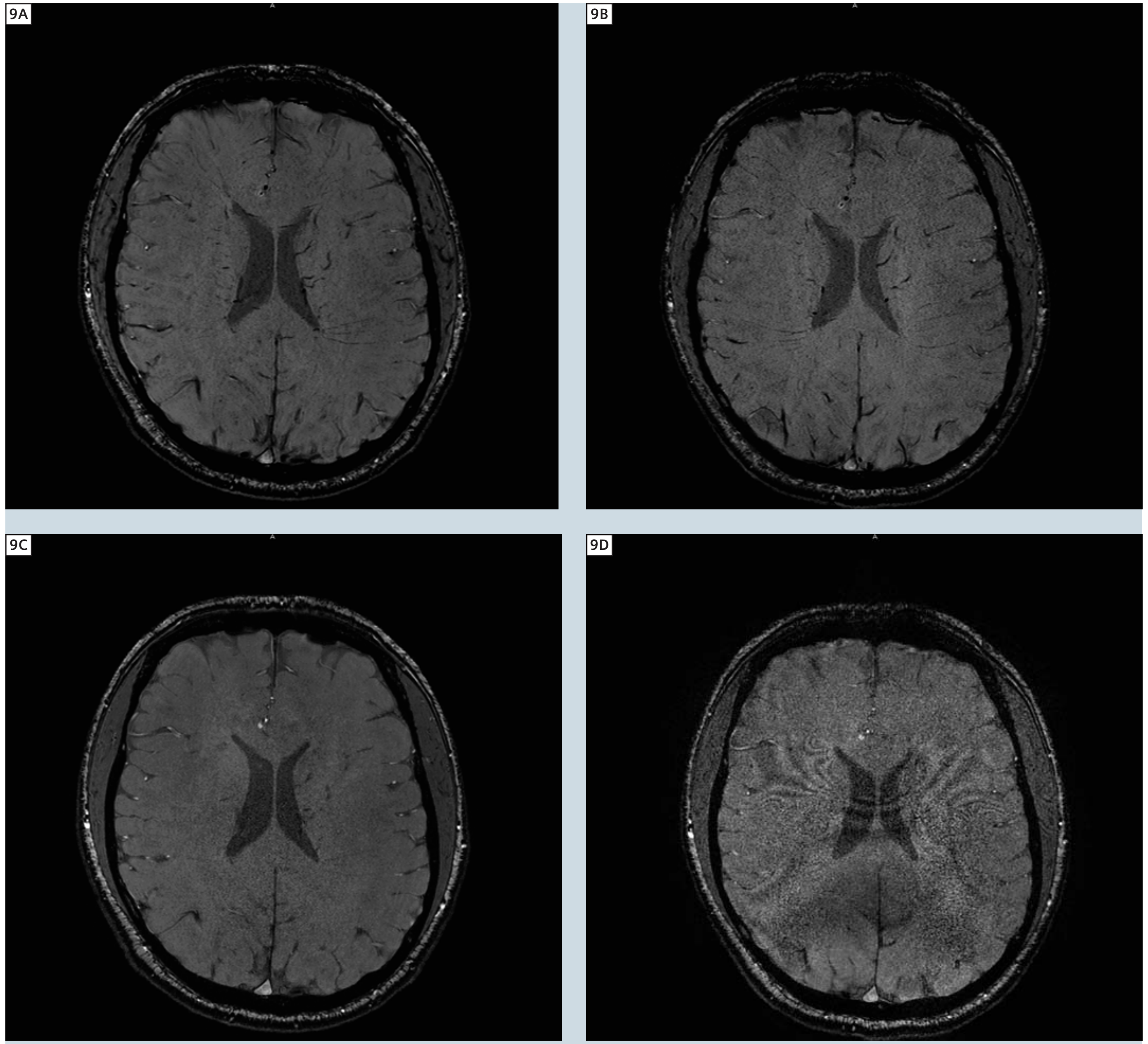

9 Susceptibility-weighted imaging (SWI) 3D FLASH (transversal orientation, PAT factor 2): PAT 2; bottom row: PAT 2x2; left column: 32-channel head coil; right column: Head Matrix coil. **32, Matrix:** SWI 3D FLASH (transversal orientation, PAT factor 2), TR 28 ms, TE 20 ms, FOV 230 × 179.6 mm², matrix 448 × 297, 72 slices per slab, slice thickness 1.2 mm, slice oversampling 22.2%, bandwidth 120 Hz/pixel, flip angle 15°, 1 acquisition, PAT mode GRAPPA, acceleration factor PE 2, reference lines PE 24, acceleration factor 3D 1, matrix coil mode auto (triple), reference scan mode integrated, coil combine mode adaptive combine, pre-scan normalize filter, TA 6:38 min; **32, Matrix:** SWI 3D FLASH (transversal orientation, PAT factor 2x2), same as above but for: acceleration factor 3D 2, reference lines 3D 24, TA 3:17 min.

32-channel head coil.

Figure 9 again demonstrates the better g-factor of the 32-channel head coil compared to the Head Matrix coil. While image quality is acceptable when using the Matrix coil at PAT 2, it becomes unacceptable when using an acceleration factor of 2×2. At this setting, the 32-channel head coil still performs well. At similar image quality, a 50% reduction of scan time from 6:38 min to 3:17 min is achievable with the 32-channel head coil.

Conclusions

The 32-channel head coil provides better performance compared to the Head Matrix coil in terms of SNR and parallel imaging capabilities. The SNR is improved over the whole head with the periphery of the brain benefitting the most.
Because of the almost 3x number of coil elements, parallel imaging performance is improved i.e. the acceleration factor can be increased without imaging artifacts and with an SNR that is comparable to that of the Matrix coil at a lower PAT factor. It should also be noted that acceleration is possible in any direction with the 32-channel head coil since the coil elements are distributed on a helmet shaped geometry, thereby allowing arbitrary slice prescriptions without having to consider the direction of the acceleration.
Because of the helmet shaped form that conforms closely to the head, the 32-channel head coil has the disadvantage that some subjects with large head circumference will not be able to fit into the coil and will have to be scanned using the Matrix coil instead. Image reconstruction times can be slightly increased as well when using the 32-channel head coil since about 3 times the data volume has to be processed. However, this is not a problem in routine imaging when using the high-end image reconstruction computer.

References

1 Stapf J. 32-Channel Phased-Array Head Coil for 1.5T and 3T. MAGNETOM Flash 1/2008, 45.
2 Wald LL; Wiggins G. Highly Parallel Detection for MRI. MAGNETOM Flash 1/2008, 34–44.
3 van der Kouwe AJ, Benner T, Fischl B, Schmitt F, Salat DH, Harder M, Sorensen AG, Dale AM. On-line automatic slice positioning for brain MR imaging. Neuroimage. 2005 Aug 1;27(1):222–230.
4 Benner T, Wisco JJ, van der Kouwe AJ, Fischl B, Vangel MG, Hochberg FH, Sorensen AG. Comparison of manual and automatic section positioning of brain MR images. Radiology. 2006 Apr;239(1):246–254.
5 Scott KT. Software Compensation for Patient Position Enabling Reproducible Slice Positioning – AutoAlign. MAGNETOM Flash 1/2006, 98–103.

Contact
Thomas Benner
Athinoula A. Martinos Center
for Biomedical Imaging
Dept. of Radiology
Massachusetts General Hospital
and Harvard Medical School
Boston, MA
USA
benner@nmr.mgh.harvard.edu

New with *syngo* MR B17: *syngo* Native – Non Contrast MR Angiography Techniques

Peter Weale

Siemens Medical Solutions, Inc., Cardiovascular Research and Development, Chicago, IL, USA

With the need to carefully consider the risk vs. benefit of contrast agent administration with the advent of Nephrogenic Systemic Fibrosis (NSF), as well as the need to perform cost effective MR studies, there is a demand for improved methods for performing angiography using intrinsic rather than extrinsic contrast mechanisms.

To address this need, with the release of software version *syngo* MR B17 comes *syngo* Native encompassing two new methods of non contrast MRA exploiting new methods for generating angiographic contrast.

The two varieties of Native are Native TrueFISP and Native SPACE – the former being more appropriate for abdominal imaging and the latter for peripheral arterial evaluation.

syngo Native TrueFISP

syngo Native TrueFISP is a new technique which enables the visualization of blood which flows into a vascular territory after preparation of the imaging volume with an inversion recovery pulse.

The sequence is derived from the 3D TrueFISP sequence which is regularly used for coronary angiography and has the benefit of 1D PACE for respiratory synchronization. Alternatively the respiratory cushion can be used which allows more flexibility and choice in the method of synchronization.

If 1D PACE is used ECG triggering can be added for additional improvements in image quality.

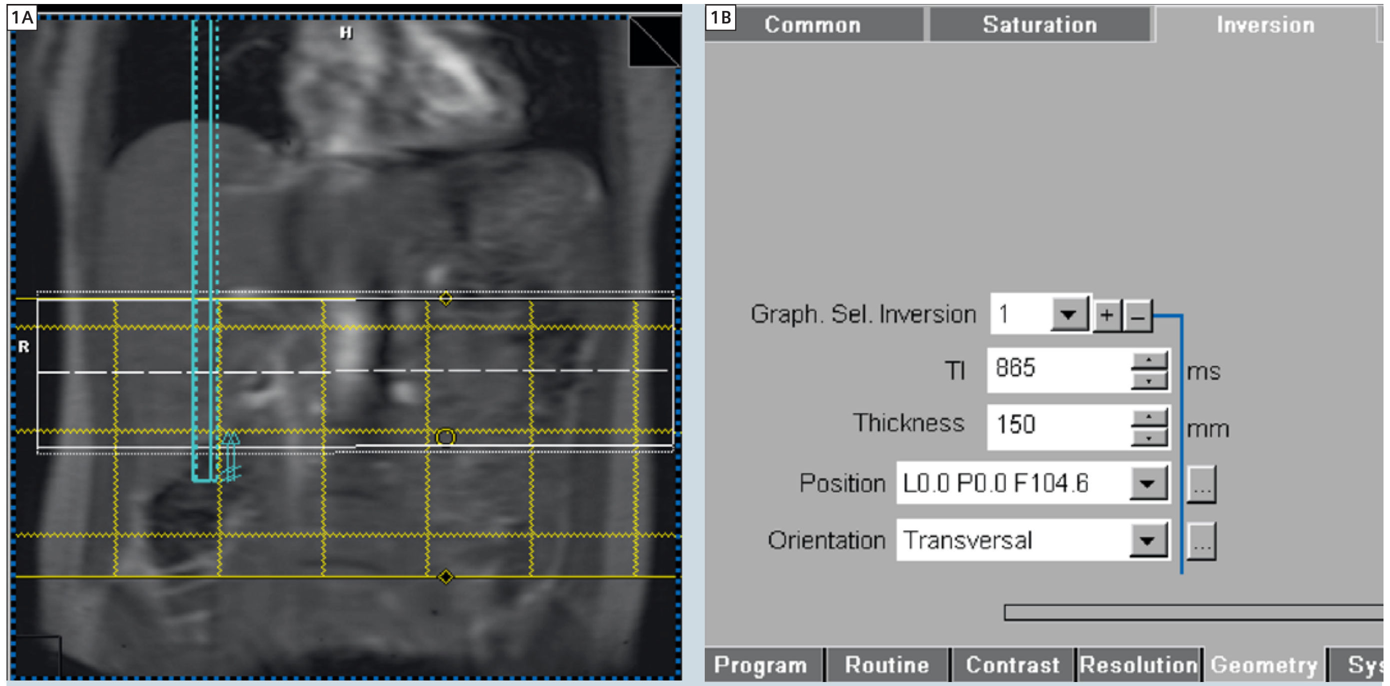

Graph. Sel. Inversion 1

TI 865 ms

Thickness 150 mm

Position L0.0 P0.0 F104.6

Orientation Transversal

1 The *syngo* Native TrueFISP regional saturation with control of inversion time and geometry for up to four independent graphically positioned inversion preparation regions. The new graphic elements depicting the position of the inversion region are also shown.

2 Coronal 3D *syngo* Native TrueFISP with freely positionable inversion preparation positioned over the renal arteries – an additional inversion preparation area was positioned inferior to reduce signal from the inflow of non-inverted blood in the IVC. Spatial resolution 1.3 x 1.2 x 0.9 mm (65% slice resolution). Total scan time with 1D PACE (efficiency 38%) – ECG Gated 5:30 min. In this subject with good cardiac output a successful result is achieved with an Inversion time of 850 ms.

Native TrueFISP introduces a novel element to the user interface for *syngo* MR – regional inversion preparation. In a similar manner to regional saturation, the user can now use freely positionable regional inversion preparation (Fig. 1). Up to four different inversion preparation regions can be prescribed – this flexibility means that the user can tailor the preparation to different approaches and to different vascular territories. The sequence flexibility allows 2D and 3D approaches and various different methods for labeling the inflowing blood – for example by inverting either the inflowing blood or the vascular bed into which it is flowing.

Many of these new approaches remain to be explored and we expect that, in the near future, many variations of this method will appear as the possibilities become clear.

Until now the main application of Native TrueFISP has been the evaluation of abdominal arteries, particularly the renal arteries. It has also been shown to be a good method for evaluation of transplanted kidneys where the lack of motion enables the scan to be completed quickly – a time efficient method for evaluating these patients where other methods may be contraindicated.

The basic method behind the generation of contrast is that the vascular territory of interest is inverted and during the inversion time there is inflow of non-inverted blood. This blood gives rise to a high signal when the TrueFISP scan is executed after the inversion time.

This reliance on in-flow means that the method requires consideration of additional inputs into scan optimization, for example, a relatively healthy 25-year-old patient with good cardiac function would most likely fill the renal arterial tree with the blood ejected within a single heart beat. However, in an elderly patient with heart failure, the volume of blood available to fill the vessel of interest most likely will be smaller and in these patients more careful planning of the inversion preparation and extended inversion times, to allow longer for inflow, may be necessary.

syngo Native TrueFISP is a flexible method and can be applied to many vascular territories. The underlying limiting factor in this method is the volume of blood entering the inverted target region within an inversion time. The maximum inversion time which can be used is limited by the recovery of the magnetization of the targeted area – in practice this means a maximum TI of around 1400 ms can be used without intolerable loss of contrast.

The use of this technique has been successfully applied in renal angiography as well as in the assessment of transplanted kidneys to rule out anastomotic stenosis [1, 2].

syngo Native SPACE

The second new angiographic method introduced with *syngo* Native is Native SPACE. This approach exploits the difference in signal between data acquired when blood flow is minimal and when it is maximal. The Native SPACE user interface allows two sequential measurements of a high resolution 3D SPACE sequence with different ECG trigger times. Inline subtraction and maximum intensity projections allow a seamless workflow. Scan planning and processing

3

3 *syngo* Native TrueFISP performed in an arteriopath patient with bilateral renal artery stenosis. *(Courtesy of Dr. G. Houston, S. Gandy, Ninewells Hospital, Dundee, Scotland)*

4A

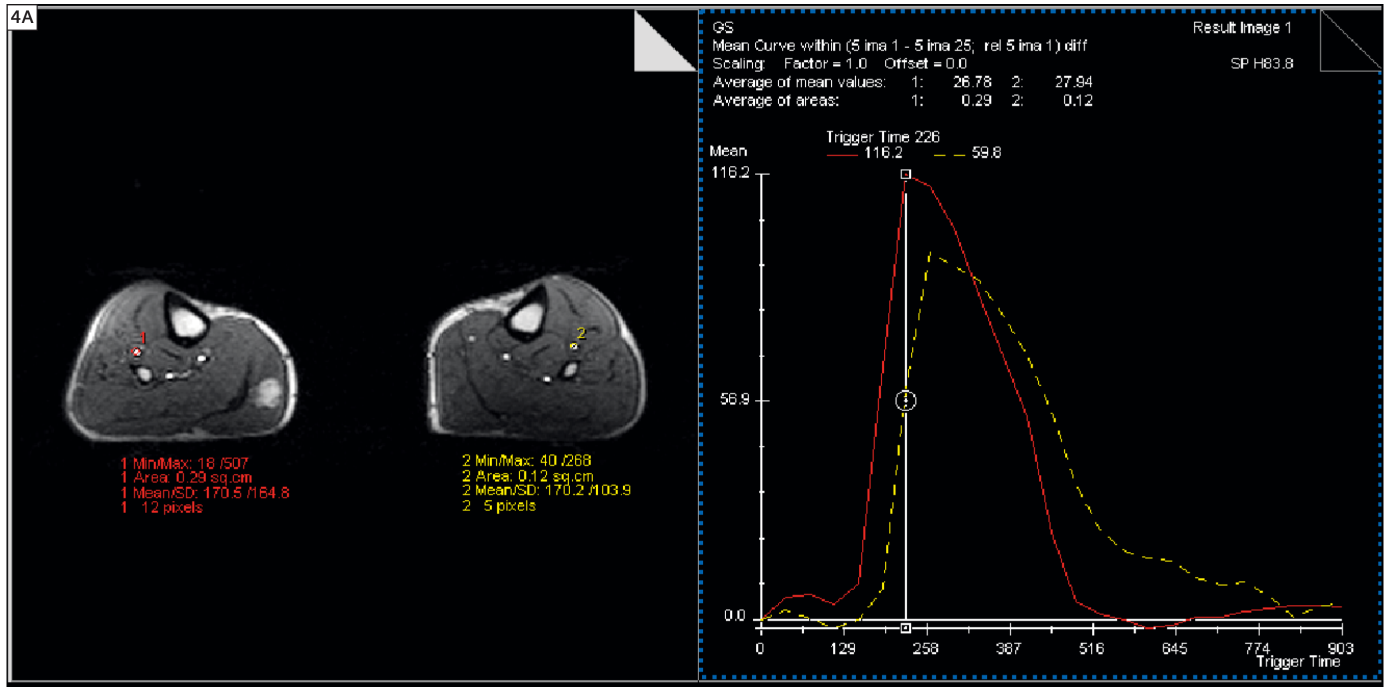

```
GS                                                          Result Image 1
Mean Curve within (5 ima 1 - 5 ima 25;  rel 5 ima 1) diff
Scaling:   Factor = 1.0   Offset = 0.0                        SP H83.8
Average of mean values:   1:    26.78   2:    27.94
Average of areas:         1:     0.29   2:     0.12
```

```
1 Min/Max: 18 /507
1 Area: 0.29 sq.cm
1 Mean/SD: 170.5 /164.8
1   12 pixels
```

```
2 Min/Max: 40 /268
2 Area: 0.12 sq.cm
2 Mean/SD: 170.2 /103.9
2   5 pixels
```

4B

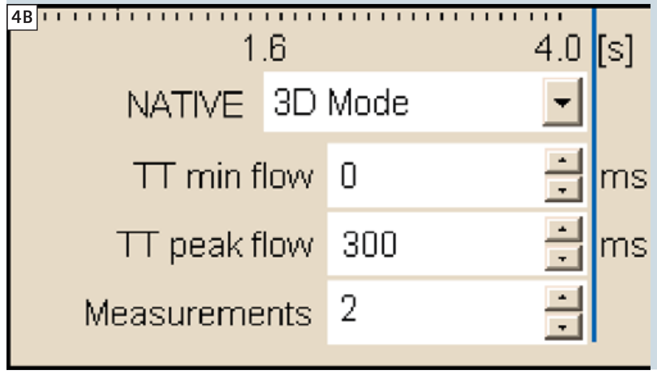

NATIVE: 3D Mode

TT min flow: 0 ms

TT peak flow: 300 ms

Measurements: 2

4 Cross sectional cine imaging in the region of interest allows determination of times of maximal and minimal flow within the cardiac cycle. This information can also be useful in determining the presence of asymmetric flow or complete absence of pulsatility which would decrease the likelihood of successful visualization of the vessel in this area.

is very similar to current angiographic techniques. Typical scan times are around three to four minutes per anatomical location (depending on heart rate).
Success with *syngo* Native SPACE depends on the accurate identification of the fast and slow flow times in relation to the trigger source (typically ECG is used). This is easily achieved with a simple cine FLASH sequence which is performed with the slice oriented perpendicular to the flow direction. Evaluation of this in "Mean Curve" allows precise detection of the fast and slow flow periods which can be used directly as input into the trigger delay times for fast and slow flow (Fig. 4).
The contrast generating mechanism, therefore, depends on the maintenance of a degree of pulsatility in the vessel of interest – if this disappears or is significantly attenuated the method may be challenging. However it seems that in many cases of chronic ischemic disease pulsatility is maintained to a sufficient degree, even in collateral vessels, to generate sufficient contrast.
It should be kept in mind that there may be cases where the pulsatility which this technique relies on may not be present – in which case the visualization of the vessel of interest may not be possible.

Summary

syngo Native SPACE and *syngo* Native TrueFISP are complimentary methods for MR angiography. Native SPACE being more appropriate in areas where large fields of view are required and where the area of interest is stationary (to accommodate the subtraction necessary for this method). Native TrueFISP is more suited to imaging of abdominal vessels where the integration of respiratory and cardiac synchronization can be of benefit. Native TrueFISP is a targeted method where the vascular anatomy which is demonstrable is determined by the volume of blood entering the prepared territory whereas Native SPACE requires pulsatility in the vessel to visualize it. An understanding of the basic contrast mechanisms will enable appropriate choice of sequence and appropriate choice of scan parameters to produce optimal image quality.

5

5 Maximum intensity projection of composed three-station study. Typical achievable resolution is 0.9 x 0.9 x 1.5 mm with scan times around three to four minutes per station, depending upon heart rate.

References

1 Non-Contrast Enhanced Renal MR Angiography Using NATIVE TrueFISP Initial Experience for Clinical Imaging of Patients with Renovascular Disease <http://cds.ismrm.org/protected/09Presentations/404/>. S Gandy et al Oral Presentation 404, ISMRM 2009. Hawaii.

2 Renal transplant: nonenhanced renal MR angiography with magnetization-prepared steady-state free precession. Liu et al. Radiology. 2009 May;251(2):535-42.

Contact
Peter Weale
Siemens Medical Solutions USA, Inc.
Cardiovascular Research and Development
737 N Michigan Ave.
STE 1600
Chicago, IL 60611USA
peter.weale@siemens.com

What's New for Cardiac in Software Version *syngo* MR B17

Peter Weale

Siemens Medical Solutions USA, MR RD Cardiac Collaborations, Hoffman Estates, IL, USA

The *syngo* MR B17 software release for MAGNETOM Tim systems brings some exciting new features and some minor “tweaks” which together will further strengthen your capabilities in the cardiovascular imaging arena.

tPAT

The major innovation with this software release is the introduction of tPAT as an alternative method for parallel imaging in the case of time resolved acquisitions using the *syngo* BEAT sequence.
tPAT (temporal parallel acquisition technique) uses a different method of collecting the data for the coil sensitivity map as compared to iPAT (integrated parallel acquisition technique). For cardiac imaging, tPAT is therefore resulting in an achieved acceleration factor which always matches the nominal acceleration selected.

How is this achieved? In iPAT the coil sensitivity map is created by acquiring additional data in the center of k-space which slightly reduces the achieved acceleration. For example in the case of a scan where 192 phase-encoding steps are required, for the final reconstruction, if an iPAT acceleration factor of 2 is chosen to shorten scan time, then the system will measure 192 / 2 = 96 lines plus some additional lines in the center of k-space for the coil sensitivity map – for example an additional 12 phase encode steps may be measured, which, in this example would result in an achieved acceleration of approximately 1.8.
In a tPAT acquisition the extra lines required for a fully sampled central k-space region for the coil sensitivity map are not created by collecting extra k-lines but by using lines from other time points in a time resolved sequence (e. g. cine or dynamic) to reconstruct the sensitivity map. This is achieved by ensuring that, for example in the case of an acceleration factor of two, alternate phases in the time resolved sequence acquire different phase encoding steps – e. g. odd steps for the first frame, even steps from the second frame, and so on. Then it is possible to combine the data from adjacent, or indeed all the frames in the time resolved data to generate a fully sampled coil sensitivity map without the need to acquire additional data (Fig. 1). Although the temporal resolution of the sensitivity maps is decreased due to line sharing between neighboring frames, the temporal resolution of the reconstructed images is not decreased because each frame is reconstructed separately.

1

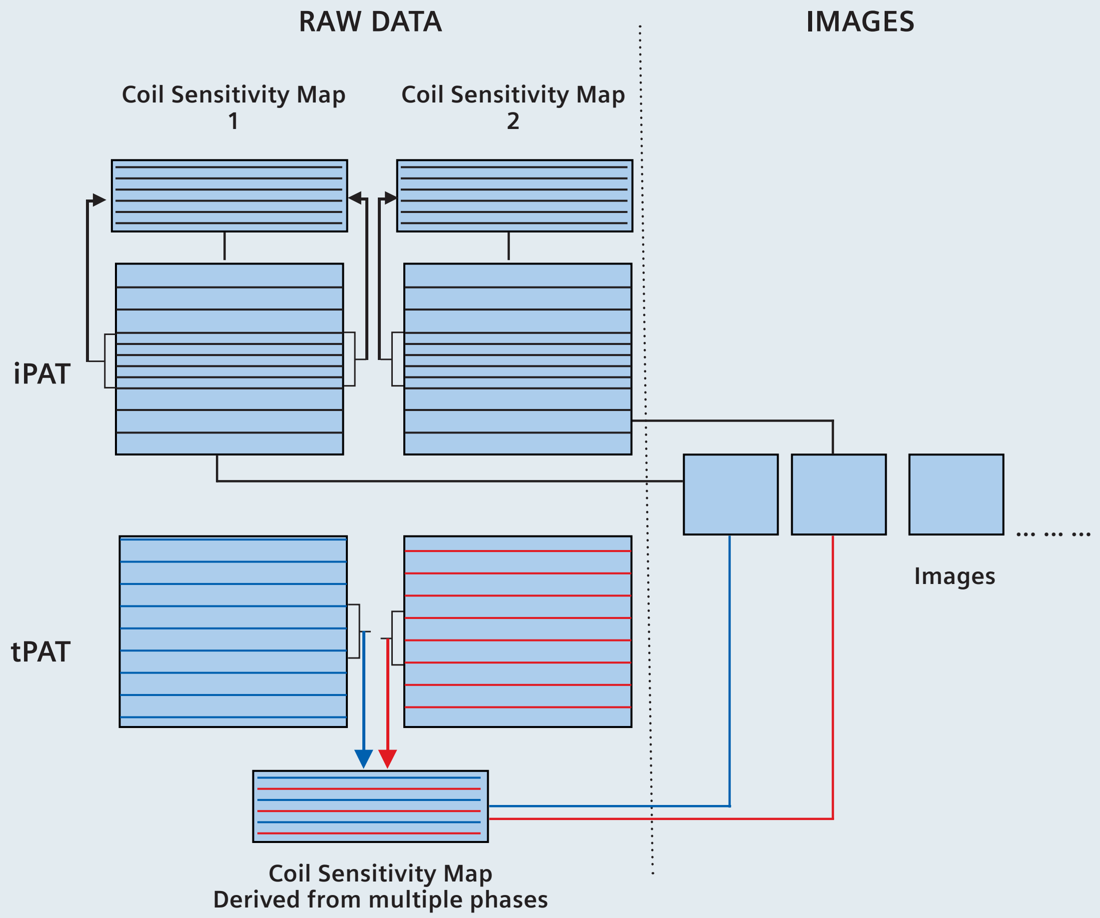

1 A simplified illustration of the essential differences between iPAT (above) and tPAT (below) – additional data is needed for every image in iPAT but not for tPAT. When high acceleration factors are selected this difference results in significant time saving either in “shot time” in single shot dynamic imaging or total scan time in segmented sequences.

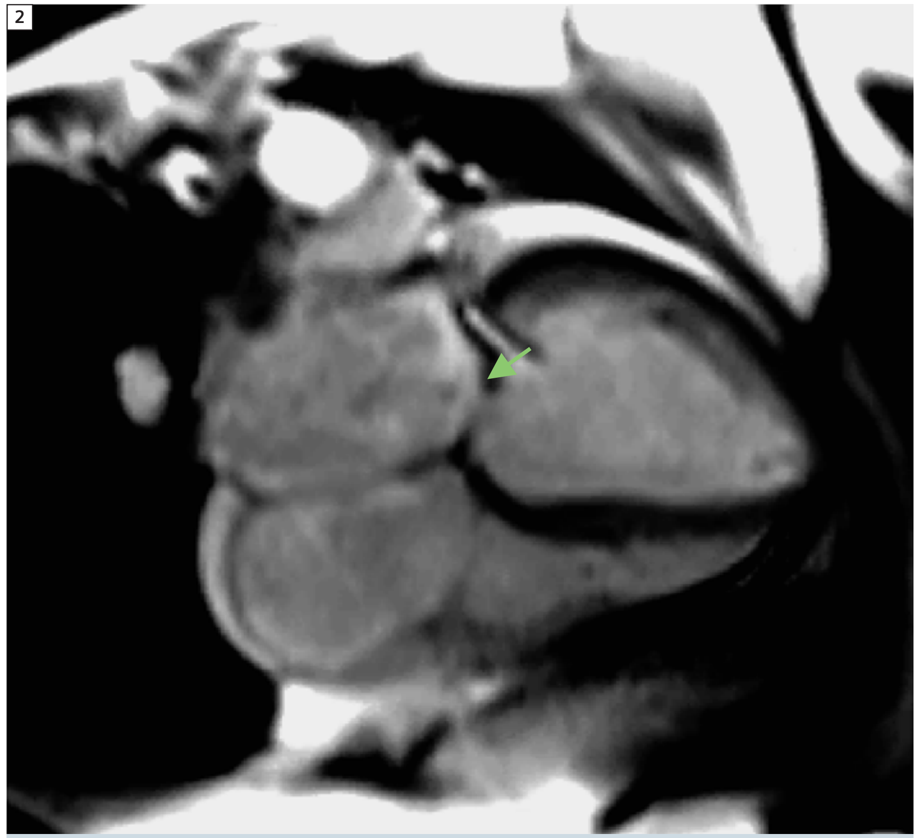

2 Single image from a real-time true-FISP cine study acquired during free breathing in this patient with temporal resolution of 49 ms. This is achieved by using the new t-PAT function to accelerate the imaging – reasonable spatial resolution is also achievable as demonstrated by the excellent depiction of the mitral regurgitation (arrow) in this subject.

Where is tPAT useful? In any situation where the data acquired is acquired in a “time resolved ” manner – this would include cine sequences (segmented with prospective triggering and “real time”) and where the same scan is repeated frequently to monitor a dynamic process (e. g. the protocols contained in the Heart/Dynamic protocols on the system). However, tPAT is only available when the protocol is based on the “BEAT” or CV sequence.
For segmented cine sequences tPAT is not compatible with retrospective gating.

GRE EPI readout for *syngo* BEAT

For additional flexibility we have introduced a new readout in the *syngo* BEAT sequence which can be used for dynamic studies. The new approach uses a segmented Echo Planar readout scheme which supplements the existing gradient echo and TrueFISP schemes. All these methods are typically used with a saturation recovery pulse to impart T1 contrast to these single shot sequences. GRE EPI allows a shorter total shot duration for the same spatial resolution and is potentially more robust against motion during the readout as well as providing the potential of increased anatomical coverage.

Sequence preparation with “dummy heart beats” for ECG gated TrueFISP cine MRI

Until now the use of ECG triggered TrueFISP cine sequences has entailed the use of a preparation heart beat or “dummy heart beat” where the sequence is run to establish a steady state before the imaging data is acquired.
This is a significant overhead in real time imaging as the total breathhold duration is equivalent to twice the number of acquired slices. It has been shown that the slight change in contrast which is observed during the first image or two is not so great that it detracts from the visualization of cardiac motion. Depending on the clinical demands, the user is now able to decide if this preparation with a “dummy heart beat” is essential or not. If not, for example, a multi-slice, real time, short axis study of the left ventricle can now be completed in total breathhold duration of half that previ-

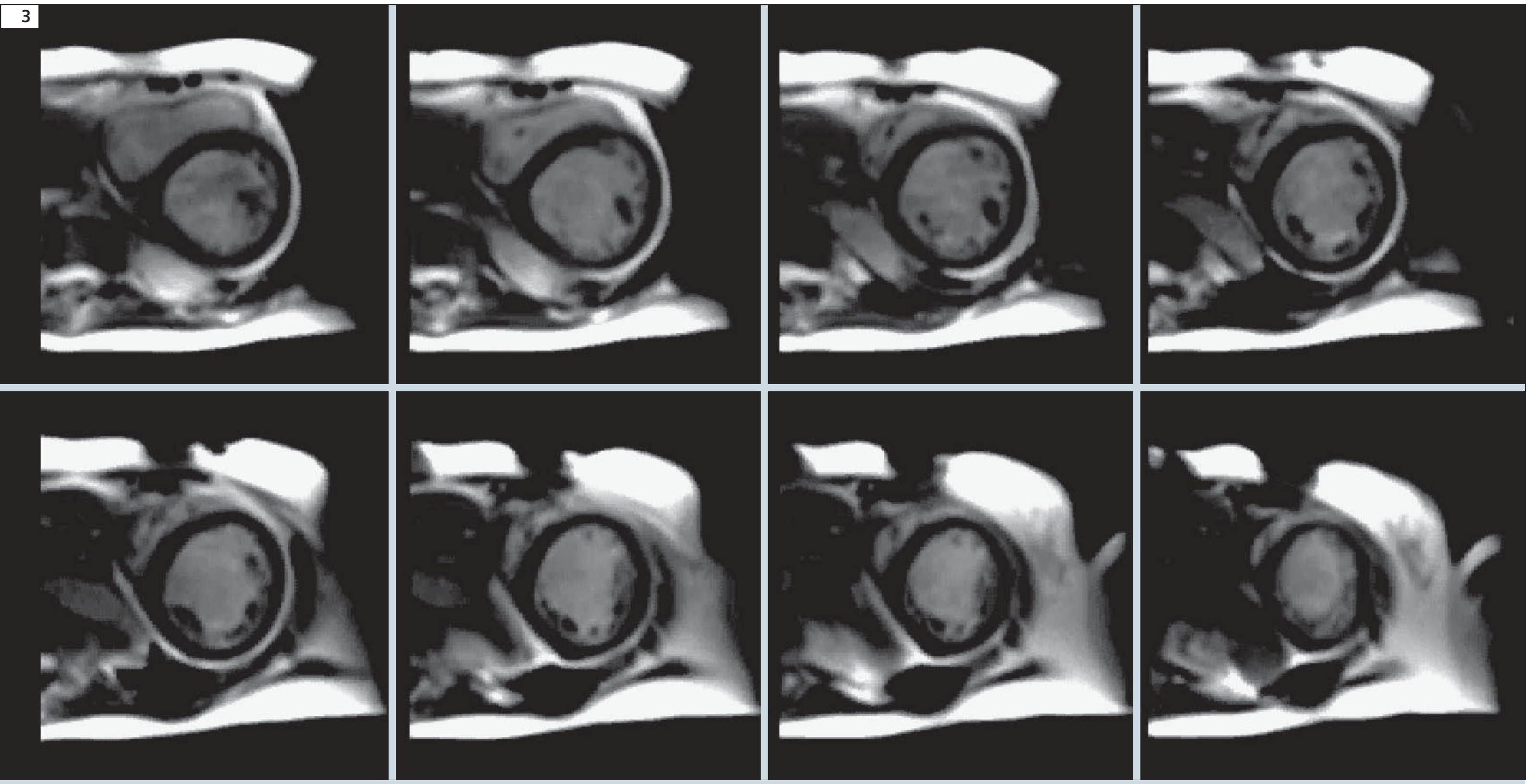

3 In this claustrophobic patient with shortness of breath the tPAT accelerated multi slice real time imaging allowed speedy evaluation of cardiac function. The complete scan was achieved in 10 heart beats for the 10 slices acquired (8 representative slices shown). The ability to perform studies of this quality in such a short time can reduce the number of failed examinations due to breathholding limitations and patient tolerance.

ously achievable. This is a clear benefit especially for patients with dyspnea, a not uncommon condition in cardic imaging.

Other new features

Some smaller features are introduced with the aim of improving image quality. It is now possible to select if the phase-encoding rewinder is used or not in the dynamic Turbo FLASH protocols – this allows the user to trade off speed of data acquisition against slightly compromised image quality – this is especially true if the operator chooses to use high flip angles in these protocols.
To help with planning scans using the 1D PACE option (mainly coronary imaging) the behavior of the graphics relating to the positioning of the navigator is changed so that the head to foot off-center position is taken from the graphics during positioning so that if the center of the navigator is placed on the diaphragm this will be the center of the search position in the PACE card. This is of high relevance for a precise and fast set-up especially if the diaphragm position is off-set from the isocenter.

Contact
Peter Weale
Siemens Medical Solutions USA, Inc.
Cardiovascular Research and Development
737 N Michigan Ave
STE 1600
Chicago, IL 60611
USA
peter.weale@siemens.com

Improved Workflow and Performance for Contrast-Enhanced MR Angiography Sequences

Gary R. McNeal, MS BME; Yutaka Natsuaki, Ph.D.; Randall Kroeker, Ph.D.; Peter Schmitt; Gerhard Laub, Ph.D.

Siemens Medical Solutions, Inc., USA

The new software version *syngo* MR B17 provides several improvements for *syngo* TWIST (dynamic ceMRA) and FL3D_CE (static ceMRA) sequences, thereby leading to decreased scan time, reduced acoustic noise, and improved workflow.

syngo TWIST (dynamic ceMRA)

- New asymmetric slab-selective RF pulses with better slice profiles allow less slice oversampling, thereby decreasing scan time.
- New symmetric non-selective RF pulses with shorter pulse durations allow shorter TR, thereby decreasing scan time.
- New spiral centric phase-encoding trajectory allows reduced acoustic noise and reduced phase coherence artifacts.
- Switchable phase-encoding rewinder allows shorter TR, thereby decreasing scan time.

FL3D_CE (static ceMRA)

- All of the above, and:
- Freely-adjustable Time-To-Center (TTC) parameter allows improved workflow and improved visualization of arteries without venous contamination.

Probably the most significant improvement is the freely-selectable TTC. The FL3D_CE sequence is designed to visualize the signal enhancement in the vessels after the injection of a T1-shortening contrast agent. For the best visualization of the arteries, the center segment of the ky-kz plane must be acquired during the first pass of the contrast injection when only the arteries are filled with the contrast agent (will be referred to as the *Arterial Window*). Unlike the previous version of FL3D_CE which only allowed a centric ordering with the trajectory starting at kr = 0, the new version allows the use of a delayed centric ordering where the k-space trajectory starts at the edge of the center segment moving towards kr = 0, then moves outwards again, and finally scans the region outside of the center segment as shown in figure 1. The selection of k-space points is following a spiral centric trajectory in k-space.

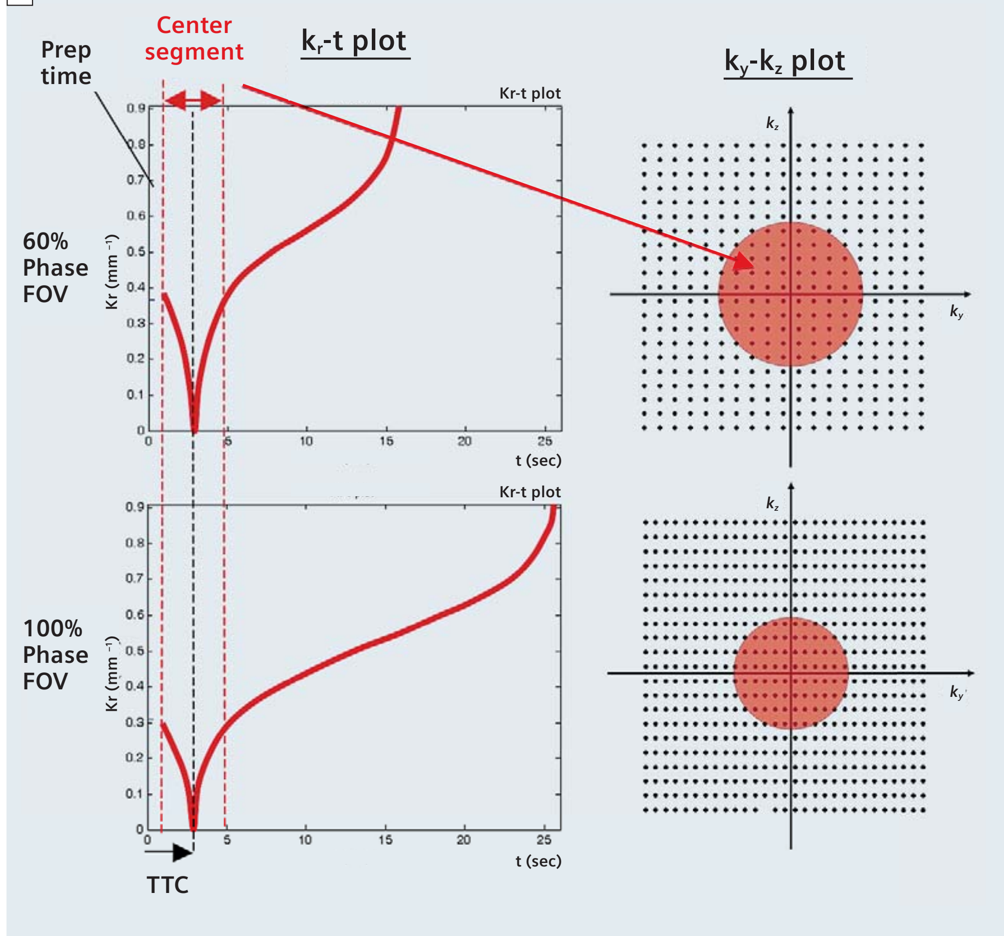

1 k_r-t and k_y-k_z plots of the spiral centric reordering for two different phase FOVs (as an example, 60% and 100%). The center segment of k-space and the TTC remain independent of other sequence parameters that effect resolution and scan duration.

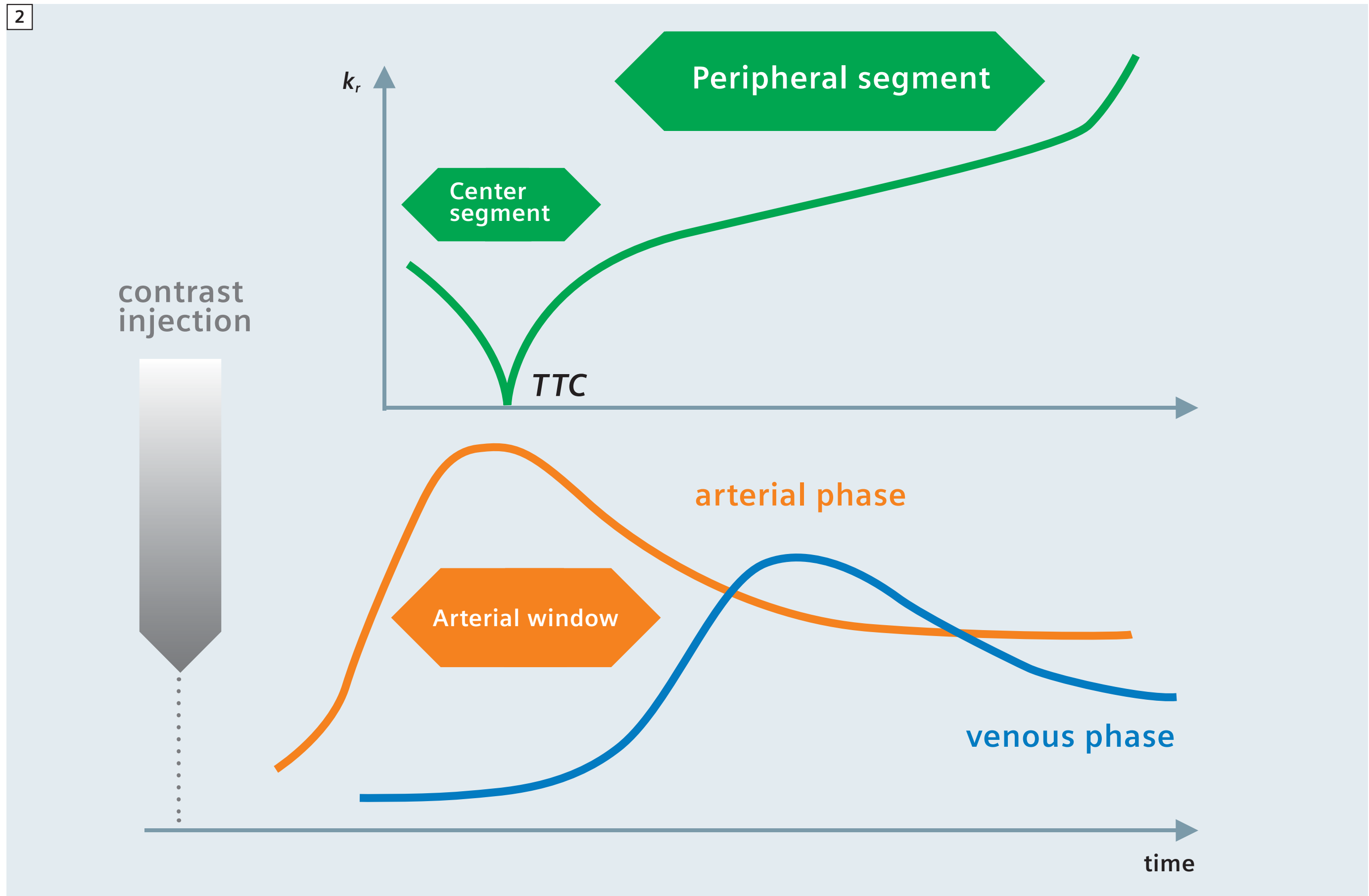

2 Choose TTC such that the center of k-space overlaps the center of the arterial window, as determined from a test bolus scan. The TTC remains fixed even if the scan time changes due to protocol changes.

It is important to note that the time-to-center (TTC) is independent of other geometric parameters used in the imaging protocol. For example, if the phase FOV is increased from 60% to 100% as shown in figure 1, the TTC will not change. What happens instead is a corresponding size (area) reduction of the center segment in k-space, while the number of k-space points in the center segment stays the same, independent of the actual value for the phase FOV. Similarly, changing other parameters (e.g., phase and slice resolution, the number of slices, or phase/slice oversampling) will not change the selected value for TTC. This has important practical implications. The center segment can be adjusted to the arterial window as demonstrated in figure 2 independent of the geometric parameters in the protocol, unlike the previous version where the TTC in the linear sequential phase encode mode (care bolus unchecked) is greyed out, and is always 3/8th of the total scan time.

When performing ceMRA using the FL3D_CE sequence, the arteries are best visualized if the center of k-space is acquired only when the arteries are filled with the contrast agent *(arterial window)*, thereby avoiding the venous phase. In combination with the new spiral centric trajectory, the new freely-adjustable Time-To-Center (TTC) parameter in *syngo* MR B17 allows the user to more easily and consistently acquire the center of k-space near the center of the arterial window because TTC is independent of other geometric parameters used in the imaging protocol (slices, matrix, FOV, oversampling, partial Fourier). This has important practical implications for workflow and image quality. As shown in figure 2, by using the new spiral centric trajectory with freely-selectable TTC one can freely change geometric protocol parameters on-the-fly (resolution and slab coverage) without using a complex formula to recalculate the appropriate scan-delay time needed to synchronize the center of k-space to the arterial window. The duration of the center segment remains fixed, while the duration of the peripheral segment increases or decreases to accommodate the protocol changes. This ensures optimal visualization of the arteries without venous contamination. Furthermore, depending on the relation between the cardiac cycle and the duration of the phase encoding loops, ghosting artifacts sometimes occur due to arterial pulsatility when using the older linear phase-encoding method. These newer methods significantly reduce such ghosting artifacts because the cardiac motion cannot create any periodic structures in k-space when a centric reordering is used.

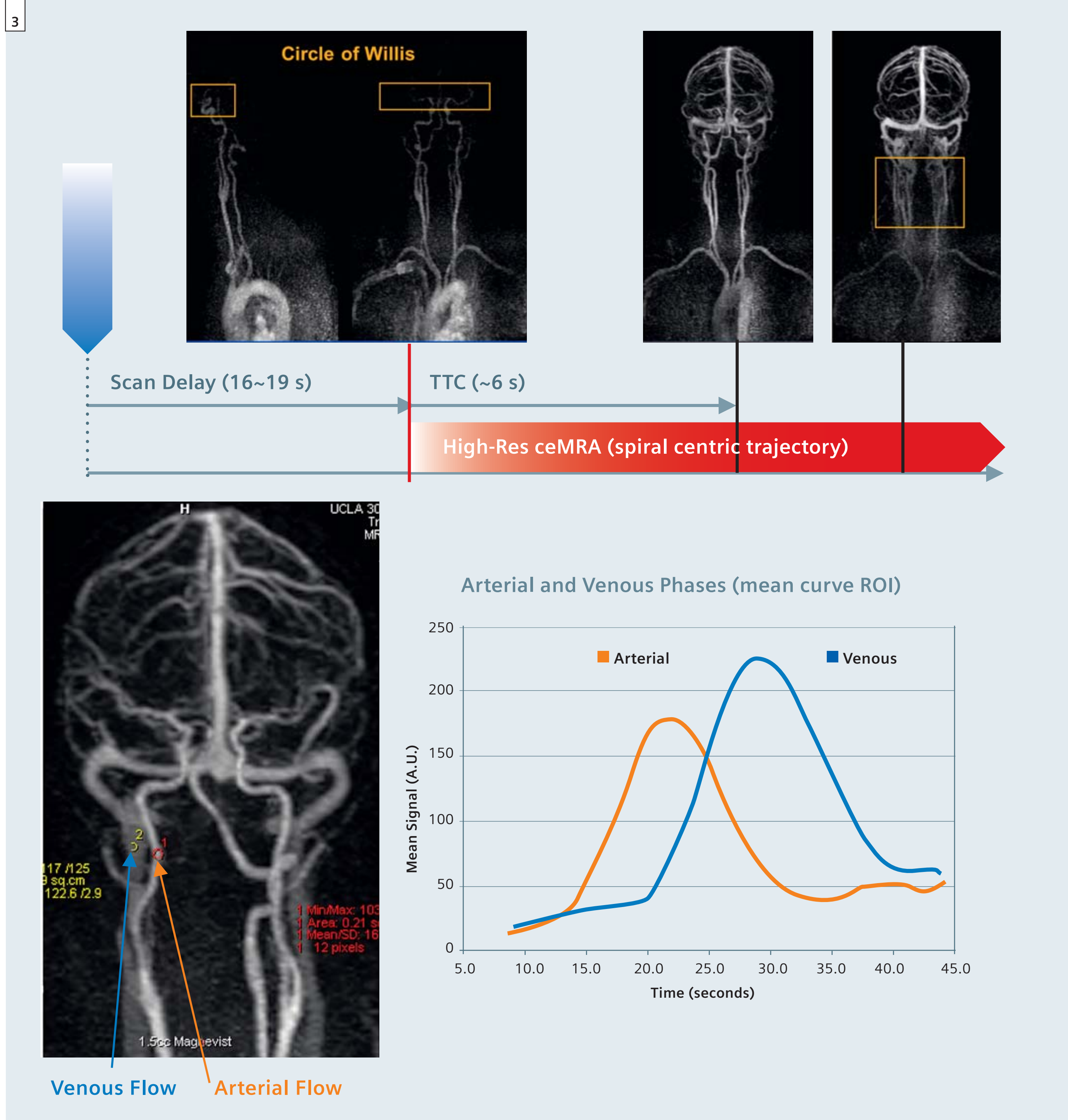

3 Optimal timing of contrast agent using *syngo* TWIST with test bolus.

MR technologists at UCLA Medical Center in Los Angeles, USA have optimized the workflow to consistently yield high quality ceMRA exams of the carotids and intracranial arteries without venous contamination. For over a year this workflow has proven successful on both the 1.5T MAGNETOM Avanto and the 3T MAGNETOM Trio, A Tim System scanners at UCLA. As depicted in figure 3, the arterial window and venous phase are determined from a *syngo* TWIST timing bolus scan (both sagittal and coronal MIPs), but any other test bolus measurement showing the signal intensity in the carotid artery and jugular vein can be used as well. The high-resolution ceMRA scan is started when the test bolus arrives at the Circle of Willis (typically about 16–19 seconds after injection). TTC is typically set to about 6 seconds, or as needed to ensure that the center of k-space is acquired just prior to jugular vein enhancement. This can be done most easily by reviewing the *syngo* TWIST timing bolus images, or more methodically by assessing the time-intensity curves of ROI's drawn on a carotid artery and a jugular vein, as in figure 3.

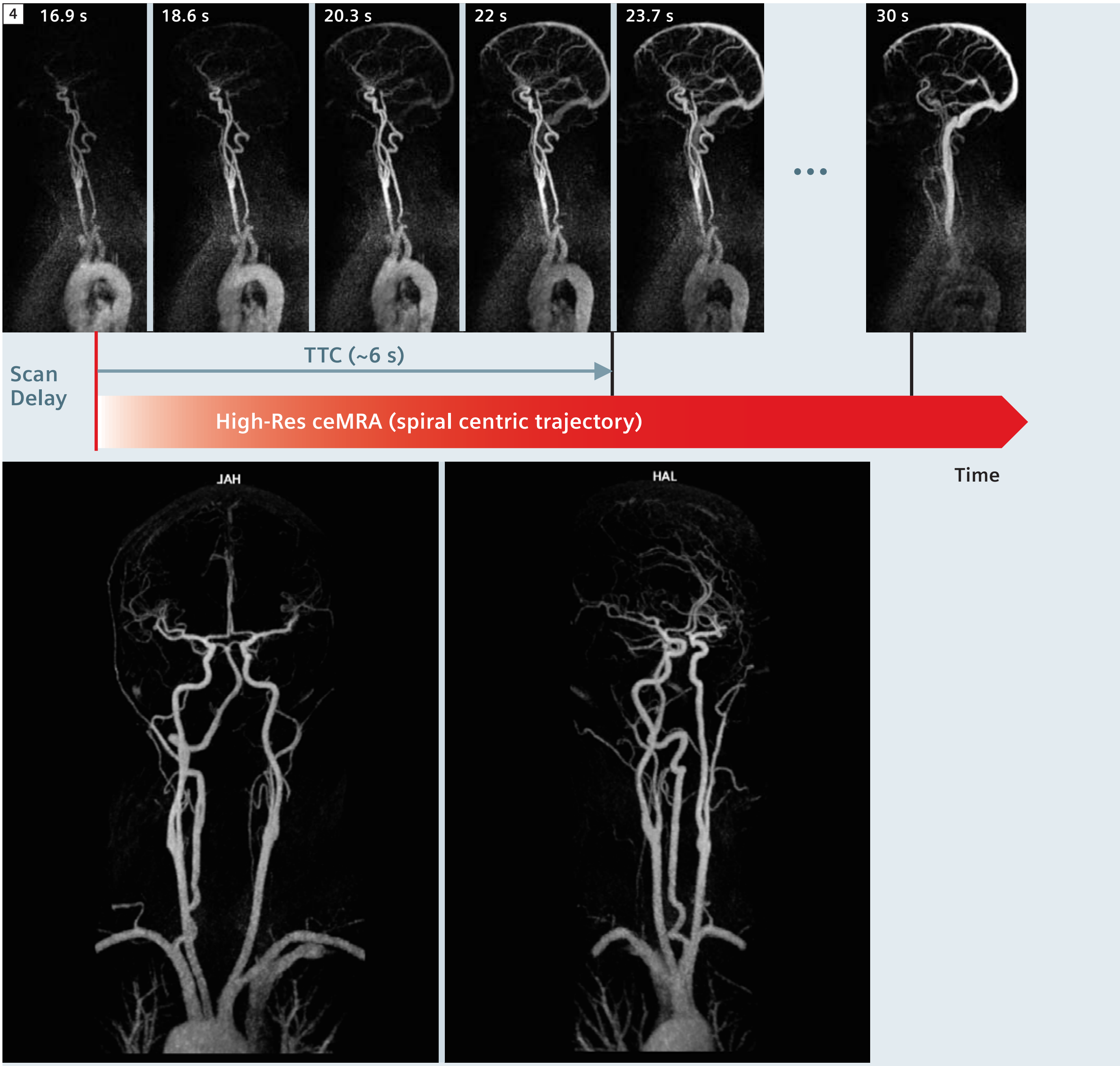

4 Results of optimized ceMRA workflow and image quality.

The results of the optimized workflow from UCLA are shown in figure 4. The *syngo* TWIST timing bolus scan shows that the bolus arrived at the Circle-of-Willis at about 17 seconds, which was used for the scan delay of the ceMRA scan. The bolus transit time from carotid arteries to jugular veins was an additional 6 seconds, which was used for the TTC of the ceMRA scan. TTC is reduced for patients with a faster venous return. The resulting high resolution MIP images of the carotids and intracranial arteries demonstrate full enhancement without venous contamination. In conclusion, the new *syngo* MR B17 version of FL3D_CE with spiral centric reordering does indeed improve workflow and improve image quality of ceMRA.

Contact
Gary McNeal
Advanced Application Specialist
Cardiovascular MR R&D
Siemens Medical Solutions USA, Inc.
737 N Michigan Ave
Suite 1600
Chicago, IL 60611
USA
Gary.mcneal@siemens.com

Further Reading Case Report: Trevor's Disease

The fascinating article on Trevor's Disease, by Yoshihiko Fukukura, M.D. (Kagoshima University, Japan), profiled on the cover of the most recent issue of MAGNETOM Flash, has unsurprisingly attracted huge interest from our readers.

In response, we are delighted to include further information on this interesting topic on our MAGNETOM World website.

For extra details and clinical images, visit

www.siemens.com/magnetom-world

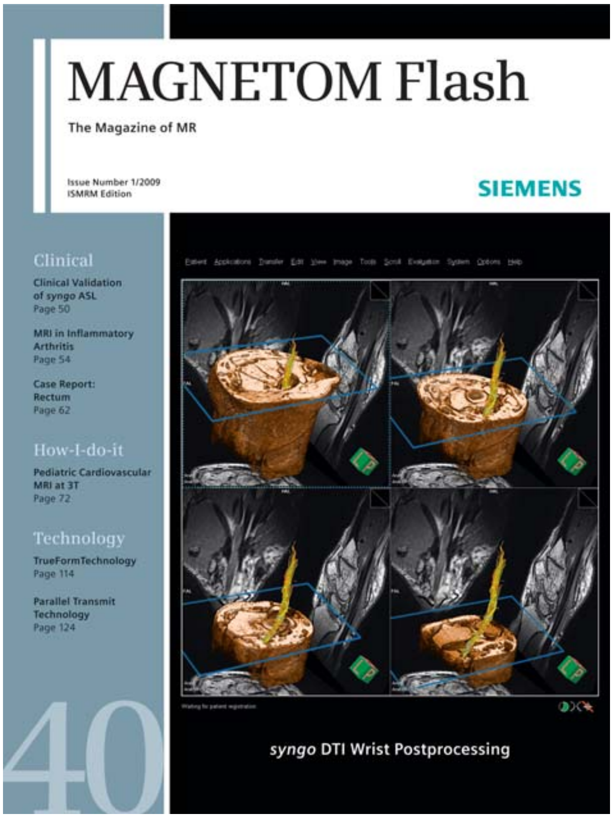

MAGNETOM Flash

The Magazine of MR

Issue Number 1/2009
ISMRM Edition

SIEMENS

Clinical
Clinical Validation of syngo ASL
Page 50
MRI in Inflammatory Arthritis
Page 54
Case Report: Rectum
Page 62

How-I-do-it
Pediatric Cardiovascular MRI at 3T
Page 72

Technology
TrueFormTechnology
Page 114
Parallel Transmit Technology
Page 124

40

syngo DTI Wrist Postprocessing

MAGNETOM Flash – Imprint

Publisher:
Siemens AG
Medical Solutions
Business Unit Magnetic Resonance,
Karl-Schall-Straße 6, D-91052 Erlangen,
Germany

Editor-in-Chief: Dr. Matthias Lichy, M.D.
(matthias.lichy@siemens.com)

Associate Editor: Antje Hellwich
(antje.hellwich@siemens.com)

Production: Norbert Moser, Siemens AG,
Medical Solutions

Layout: independent Medien-Design
Widenmayerstrasse 16, D-80538 Munich

Printers: Farbendruck Hofmann, Gewerbestraße 5,
D-90579 Langenzenn, Printed in Germany

MAGNETOM Flash is also available on the internet:
www.siemens.com/magnetom-world

Note in accordance with § 33 Para.1 of the German Federal Data Protection Law: Despatch is made using an address file which is maintained with the aid of an automated data processing system.
MAGNETOM Flash with a total circulation of 20,000 copies is sent free of charge to Siemens MR customers, qualified physicians, technologists, physicists and radiology departments throughout the world. It includes reports in the English language on magnetic resonance: diagnostic and therapeutic methods and their application as well as results and experience gained with corresponding systems and solutions. It introduces from case to case new principles and procedures and discusses their clinical potential.
The statements and views of the authors in the individual contributions do not necessarily reflect the opinion of the publisher.
The information presented in these articles and case reports is for illustration only and is not intended to be relied upon by the reader for instruction as to the practice of medicine. Any health care practitioner reading this information is reminded that they must use their own learning, training and expertise in dealing with their individual patients. This material does not substitute for that duty and is not intended by Siemens Medical Solutions to be used for any purpose in that regard. The drugs and doses mentioned herein are consistent with the approval labeling for uses and/or indications of the drug. The treating physician bears the sole responsibility for the diagnosis and treatment of patients, including drugs and doses prescribed in connection with such use. The Operating Instructions must always be strictly followed when operating the MR system. The sources for the technical data are the corresponding data sheets. Results may vary.
Partial reproduction in printed form of individual contributions is permitted, provided the customary bibliographical data such as author's name and title of the contribution as well as year, issue number and pages of MAGNETOM Flash are named, but the editors request that two copies be sent to them. The written consent of the authors and publisher is required for the complete reprinting of an article.
We welcome your questions and comments about the editorial content of MAGNETOM Flash. Please contact us at magnetomworld.med@siemens.com. Manuscripts as well as suggestions, proposals and information are always welcome; they are carefully examined and submitted to the editorial board for attention. MAGNETOM Flash is not responsible for loss, damage, or any other injury to unsolicited manuscripts or other materials. We reserve the right to edit for clarity, accuracy, and space. Include your name, address, and phone number and send to the editors, address above.


MAGNETOM Flash

The Magazine of MR

Issue Number 2/2009
ASTRO/ESTRO Edition

SIEMENS

Clinical

Prostate Imaging at 3T
Page 6

IVIM f-maps of Pancreatic Lesions
Page 26

Nonsecretory Multiple Myeloma
Page 34

TWIST MRA of Pelvic Congestion Syndrome
Page 58

Product News

What's new with software version syngo MR B17
Page 92

41

SUBSCRIBE NOW!

– and get your free copy of future MAGNETOM Flash! Interesting information from the world of magnetic resonance – gratis to your desk. Send us this postcard, or subscribe online at **www.siemens.com/MAGNETOM-World**

Siemens AG
Medical Solutions
Magnetic Resonance
Antje Hellwich - Marketing
P.O. Box 32 60
D-91050 Erlangen
Germany

MAGNETOM
Flash

Subscription

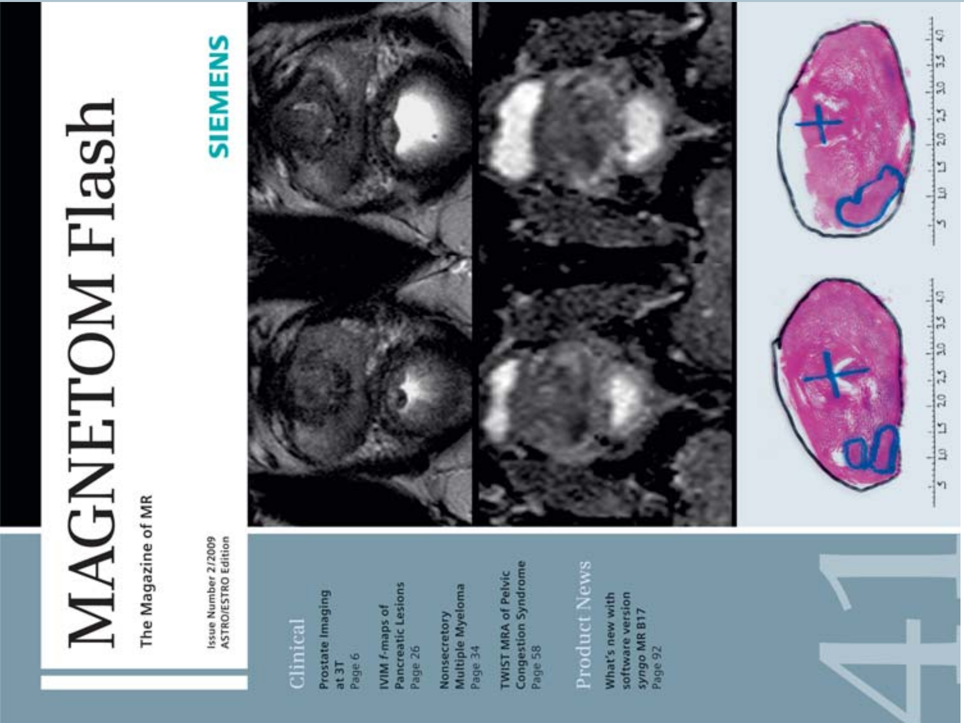

MAGNETOM Flash

The Magazine of MR

Issue Number 2/2009
ASTRO/ESTRO Edition

SIEMENS

Clinical

Prostate Imaging at 3T
Page 6

IVIM *f*-maps of Pancreatic Lesions
Page 26

Nonsecretory Multiple Myeloma
Page 34

TWIST MRA of Pelvic Congestion Syndrome
Page 58

Product News

What's new with software version *syngo* MR B17
Page 92

41

Please enter your business address

Institution

Department

Function

Title

Name

Street

Postal Code

City

State

Country

MR system used

Please include me in your mailing list for the following Siemens Healthcare customer magazine(s):

☐ Medical Solutions

☐ MAGNETOM Flash

☐ SOMATOM Sessions

☐ AXIOM Innovations

Stay up to date with the latest information
Register for:

☐ the monthly e-Newsletter

E-mail

☐ Yes, I consent to the above information being used for future contact regarding product updates and other important news from Siemens.

☐ unsubscribe from info service

Please print clearly!

Global Siemens Headquarters

Siemens AG
Wittelsbacherplatz 2
80333 Muenchen
Germany

Global Siemens Healthcare Headquarters

Siemens AG
Healthcare Sector
Henkestr. 127
91052 Erlangen
Germany
Phone: +49 9131 84-0
www.siemens.com/healthcare

www.siemens.com/healthcare-magazine

Order No. A91MR-1000-64C-7600 | Printed in Germany | CC MR 01000 ZS 080910. | © 08.09, Siemens AG

Global Business Unit

Siemens AG
Medical Solutions
Magnetic Resonance
Henkestr. 127
DE-91052 Erlangen
Germany
Phone: +49 9131 84-0
www.siemens.com/healthcare

Local Contact Information

In Asia
Siemens Pte Ltd
The Siemens Center
60 MacPherson Road
Singapore 348615
Phone: +65 6490-8096

In Canada
Siemens Canada Limited
Medical Solutions
2185 Derry Road West
Mississauga ON L5N 7A6
Canada
Phone: +1 905 819-5800

Europe/Africa/Middle East
Siemens AG
Medical Solutions
Henkestr. 127
91052 Erlangen
Germany
Phone: +49 9131 84-0

Latin America
Siemens S.A.
Medical Solutions
Avenida de Pte. Julio A. Roca No 516,
Piso 7
C1067ABN Buenos Aires
Argentina
Phone: +54 11 4340-8400

USA:
Siemens Medical Solutions U.S.A., Inc.
51 Valley Stream Parkway
Malvern, PA 19355-1406
USA
Phone: +1-888-826-9702